Overall Performance Evaluation of Building Integrated Photovoltaics (BIPV) as Active Building Envelope Systems

Kai Ye

A Thesis

in

The Department

of

Building, Civil, and Environmental Engineering

Presented in Partial Fulfillment of the Requirements

for the Degree of Master of Applied Science (Building Engineering) at

Concordia University

Montreal, Quebec, Canada

August 2023

© Kai Ye, 2023

CONCORDIA UNIVERSITY
School of Graduate Studies

This is to certify that the thesis prepared

By: Kai Ye

Entitled: Overall Performance Evaluation of Building Integrated Photovoltaics (BIPV) as Active Building Envelope Systems

and submitted in partial fulfillment of the requirements for the degree of

Master of Applied Science (Building Engineering)

complies with the regulations of the University and meets the accepted standards with respect to originality and quality.

Signed by the final examining committee:

_____ Chair
Dr. Liangzhu Wang

_____ Examiner
Dr. Caroline Hachem-Vermette

_____ Examiner
Dr. Liangzhu Wang

_____ Thesis Supervisor(s)
Dr. Hua Ge

_____ Thesis Supervisor(s)
Dr. Andreas Athienitis

Approved by _____
Dr. Chunjiang An, Graduate Program Director

August 14, 2023 _____
Dr. Mourad Debbabi, Dean of Gina Cody School of Engineering and Computer Science

ABSTRACT

Overall Performance Evaluation of Building Integrated Photovoltaics

(BIPV) as Active Building Envelope Systems

Kai Ye

The application of photovoltaics in buildings for solar energy power generation in urban areas is developing quickly. As a result, building-integrated photovoltaic (BIPV) systems have emerged as multi-functional systems that not only produce electricity on-site but also replace conventional building envelope components and integrate with mechanical systems. Although characterization of the electrical performance in the photovoltaics used in these systems is provided by manufacturers, without clear evaluations of the building envelope and mechanical performance parameters of these systems for comparison to traditional building system components, it is challenging for architects, engineers, and building owners to make informed decisions regarding their implementation in building design.

This thesis aims to evaluate the characteristics of building integrated photovoltaic systems as components of the building envelope and mechanical systems. Different types of building integrated photovoltaic systems in different implementation scenarios are studied, including opaque building integrated photovoltaic/thermal (BIPV/T) systems coupled with a heat recovery ventilator (HRV) in a curtain wall construction (where the photovoltaic panels form the external cladding of the building envelope and the heat captured by the airflow behind the cladding is used in preheating the HRV), BIPV cladding integrated with wood-frame construction, and semitransparent photovoltaic (STPV) glazing units (double pane insulated glazing units forming the exterior glazing of the building envelope). The key parameters evaluated are thermal efficiency, energy generation, sensible recovery efficiency (SRE) and supply air outlet temperature increase $\Delta T_{SA,HRV}$ when coupled with HRV, the moisture content in wood frame construction for opaque BIPV building envelopes, and solar heat gain coefficient (SHGC) for STPV glazing units. Field measurements were performed for these implementation scenarios to characterize their performance and were compared to simulations. Although the simplified approaches used in this thesis to model their performance through simulation have limitations in their ability to reflect field operating conditions, the field measurements and hygrothermal modeling results show that BIPV systems in these scenarios can perform better than conventional building components.

Table of Contents

List of Figures

List of Tables

List of Abbreviations

ACH - Air Changes per Hour

Avg - average

BIPV - Building Integrated Photovolatics

BIPV/T - Building Integrated Photovolatic / Thermal System

BIPV/T+HRV - Building Integrated Photovolatic / Thermal System integrated with Heat Recovery Ventilator

BIPV-MPP - BIPV Cladding in Maximum Power-Point tracking electrical state

BIPV-OC - BIPV Cladding in Open-Circuit electrical state

CoG - Center of Glazing

ERV - Energy Recovery Ventilator

FBIPV/T - BIPV/T Integration Factor

HRV - Heat Recovery Ventilator

IGDB - International Glazing Database

IGU - Insulated Glazing Unit

IR - infrared

Max - maximum

MC - Mositure Content

Min - minimum

MPP - Maximum Power-Point

Nu - Nusselt number

OC - Open-Circuit

OSB - Oriented Strand Board

Qu - thermal energy captured by BIPV/T

Re - Reynolds number

RH - Relative Humidity

RMSE - Root Mean Square Error

SH - Short-Circuit

SHGC - Solar Heat Gain Coefficient

SRE - Sensible Recovery Efficiency

STPV - Semi-transparent Photovoltaics

U-value - Overall heat transfer coefficient

WINDOW - Berkeley Lab WINDOW, window thermal performance calculation software

WUFI - Wärme Und Feuchte Instationär, heat and moisture transient hygrothermal calculation software

XPS - extruded polystyrene thermal insulation

1. Introduction

1.1. Background

The application of photovoltaics in buildings for solar energy power generation in urban areas is developing quickly. As a result, building-integrated photovoltaic (BIPV) systems, including semi-transparent photovoltaic (STPV) and building-integrated photovoltaic/thermal (BIPV/T) systems have emerged as multipurpose systems that not only produce electricity on-site but also replace conventional building envelope components and integrate with mechanical systems. This integration of multiple aspects of a building brings the additional benefits of reduced construction material, and increasing the operating range, energy efficiency and flexibility of the active ventilation or mechanical systems it is coupled to (Yang and Athienitis, 2016; Yu et al., 2021). Despite being a promising technology with these benefits, BIPV/T is still not widely adopted in the building industry due to several barriers. Although characterization of the electrical performance in the photovoltaics used in these systems is provided by manufacturers, without clear evaluations of the building envelope and mechanical performance parameters of these systems for comparison to traditional building system components, it is challenging for architects, engineers, and building owners to make informed decisions regarding their implementation in building design. BIPV components have various interactions with the building several aspects need to be taken into consideration for a comprehensive assessment, including electrical performance, thermal processes at the component level, seasonal variations in thermal performance, ventilation performance, visual performance, as well as maintenance and durability (Bloem et al., 2012).

A BIPV module consists of multiple layers that form a laminate. The layers are the front cover, encapsulant, PV cells, encapsulant, and back cover. (Martín-Chivelet et al., 2022). The BIPV/T curtainwall ventilated façade and the semitransparent photovoltaic (STPV) windows installed at the Future Buildings Laboratory (FBL) at Concordia University fall into the category of BIPV façade systems (Bonomo et al., 2021). There is a need for more extensive research on the design and performance measurement of BIPV facade systems. Currently, significant attention has been given to BIPV systems in rooftop applications, leaving the facade systems with less extensive investigation. Many studies have been done on determining the thermal performance of BIPV/T systems using a combination of numerical modeling and controlled experiments. To theoretically evaluate the thermal performance of BIPV/T systems, the modeling of the heat transfer phenomenon in the BIPV/T air cavity needs to be accurate. Many correlations relating it to the Nusselt number and air velocity have been developed (Candanedo et al., 2011; Chen et al., 2010; Yang and Athienitis, 2015). Although the numerical models have been typically developed under well controlled boundary conditions using indoor solar simulators, testing BIPV/T outdoors is important because even testing the same BIPV/T system outdoors can result in different correlations. It has been suggested to perform both indoor and outdoor tests of a reference BIPV/T system to develop a correction factor between results which would then allow correlations from indoor tests better reflect real operating conditions (Rounis et al., 2021).

This correction method approach has also been used in the testing of solar heat gain coefficient (SHGC), which is a standard performance indicator for conventional glazing systems to compare their ability to heat up the indoor environment in the presence of sunlight. This metric has been

difficult to determine for BIPV and semi-transparent photovoltaic glazing because there can be significant differences in SHGC depending on whether or not electricity is being generated, and these systems are typically optically inhomogeneous, meaning some parts of the product would consist of clear conventional glass while other parts would be covered by PV cells (Martín-Chivelet et al., 2022). Some previous work has been done to account for these challenges in measuring the solar heat gain coefficient of these systems using indoor solar simulators and applying a correction factor for the mismatch in solar spectrum (Kapsis et al., 2017).

In terms of applying the numerical models to predict field performance, previous work studying the rooftop BIPV/T system at the Varennes library has shown that using a transient model only have marginal improvements and steady state models can provide acceptable results, and suggested that the most important parameters to determine for BIPV/T system modeling are the PV and cavity outlet temperatures (Sigounis, 2022).

To aid in the adoption of BIPV facade systems in the field of building design, quantifiable performance indicators are required. Building professionals require a means of comparing the expected field performance of BIPV systems against conventional building envelope and active system components. This thesis aims to focus on the theoretical and experimental methodologies for determining some of these performance indicators specifically relevant to BIPV facade systems including, moisture content, mould index, solar heat gain coefficient (SHGC), the increase in operating temperature range for integrated systems, and thermal efficiency.

1.2. Objectives

This thesis aims to evaluate the performance characteristics of BIPV systems as components of the building envelope and mechanical systems. Particular focus will be on BIPV façade systems, including the field performance measurement at the FBL with its BIPV/T integration with the Heat Recovery Ventilator (HRV) and STPV windows.

The goal of the experimental and simulation studies presented in the thesis is to develop practical methods for evaluating BIPV facades in key parameters which can be used to compare them with conventional construction including the overall heat transfer coefficient, and moisture damage risk (moisture content and mould growth index) for wall assemblies, U-value and solar heat gain coefficient (SHGC) for STPV windows. Temperature rise in the BIPV air cavity and the thermal efficiency of heat generation from the BIPV/T as well as the performance improvements of a heat recovery ventilator by integrating the two together are to be determined through field measurements.

A simple thermal network finite difference model was used to examine the FBL BIPV/T façade using Python and comparing to field measurements. The simple model was used to estimate the daily thermal and electric energy output of the BIPV/T system. A prototype manifold was designed to integrate the BIPV/T façade with a HRV and field monitoring data of the system was examined to evaluate the HRV performance improvement.

The hygrothermal performance of BIPV/T integrated with wood frame was evaluated using WUFI simulations based on a potential future BIPV wood frame wall assembly configuration to be tested at the FBL. A method for determining the theoretical SHGC of STPV was examined. A method for estimating the angular dependent SHGC of conventional glazing using WINDOW 7.7 was developed for an insulated glazing unit (IGU) at the FBL. An experimental method for in-situ field measurement of SHGC was demonstrated on the same IGU for comparison.

The models and measurement methods presented for these studies may be used for early design decision making. The thesis intends to be a start for developing methods for using BIPV façade system models to assess design performance pre-construction, and for commissioning of BIPV façade system performance through on-site measurements post-construction.

1.3. Scope of the thesis

The integration scenarios studied in this thesis include:

1) BIPV/T curtainwall ventilated façade – focused on the air cavity side of the integration, analysis of modeled and measured energy performance of BIPV curtainwall cladding with a mechanically ventilated cavity
2) HRV integrated with BIPV/T – focused on the HRV side of the integration, design of BIPV/T manifold for HRV integration and analysis of measured performance improvement of HRV
3) BIPV façade in wood frame construction – analysis moisture damage potential of low-rise residential wood frame construction with BIPV or BIPV/T cladding through simulation
4) STPV glazing – presentation of method to determine SHGC of STPV glazing through calculation and analysis of preliminary in-situ SHGC measurement method using an IGU as reference specimen

Chapter 1 provides the background for BIPV façade integration, and the motivation for the scope of the thesis.

Chapter 2 presents the literature review on the current state of BIPV façade integration and methods developed to characterize their performance in terms of energy and hygrothermal behavior.

Chapter 3 presents the experimental setup measured thermal efficiency, temperature profile, and heat energy captured in the BIPV/T curtain wall facade at the FBL. A simple thermal energy model of the façade system is developed and compared to the field measurements.

Chapter 4 details the process to integrate the HRV with a prototype manifold design, and the field performance of preheating the HRV using heat captured by the airflow behind the BIPV cladding. Challenges and sources of error are identified.

Chapter 5 presents hygrothermal simulations of a BIPV façade integrated in low-rise residential wood frame construction to evaluate the moisture risks of BIPV façade replacing conventional cladding.

Chapter 6 presents a theoretical workflow for determining the in-situ solar heat gain coefficient (SHGC) of STPV glazing through calculations and measurements. A preliminary experiment to perform in-situ measurements of SHGC is explored with challenges and potential sources of error identified.

Chapter 7 summarizes the studies done in the thesis. Contributions and future directions of the research have been identified.

2. Literature Review

2.1. BIPV Integration

State of the art

A recent review of the main energy-related features of building-integrated photovoltaic (BIPV) modules and systems has been published to serve as a reference for researchers, architects, BIPV manufacturers, and BIPV designers. The paper identifies the key performance characteristics for benchmarking BIPV systems: thermal and solar performance, optical performance, electrical performance. Heat transfer basics of BIPV modules were discussed in terms of energy balance at each layer of the BIPV system which can be used to examine the thermal efficiency, thermal transmittance, BIPV module temperature, and solar heat gain coefficient (SHGC). Discussion on various factors such as shading, spectral effects, and non-homogeneous irradiance conditions for BIPV systems were made, along with the consideration of optical performance for a good balance between energy saving, electricity generation, aesthetics, and visual comfort. Electrical performance of BIPV modules and systems, including the challenges faced by electrical designers due to the special operating conditions of BIPV systems, such as non-homogeneous irradiance, and how architecturally adapted BIPV design may affect the electrical performance were discussed. Several modelling software have been developed to simulate the electrical, thermal, and inverter performance of BIPV. Most of these softwares are built on the EnergyPlus whole building energy modelling engine. However, the capability of performing dynamic simulations for thermal performance presented is currently limited to BIPV module temperature. Furthermore, there seems to be a lack of identified tools or software that can effectively simulate the performance of BIPV/T systems which produce both electrical and thermal energy. The paper highlights the need for suitable standardization to evaluate the energy-related behavior of BIPV modules and systems, including the development of standards to evaluate heat transfer and solar heat gain by BIPV modules (Martín-Chivelet et al., 2022).

A state-of-the-art review of modelling and management tools relevant to BIPV integration by IEA PVPS Task 15 in 2019 found that none of the tools that were examined can address all the factors associated with project design and management for photovoltaic projects. The results indicate that most tools used for building integrated photovoltaics modeling primarily focus on PV systems and thus lack crucial features related to BIPV integration, particularly when it comes to vertical or externally mounted BIPV installations. The development of a decision support system was proposed to address practical challenges faced by stakeholders. The main features of this system include: a localized data repository encompassing weather information, building regulations, energy consumption in various building sectors, utility prices, construction and maintenance costs, contract types, financial modes, carbon prices and government incentive schemes; efficient creation of 3D models representing the physical environment; hourly comparison between energy input and output; optimization of PV layout design; simulation of installation processes and analysis of their impact; modules for monitoring and inspection with automatic diagnosis function; recording performance metrics related to PV systems; and sensitivity analysis capability along with scenario-based decision-making support (Jakica et al., 2019).

Technological design options for BIPV components and systems have been previous reviewed in literature with focus on their relevance for renewable energy systems in the German BIPV market. The review concludes that crystalline silicon-based solar cell technologies offer the greatest advantages for BIPV applications, and future development should include demonstration projects that increase visibility and experience with BIPV, innovative business models, and increased digitalization throughout the construction process (Kuhn et al., 2021).

Façade-based BIPV/T systems, which combine solar photovoltaics and solar collectors to generate electricity and produce thermal energy, have been reviewed in literature. A review paper examined the development of BIPVT systems and their designs, focusing on their influence on electricity generation, thermal performance of PV cells, and energy consumption of buildings for space heating and cooling. The paper classifies façade-based BIPV/T systems into seven types based on the use of thermal energy from the claddings. These types are: Cooling of PV by air, space heating systems, ventilation systems, water heating systems, PV-Phase Change Material (PCM) systems, heat pump integrated systems, and photovoltaic thermoelectric wall systems. The BIPV/T ventilation systems are similar to passive space heating BIPV/T systems, where BIPV/T systems are designed for fresh air heating through an air cavity between the PV panels and the wall, but the airflow within the air cavity is mechanically ventilated. The air cavity enhances the system's electrical efficiency, and the airflow within the air cavity can be captured by mechanical ventilation for preheating fresh air. Most mathematical modeling and experimental verification studies for these systems are classified as PV double skin wall. During summer, the heated airflow is often released directly to the outdoors, and during winter, it is directed into the building through wall openings which require design consideration to avoid undesirable air infiltration. To increase thermal energy conversion efficiency, a different design category combines photovoltaic and unglazed transpired collector (UTC) on a façade through an improved air cavity design. The BIPV-UTC system draws outdoor air through a heated porous plate and PV panels, resulting in a total equivalent thermal efficiency of the BIPV-UTC system slightly higher than that of a single UTC. The paper provides a comprehensive review of various typical and novel designs developed globally over the past 20 years, assessing their electrical output, thermal performance, and impact on building's heating/cooling load. The paper proposes more research on the shading effects of façade-based BIPV/T, BIPV/T using refrigerants for heat absorption or anti-freezing purposes, and Life Cycle Cost of Assessment (LCCA) of BIPV/T systems. The paper suggests future research directions of improving the performance and reducing costs of water-based BIPVT systems, and the analysis of heating and cooling loads effected by the integrations of PVT collector with building façades (Yu et al., 2021).

Integration barriers

An extensive review of the challenges in implementing BIPV in the construction field has been performed. Several technical barriers and risks associated with the application of BIPV from building design through to operation stages were identified. The technical barriers and risks are categorized into three stages: design, construction and installation, and commissioning. At the design stage, there is lack of knowledge and experience of architects and engineers in considering maintenance and replacement, structural and mechanical loads, BIPV system choice and positioning, heat transfer issues, fire safety and noise protection, lack of BIPV specific design standards, and difficulty in predicting technical issues. Solutions to these barriers include engaging BIPV technicians at the early design stage and using advanced simulation tools to predict technical issues relating to BIPV. At the construction and installation stage, there is difficulty in fixing BIPV

modules to building envelopes, wind-driven rain penetration, cabling protection, and islanding issues. Solutions are lacking and need to be developed for these issues. At the commissioning stage, there is technical difficulty in commissioning BIPV systems and lack of knowledge and experience of technicians in BIPV commissioning. Recommendations include providing training and education for technicians in BIPV commissioning and using energy performance monitoring platforms for fault detection and maintaining proper function of BIPV systems. Suggested directions for future research in the field of BIPV include developing design improvements to solve heat, noise, and corrosion issues, investigating lifecycle cost analysis to assess the costs associated with owning BIPV systems, developing innovative procurement strategies to promote the application of BIPV in larger communities, identifying the critical stakeholder relationship and information flows in the problem solving process, and developing BIM technology-based BIPV visualization during the design stage to increase constructability, planning, scheduling, and reduce safety risks (Yang, 2015).

Technical barriers and risks associated with the application of BIPV have been identified in a literature review from building design to operation stages. The review paper shows that although research in BIPV performance and optimization has gained increasing attention recently, their practical applications have been slow in comparison with the conventional rack-mounted PV panels. The review identified the most studied topics related to the BIPV systems which are mainly on the performance of the system and the heat transfer mechanisms taking place in the systems. From the literature review, 10 barriers were identified that limit the adoption and application of BIPV systems in practice. These barriers include heat transfer issues related to overheating modules and transfer of heat into the building, the lack of system performance monitoring and commissioning post-installation, the lack of modelling the expected behavior of the system during the design phase, the lack of easy access for maintenance and replacement in BIPV designs, the lack of standardization in integrating PV to the building envelope necessitating custom-made structures and components, the lack of standards and regulations for the fire and electrical safety of BIPV installations, the unclear codes or standards for noise control of BIPV systems in the building envelope, limitations of BIPV positioning due to aesthetic considerations, the lack of allowance for extra live loads related to PV modules in extreme weather conditions leading to failures, and concerns for the lifecycle costs of the BIPV system in both new construction and retrofits. It was concluded that several areas of improvement are needed for BIPV systems, including the reduction of weight in panels, management of aesthetic and safety concerns for the PV panel and cables, integration of PV panels as a construction material to the building envelope, elimination of glare with use of proper coatings on external panel surfaces, development of color, thickness and shape variety in PV panels, integration for other building elements such as balconies and canopies, design of water-based heat transfer in BIPV systems, integration of PV in earlier stages such as PV cells in pre-fabricated concrete plates, development of smart glazing that dynamically respond to shading requirements using thin laminate or paint layer solar cell materials, integration of PV to existing building retrofits, optimization of air cavity width at different heights for naturally ventilated BIPV systems, application of advanced simulation tools outside of scientific publications to predict BIPV system performance for use by building industry stakeholders, and the development of guidelines and standards for BIPV from installation to operation and maintenance (Agathokleous and Kalogirou, 2020).

Integration of BIPV/T+HVAC

Simulations were performed using code implemented in MATLAB for four different configurations of the BIPV/T systems integrated with HRVs for a 120 m^2 house located in Iqaluit, NU, Canada, including a south-facing façade 1.65 to 8.25 m^2 installation and three south-facing roof 2.75 to 13.75 m^2 installations with different tilt angles (from 10 to 30 degrees). One-year simulation is performed for each configuration using hourly weather data and different air speeds (0.5 to 2.5 m/s) in the cavity behind the PV panels. The results of the simulations are analyzed to determine the air speed that maximizes integration with the HRV system. The HRV operation control strategy is optimized based on the level of thermal energy available and the outlet air temperature from the BIPV/T system. Results show that the outlet air of a BIPV/T façade installation can be 14.8 °C higher than outdoor air on a clear sky winter day. The defrost cycle of the HRV system can be reduced by 13% (up to 619 hours) for the south-facing façade, and 11.17 to 12.93% for the south facing roof installations annually, by pre-heating the incoming fresh air with the heat generated by the BIPV/T system. The air speed of 0.5 m/s maximizes the frost control time and, therefore, the integration with HRV. The paper concludes that integrating BIPV/T systems with HRVs can improve the performance of HRVs under extreme cold climates. The results show that pre-heating the incoming fresh air with the heat generated by the BIPV/T system can reduce the defrost cycle of the HRV system and improve the reliability of HRVs to provide adequate ventilation required for maintaining a healthy indoor environment. The simulation results show that integrating BIPV/T systems with HRVs can be viable in the northern climate and implementing the HRV integration on the south-facing façade can be slightly better than on roof installations (Toffanin et al., 2019).

Whole building simulation involving BIPV/T

Attempts have been made to perform dynamic building performance modelling of an active BIPV façade using BIM. Specially, using Autodesk Revit for BIM modeling of the building, the visual programming add-in Dynamo for computationally generating the complex geometry of the active BIPV facade, and Autodesk Insight 360 for cloud-based energy and environmental performance simulation powered by Green Building Studio. The study demonstrated problems in software interoperability due to errors in converting the complex geometry generated by Dynamo to the Energy Analytical Model (EAM) format in Insight 360. With most of the geometries of the transferred EAM being broken and inconsistent with the intended design, the building performance simulation results from Insight 360 may be unreliable in this application (Somboonwit et al., 2017).

In a simulation-based study for the optimization of BIPV/T system and passive solar design in northern housing, it has been shown that BIPV integration with HVAC systems can have quantifiable energy efficiency benefits, but with more significant improvements in defrost time and cold weather extended operation than in total energy consumption. Integration with HRV may be overall more beneficial in reducing energy consumption than ASHP due to mismatch of solar availability and heating energy demand. First, optimization of the envelope design parameters based on a reference house in compliance with NBCC under climate condition of Yellowknife were investigated. Then, multi-objective optimization is carried out to determine the optimal values of the design parameters by considering the initial construction cost and life-cycle operational energy cost. The modelling of the integration of BIPV/T with HVAC systems on the optimized house was performed by modelling the BIPV/T system using a thermal network and finite difference model of the BIPV/T's electric and thermal energy in MATLAB, modelling a

reference house in EnergyPlus, rewriting the EnergyPlus .idf file using MATLAB, then using EnergyPlus to perform simulation on the modified .idf file, and using MATLAB to analyze the results and rewrite new iterations of the .idf file using the Multi-Objective Genetic Algorithm optimization tool box. Three different integration strategies, the outdoor air mixer, heat recovery ventilator (HRV), and air source heat pump (ASHP) were investigated. In the outdoor air mixer integration strategy, the heated air under PV panel is directly mixed with return air and sent to rooms for space heating. In the HRV integration, the heated air is sent to the outdoor air inlet of HRV to reduce the defrost time and preheat outdoor air. In the ASHP integration, the heated air is sent to the outdoor unit of ASHP to improve its Coefficient of performance (COP) and extend operation in cold outdoor conditions. The climatic effect is investigated by analyzing the performance for two additional locations, Kuujjuaq in Northern Quebec and Resolute in Nunavut. In all cases, a constant outdoor air flowrate of 0.3ACH (0.5m/s BIPV cavity flowrate) was modeled to maintain acceptable indoor air quality, and the air-based BIPV/T system was modeled as the south-facing roof with a 26.6° angle.The results show that the optimal passive solar design can reduce the heating energy demand by 42% with an incremental construction cost of 8% for Yellowknife and by 27% without incurring an incremental cost for Kuujjuaq. With higher energy price, the optimal house tends to be more energy-efficient. When thermal mass optimization is included, the optimal house in Kuujaq can reduce energy demand by up to 16%. Integrating BIPV/T with HRV can reduce the defrost risk time and defrost time from 4.5 to 8.2% and 5.7 to 8.0% respectively. Integrating BIPV/T with ASHP can extend the working hours by about 86 hours and improve the COP of ASHP by 1.4 to 2.0 % on average with a maximum hourly COP improvement of 30 to 33%. The reduction in the total energy consumption is in the range of 1.4% to 3.0% by integrating HRV and 0.3% to 0.6% by integrating ASHP. ASHP energy reduction is lower due to the additional energy required for defrosting during its extended work period and the mismatch of solar availability and heating energy demand. The paper concludes that the optimization of passive solar design parameters to minimize the total of initial construction cost and life-cycle operational energy cost can significantly reduce the heating energy demand of northern housing. The integration of BIPV/T with HVAC systems can further improve energy efficiency and operation time, but the reduction in total energy consumption is insignificant due to the low outdoor air flowrate for the HRV, additional energy consumption for defrosting the ASHP during extended working period, and mismatch between solar availability and heating demand. The study suggests further investigation with consideration for design with thermal mass and energy storage (Ma et al., 2021).

Measurement of BIPV/T in field conditions

A literature review has been previous performed for 35 different outdoor test systems for BIPV focusing on the quantitative electrical performance and economic parameters of the testbeds, such as test duration, specific energy yield, energy efficiency, system type, module interconnection, inverter efficiency, performance ratio, payback period, and unit energy cost. The review concludes that BIPV has enormous potential for on-site renewable energy generation in urban environments. However, BIPV systems are still in a relatively nascent stage with few commercial installations. An annual specific yield benchmark value of 1000 kWh/kWp to gauge the performance of BIPV test systems quantitatively is proposed. The results obtained indicate that 62% of the BIPV test beds evaluated in this work are underperforming and are predominantly façade-based systems. The paper provides suggestions to improve the performance of existing test beds and the scope of utilizing such systems for predictive maintenance (Pillai et al., 2022).

A common Test Reference Environment (TRE) for double skin applications of Building Integrated PhotoVoltaic (BIPV) Systems has been proposed in literature. The TRE is an outdoor test set-up that allows the assessment of experimental data for electrical and thermal performance evaluation of photovoltaic systems integrated as double skin applications in the building envelope. The TRE is an experimental setup constructed by a wooden box with an air inlet at the bottom and a 20°Cm diameter tube at the top for extraction of the heated air. Expanded polystyrene of at least 30°Cm thick is positioned towards the interior side of the wooden box. The structure is designed to work in a PASSLINK test cell as the exterior envelope element. The energy balance for BIPV double skin applications is presented as well. The experimental data has been used for validation of modelling work by several academic groups which has resulted in an improved knowledge on the heat transfer, in particular the convective heat exchange coefficient for the specific double skin boundary conditions. The author notes that its performance varies seasonally and in BIPV/T systems the preheated air may be undesirable for the indoor environment if used for ventilation, so different operation strategies and performance evaluation may be needed for summer and winter conditions. For STPV elements, the direct solar gains need to be evaluated as well. The paper suggests a common way of evaluating the data obtained from the experiments using the TRE. Mini-modules are proposed to get the required information for evaluation. These modules give an indication of the BIPV performance range, introducing an additional point for reference. The paper recommends defining a common outdoor test environment to harmonize experimental work for the assessment of electrical as well as thermal characteristics of photovoltaic systems in the building envelope. The definition of an Insulated Test Condition for PV modules as described in this paper supplements the existing range of test boundary conditions in BIPV applications (Bloem et al., 2012).

2.2. BIPV hygrothermal simulation

A challenge with the modeling of BIPV wall assemblies is the need to account for natural or forced airflow within the air cavity behind the cladding. The NREL DOE Strategy Guideline: Modeling Enclosure Design in Above-Grade Walls discusses the appropriate model settings to be used for various wall assembly designs in WUFI Pro. In particular, the assignment of cavity ventilation and air leakage is explained in detail. The hygrothermal simulation results are compared to field measurements and show good agreement (Lstiburek et al., 2016). The strategy guideline serves as a good reference for setting up most of the significant inputs in WUFI Pro models.

WUFI-Pro Ver. 6.5 has been used to simulate the hygrothermal conditions that occur in the air gap located behind wood cladding and building integrated photovoltaics within a Zero Emission Building situated in Trondheim, Norway. The researchers calibrated this model by comparing its outputs with field measurements collected between September 01, 2020 and August 31, 2022, which captured data on both the surface temperature of the wind barrier and the relative humidity found within the middle portion of the air gap. By examining various scenarios involving different air change rates within this specific region, they discovered that maintaining a constant air change rate at approximately 100 h^{-1} exhibited optimal performance overall. The performance of the WUFI simulation model and its accuracy in predicting surface temperatures are discussed. Overall, the study found that the WUFI simulations showed satisfactory results when comparing them to a dataset comprising 16,633 data points. However, it was observed that certain peculiarities specific

to building envelope characteristics accounted for a significant portion of the deviations between simulated and measured values. Specifically, at the northern façade of buildings, where wind barriers are present, there was an overestimation of surface temperatures by the WUFI simulations within a temperature range of approximately 10 to 30°C. The largest discrepancies between simulation results and measurements were primarily attributed to uncertainties in climate data input (Brozovsky et al., 2023).

2.3. BIPV SHGC and U-value Characterization

Indoor SHGC and U-value testing have been performed using a hot box calorimeter and solar simulator. The study provided derivation a thermal performance η was described and the results of η vs. $\Delta T/G$ were shown as linear plots. The slope and y-intercept of the plots were used to determine the U-value and SHGC of the specimens respectively. Detailed analysis of the uncertainty in SHGC and U-value were shown based on systematic errors and random uncertainties. Sensitivity analysis was performed to find the dominant sources of uncertainty, The U-value was found not sensitive to the solar irradiance, while Q_{loss} from interior to exterior of the calorimeter box was found to be the largest (up to 40%). The author suggested that lowering the flow rate through the absorber plate can reduce the uncertainty in pump energy consumption. The method resulted in larger uncertainty when determining U-value (8 to 22% for high performance window) if the slope of η vs. $\Delta T/G$ is too small, while uncertainty for SHGC is smaller (2%) (Harrison, 1992).

The above indoor experiment using hot box calorimeter and solar simulator has been described in further detail in another publication. The glazing optical properties were measured in a spectrophotometry facility according to ASTM Standard E903(ASTM International, 1996). SHGC was measured and simulated using VISION 3 and FRAME under CSA Standard A440.2 winter design conditions(Canadian Standards Association., 1993). Near infrared (NIR) lamps were used to boost the solar spectrum energy between 1.0 to 2.5 μm. Using an NIR correction factor improved the measured vs. simulated SHGC difference from up to 19% to less than 2% in spectrally selective glazing. The approach used to measure SHGC and U-value differed in this study rather than being measured simultaneously. For measuring U-value, the incident irradiance was varied from 200 to 1000 W/m2, while the ΔT across the fenestration was kept constant at 40°C. For measuring SHGC, the incident irradiance was kept constant at 783 W/m2, while the ΔT across the fenestration was kept as close to 0°C as possible, so that $\eta = SHGC$ in the η vs. $\Delta T/G$ plot. Sensitivity analysis was performed on varying exterior air temperature, film coefficient and solar spectral distribution, interior convective and radiative heat transfer coefficients and effective absorptance of the enclosure. Results show that the largest deviation of SHGC is 0.03, and average measurement uncertainty was ±4.9% (Harrison & Van Wonderen, 1994).

The SHGC of STPV glazing at varying incident irradiance angles have been experimentally determined and showed differences in SHGC between the maximum power-point (MPP) and open circuit (OC) operating states. The experiment was performed indoors with a solar simulator and a hot box calorimeter. Due to differences in experimental and actual field conditions, a sensitivity analysis using WINDOW results was performed. The solar spectral mismatch and battle plate reflection were determined to be the most sensitive factors that need correction.

$$c_1 = \frac{G_{sim,AM\ 1.5}}{G_{sim,simulator}} \quad (2.3.1)$$

$$c_2 = \tau^2 \rho_b \quad (2.3.2)$$

$$G_{corr} = c_1(G_{meas}) + c_2 \quad (2.3.3)$$

Due to the output spectrum of the solar simulator being different from the Air Mass 1.5 (AM1.5) standard reference spectrum, a correction factor was derived (Equations (2.3.1) to (2.3.3)) based on the WINDOW simulated SHGC vs. solar simulator measured SHGC, the solar reflectance of the baffle plate, and solar transmittance of the STPV. Results show the SHGC reduces as the incident irradiance angle increases, about -5% from 0 to 4 degrees, to -20% from 45 to 70 degrees. The SHGC also reduces in the MPP state by -3% to -6% (F. Chen et al., 2012).

Indoor measurements of SHGC have been performed on STPV specimens with various degrees of geometrical transparency using a calorimeter. Calibration was needed to determine box losses and capacitive parameters. For energy measurements, 30 measurements were performed with a 2s sampling period. Uncertainty analysis was performed on systematic errors with results showing total uncertainty in RMSE of SHGC was ± 0.03. The maximum relative difference between the SHGC measurements was -2%. The decrease in SHGC due to electrical state was shown, up to 5.3% between MPP and short circuit (SC) conditions (Olivieri et al., 2015).

Indoor measurements of SHGC on STPV specimens using a hot box calorimeter and solar simulator at a fixed incident angle have been performed. The Harrison and Dubrous method was used with spectral mismatch correction factor. The procedure described the application of this method to determine the SHGC of STPV. The spectral correction factor was determined using WINDOW simulation. The results show that SHGC is reduced when operating in MPP state. MPP resulted in 2% SHGC reduction for a 40% visual transmittance (VT) & 7% electrical conversion efficiency (η_{el}) specimen, and a 23% SHGC reduction for a 6% VT & 15% η_{el} specimen. The study noted the limiting of operating temperature of up to 55.3°C and ΔT between PV cells and Encapsulant up to 13°C (due to 3D Heat transfer), to limit the negative impact on the durability of PV, spacers, sealants and framing (Kapsis et al., 2017).

Derivations of energy balance equations for determining solar-optical properties and SHGC of glazing systems with complex shading features have been presented using the assumption that all shading layers act as uniform diffusers in transmission and reflection of radiation. The equations are later implemented into the WINDOW simulation software for shading features such as shading layers with gaps and between-glass shading. Examining the theoretical derivations for shading layers with gaps may provide insight on the SHGC calculation methodologies which need to consider the optical inhomogeneity of STPV glazing (Klems, 2000).

The indoor measurement methods of measuring SHGC on glazing using a hot box calorimeter and solar simulator has been described in detail in literature. Two methods were presented: the cold plate method and cold box method. In both methods, a hot box calorimeter is placed inside an environmental chamber with a solar simulator. The cold plate method is recommended for testing where a flat glass pane is the indoor-facing surface (which also applies to IGU and between-glass shading) but cannot test internal venetian blinds. The cold box method, which adds an additional cooling system to the interior of the hot box calorimeter (on the interior side of glazing) needs to

be used for internal venetian blinds. Correction factors for spectral mismatch and non-reference heat transfer coefficients were described. The method to calculate uncertainties due to heat flux of the absorber and non-parallel solar simulator irradiance on the SHGC was presented (Kuhn, 2014). Similar to (Harrison and Collins, 1999), it was suggested to keep ΔT across the hot box calorimeter as close to 0°C as possible.

Outdoor testing of SHGC for STPV as well as conventional glazing can provide measurements which reflect real boundary conditions of the specimens when installed. The main considerations in favor of performing outdoor testing of SHGC are that the incident angle of solar irradiance is rarely normal to the glazing (the angle at which standard indoor testing of SHGC are performed) and that the solar irradiance spectrum are closer to the AM1.5 reference spectrum than those of indoor solar simulators. Obtaining angular dependent properties of the specimens under reference solar spectrum conditions can provide insight on the energy performance of the specimens under real conditions. Outdoor testing presents the challenge of having difficult-to-control exterior radiative and convective heat transfer boundary conditions. This makes measured results difficult to compare. Some studies opt for side-by-side comparison using two specimens, while others normalize the changing outdoor conditions (for example by interpreting results as a function of indoor-outdoor temperature differential and incident irradiance). Due to angular dependence of SHGC, a solar tracker is often used.

The Passive Solar Systems and Component Testing (PASSYS) outdoor test cells used for outdoor measurements and the various improvements made have been described in literature. The PASSYS test cells have 35 set up in 10 European countries. The test cells can be used to evaluate SHGC, U-value, and thermal capacity. A limitation of the test cells is the long testing time due to low ratio of heat flux from components to that of the envelope, resulting in a time constant of 4 days, 1 week needed per procedure, typically with each experiment lasting 8 weeks. A pseudo adiabatic shell (PAS) was introduced which can reduce the test duration to 2 weeks. The PAS uses electric heating foil to balance heat loss through the envelope, with a thermopile (16 thermocouples in series to detect ΔT), the PAS can control heat flux to near 0. Heat flux sensitive (HFS) tiles made of pertinax plastic and aluminum plate with spirally wound thermopile was used to setup a grid of heat flux sensors to measure the total heat flux through the envelope. Large area heat flux (LAH) sensors were made to detect heat flux perturbation in parallel isotherms using finite difference calculations and can be used as lower cost alternatives to HFS tiles. A movable cold box was designed to help measure standard U-value of the tested envelope which requires steady-state. It controls the exterior envelope conditions to low temperature ($\pm 1C$), constant wind speed, blocks solar radiation. This enables year-round U-value testing and helps maintain stable steady state conditions (±0.2Kmax deviation over 24 days) at 30°C ambient temperature (Hahne and Pfluger, 1996).

Outdoor testing of SHGC and U-value of glazing specimens using a small hot box calorimeter with a solar tracker was performed. The solar tracker tracked using 2 potentiometers with $\pm$ 1 degree accuracy. The methodology outlined is suitable for rapid testing. Calibration process showed <2% error of input vs. output power from 50 to 600W. The response time of the system was 7.4min, assuming 1st order response of step input. Limitations of the method include: if interior temperature is colder than exterior, thermal guard heater won't turn on, and in non-steady state conditions, the overshoot & response lag results in about 0.5% of total energy in error (Harrison and Collins, 1999).

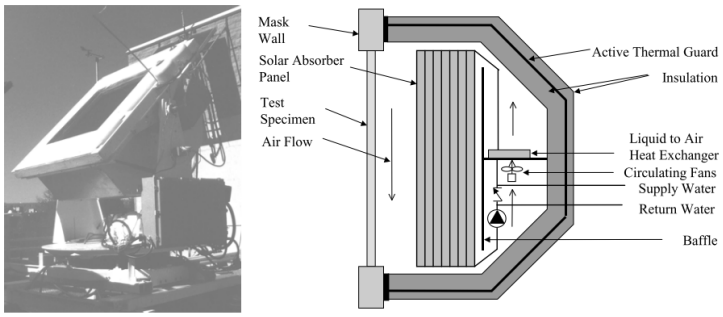

Fig. 1: Queen's Solar Calorimeter. Photo of the calorimeter and cross-sectional schematic.

Figure 2.3.1 (Harrison and Collins, 1999)

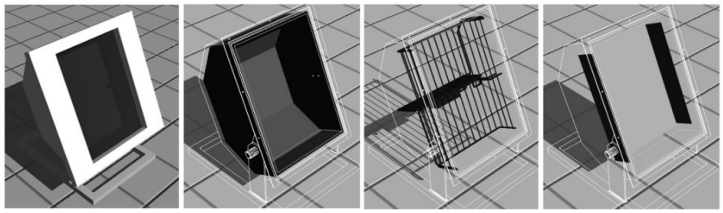

Fig. 2: Calorimeter construction details. (a) Complete Calorimeter with mask wall, (b) active thermal guard, (c) flow loop, and (d) absorber panel.

Figure 2.3.2 (Harrison and Collins, 1999)

An outdoor SHGC measurement of a glazing system has also been performed using 2 side-by-side solar test boxes. The test boxes were not calorimeters and did not have solar tracking or cooling systems. One box is installed with the test specimen while the other is installed with a reference specimen with known properties. Thermistors were used to measure the inner box temperature and ΔT across the glazing. A pyrheliometer and a pyranometer on a sun tracker was used to measure the direct & diffuse solar irradiance. A weather station was used to measure outdoor temperature and relative humidity, vertical plane irradiance, and wind speed & direction. It was noted that the alignment to true South was a major source of error. The test period lasted 4 days to collect the necessary data. The data from the reference test box was used to calibrate a simulation model using IDA Indoor Climate and Energy to minimize the RMSE between simulated and measured inner box air temperature. The calibrated model is then used to simulate the test specimen box inner air temperature condition by using various SHGC values. Based on trial and error, the SHGC which results in the lowest RMSE between simulated and measured inner box temperature is then the SHGC of the test specimen. A limitation of this method is that it is sensitive to ΔT across the test box and cannot determine the U-value correctly (estimate can be between 3.2-4.2 W/m2K) if the ΔT is too low. Due to this, the U-value input into the IDA energy model was the value given by the manufacturer for both reference and test cases. It was recommended to attempt this measurement in winter with a clear sky. The SHGC determined by this method was 0.45 ± 0.042 compared to 0.46 given by the manufacturer (Cornaro et al., 2015).

The above methodology was improved upon to perform outdoor measurements of SHGC and U-value of STPV glazing. Despite limiting the U-value determination to the night-time data, the heat flux was still too small, so they were additionally validated through indoor steady state tests. The

STPV specimen was a custom-made dye sensitized solar module (DSM) inserted between double pane glazing. The determined SHGC was 0.2 with a U-value of 3.6 W/m²K (Cornaro et al., 2018).

The difficulties in measuring the U-value of a built structure have been attributed to the thermal mass of structures and the inevitable diurnal temperature variations that prevent steady state conditions from ever being realized. The conventional U-value meter takes a simultaneous measure of heat flow and temperature difference across the wall, and computes the U-value as their quotient. However, this can result in gross errors, large enough to render the technique virtually useless. The paper proposes recording heat flow and temperature difference over a period of some days and calculating the U-value as the quotient of the means for more reliable measurements. This technique allows for satisfactory measurements of insulation even in the presence of sunshine or with intermittent heating regimes (McIntyre, 1985).

An external infrared thermography (IRT) method has been developed to determine the clear wall U-values of wood-framed wall assemblies. The proposed method was compared with the parallel path method and 3D thermal simulations. The IRT measurements were conducted on a conditioned at-scale insulated wood-framed wall structure. The study found that the location of the region of interest (ROI) plays a key role in U-value measurement due to the vignetting effect and colder thermal bridges at corners. It was also found that non-uniformity corrections (NUC) should be considered during the survey. The total surface resistance coefficient (R-value) in this study was calculated using outdoor convective and radiative energy balance equations. The convective heat transfer coefficient was determined from Nusselt number correlations and the radiative heat transfer coefficient was determined from the Stefan-Boltzmann law. The results showed that U-value measurement with IRT in the best-case scenario (depending on the location of ROI) deviated from nominal U-values by 6.25%-25.00%. The clear wall U-value results with IRT were validated with three-dimensional (3D) finite element analysis software, Siemens NX, which differed by −11.53%-10.00% in the best-case scenario. Additionally, the clear wall U-values obtained with parallel path method were comparable with simulation values, but only for walls without highly conductive materials such as metal (Mahmoodzadeh et al., 2021).

2.4. Literature Review Conclusions

The literature reviewed in this Chapter regarding the integration of BIPV show that there is a general lack of standardization and design guidelines for integrating BIPV, BIPV/T and STPV as a building envelope system. There is also a lack of standardized evaluation methods of performance metrics for comparing BIPV/T to conventional building components and active systems. Due to the lack of a clear workflow in incorporating modeling of BIPV systems in whole building energy simulations, it is difficult to quantify the overall benefit of a design incorporating BIPV compared to other conventional design options.

A good starting point to address the modeling of BIPV systems is to perform field measurements of the real performance of buildings with BIPV systems and to develop workflows using existing modeling techniques to closely match the measured performance. An examination of the hygrothermal performance of incorporating BIPV systems is also needed to assess the potential conditions in which moisture damage could be a concern when implementing BIPV.

Many aspects of the BIPV can affect the heat transfer phenomena within the BIPV air cavity. Multiple inlets result in lower PV surface temperatures, but more heat energy captured. To optimize the BIPV/T, a possible design is to integrate the façade section of BIPV/T with the roof sections of BIPV/T, which would increase the outlet temperature. However, longer air cavity lengths would lead to PV with higher temperature at the top end of the air cavity, leading to the PV cells positioned at the top to be more vulnerable to overheating, reduction in electrical conversion efficiency and durability.

Other considerations for building envelope integration of BIPV are also lacking, such as the issues surrounding the opening of the BIPV/T manifold which are important for the integration of BIPV/T with active systems such as the mechanical ventilation system or heat recovery ventilator. Air leakage, thermal bridging need to be minimized in the manifold design. A damper design for switching of day/night operation will need to be addressed. Water and moisture infiltration in such large openings in the building envelope need to be considered as well.

In general, literature review of the BIPV integration and SHGC/U-value measurement methodologies identified several important factors to consider when measuring the solar heat gain coefficient (SHGC). Angular dependence of SHGC is a significant factor that needs to be accounted for, as well as considering the electrical state of STPV modules. There are challenges associated with indoor measurements such as correcting for indoor solar simulator, uncertainties in calorimeter box system and determining accurate U-value due to its sensitivity to temperature differences between interior and exterior conditions. Similarly, outdoor measurements pose challenges related to reference comparison or solar tracking techniques, achieving repeatability in measurement results which impact the accurate determination of SHGC, but provide the SHGC values under real boundary conditions that exist in constructed projects.

Table 2.4.1: Summary of advantages and disadvantages of studies using calorimeters to determine the SHGC and U-value of glazing specimens

Type of Calorimeter	Advantage	Disadvantage
Indoor w/solar simulator	• Steady state • Repeatability	• Spectral mismatch • Cannot accurately measure angle of incidence effects
Outdoor w/o sun track	• Real conditions	• Dynamic conditions • Difficult to reproduce • Need comparative study (side-by-side with known specimen)
Outdoor w/sun track	• Real conditions • Steady state*	• Still affected by weather, outdoor temp cannot be controlled • Tracking affects measurement

3. BIPV/T Curtain Wall Monitoring & Comparison to Model

The intent of the monitoring experiment performed and analyzed in this Chapter is to quantify the field performance of a BIPV/T system with a short air cavity height (about 2m) through measurements and also compare the measured results to the outputs from a simple thermal network steady-state model. The modeling of heat transfer phenomena within a short BIPV/T air cavity (much less than a typical application with >5m of cavity length) is challenging in that it is highly influenced by the entrance effects within a 30cm region at the bottom of the BIPV/T air cavity and the outlet effects at the BIPV/T manifold opening at the top (another 30cm region) of the BIPV/T air cavity(Rounis et al., 2021). Measuring the field performance of such this short cavity condition can help develop empirical correlations which would be difficult to model. Temperature measurements from bottom to top of the air cavity will allow for monitoring of the temperature profile and temperature rise in the air cavity, which can then be compared to the model which calculates the temperature based on empirical correlations. The model will use the local hourly weather data as inputs and output the cavity temperature profile, thermal energy capture, and thermal efficiency. In real applications such as developing control strategies for this system, a calibrated model would be used, and a separate inlet would be installed for the system to draw fresh air from the outdoors at night. Because of the influence from entrance and outlet effects and this separate night time operation strategy in real applications, only results from periods of higher solar irradiance from 10:00 to 14:00 are analyzed in detail.

3.1. Experiment instrumentation & data collection

The experimental design is setup for monitoring the BIPV/T system installed on the south facade at the exterior of Test Cell 2 at the FBL. The BIPV/T system consists of a 992mm x 1968mm x 5.8mm 290W PV module (Canadian Solar CS6X-290P-FG) integrated into the building envelope using a curtain wall pressure plate system. The air cavity behind the PV module has a depth of 30mm to accommodate for up to 44 L/s of forced ventilation airflow at 1.5 m/s of air velocity. Extruded polystyrene (XPS) sandwiched between two thin aluminum sheets (black with matte finish as seen from the exterior in Figure 3.1.1) is the thermal insulation and water control layer of the curtain wall section. Three rectangular openings of 144mm x 75mm are cut from the layer for the BIPV/T manifold to draw the airflow from the air cavity into the interior ductwork. More details of the BIPV/T manifold and mechanical ventilation are discussed in Chapter 4.

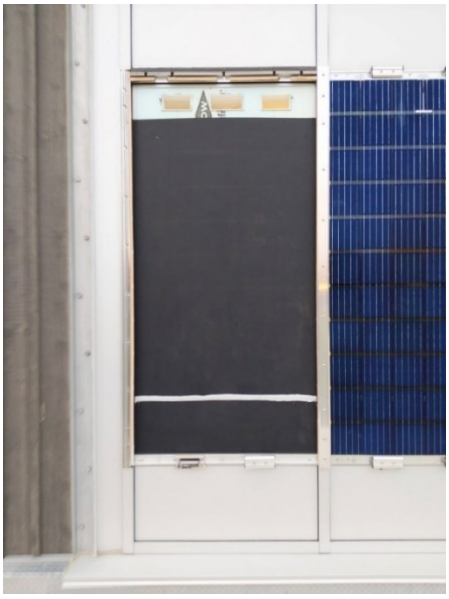

Figure 3.1.1: BIPV/T curtain wall (left) without the PV cladding

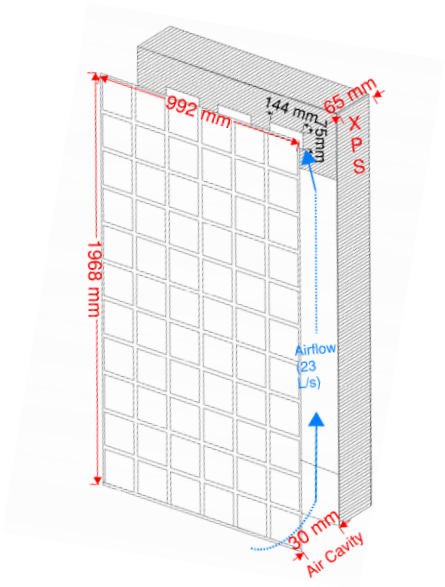

Figure 3.1.2: BIPV/T curtain wall schematic of main layers and airflow

The purpose of the experiment is to measure the performance of the curtain wall BIPV/T system in terms of thermal efficiency and the temperature distribution of the airflow inside the air cavity under field operating conditions. The goal is to compare the experimental results with that of a simple thermal network finite difference model to examine the model's accuracy in predicting the thermal performance of the system.

Type T thermocouples made to monitor the BIPV/T back of cell, air cavity, and the insulation exterior (black aluminum back pan) temperatures. The thermocouples have an accuracy of ± 0.5°C. The temperature variations due to edge effect and asymmetry in boundary conditions of this southwest corner of the FBL were monitored with Type T thermocouples as well for future work but is not analyzed within this thesis. The thermocouples were secured to either the surface of the monitoring point or the tip of an aluminum clip using sheathing tape and foil reflective tape.

Figure 3.1.3: Thermocouple fixed to the back of the PV module, positioned at the center of the PV cell

Figure 3.1.4: One thermocouple fixed to black aluminum using foil tape to measure the back pan

Temperature at each of the manifold inlets was measured using 4 Type T thermocouples at each inlet. The 4 thermocouples are spaced symmetrically around the inlet opening and fixed in position using metal clips and sheathing tape. The 4 thermocouples are connected in parallel and output a single average temperature signal to the data acquisition system.

Figure 3.1.5: Thermocouples placed symmetrically around the manifold inlet opening to measure average manifold inlet air temperature.

The relative humidity within the BIPV/T air cavity is monitored with a HMP50 sensor with ±5%RH accuracy shown in Figure 3.1.6. Pressure and air flowrate sensors have not yet been installed for the current monitoring period.

Figure 3.1.6: Sensor setup for the air cavity and back pan, the HMP50 relative humidity sensor (circled in red) is positioned near the center of the wall cavity and fixed with sheathing tape.

The schematic diagrams on the FBL elevation and section drawings in Figure 3.1.7 and Figure 3.1.8 show the current placement of the temperature and relative humidity sensors on the BIPV/T wall section and the future airflow and pressure sensors to be installed.

Figure 3.1.7: Positions of monitoring sensors in elevation view

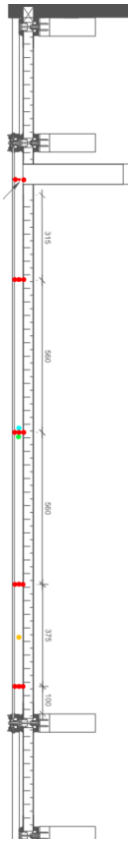

Figure 3.1.8: Positions of monitoring sensors in section view

Figure 3.1.9: Type T thermocouple fixed to a wooden stick on the left, LI-COR LI-200 pyranometer on the right.

One LI-COR LI-200 pyranometer with ± 1%W/m² accuracy was mounted on the surface of the spandrel section slightly above the BIPV/T to measure the normal incident solar irradiance on the PV surface.

Due to the lack of a weather station at the beginning of the monitoring period, Type T thermocouples were fixed to a wooden stick protruding from the spandrel section and shielded using reflective tape as a temporary method for monitoring outdoor temperature at the FBL.

Figure 3.1.10: WS800 Weather Station secured to the guard rail at southwest corner of rooftop

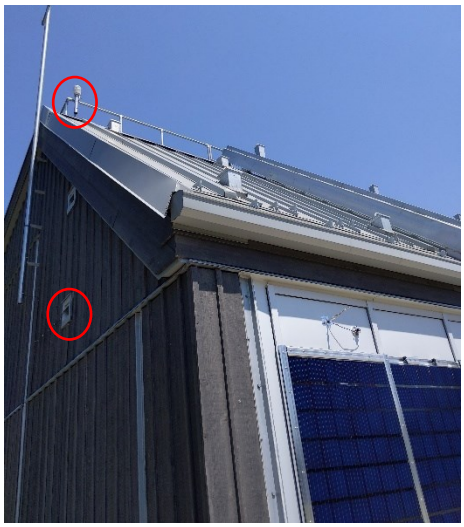

Figure 3.1.11: WS800 Weather station with its data cable passed through a vent opening on the west façade (circled in red)

The WS800 Weather Station with ±0.5°C temperature accuracy and ±5% wind speed accuracy was installed on the rooftop of the FBL, mounted on a metal mast fixed to the guard rail. Due to the site plan of the FBL, the geographic (true) south is aligned exactly with the south orientation of the building's façade, and so the north compass alignment of the weather station is aligned exactly with the north orientation of the building. The data cable of the WS800 is passed through a vent opening on the west façade of the FBL to reach Test Cell 2 where it interfaces with the manufacturer's software (Lufft ConfigTool.Net) installed on a computer to log the weather data at 1-minute intervals.

The weather station began collecting data on April 24, 2023. The outdoor temperature data from the weather station was significantly different from the measurements taken by wooden stick thermocouple. These differences are discussed in detail in Chapter 3.2.

An Agilent 34970A data acquisition (DAQ) unit was used to collect data from the analogue voltage or current signals from above sensors. The DAQ was connected to a computer via USB at the test cell. The sensor data were monitored from the DAQ and exported through the BenchLink software.

Figure 3.1.12: BIPV/T connected to the Venmar EKO 1.5 HRV through a prototype manifold and ductwork to capture the preheated cavity ventilation air

Figure 3.1.13: BIPV/T manifold insulated and thermocouples connected to data acquisition system

The BIPV/T curtain wall section was coupled with a Venmar EKO 1.5 HRV unit through a custom manifold as described in Chapter 4. Temperature, relative humidity, and air flowrate are monitored at the outside air inlet, supply air, and exhaust air ductwork.

Monitoring data of the operating BIPV/T system was collected during the winter/spring season from December 2022 to May 2023. Since the weather station was not in operation until April 24, 2023, the monitored outdoor temperature data from before this time were not used in the analysis. This chapter focuses on the analysis of the monitoring period between 11:00 AM on April 24 to 11:00 AM on April 29, 2023.

3.2. Calibration of simplified model for BIPV/T Curtain Wall

Based on the steady-state thermal network model and heat transfer correlations described by Candanedo et al., 2011; Charron & Athienitis, 2006; and Chen et al., 2012, a simple finite difference model of a BIPV/T curtain wall was built in Python. The convective heat transfer coefficient assumed to be equal at both front and back of the cavity (Ua=Ub).

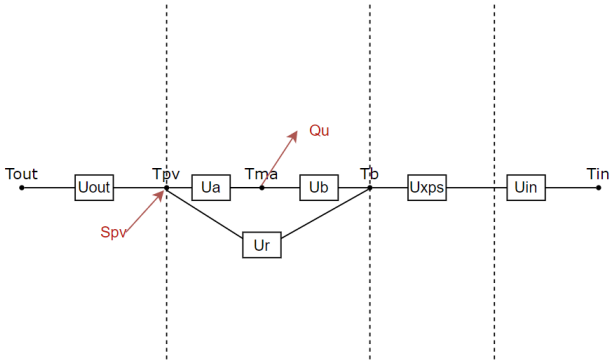

Figure 3.2.1: Thermal network diagram of BIPV/T curtain wall system at Test Cell 2

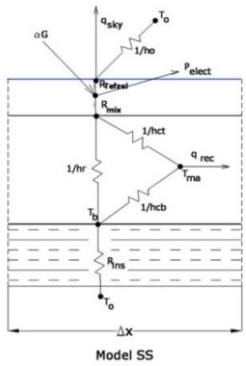

Figure 3.2.2: Thermal network diagram of a typical BIPV/T system (Candanedo et al., 2010)

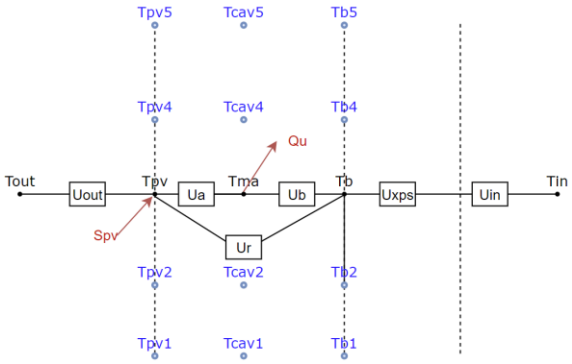

Figure 3.2.3: Schematic of the thermocouple positions being monitored and modeled (in blue) superimposed on the BIPV/T curtain wall thermal network diagram

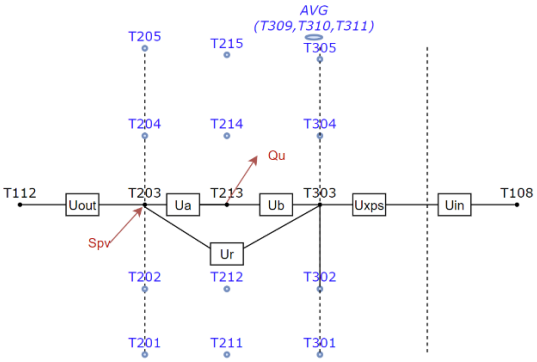

Figure 3.2.4: Schematic of thermocouple data channels on the data acquisition system being monitored (in blue) superimposed on the BIPV/T curtain wall thermal network diagram

A 72-cell PV array (Model CS6X-290P-FG) from CanadianSolar was installed as the cladding on this BIPV/T curtain wall. Throughout the monitoring periods, the PV cladding was not connected to a load and was therefore operating in its open circuit (OC) state for the entirety of this study. Based on Optics 6 simulation of STPV solar optical properties from the IEA Task 15 exercise described later in Chapter 6.1, the 72-cell PV array is 92.2% opaque and was determined to have solar optical properties of $\tau_{sol} = 0.0662, \rho_{sol} = 0.0894, \alpha_{sol} = 0.8444$ respectively.

At the time of this field experiment, the façade PV module was not connected to an inverter and therefore was operating in the open circuit (OC) state and not generating any electricity. For this simplified BIPV/T model, solar absorptance $\alpha_{sol} = 0.8444$ and electrical efficiency $\eta_{el} = 0$ (due to OC state) were important input parameters for the purposes of this simulation. The model determines the solar irradiance which is converted into heat by the BIPV cladding based on the equation:

$$S_{pv} = S_{total} - E_{electric} \quad (3.2.1)$$
$$S_{total} = \alpha_{sol} I_s A \quad (3.2.2)$$
$$E_{electric} = \eta_{el} I_s A \quad (3.2.3)$$

Where S_{pv} is the solar power in W converted into heat by the BIPV cladding, S_{total} is the total solar power absorbed in W by the BIPV cladding, $E_{electric}$ is the electrical power generated by the BIPV cladding and extracted from the system, I_s is the incident solar irradiance in W/m^2 and A is the surface area of the PV cladding in m^2.

The model performed calculations by taking the hourly averaged WS800 weather station data (outdoor temperature, outdoor humidity, wind direction and wind speed), the incident solar irradiance measured by the LI-COR LI-200 pyranometer, the HRV inlet airflow rate measured by the flowmeter, and the Test Cell 2 room temperature measured by an indoor thermocouple as inputs. The outputs of the model were also given on an hourly basis.

BIPV/T air cavity convective heat transfer coefficient

During early stages of comparison between the modeled and measured cavity temperature profile, it was apparent that there was a mismatch between the actual BIPV/T inlet (bottom of cavity) temperature and the temperature assumed by the simplified model. An adjustment based on solar irradiance was made to the bottom cavity inlet temperature as shown in Appendix 9.1.

Wind effects have been modeled, since the rooftop weather station provides both the magnitude of the wind velocity as well as its direction. The convective heat transfer correlation by (Liu and Harris, 2007) is used since the size of the monitored building is similar. Details of determining the outdoor heat transfer coefficient based on this correlation and the measured wind data is shown in Appendix 9.2.

BIPV/T cavity convective heat transfer coefficient may be determined by the monitoring data by modifying Equation (9.1.1) to use T_{cav1} in place of T_{out} as discussed above, and solving for the temperature at the end of the airflow path (T_{cav5} at the top of the cavity):

$$T_{cav5} = \frac{T_{pv,avg} + T_{b,avg}}{2} + \left(T_{cav1} - \frac{T_{pv,avg} + T_{b,avg}}{2}\right) e^{-\frac{2H_{cav}}{a}} \quad (3.2.4)$$

$$T_{pv-b,avg} = \frac{T_{pv,avg} + T_{b,avg}}{2} \quad (3.2.5)$$

$$a = \frac{-2H_{cav}}{ln\left(\frac{T_{cav5} - T_{pv-b,avg}}{T_{cav1} - T_{pv-b,avg}}\right)} \quad (3.2.6)$$

Where $H_{cav} = 2m$ is the height of the BIPV/T air cavity for this study.

The exponential coefficient a in Equation (3.2.4) is determined by(Charron and Athienitis, 2006):

$$a = \frac{\rho_{air} c_{air}}{h_{PVT} W_{PVT}} \dot{\forall}_{air} \quad (3.2.7)$$

Where $\dot{\forall}_{air}$ is the volumetric flowrate of the air in the cavity in m^3/s, $W_{PVT} = 1m$ is the width of the BIPV/T curtain wall section, h_{PVT} is the convective heat transfer coefficient within the BIPV/T cavity, ρ_{air} is the density of air and c_{air} is the specific heat capacity of air.

For the purposes of this simple model, the changes in air properties are assumed to be negligible and constant at

$$\rho_{air} = 1.244 \frac{kg}{m^3}$$

$$c_{air} = 1000\, J/kgK$$

$$k_{air} = 0.025\, W/mK$$

Since $T_{cav5}, T_{pv,avg}, T_{b,avg}, T_{out}, \dot{\forall}_{air}$ are given by the monitoring data, the temperature gradient exponent a can be calculated for each timestep, and the convective heat transfer coefficient h_{PVT} can be determined from using Equations (3.2.4) to (3.2.7) in reverse, assuming steady-state conditions without thermal storage effects in the system and ρ_{air} and c_{air} are constant (or have negligible variations):

$$h_{PVT} = \frac{\rho_{air} c_{air}}{-2 W_{PVT} H_{cav}} \dot{\forall}_{air} \ln\left(\frac{T_{cav5} - T_{pv-b,avg}}{T_{cav1} - T_{pv-b,avg}}\right) \qquad (3.2.8)$$

The limitation is that the solution is undefined when $T_{pv-b,avg} \geq T_{cav5}$ or $T_{pv-b,avg} \geq T_{cav1}$. This usually occurs in the absence of solar irradiance, when $T_{b,avg} > T_{pv,avg}$, but allows the Nusselt number Nu correlation to be curve fitted when a good amount of solar irradiance is present (which is the most important conditions for BIPV/T operation and when the accuracy of the model truly matters). Unfortunately, due to having a constant flowrate setting on the HRV during the monitoring period, the recorded range of Re was very narrow with inconclusive results shown in Appendix 9.3.

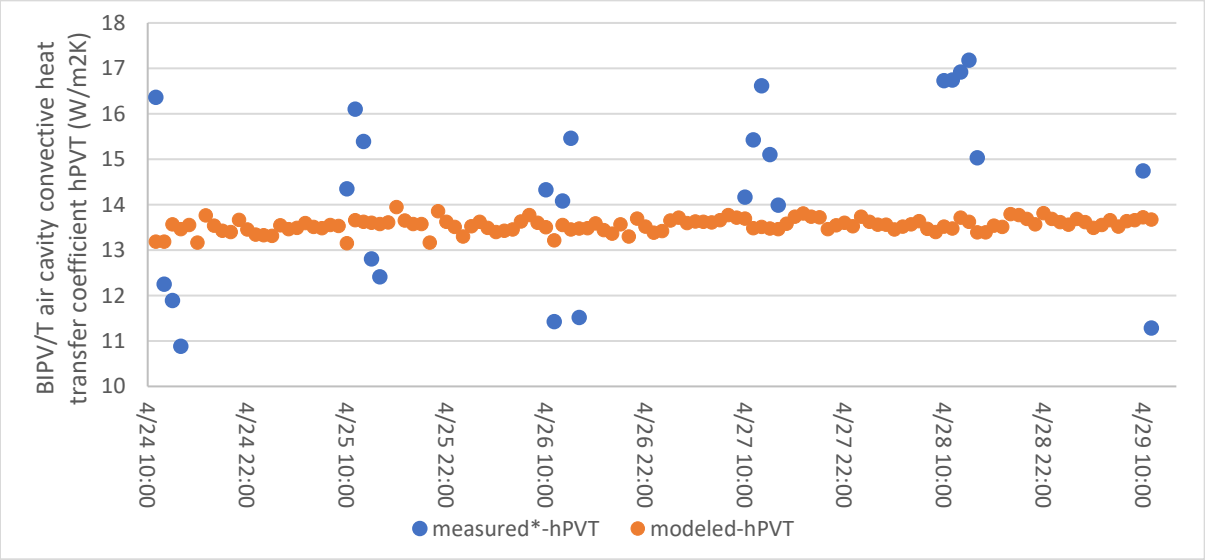

Figure 3.2.5: Comparison of convective heat transfer coefficient within the BIPV/T air cavity as determined by the monitoring data and the modeled outputs.

The h_{PVT} calculated by the model is nearly constant regardless of outdoor conditions at around 13 W/m^2K. The h_{PVT} determined by analyzing the monitoring data on the other hand is strongly influenced by the day-night cycle, reaching its peak values at the hours around noon. This may be due to the higher influence from entrance and outlet effects and lower temperature differences during periods of low solar irradiance. Due to this consideration, only periods between 10:00 to 14:00 have been analyzed. The h_{PVT} values calculated from the measured data using Equation (3.2.8) show an average of 14.3 W/m^2K between 10:00 to 14:00 and a range between 11 to 17 W/m^2K. These values have been observed in h_{PVT} determined from Nusselt number correlations in previous studies from both outdoor measurements and indoor solar simulators (Rounis et al., 2022, 2021).

In terms of modeling, the lower h_{PVT} results in lower cavity temperatures in the model, but the current model still overestimates the cavity temperatures during the day (which is discussed later in this chapter). It is therefore unlikely that this mismatch in h_{PVT} is the main contributor to the inaccuracy in the model.

BIPV/T air cavity temperature gradient

The temperature gradient in the BIPV/T air cavity has been modeled for each of the five points shown in Figure 3.2.3 and Figure 3.2.4. A detailed comparison of the temperature differences between the model and measurements is shown in Appendix 9.5.

Data from April 27 and 28 were chosen for more detailed analysis based on the sky clearness index using Hottel's clear sky model (Hottel, 1976). More details on the clearness index are discussed in Appendix 9.4.

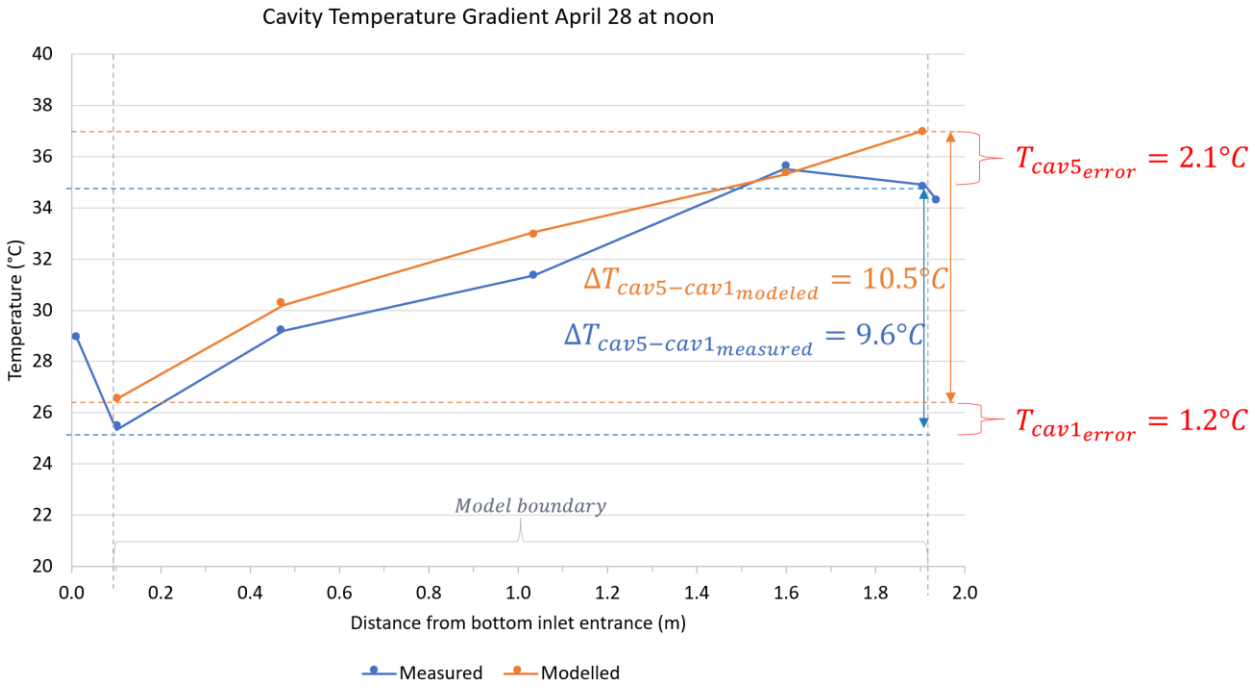

Figure 3.2.6: Comparison between measured and modeled values of BIPV/T air cavity temperature gradient from bottom inlet entrance to top of air cavity (leading into manifold opening) on April 28 12:00 noon.

The outlet effect of the BIPV/T air cavity can be seen in the reduction in temperature further downstream due to turbulence of the cavity ventilation and is evident as the lower average manifold inlet temperature (measured by the thermocouples at the entrance of the BIPV/T manifold, graphed at distance 1.935m, about 25mm above the T_{cav5} monitoring position) in Figure 3.2.6. The measurements suggest that the actual temperature of the pre-heated cavity air stream entering manifold, which would be used for ventilation or integration with other mechanical system, is slightly lower than the temperature measured at the position slightly upstream (T_{cav4}). A thermocouple mounted just at the entrance of the bottom inlet (90mm below T_{cav1}) showed the entrance effect, but it is likely due to its proximity to the bottom metal pressure cap of the BIPV/T curtain wall, which could be heated up by solar irradiance and consequently warmed up the turbulent air at the bottom of the inlet by convection. The modeled temperature gradient is determined using the WS800 weather station data and Equation (9.1.1) as inputs. There is good agreement on the measurement of T_{cav4} (at a distance of 1.6m) but the model overestimates the temperature values at other positions by $1.2°C$ to $2.1°C$.

In terms of temperature rise from the bottom (T_{cav1}) to top (T_{cav5}) of the air cavity, the temperature increases by 10.5 ± 0.7°C from the model outputs while the measurements show a lower increase of 9.6 ± 0.7°C.

Heat energy captured

An important parameter being measured for this BIPV/T field monitoring study is the amount of heat energy captured by the BIPV/T system. This can be determined by:

$$Qu = \dot{\forall}_{air}\rho_{air}c_{air}(T_{cav5} - T_{cav1}) \qquad (3.2.9)$$

Where Qu is the heat energy captured in Wh, $\dot{\forall}_{air}$ is the volumetric flowrate of the air cavity in m^3/s, ρ_{air} is the density of air in J/kgK, c_{air} is the specific heat capacity of air in J/kgK.

Since the BIPV/T curtain was not connected to a load (operating in OC state) during the monitoring period between 2023 April 24 to April 29, there is no electrical energy generated from the BIPV/T system. However, the portion of electrical energy which would have been generated is instead converted to additional heat energy which is then captured by the cavity airflow.

Over the monitoring period from April 24 11:00 am to April 29 11:00am, the BIPV/T system captured 10.326 kWh (net) of thermal energy (calculated based on the measured data), with 0.609 kWh at its peak hour.

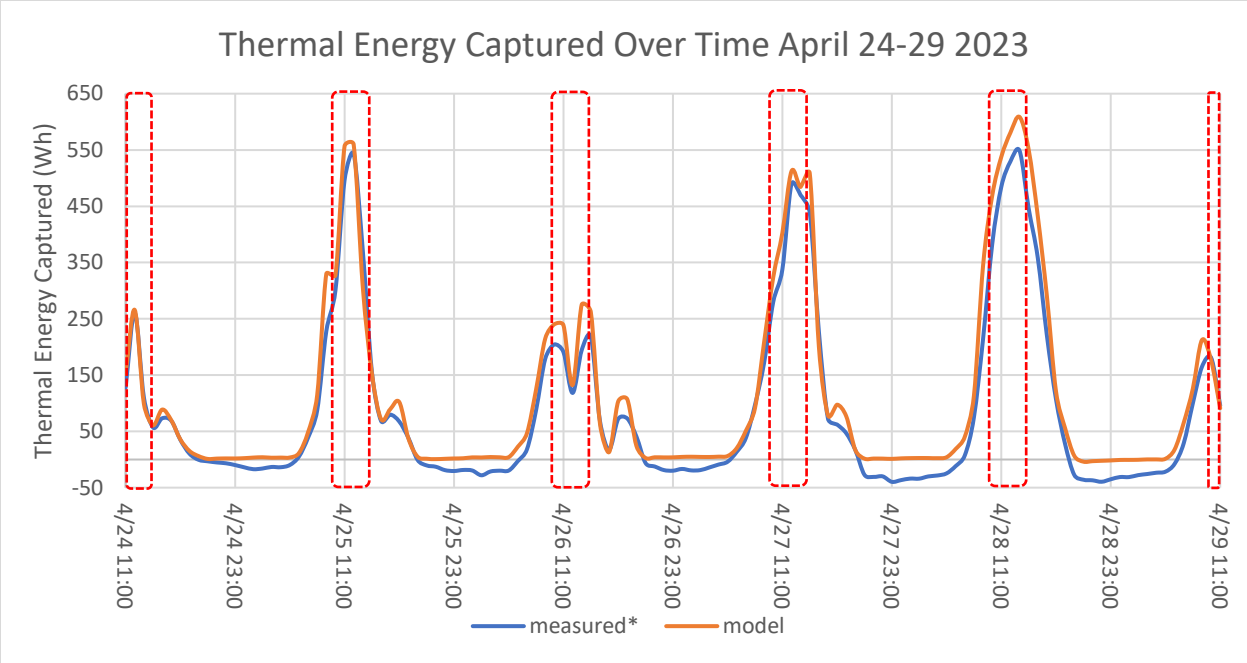

Figure 3.2.7: Comparison of measured and modeled thermal energy captured Qu for the monitoring period from 2023 April 24 to April 29. Measured* values are Qu calculated from measured temperature data using Equation (3.2.9).*

This amount includes the deduction from the cooling effect of the BIPV/T system during nighttime operation likely due to radiative sky losses. The simplified model showed good agreement on the trend in thermal energy capture, but the total amount summed up to be higher (13.414 kWh) due the large discrepancies during nighttime. This is not a concern since in real applications the BIPV/T system would bypass the cavity ventilation at night using a damper and a separate outdoor air inlet to prevent the system from drawing the cooled nighttime air. The analysis will focus on the period between 10:00 to 14:00 (indicated by red dashed line regions) which are periods with high temperature differential when results that are proportionately less influenced by entrance and outlet effects and measurement errors.

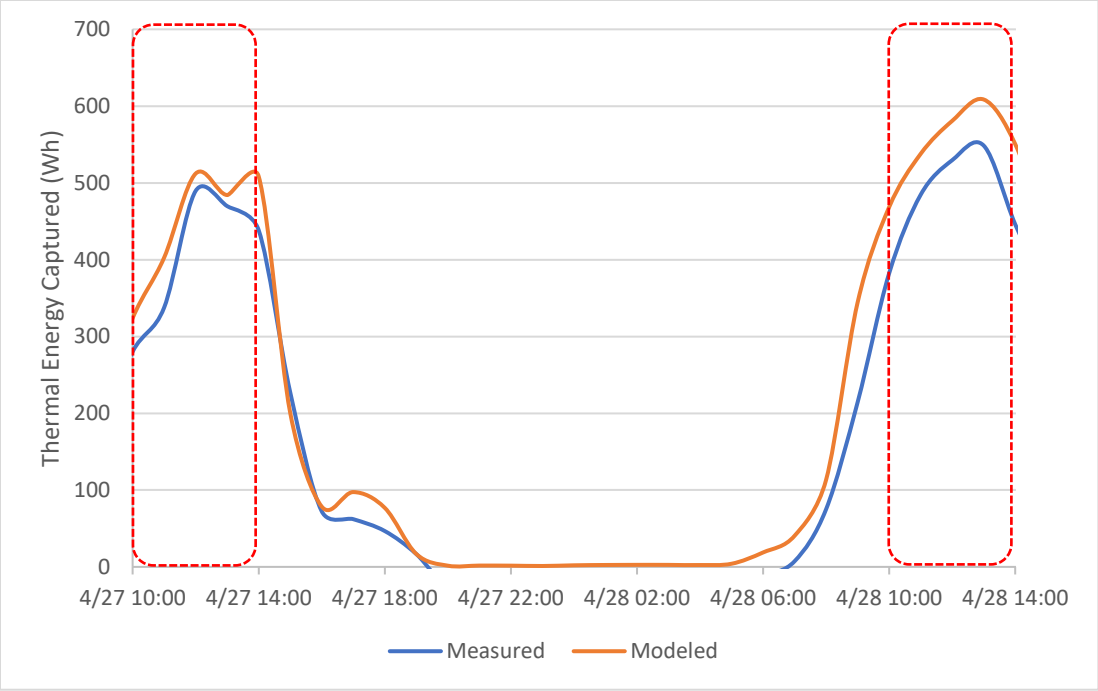

Figure 3.2.8: Comparison of measured and modeled thermal energy captured Qu for the monitoring period for 2023 April 27-28.

On April 27 and 28, a typical day with mostly clear sky and up to 608 W/m2 of solar irradiance, the thermal energy captured throughout the day as calculated from the monitoring data is 3.03 kWh based on Equation (3.2.9). During the 10:00 to 14:00 periods, the average thermal energy captured per hour is 0.44 ± 0.04 kWh. During these periods, the model overestimates thermal energy captured by 13% on average and up to a maximum of 19.1%.

Thermal efficiency

The thermal efficiency of the BIPV/T system can be determined by the fraction of thermal energy collected compared to the solar irradiance (Rounis et al., 2021):

$$\eta_{th} = \frac{Qu}{A_{PVT}G} \qquad (3.2.10)$$

Where η_{th} is the thermal efficiency of the BIPV/T system, Qu is the thermal energy captured in W, as determined by Equation (3.2.9, A_{PVT} is the area of the PV module ($2m^2$ for this experiment) and G is the solar irradiance in W/m^2 incident on the BIPV/T façade.

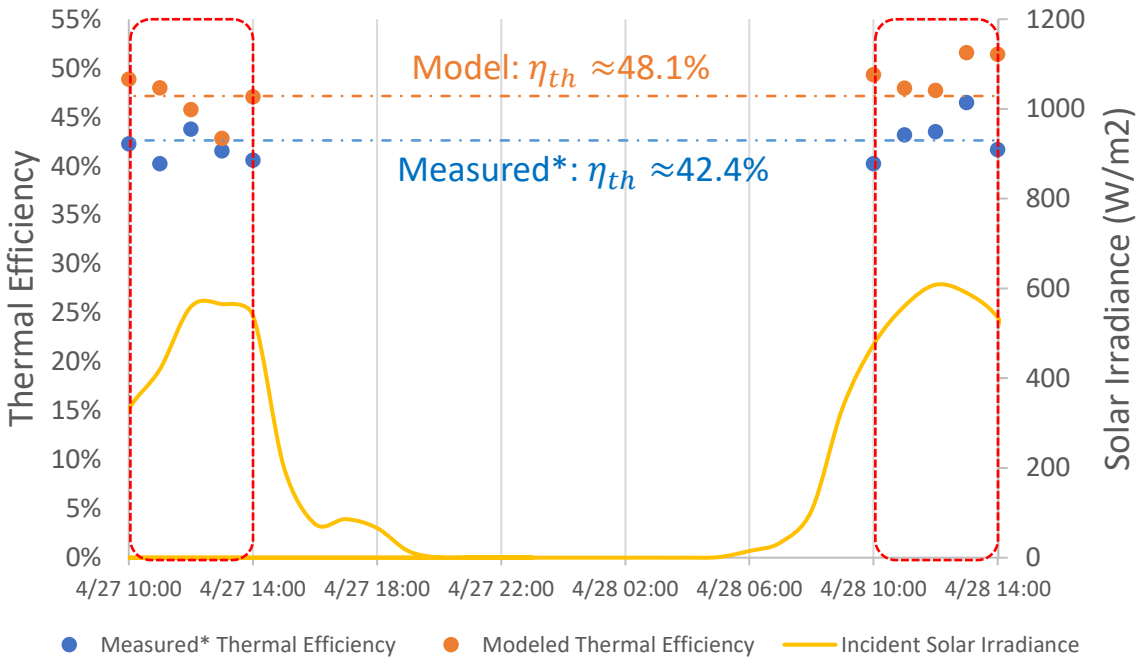

Figure 3.2.9: Thermal efficiency η_{th} of the BIPV/T curtain wall system determined based on field measurement data from the monitoring period between 2023 April 24 11:00 am to April 29 11:00 am.

The thermal efficiency has been calculated based on the hourly average of the thermal energy captured and solar irradiance. Using Equation (3.2.10), thermal efficiency is calculated from the measured temperature data (noted as "measured*") and the modeled temperature data (noted as "modeled"). Like the thermal energy captured, at low irradiance ($< 200 W/m^2$) conditions, where the thermal efficiency η_{th} values are significantly influenced by the inlet and outlet effects as well as thermocouple measurement errors. Therefore, only the period between 10:00 to 14:00, when the incident solar irradiance is the highest (between about $400 W/m^2$ to $600 W/m^2$) are examined. On average, the thermal efficiency calculated based on measured temperature data is about 42.4 ± 3% from 10:00 to 14:00. The thermal efficiency determined by the model during the same period is 48.1% on average, which is an average overestimate of about 5.7%. The maximum overestimate from the model is up to 9.8% for the April 29 data.

Potential sources of error in the comparison of model and monitoring data include model energy balance convergence errors, the lack of nighttime radiative heat loss in the model, shading of the pyranometer during measurements, incorrect positioning of thermocouples, and uncertainty of measurements from each instrument used for the monitoring setup. These issues are discussed in detail in Appendix 9.6.

4. BIPV Integration with HRV

Heat recovery ventilators (HRVs) transfer heat from the mechanical system's exhausted stale air to the incoming fresh air. In heating seasons, this can provide significant energy savings for heating and humidification. However, in cold climates like Montreal, HRVs often need to operate defrost cycles to prevent freezing from low outdoor temperatures which reduces the total energy savings over time. A method to reduce the need for defrost cycles is to pre-heat the incoming fresh air using the heat recovered from the BIPV/T before the air enters the HRV core. This was investigated by connecting the BIPV/T section in FBL Test Cell 2 to an HRV using a prototype manifold. The manifold was designed and manufactured with good resulting temperature uniformity within the BIPV/T air cavity. Through a field monitoring experiment, data from daytime and nighttime measurements from the monitoring period were analyzed separated as the HRV+BIPV/T integrated case and the HRV-only case performance. The potential improvement due to the BIPV integration on the HRV supply air temperature and reduced defrost operation time without loss of sensible recovery efficiency are examined and quantified**.** In a practical application of the HRV+BIPV/T integration, the air intake at the BIPV/T manifold opening would incorporate a damper system which would bypass the BIPV/T air cavity at night and during the hot summer season to avoid bringing in excessively cold or hot air which do not benefit the ventilation function of the system. For these reasons, along with the entrance and outlet effects mentioned in Chapter 3, the analysis of the HRV+BIPV/T integration focused on data with periods of $> 200 W/m^2$. solar irradiance.

4.1. Experimental Setup

The experiment setup consists of the same PV module (CS6X-290P-FG) integrated into the BIPV/T curtain wall described in Chapter 3. The monitoring of the BIPV/T curtain wall air cavity and surrounding surfaces as well as the BIPV/T manifold inlet temperatures with Type-T thermocouples are the same as described in Chapter 3.1. This chapter focuses on this BIPV/T system's integration on the mechanical ventilation side and examining the potentially improved performance of the Venmar EKO1.5 HRV unit due to the integration with the BIPV/T system. A schematic diagram of the experimental setup is shown in Figure 4.1.3. The air stream from the BIPV/T air cavity is brought into the HRV through openings in the XPS insulation layer which is connected to a 3D printed BIPV/T manifold, which is then coupled to a 152.4mm (6") diameter straight aluminum duct through a 152.4mm (6") diameter flexible duct. Downstream of the straight duct, an airflow meter built into a duct mounted airflow measurement station is installed at a distance of 457.2mm (18") from the manifold which is then continued by the straight duct until a 152.4mm (6") dimeter flexible duct is used again to couple the straight duct with the inlet air port of the HRV. The design and construction of these BIPV/T manifold is shown in more detail in Chapter 4.2. The airflow rate at the HRV's inlet air and exhaust air inlet/outlet ports are measured by a differential pressure generated within two Dwyer STRA-C6 airflow measurement station sections and is accurate within 2% of the actual flowrate. The HRV was set to operate at a constant airflow rate of 44±0.88L/s (about 1.4 m/s in the BIPV/T air cavity). The airflow measurement stations have honeycomb airflow straighteners built in to accommodate potential turbulence (for

example turbulent flow from the converging wye at the manifold). HMP50 relative humidity sensor are also installed near the HRV inlet air port, in the middle of the room near the HRV in Test Cell 2, and at the supply duct section slightly above the Test Cell 2 ceiling. The same Agilent 34970A data acquisition (DAQ) unit was used to collect data from the analogue voltage or current signals from these sensors. The sensor data were monitored from the DAQ and exported through the BenchLink software on a laptop computer via USB. The field monitoring of the HRV performance was performed from January 26 16:00 to February 8 16:00, 2023.

Figure 4.1.1: Opening in XPS for manifold inlet and PV connectors (red) and HRV supply air duct (green) and exhaust air duct (blue) leading to the mezzanine outside the test cell.

Figure 4.1.2: 3D printed manifold connected to HRV through a straight aluminum duct with flexible duct for coupling on both ends and wrapped in insulation.

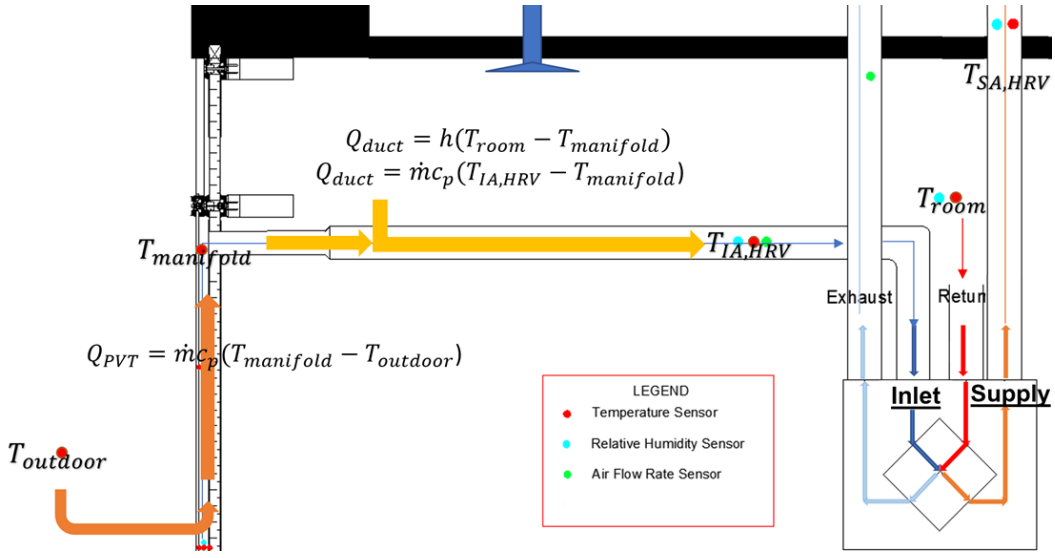

Figure 4.1.3: Schematic of the BIPV/T+HRV integration experimental setup, with orange arrows indicating heat captured from the air cavity and heat gain in the manifold inlet duct due to room air thermal transmission leading to the HRV outdoor air inlet and yellow arrows indicating airflow paths at each port of the HRV. $T_{manifold}$, $T_{IA,HRV}$, T_{room} and $T_{SA,HRV}$ are the average BIPV/T manifold temperature, HRV inlet air temperature, Test Cell 2 room air temperature, and the HRV supply air temperature respectively.

4.2. BIPV Manifold Design

A Building Integrated Photovoltaic/Thermal (BIPV/T) manifold was designed to connect the air cavity behind the cladding to the HRV. This allows forced ventilation to cool down PV modules and preheat the air supplied to heating systems for higher energy efficiency.

The main design criteria of the BIPV/T manifold are:

1. Allow a maximum cavity air velocity of $0.6\ m/s$ to $1.5\ m/s$ to minimize noise
2. Balance total pressure loss of each air flow path by equalizing friction loss
3. Reduce dynamic loss where possible while keeping the geometry simple for production

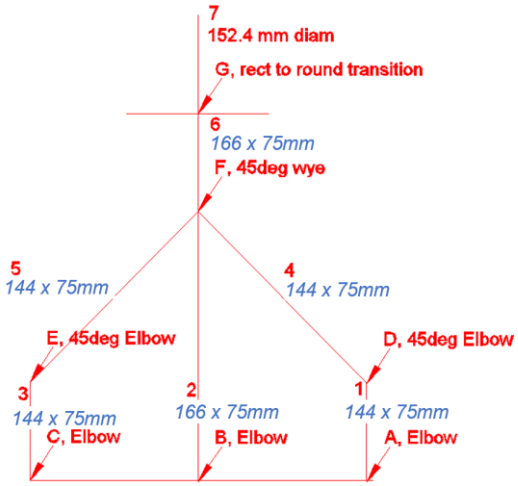

Figure 4.2.1: Schematic diagram (plan view) of duct fitting. (Duct sizing at each section were determined through design iterations with equal friction method calculations. Final sizing shown in blue are summarized in Table 4.2.1.)

To achieve a BIPV/T cavity air velocity of 1.5 m/s at an expected volumetric flowrate of 45 L/s (based on the HRV specifications), the manifold inlet and joint sizes were designed using the equal friction method commonly used in duct design (American Society of Heating, Refrigerating and Air-Conditioning Engineers, 2013). The dynamic pressure losses for the converging branches of the wye fitting at section F were determined based on the coefficients given for the four-way wye piece at side branch angles of 45° described by (Idel′chik & Ginevskiĭ, 2007, Diagram 7.35). The dynamic pressure losses for the other fitting sections with conventional elbow and transition geometries were determined based on fitting loss coefficients compiled by (Howell et al., 2013). The part of the BIPV/T curtain wall air cavity where the airflow reaches the top end of the cavity forces the air to abruptly turn 90° to meet the inlet entrance of manifold, so fitting coefficient for a 90° rectangular mitered elbow is considered for fitting sections A, B, and C.

The equations used to determine the total pressure loss (and by extension, the duct dimensions) are shown in Appendix 9.7.

Table 4.2.2: Duct path length design flowrate, dimensions and Reynold's number for each section and fitting.

Section	Length (m)	Airflow (m3/s)	Airflow (CFM)	Velocity (m/s)	W Rectangular Duct Width (mm)	H Rectangular Duct Height (mm)	$D_h(=D_e)$ Hydraulic Diameter (= Equivalent Diameter) (mm)	Re Reynold's number
1	0.15	0.0139	29	1.4	*144*	*75*	112	10437
2	0.41	0.0168	36	1.5	*166*	*75*	120	11905
3	0.15	0.0139	29	1.4	*144*	*75*	112	10437
4	0.368	0.0139	29	1.4	*144*	*75*	112	10437
5	0.368	0.0139	29	1.4	*144*	*75*	112	10437
6	0.15	0.0446	94	4.0	*166*	*75*	120	31478
7	0.3	0.0446	94	4.0	*166*	*75*	120	31478
A	2	0.0139	29	1.4	*144*	*75*	112	10437
B	2	0.0168	36	1.5	*166*	*75*	120	11905
C	2	0.0139	29	1.4	*144*	*75*	112	10437
D		0.0139	29	1.4	*144*	*75*	112	10437
E		0.0139	29	1.4	*144*	*75*	112	10437
F-b		0.0139	29	1.4	*144*	*75*	112	10437
F-s		0.0168	36	1.5	*166*	*75*	120	11905
G	0.1524	0.0446	94	4.0	*166*	*75*	120	45538

Table 4.2.3: Duct friction loss and fitting dynamic loss calculations.

Section	ε Roughness (mm)	f Friction Factor	Friction Loss (Pa/m)	Section Friction Loss (Pa)	H/W Aspect Ratio	C_o'	K_{Re}	C_o	Fitting Dynamic Loss (Pa)	Total Pressure Loss (Pa)
1	0.046	0.031	0.328	0.049	0.519					0.049
2	0.046	0.030	0.342	0.140	0.453					0.140
3	0.046	0.031	0.328	0.049	0.521					0.049
4	0.046	0.031	0.328	0.121	0.521					0.121
5	0.046	0.031	0.328	0.121	0.521					0.121
6	0.046	0.024	1.915	0.287	0.452					0.287
7	0.046	0.024	1.897	0.569	0.452					0.569
A	0.046	0.031	0.328	0.655	0.521	1.292	1.394	1.800	2.124	2.780
B	0.046	0.030	0.342	0.683	0.452	1.300	1.373	1.785	2.418	3.101
C	0.046	0.031	0.328	0.655	0.521	1.292	1.394	1.800	2.124	2.780
D	0.046	0.031	0.328	0.000	0.521	0.369	1.394	0.515	0.607	0.607
E	0.046	0.028	0.37	0.000	0.521	0.369	1.394	0.515	0.607	0.607
F-b	0.046	0.028	0.37	0.000	0.521			0.503	0.593	0.593
F-s	0.046	0.028	0.37	0.000	0.452			0.520	0.704	0.704
G	0.046	0.028	0.37	0.056	0.452			0.554	5.235	5.291

For fittings labeled Sections A,B,C,D, and E, the fitting loss coefficient C_o' needs to be corrected by the Reynold's number correction factor K_{Re} using the equation $C_o = K_{Re}C_o'$, where C_o is the corrected fitting loss coefficient and K_{Re} and C_o are given by tables in (Howell et al., 2013).

Table 4.2.4: Total friction, dynamic and pressure loss in each airflow path

Path	Total Friction Loss (Pa)	Total Dynamic Loss (Pa)	Total Pressure Loss (Pa)
A-1-D-4-Fb-6-G-7	1.7	8.6	10.3
B-2-Fs-6-G-7	1.7	8.4	10.1
C-3-E-5-Fb-6-G-7	1.7	8.6	10.3

To maintain a low duct height for the manifold (considering limited ceiling height in practical applications), a rectangular duct height of 75mm was designed throughout. The width of the

rectangular duct was varied iteratively to balance the final total pressure loss across each path of the airflow.

Originally, the design considered using dampers for balancing the final pressure long each path, since having dampers would be useful in reducing air leakage when the BIPV/T system is not mechanically ventilated (for example during nighttime when the BIPV/T sky losses causes the cavity ventilated air to be cooler than taking it directly from outdoor). However, the damper pressure required to balance the losses at each path were in the magnitude of less than 10 Pa, so to simplify the experimental setup, the decision was made to design the duct sizing to have as close to matching total pressure loss as possible without the use of dampers. This was accomplished by slightly increasing the center inlet (Section 2) opening and finding iterations of the angles at E, D, and F which resulted in the most balanced pressure loss while keeping the design simple to build. The total pressure loss in Path B-2-Fs-6-G-7 needed to be reasonably close to the 10.3 Pa experienced by the other two flow paths, so for the final iteration, the duct width for Section 2 converging into the straight path of the Section F (F-s) wye is increased to 166mm which worked with a 45° angle for the four-way wye piece to reduce the total pressure loss to 10.1 Pa. Other angles for the four-way wye at E and D were considered from 30° to 60° in earlier iterations but resulted in greater imbalance in total pressure losses and were more difficult to work within the dimensional constraints of the 3D printer.

The prototype was 3D-printed in multiple parts. AutoCAD was used to model the 3D geometry of the manifold based on the design calculations. Additional details were modeled to allow the geometry to separate into parts due to the 3D printer's size constraints, and structural reinforcement were added to resist bending and shear forces on the 3D printed material.

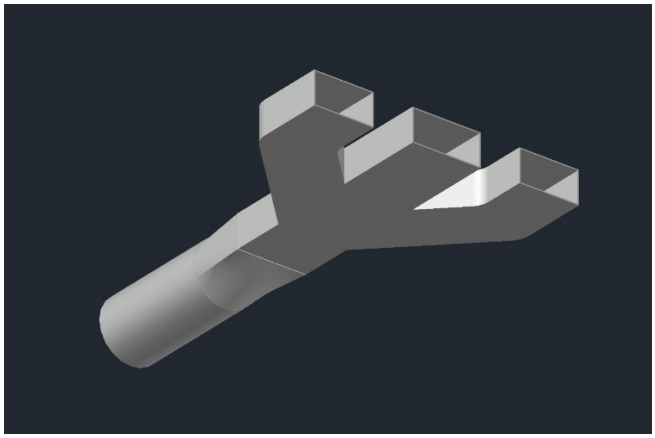

Figure 4.2.2: Base manifold design 3D geometry modeled in AutoCAD

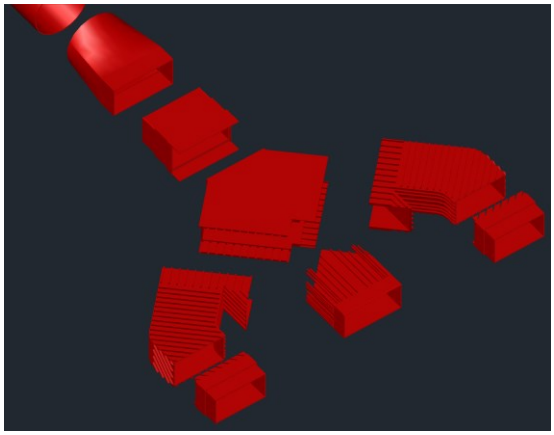

Figure 4.2.3: Final manifold parts design for 3D printing

Due to the size limitations of the 3D printer, the manifold design needed to be split into 8 separate parts. The individual parts required modelling additional corrugations on top of external surfaces to reinforce the structural rigidity of each part to resist mechanical stress that may be exerted on the 3D printing material when the manifold is fully assembled, hanging from the Test Cell 2 ceiling and pressurized by the HRV. The corrugations also doubled as guides for friction fitting each separate part together during the final assembly.

Each part was imported from AutoCAD into the Ultimaker Cura slicing software to be converted into a 3MF file format for 3D printing using the Ultimaker S5 3D printer. The material used for 3D printing the manifold prototype is acrylonitrile butadiene styrene (ABS) due to its high glass transition temperature of 105°C being far above the expected operating temperature of the BIPV/T air cavity (Kumar et al., 2022).

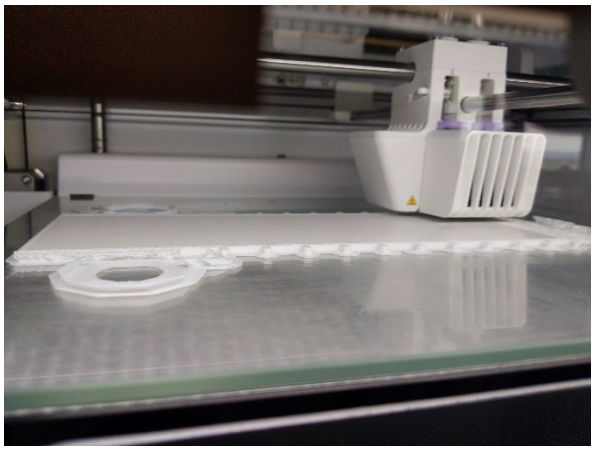

Figure 4.2.4: The Ultimaker S5 3D printing the base layer of one of the manifold side inlet parts

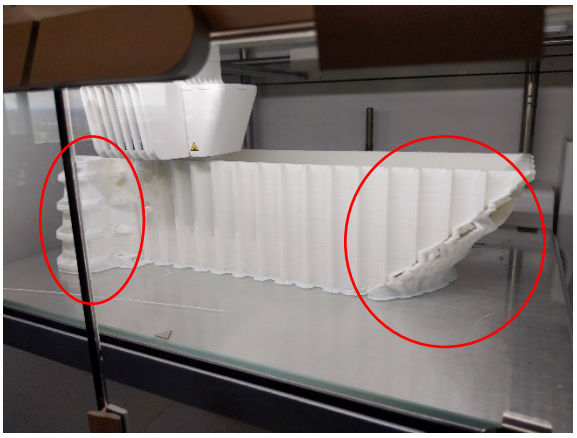

Figure 4.2.5: Tree branch temporary structures to structurally support the printed material during 3D printing (in red).

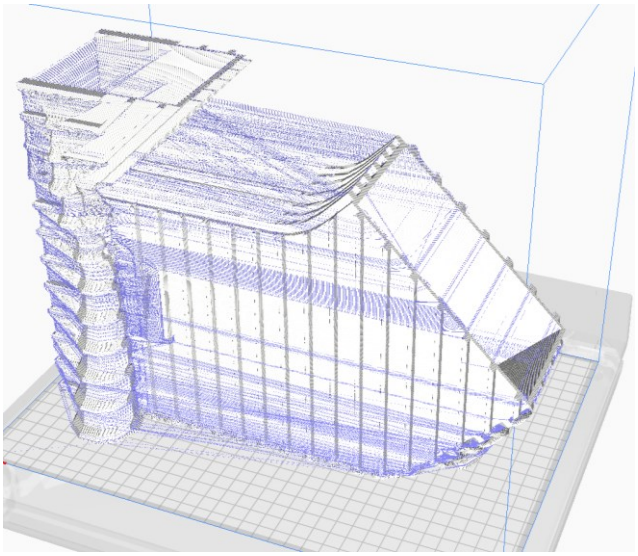

Figure 4.2.6: Sliced and structurally supported geometry generated in Ultimaker Cura

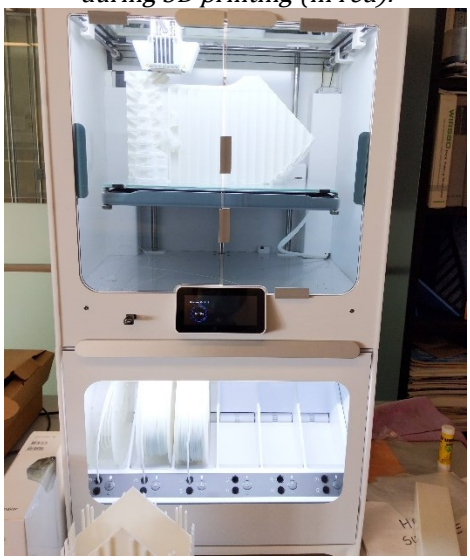

Figure 4.2.7: The Ultimaker S5 3D printer nearing completion on the printing the part

Due to the size constraints of the 3D printer's printing space, there was often only one single orientation that each part is able to be printed at. The consequence is that the surface that is lying directly against the 3D printer's glass plate and the vertical surfaces of each part have better structural integrity than the "floating" horizontal surfaces that need to be supported against gravity by a scaffold of temporary 3D printed structures. These horizontal surfaces have rougher surfaces and imperfections in material density when the supporting scaffold structure is removed. The hollow tree branch style support structures were generated by Ultimaker Cura to prioritize the reduction of printing time and wasted ABS material. However, removal of these support structures

from the interior side of the final printed part left residual material and rough surfaces that required significant manual sanding and cleaning to address. The larger and more complex parts took about 50 hours each to print while the smaller less intricate parts took about 12 hours. When every part has been printed, the combined parts were joined with heat resistant epoxy putty at the seams.

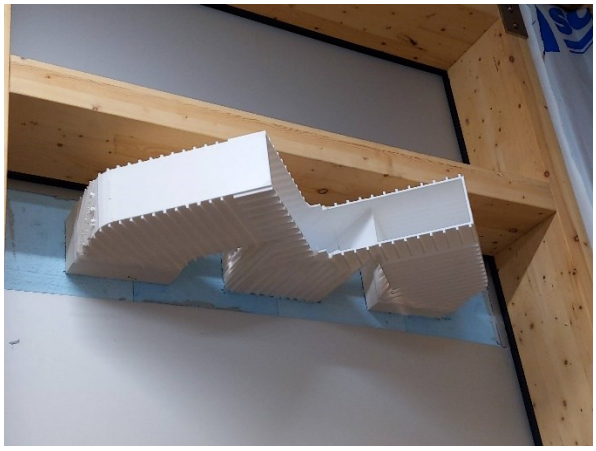

Figure 4.2.8: The 3D printed manifold made to have a friction fit with the XPS openings

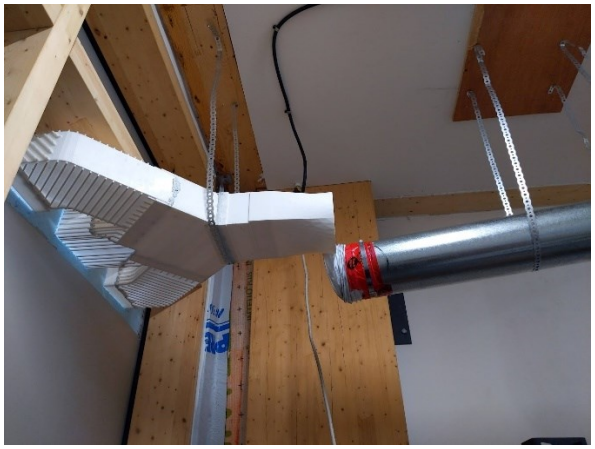

Figure 4.2.9: The manifold and ductwork are suspended from the ceiling using aluminum hangers

Openings were cut in the XPS based on the final manifold design to form a tight friction fit with the final printed ABS parts. During the installation in Test Cell 2, care was taken to not put too much pressure on the seams of the manifold parts where the sealant can be damaged.

Flow Uniformity

The uniformity of the airflow within the BIPV/T cavity depends on the design of the manifold. With three manifold openings to the air cavity, it is expected to provide more evenly distributed airflow behind the entire BIPV cladding than one single manifold opening of similar total dimensions.

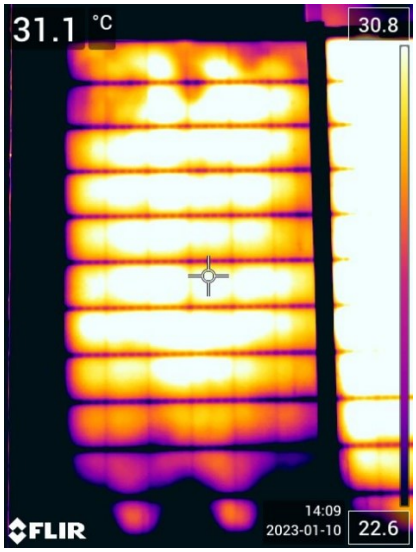

Figure 4.2.10: Infrared imaging of BIPV/T cladding temperature in a January afternoon

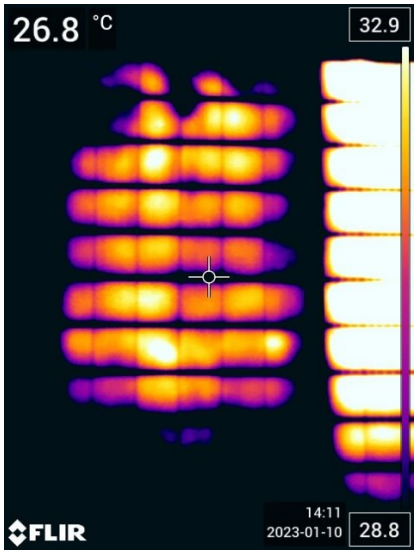

Figure 4.2.11: Infrared imaging of BIPV/T cladding temperature in a January afternoon with narrower range of temperature display

The infrared imaging in Figure 4.2.10 and Figure 4.2.11 show that the positions of the cladding where the airflow is directed to the manifold openings are colder than the temperature of the rest of the cladding during winter.

Figure 4.2.12: BIPV/T (left) cladding and BIPV (right) cladding temperatures in the afternoon on June 3, 2023

The infrared imaging does not show significant cold spots aside from the areas around the manifold opening and the bottom inlets. Most of the BIPV cladding have a similar temperature across horizontally, which suggests the airflow is quite uniform. The temperature near the top of the BIPV/T manifold appears to be slightly lower than that of the upper middle area. This suggests that there is some influence from the thermal bridging effect from the sides and also from the turbulence at the BIPV/T inlet.

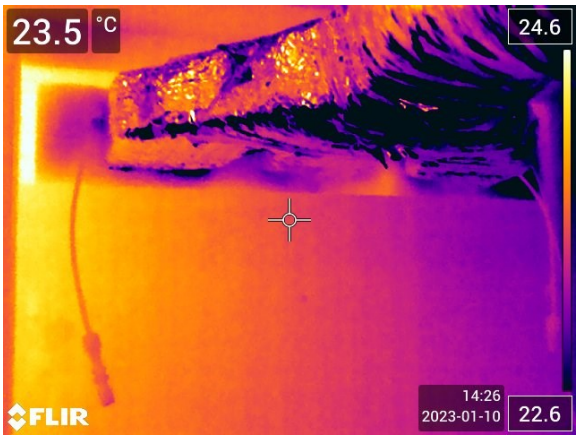

Figure 4.2.13: Infrared imaging of BIPV/T manifold showing thermal bridging effects near the perimeter of the manifold inlet

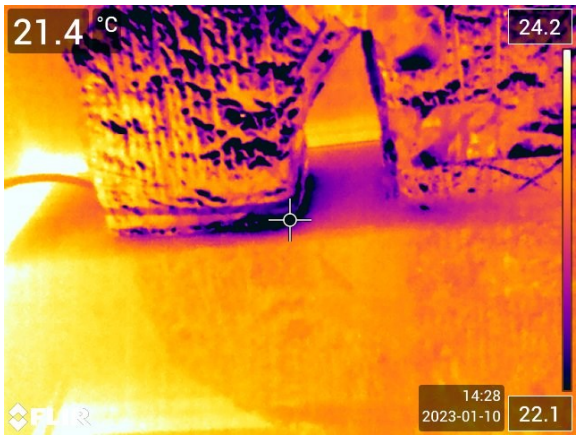

Figure 4.2.14: Infrared imaging of BIPV/T manifold showing thermal bridging effects near the perimeter of the east manifold inlet

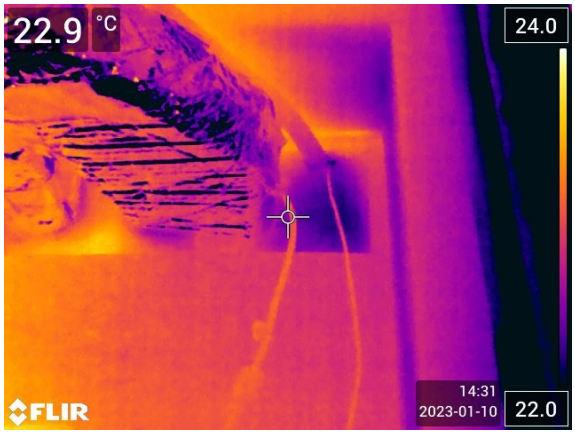

Figure 4.2.15: Infrared imaging of BIPV/T manifold showing large cold spot near the west manifold inlet in January

Figure 4.2.16: Infrared imaging of BIPV/T manifold showing more minor thermal bridging effects near the perimeter of the middle manifold inlet

Figure 4.2.17: BIPV/T manifold lets and their corresponding thermocouple DAQ channels

Figure 4.2.18: BIPV/T manifold after additional layer of reflective insulation

Four Type-T thermocouples were added at each inlet of the manifold. When connected in parallel to the data acquisition system, they provide the average temperature of the airflow entering the manifold at each inlet.

Figure 4.2.19: Four Type-T thermocouples at each manifold inlet to measure temperature of the air stream

After the installation of sensors, the thermal insulation of the manifold is improved with an additional layer of reflective foil insulation (R4.2 per layer) and sealed with plastic zip ties and

foil tape. The importance of minimizing the thermal transmission losses are discussed in the Appendix.

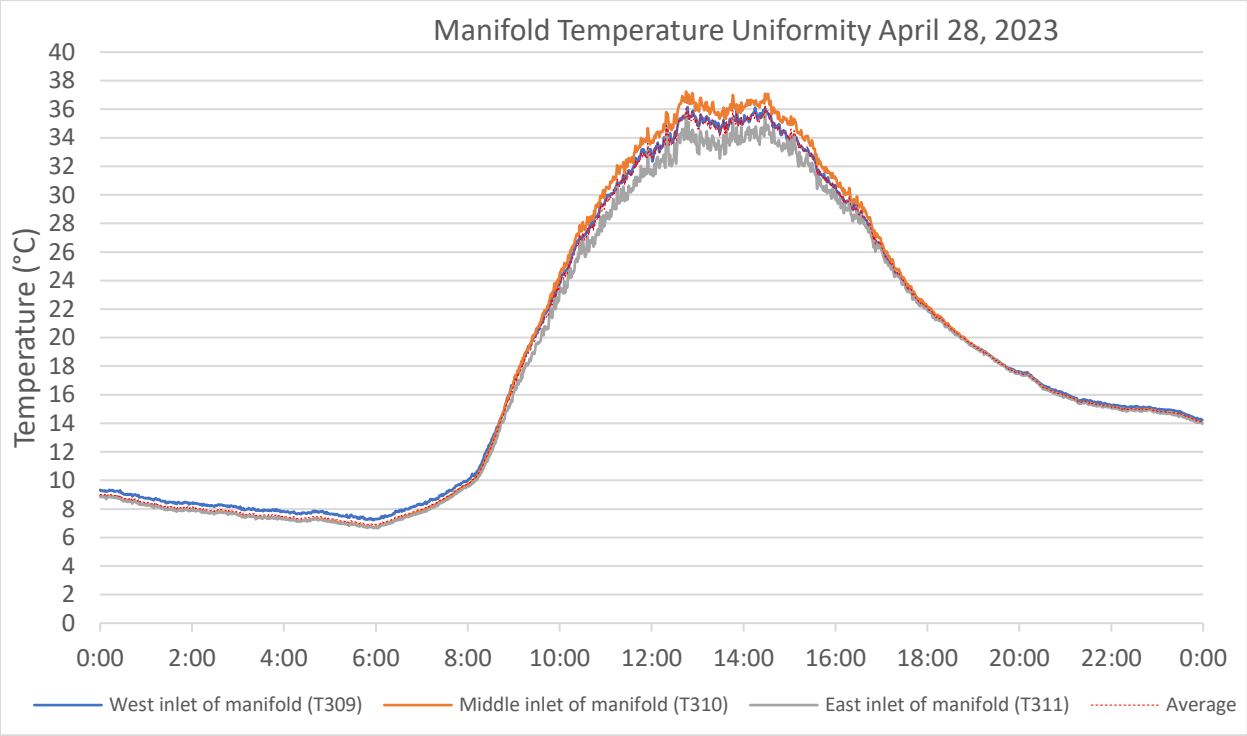

Figure 4.2.20: Temperature profile at 1-minute intervals through April 28 for each of the inlets of the manifold. Average of the three values is shown in red dashed line.

The temperature at the middle inlet is the highest during the day compared to the other inlets. This may be due to the slightly higher airflow rate in the middle portion of the manifold resulting in greater convective heat gains from the PV module to the air stream. However, it's unclear why the east inlet experiences lower inlet temperatures. The inherent error within Type-T thermocouples of $\pm$1.0C may have contributed to these differences in measurements(Lundström and Mattsson, 2021). Care will be taken in the future to calibrate and correct for differences between the thermocouples when measuring the same reference temperature.

The maximum difference at 1-minute intervals between the inlets with the highest and lowest temperatures throughout the day is 3.0°C (which occurs during noon time between the middle inlet and the east inlet). The west inlet temperature is the closest to the average value of all three inlet temperatures, with an average difference of 0.1°C during 10:00 to 14:00 and 0.2°C during the rest of the day between the west inlet temperature and the average temperature. The maximum difference between the average temperature and the west, middle, and east inlets are 0.9°C, 1.4°C and 1.7°C respectively. The average difference between the average temperature and the west, middle, and east inlets are 0.2°C, 0.2°C and 0.4°C respectively. These differences in relation to the 9.6°C temperature rise as shown in Figure 3.2.6 indicate that the uniformity of cavity airflow from the manifold design is acceptable.

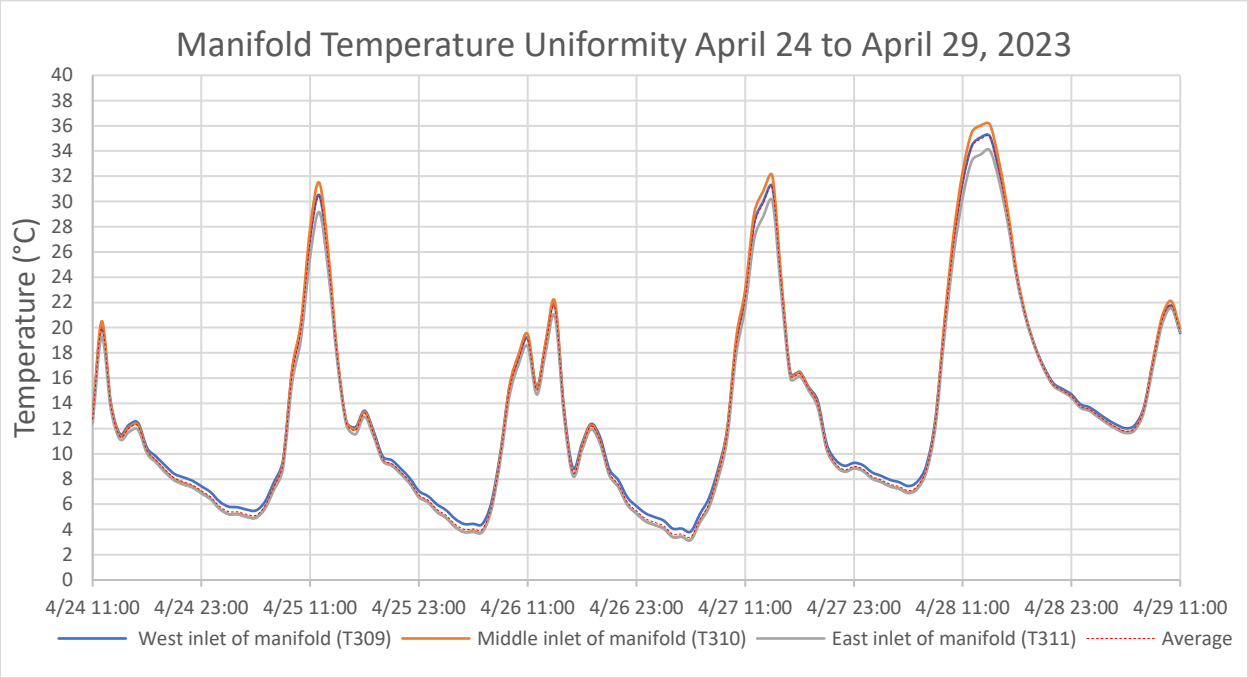

Figure 4.2.21: Hourly averaged measured temperature of each manifold inlet and their average values over the monitoring period between April 24 to April 29, 2023.

Shows the temperature of each manifold inlet over the April 24 to April 29 monitoring period. The values are averaged from the 1-minute interval data to an hourly basis.

The maximum difference between the highest and lowest temperatures in the inlets is 2.4°C for the middle compared to the east inlet at noon time. The maximum difference between any of the inlet temperatures and the average of the three temperatures is ± 1.2 °C.

The west manifold inlet is within ±0.3°C of the average value of all three inlets around noon (10:00 to 14:00) and deviates farther from the average up to ±0.4°C during the mornings and evenings (the other two inlet temperatures are closer to the average during nighttime). These differences are smaller than those seen on the single day of April 29th due to the 1-minute interval being more susceptible to large swings in boundary conditions (such as non-uniform solar irradiance and wind conditions) that can result in larger instantaneous differences.

4.3. Measuring improvement of HRV Performance due to BIPV/T integration

Nighttime data has been analyzed separately from daytime data to quantify the different performance between the HRV-only and the BIPV/T+HRV cases. Due to the lack of a weather station at the time of the experiment, some adjustments had to be made regarding the outdoor temperature measurements. These topics are discussed in Appendix 9.7.

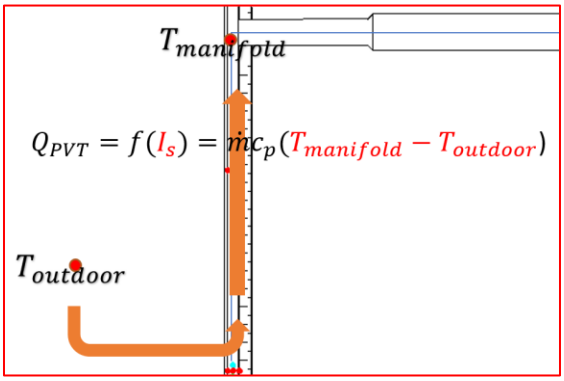

Figure 4.3.1: Stage 1 of HRV supply air heat gain: BIPV/T air cavity heat capture

By coupling the BIPV/T system with the HRV, directing the recovered warm air from the BIPV/T air cavity into the inlet air port of the HRV, both the HRV inlet air port temperature $T_{IA,HRV}$ and HRV supply air outlet port temperature $T_{SA,HRV}$ are expected to increase. As seen from Figure 4.1.3 the heat gain on the supply air temperature occurs in three stages. In the first stage, the temperature increase from the outdoor ambient air temperature T_{out} to the average BIPV/T manifold temperature $T_{manifold}$ due to the bulk movement of air within the air cavity capturing heat from the back of the PV cladding and the aluminum back pan on the exterior insulation through convection. This heat gain is correlated with the incident solar irradiance I_s on the PV cladding.

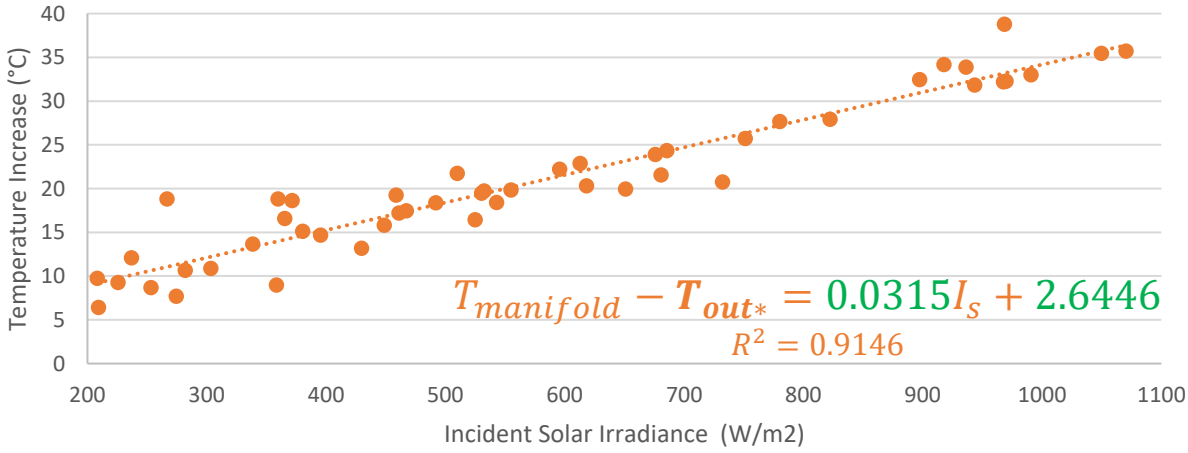

Figure 4.3.2: Comparison of linear regression correlations for manifold inlet $T_{manifold}$ temperature increase based on $(T_{manifold} - T_{out*})$ for the monitoring period from January 26 to February 8, 2023.

As shown in Figure 4.3.2, this relationship between the heat gain from the BIPV/T air cavity and the incident solar irradiance appears to be linear. The linear regression correlation follows the form:

$$T_{manifold} = k_1 I_s + k_2 + T_{out} \quad (4.3.1)$$

Since the local outdoor ambient temperature from a weather station was not always available, some other linear regression correlations are examined in Appendix 9.9 for comparison. For the purposes of clarity in this analysis workflow to quantify the benefit of BIPV/T integration with HRV, the empirical correlation for the Test Cell 2 BIPV/T curtain wall shown in Figure 4.3.2 is used throughout the analysis in this Chapter. Also, as mentioned previously, to minimize the influence of inlet and outlet effects and temperature measurement errors, only periods of significant incident solar irradiance ($I_s > 200\ W/m^2$) are analyzed.

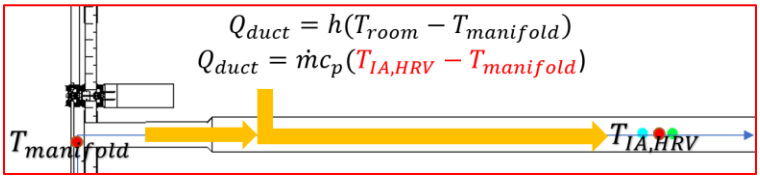

Figure 4.3.3: Stage 2 of HRV supply air heat gain: Indoor duct losses

In the second stage of the temperature increase of the HRV supply air temperature, the airflow drawn in by the HRV fan travels from the BIPV/T manifold opening to the HRV inlet air port through a length of duct. Due to imperfections in workmanship and insufficient thermal insulation around the ductwork and BIPV/T manifold, there is typically some heat transfer between the ambient indoor air and the airflow within the length of duct. Assuming that the temperature of the airflow within the duct is lower than the indoor ambient air temperature of $T_{room} = 21°C$, heat would be lost from the indoor air and be gained by the airflow within the duct. This is the case for the winter conditions of this monitoring period from January 26 to February 8. If the temperature of the airflow within the duct is higher than the indoor air temperature, then the reverse would occur and heat would be lost from the airflow within the duct and be gained by room ambient air.

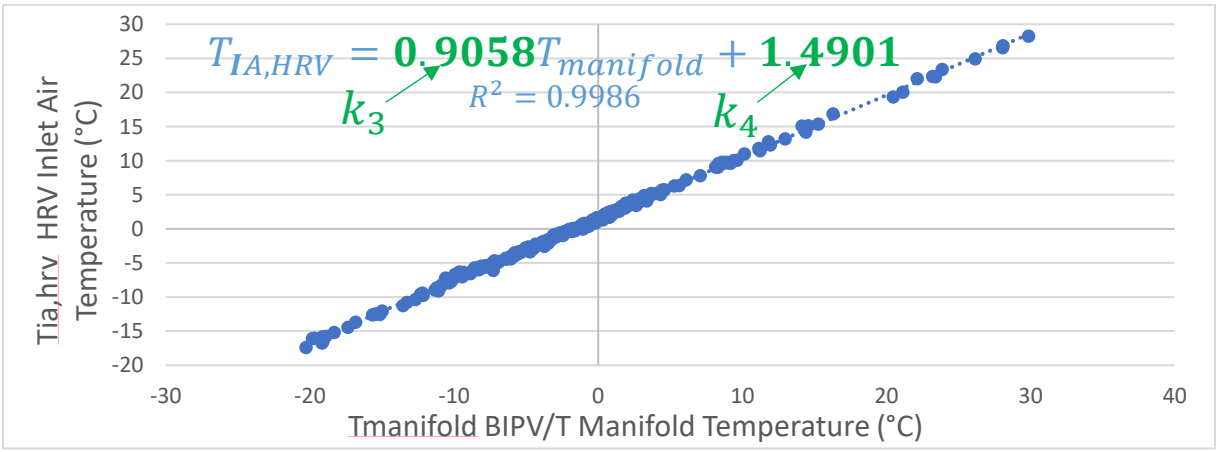

Figure 4.3.4: Correlation for HRV outdoor air inlet port temperature $T_{OA,HRV}$ and average BIPV/T manifold inlet temperature $T_{manifold}$ (including both BIPV/T+HRV and HRV only cases) during the monitoring period from January 26 to February 8, 2023.

Figure 4.3.4 confirms that there is a good linear correlation ($R^2 = 0.9986$) between the HRV inlet air temperature $T_{IA,HRV}$ and the average BIPV/T manifold temperature $T_{manifold}$. This is because the room temperature is kept relatively constant at an average temperature of $T_{room} = 21°C$, so the overall heat transfer coefficient between the room air and the airflow within the duct are not expected to change significantly and should only depend on the temperature of $T_{manifold}$. The linear regression follows the form:

$$T_{IA,HRV} = k_3 T_{manifold} + k_4 \qquad (4.3.2)$$

Where $k_3 = 0.9058$ and $k_4 = 1.4901$ are constants obtained from the linear regression using the measured field monitoring data.

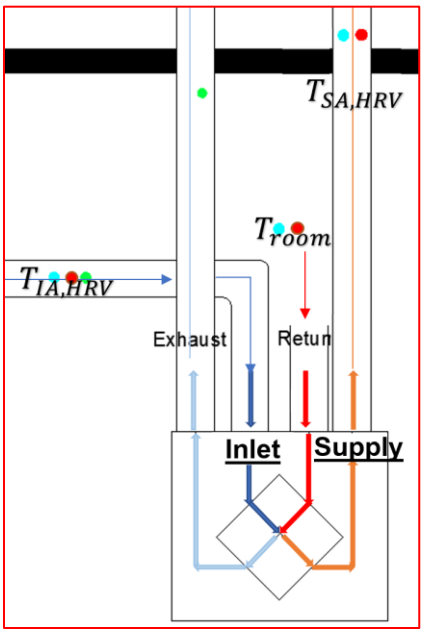

Figure 4.3.5: Stage 3 of HRV supply air heat gain: HRV heat recovery core

In the third stage of the HRV supply air heat gain, the HRV inlet air goes through the HRV heat exchanger core. In the case of the Venmar EKO1.5 HRV, the cross-flow heat exchanger design of the heat recovery core directs the air streams from the stale indoor room air (also known as return air) and the fresh inlet air as shown in the schematic in Figure 4.3.5. The heat recovery core keeps the two streams of air separate through the walls in its structure while allowing for the heat to transfer from the warm indoor room air to cold inlet air. This results in the inlet air stream recovering a portion of the heat from the indoor room air stream and becoming a warmer air stream, the HRV supply air, that is outlet from the HRV port and used for either indoor air ventilation or to be supplied to another active system such as an air-source heat pump.

The sensible recovery efficiency (SRE) describes the efficiency of an HRV system and its heat exchanger core to perform this transfer of heat from the stale indoor air from the room to the fresh inlet air stream.

The SRE can be defined by:

$$SRE = \frac{T_{SA,HRV} - T_{IA,HRV}}{T_{room} - T_{IA,HRV}} \quad (4.3.3)$$

Where $T_{SA,HRV}$ is the HRV supply air outlet temperature in °C, $T_{IA,HRV}$ is the HRV inlet air temperature in °C, and T_{room} is the indoor room air temperature (to be exhausted to outdoors downstream of the HRV heat exchanger core) in °C.

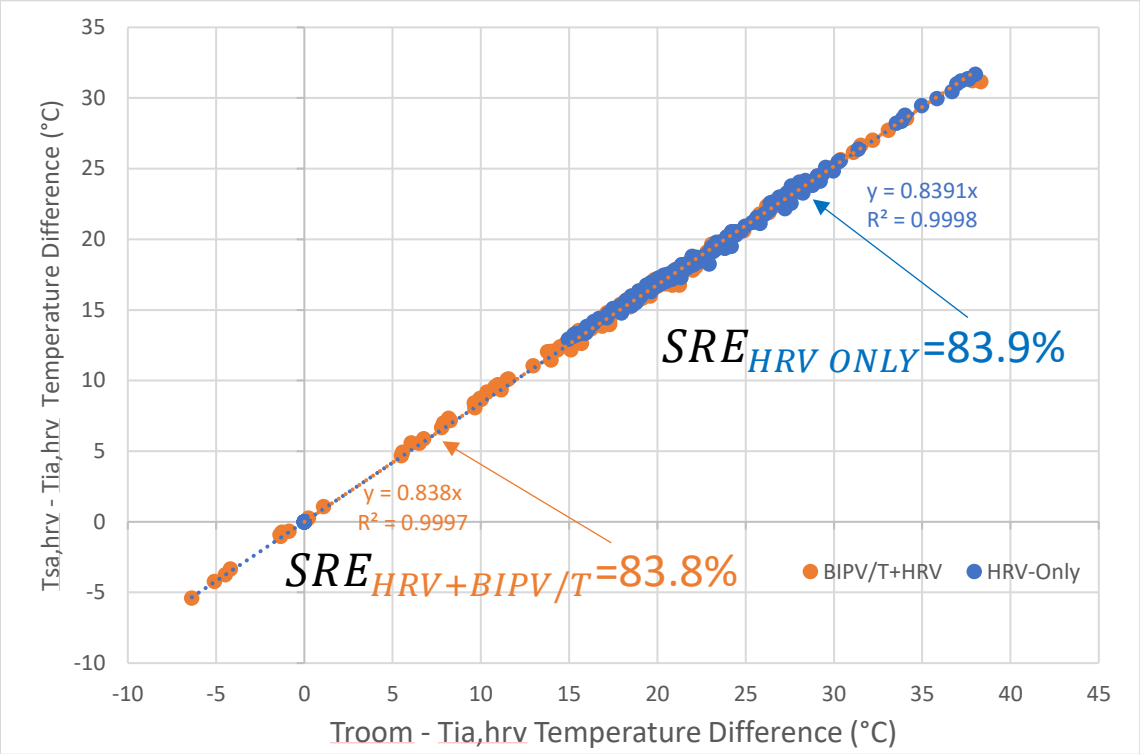

Figure 4.3.6: Determination of SRE through linear regression for both cases.

The HRV core was thought to be less efficient as a heat exchanger at lower outside air inlet temperatures. However, the monitoring results from January 26 to February 8 2023 showed no significant change in SRE between integrating with BIPV/T compared to the case with the HRV alone. By plotting the measured data of $T_{SA,HRV} - T_{IA,HRV}$ against $T_{room,HRV} - T_{IA,HRV}$, the SRE can be determined through linear regression where the slope of the line is the SRE. The correlations shown for both BIPV/T+HRV and HRV-only cases in Figure 4.3.6 indicate that there is no significant change in the SRE of the HRV due to the presence the BIPV/T preheating. The slopes of both cases are nearly identical and indicate an insignificant change in SRE from 83.9% to 83.8% when $T_{IA,HRV}$ is preheated by the BIPV/T. For the purposes of further analysis in this chapter, the SRE of the HRV is considered constant at 83.9%.

The airflow from the HRV supply air outlet is typically used to provide ventilation air to the indoor environment, and in the case where $T_{SA,HRV}$ is lower than the indoor temperature setpoint T_{room} additional heating energy is used by a heating coil to heat up the airflow such that $T_{SA,HRV} = T_{room}$. This additional heating coil energy consumption can be reduced by increasing $T_{SA,HRV}$ through integrating the HRV system with BIPV/T for its air cavity preheating. Similarly, in the case where

the BIPV/T+HRV system is additionally coupled with an air-source heat pump system, the airflow from the HRV supply air outlet is used as the inlet for the heat pump system. In this case, the HRV supply air is also able to improve the heat pump system's coefficient of performance (COP) when $T_{SA,HRV}$is increased. In both cases, the integration of BIPV/T with an HRV system can provide energy savings which can be quantified when $T_{SA,HRV}$ is known.

Given the correlations found through field monitoring as shown in Figure 4.3.2 and Figure 4.3.4 and the determination of SRE through linear regression in Figure 4.3.6, it is possible to derive the dynamic solar irradiance dependent increase of $T_{SA,HRV}$ due to BIPV/T integration:

$$T_{SA,HRV} = (1 - SRE)T_{IA,HRV} + SRE(T_{room}) \quad (4.3.4)$$

$$\Delta T_{SA,HRV} = T_{SA,HRV_{(I_S>0)}} - T_{SA,HRV_{(I_S=0)}} \quad (4.3.5)$$

Where $\Delta T_{SA,HRV}$ is the increase in HRV supply air outlet port temperature in °C, $T_{SA,HRV_{(I_S>0)}}$ is the value of $T_{SA,HRV}$ in the case of HRV+BIPV/T integration as determined from Equations (4.3.1), (4.3.2) and (4.3.3) evaluated at incident solar irradiance $I_S > 0$, and $T_{SA,HRV_{(I_S=0)}}$ value of $T_{SA,HRV}$ in the HRV-only case as evaluated at incident solar irradiance $I_S = 0$.

Equation (4.3.5) can be rewritten in the following form by combining with Equations (4.3.1), (4.3.2) and (4.3.3):

$$\Delta T_{SA,HRV} = (1 - SRE)(k_1 k_3)I_S \quad (4.3.6)$$

Where k_1 and k_3 are constants determined from the linear regression of measured data as shown in Figure 4.3.2 and Figure 4.3.4. The resulting equation suggests that the increase in HRV supply air temperature $\Delta T_{SA,HRV}$ mainly depends on SRE, k_1 from the BIPV/T air cavity heat gain correlation, k_3 from the indoor duct loss correlation, and incident solar irradiance I_S. More details of the derivation are shown in Appendix 9.10.

$$F_{BIPV/T} = (1 - SRE)(k_1 k_3) \quad (4.3.7)$$

$$\Delta T_{SA,HRV} = F_{BIPV/T} I_S \quad (4.3.8)$$

Given that the SRE, k_1 and k_3 are constant values, the performance improvement from integrating BIPV/T with HRV in terms of increased $\Delta T_{SA,HRV}$ can be quantified by a BIPV/T temperature gain factor $F_{BIPV/T}$ in $°C/\frac{W}{m^2}$ to measure the ability of the BIPV/T system to increase $\Delta T_{SA,HRV}$ depending on the available solar irradiance.

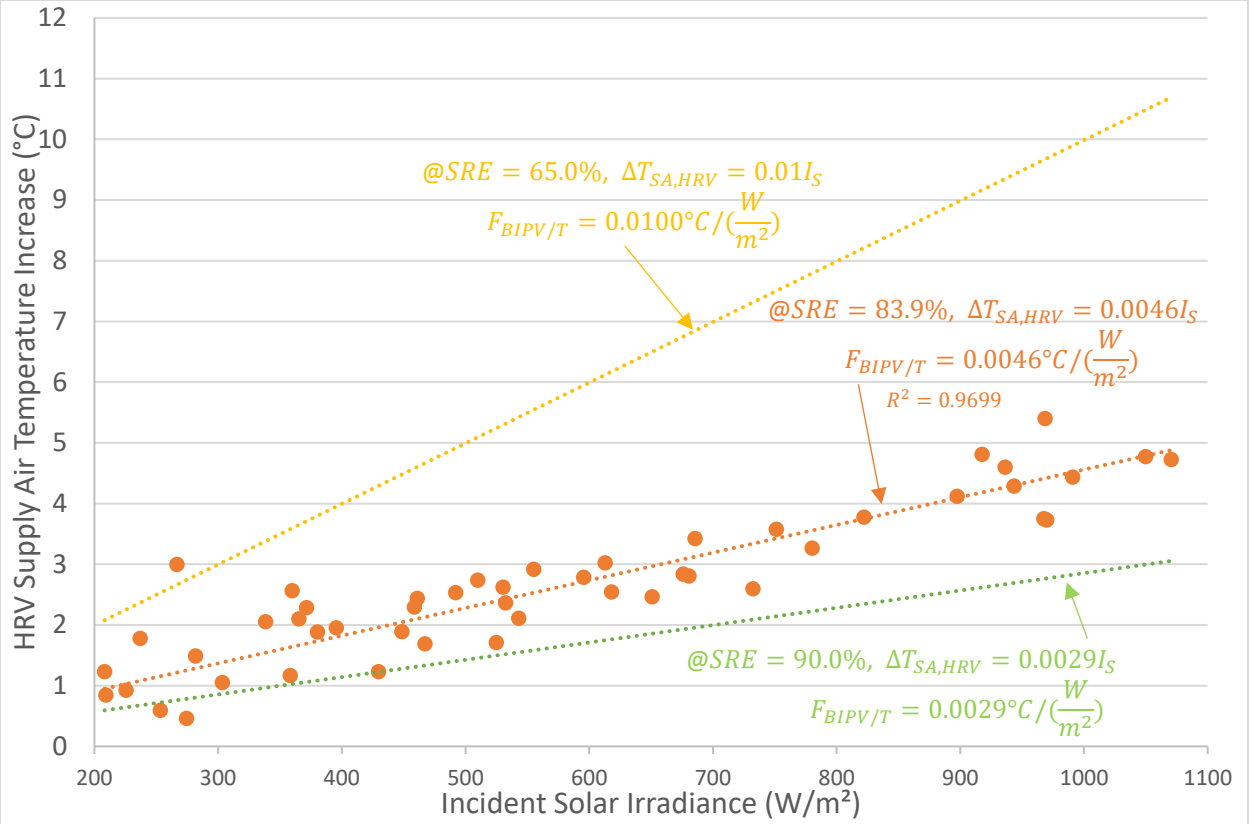

Figure 4.3.7: Predicted HRV supply air temperature increase $\Delta T_{SA,HRV}$ as incident solar irradiance I_s increases for sensible recovery efficiency SRE=0.650, SRE=0.839 and SRE=0.900.

Figure 4.3.7 illustrates the predicted $\Delta T_{SA,HRV}$ based on the T_{out} correlations as solar irradiance is increases. The $F_{BIPV/T}$ has also been determined using Equation (4.3.7) for hypothetical HRV performance of SRE=0.650 and SRE=0.900. The correlations suggest that the effect of BIPV/T preheating on the HRV supply air temperature $T_{SA,HRV}$ is greater when the HRV's SRE is lower. This means that a highly efficient HRV would not benefit as much from integrating with a BIPV/T air cavity because its heat recovery core is already capable of significantly increasing the supply air temperature. However, in the case of lower efficiency HRV units, such as those that are intended for small residential spaces with SRE=0.650, the HRV can benefit greatly from the additional preheating provided by the 2m tall BIPV/T air cavity monitored for this experiment (up to an additional supply air temperature increase $\Delta T_{SA,HRV}$ of 10°C when incident solar irradiance is 1000 W/m²).

For the current HRV+BIPV/T integration examined in this monitoring experiment, the HRV supply air temperature $T_{SA,HRV}$ is increased by the BIPV/T integration by a factor of $0.0046°C$ per W/m^2 of incident solar irradiance. This is an increase of about 1°C to 5°C throughout the monitoring period depending on the available solar irradiance. The range of $\Delta T_{SA,HRV}$ estimated by Equation (4.3.8) is consistent with the typical increases seen in $T_{SA,HRV}$ when comparing the two cases of data within the same temperature ranges as shown in Figure 4.3.8.

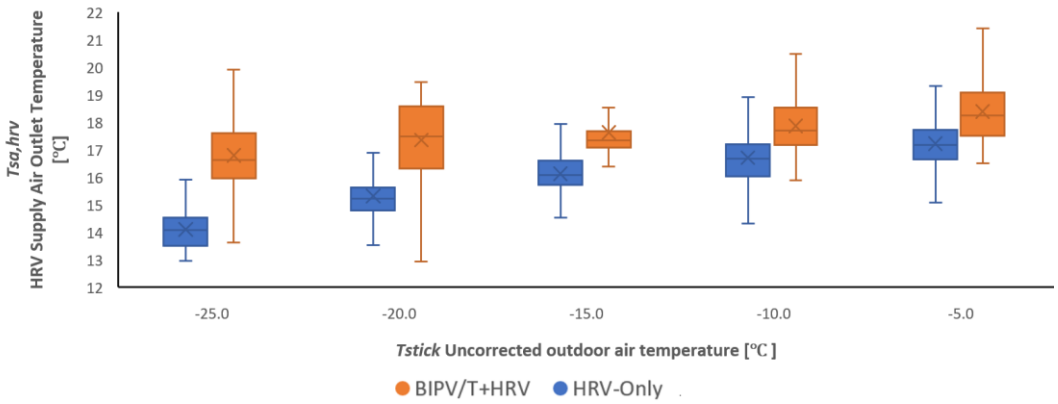

Figure 4.3.8: Comparison of integrated BIPV/T+HRV case and the HRV-only case in terms of measured $T_{SA,HRV}$ within the same temperature ranges.

Since the SRE of 83.9% remained effectively constant throughout field testing despite the outdoor air temperature ranges between -25°C to -5°C, the BIPV/T temperature gain factor $F_{BIPV/T}$ can be determined separately without the presence of the specific HRV unit. This suggests that field performance testing is not strictly necessary for the HRV section of the integration. The field performance can be measured in two parts: first by field measurements of the temperatures from the bottom of the BIPV/T cladding to manifold inlet and to the end of the duct section leading to the inlet air port of the HRV to determine k_1 and k_3, then second by indoor tests of the HRV operation to measure the return air inlet and supply air outlet temperatures under a wide range of outdoor air inlet port temperature to determine SRE. The results of the two parts can then be used to determine the $\Delta T_{SA,HRV}$ for any of the field monitored outdoor weather conditions.

There were significant limitations with this experiment. The analyzed monitoring period is short and exposed to unfavorable outdoor air and solar irradiance conditions for the BIPV/T system. The thermal transmission losses at the manifold to HRV duct section may have affected the quality of the monitoring data. The PV cladding for the BIPV/T system is also only 2m long. With such a short path length, the temperature rise from bottom to top of the BIPV/T is not as significant as it would be for rooftop applications or larger building facades. The HRV core of this unit also may not be sensitive enough for significant frosting to occur (no physical frosting or condensation was detected during the monitoring period).

One of the objectives of this monitoring experiment was to quantify the reduction in the HRV's defrost operation time due to integration with BIPV/T. However, due to the inability to control to the outdoor boundary conditions in field monitoring experiments, the monitoring data lacked measurements for periods when $T_{IA,HRV}$ fell below the programmed defrost operation conditions. From examining the $T_{IA,HRV}$ data, out of the 312 hours within the monitoring period, there were less than 6 hours during daytime and less than 12 hours during nighttime when the average $T_{IA,HRV}$ temperature is between the pre-programmed -10°C to -27°C condition which would trigger the HRV's defrost operation. The amount of data was not sufficient to make conclusions about the reduction in HRV's defrost time. The collection of more long-term field monitoring data to increase the odds of measuring the HRV's performance during these cold weather conditions can help analyze the relationship between the unit's $T_{IA,HRV}$ and defrost time in the future.

5. BIPV Hygrothermal Simulation

With the increasing demand for renewable energy in the building industry, BIPV systems are now being developed for the exterior wall construction of low-rise residential buildings. However, the simple replacement of cladding with BIPV systems in standardized wall construction practice may lead to unknown adverse effects on the hygrothermal performance of the wall assembly. BIPV and PV systems in general convert a portion of solar radiation into electricity and removes this portion of energy from the system which would otherwise be converted into heat. This is typically accounted for in models with the solar absorptance α subtracted by the electrical efficiency η_{el} (Candanedo et al., 2010). For simplicity, when the BIPV system is connected to a load, such as an energy storage device or the grid, the system is assumed to be in the maximum power point tracking (MPP) state. When it is not connected to a load (hence not generating electricity), it is assumed to be in the open circuit (OC) state.

This study investigates the effect of BIPV application on durability by comparing the hygrothermal performance of a conventional low-rise residential wood-frame wall assembly under different options for exterior cladding. To examine the potential for any moisture issues, hygrothermal modelling was performed in WUFI Pro 6. Hygrothermal simulation results were compared between 3 groups: BIPV in open circuit state (BIPV-OC), BIPV in maximum power point tracking state (BIPV-MPP), and fiber cement. This is done by varying cladding construction properties of Layer 1 as shown in Figure 5.1.1.

5.1. BIPV hygrothermal modelling methodology in WUFI

The hygrothermal simulation program WUFI Pro 6 is used to model the hygrothermal performance of three different wall assembly cases. A typical wood frame low-rise construction wall is modelled as shown in Figure 5.1.1 and Figure 5.1.2.

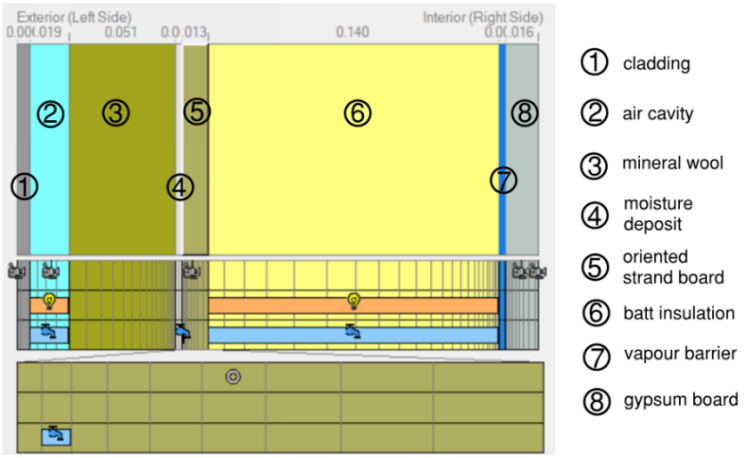

Figure 5.1.1: Wall assembly setup in WUFI Pro 6.

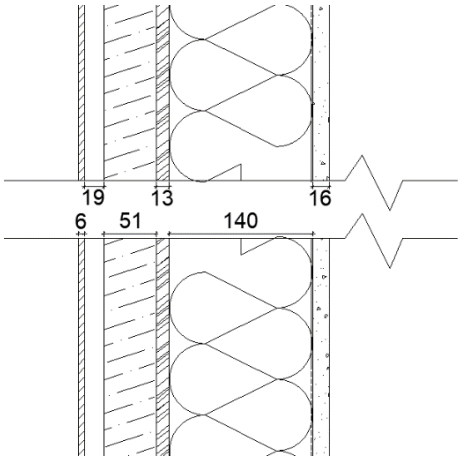

Figure 5.1.2: Wall assembly section drawing

The properties of the fiber cement cladding are given from the WUFI material database's "Fiber Cement Sheathing Board". The BIPV wall assembly uses an identical setup to the Fiber Cement wall assembly and only replaces the fiber cement cladding layer with a custom material with BIPV cladding properties. Since in a BIPV cladding the PV modules would be integrated with glass panes, the properties of the BIPV cladding layer are assumed to be similar to those of glass. Table1 shows the properties used for the simulations. The moisture storage function is set to a constant near-zero value to reflect the lack of moisture storage properties of the impermeable BIPV cladding. The water vapour diffusion resistance factor is set to a constant 30000 μ-value. The thermal conductivity of the BIPV is not moisture dependent nor temperature dependent, so its value is set to be a constant value of 5.004 W/m.K.

Table 5.1.1: Material properties of the BIPV-OC, BIPV-MPP, and fiber cement cladding types compared. The oriented strand board (OSB) material properties are also included for reference.

Property	BIPV-OC	BIPV-MPP	Fiber Cement	OSB
Bulk Density (kg/m^3)	2470	2470	1380	650
Porosity (m^3/m^3)	10^{-5}	10^{-5}	0.479	0.95
Specific Heat Capacity (J/kg.K)	750	750	840	1880
Thermal Conductivity (W/m.K)	5.004	5.004	0.245	0.092
Water Vapour Diffusion Resistance Factor (-)	30000	30000	990.9	812.8
Typical Built-In Moisture (kg/m^3)	10^{-5}	10^{-5}	190	90
Layer Thickness (m)	0.006	0.006	0.006	0.013
Short-Wave Radiation Absorptivity	0.8444	0.6944	0.8	-
Long-Wave Radiation Absorptivity	0.9	0.9	0.9	-

The surface transfer coefficient inputs are modified such that the short-wave radiation absorptivity of BIPV in the OC state matches a typical solar absorptivity α=0.8444. While for BIPV in the MPP state, the short-wave radiation absorptivity is represented by subtracting the electrical conversion efficiency $\eta_{el} = 0.15$ from the OC state solar absorptivity to account for the extraction of solar energy from the system that would have otherwise become additional heat. The long-wave radiation emissivity is assumed to be equivalent to the front/back emissivity of a typical grey surface for all three cladding options.

To model the effect of air leakage, an air change source on fiberglass batt insulation (layer 6) is set as 1.5 ACH with spread area over the whole layer and mixes with air from the left-hand side. The air change source in the air cavity (layer 2) is setup the same way, but the air change rate is varied between 0 to 100 ACH for each simulation.

The simulate rainwater deposit, 1% of rain load based on ANSI/ASHRAE Standard 160 is modeled as a moisture source at a 0.001m depth within the OSB (layer 4), with one element spread area and cut-off at free water saturation.

The mould risk of the OSB layer for each cladding option is determined using the WUFI Mould Index VTT Add-on, which evaluates both the mould index M and average mould growth rate $\frac{dM}{dt}$ using the empirical model by (Hukka and Viitanen, 1999).

$$\frac{dM}{dt} = \frac{1}{7\,exp(-0.68lnT - 13.9lnRH + 0.14W - 0.33SQ + 66.02}k_1k_2 \qquad (5.1.1)$$

where k_1 is the intensity coefficient of mould growth depending on if $M > 1$ or $M < 1$, and k_2 is the corrective coefficient as M approaches maximum value, SQ is the surface quality value (0=resawn, 1=original kiln-dried), T is temperature in $°C$, RH is relative humidity in %.

The parameters RH, M and MC together are used to quantify and compare the hygrothermal performance of each cladding option.

5.2. Effects of airflow on BIPV-clad wood-frame Wall WUFI

Hygrothermal simulation was performed for the three cladding options without any ventilation in the air cavity to examine the baseline annual profiles of each parameter. Figure 2 shows the trends in the OSB RH and MC after 2 years of simulation. The RH values are high for all three options, with the maximum RH being above 86% for fiber cement and 93% for the BIPV options. However, the fiber cement option performs significantly better in terms of MC, where it only reaches 106 kg/m^3 (16% in OSB) at maximum while both BIPV options are still consistently nearly double that value and reaching maximums of 201kg/m^3 (31% in OSB) despite the slight drying period that decreases both the RH and MC from February to April. The fiber saturation point of wood is 28% MC on average, and if the MC is greater than the fiber saturation point for a prolonged duration, the wood specimen is likely to experience deterioration and mould growth (Canadian Wood Council, 2000). Consequently, calculated M is much higher in the BIPV options at over 5.11 than in the fiber cement option at 3.17. However, these values indicate that all three options have significant mould risk when exposed to rain deposit and lack any air cavity ventilation.

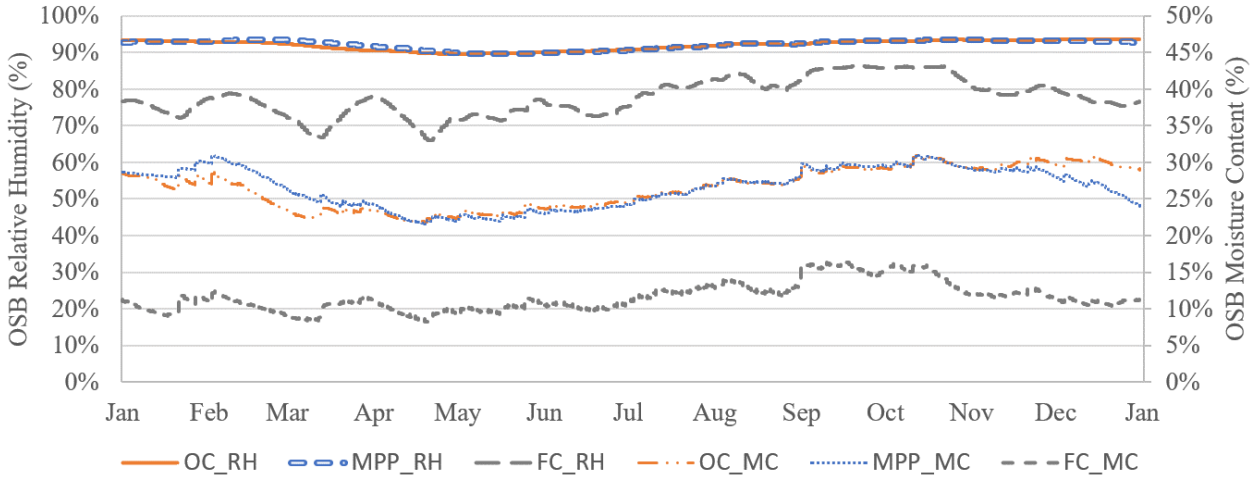

Figure 5.2.1: Comparison of RH and MC of OSB layer with rain deposit and no cavity ventilation

With all other parameters remaining constant, simulations were performed for each cladding option under various air cavity ventilation rates with rain deposit included. As cavity ventilation rates increases, the maximum RH, MC, and M all decrease. For fiber cement, this decreasing trend is gradual and steady over the 0 to100 ACH ventilation range. However, for the BIPV options, the

trend decreases significantly over a much narrower range of ventilation rates, 15 to 20 ACH for BIPV-OC and 5 to 10 ACH for BIPV-MPP.

Figure 5.2.2 shows that the fiber cement cladding option initially has significantly lower mould risk when compared to the BIPV options. However, after the cavity ventilation rate is increased above 20 ACH (or 0.017 m/s air velocity for a 3m high air cavity), the BIPV options are able to achieve negligible mould risk levels ($M < 1$) while the fiber cement option requires much higher ventilation rates to reach the same level.

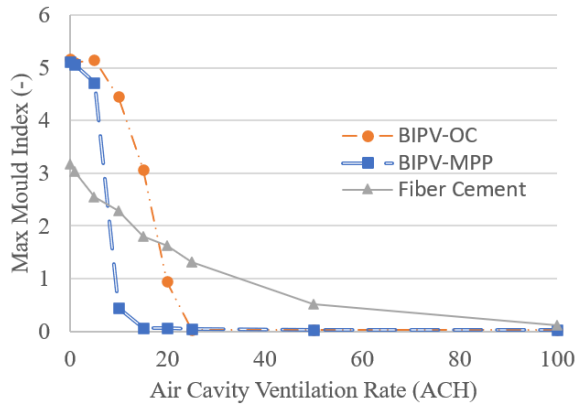

Figure 5.2.2: Max mould index of each cladding option at different air cavity ventilation rates

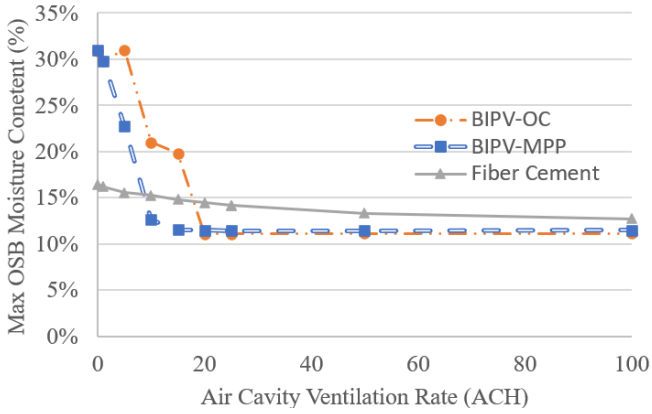

Figure 5.2.3: Maximum oriented strand board moisture content of each cladding option at different air cavity ventilation rates

Figure 5.2.3 shows that the fiber cement cladding option has lower maximum OSB moisture content than both BIPV options at low cavity ventilation rates. While the BIPV options initially have maximum MC above the fiber saturation point, as cavity ventilation increases to the 10-20 ACH range, the maximum MC significantly decrease and become dryer than the fiber cement option.

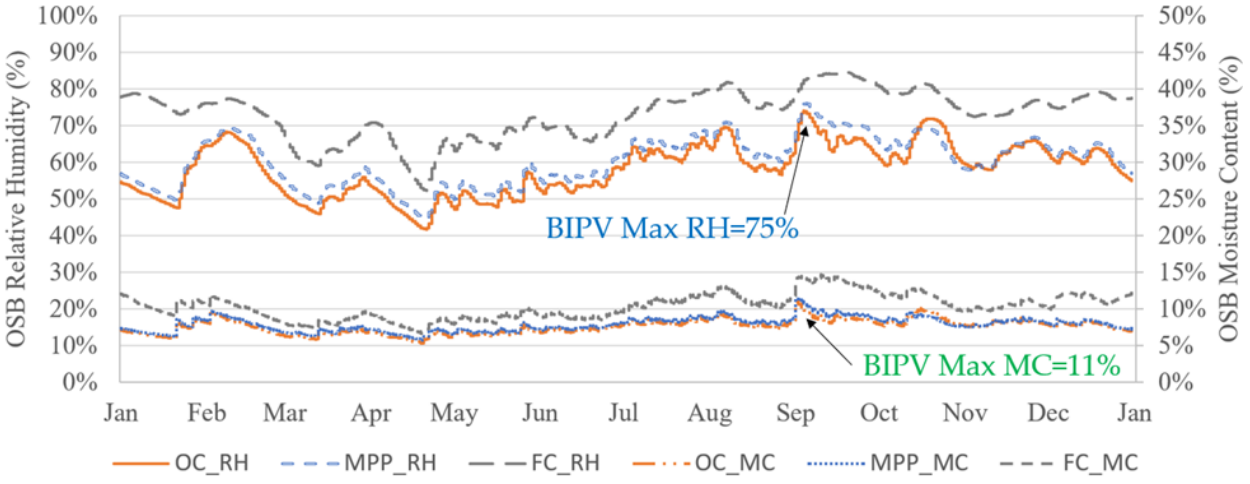

Figure 5.2.4. Comparison of RH and MC of OSB layer with rain deposit and 20 ACH cavity ventilation

For the BIPV options, the MPP-state consistently outperforms the OC-state until cavity ventilation rate exceeds 20 ACH. The difference in air cavity conditions between these two states is examined in Appendix 9.10 investigate the reason for this difference in performance. The results suggest that a solar-driven moisture accumulation effect is present during the winter and spring months.

The simulation results in this study show that the air cavity ventilation is critical in maintaining hygrothermal performance of wood-frame construction when considering the implementation of BIPV cladding for wall assembly design. While the performance of the OC and MPP states are simulated as separated cases in this study, actual BIPV facades would switch between states depending on solar irradiance. Since the actual hygrothermal performance of the BIPV system would be a combination of the two states, a minimum cavity ventilation rate requirement of a similar wall assembly should be at least 20 ACH (to account for the BIPV operating outside its MPP state. This recommendation is based solely on WUFI Pro 6 simulation, and the reliability of the results needs to be compared to laboratory or field studies in future works. Another limitation of this study is the assumption of 1% rain deposit on the exterior surface of the OSB. Due to variance in construction workmanship and wind distribution, the effects of moisture reported in this study may not reflect actual conditions of rain penetration. Similarly, the ventilation rate in the air cavity by natural forces is driven by wind pressure and thermal buoyancy, thus the cavity air change rate likely has large fluctuations and is difficult to estimate in a field installation. However, study has shown similar south-facing wall assemblies achieving average natural ventilation of at least 200 ACH(Falk and Sandin, 2013), and in the case of mechanical ventilation, a typical BIPV/T system operating at 0.5 m/s air velocity in a 19mm wall cavity behind a 1m x 3m panel can achieve 600 ACH, indicating that risks of <20ACH scenarios would be unlikely if care is taken in construction to allow for natural ventilation or to design mechanical ventilation in the air cavity. The solar-driven moisture transfer behind BIPV cladding also presents an opportunity to explore moisture recovery through energy recovery ventilators in BIPV/T systems. The system would not only recover heat from the cladding, but also remove excess moisture to improve the wall's durability and humidify the indoor space.

This study has shown through simulation that wood-frame wall assemblies with BIPV cladding can have better hygrothermal performance than those with fiber cement cladding if the air cavity is well ventilated. BIPV/T wall assemblies may experience moisture issues with ventilation rate below 20ACH with rain leakage assumed due to solar-driven moisture accumulation and impermeable cladding surface. However, this is typically not a concern since the ventilation rate achieved in BIPV wall assemblies is typically much higher, about 200ACH for naturally ventilated BIPV/T façade or 600ACH for mechanically ventilated BIPV/T systems. Difference in performance between BIPV OC and MPP states were also investigated, and it has better hygrothermal performance in its MPP state.

6. Characterization of Solar Heat Gain Coefficient for STPV

This chapter of the thesis focuses on the theoretical and experimental methods for determining the solar heat gain coefficient (SHGC) of semitransparent photovoltaic (STPV) glazing. The SHGC is an important parameter to characterize for comparison of STPV technologies as designers would need to compare the potential heat gains from implementing STPV glazing with conventional glazing alternatives to optimize energy efficiency and thermal comfort. The SHGC is an important input for building energy performance simulations during design for this purpose and may be important for general BIPV technologies as well. The BIPV cladding for the curtain wall system analyzed in Chapter 3 can technically be considered a STPV cladding as well, since the 72-cell Model CS6X-290P-FG PV array is 92.2% opaque and has a solar transmittance $\tau_{sol} = 0.0662$, there are direct solar heat gains transmitted from the BIPV cladding to the backpan surface of the curtain wall air cavity which have not been considered in detail in the experimental analysis nor modeling. Opaque BIPV systems can be considered as a special case of STPV systems where the solar transmittance is zero or negligible, thus developing methods to measure and analyze the more complex heat transfer phenomena in STPV systems may provide important insight for not only the modeling and design of STPV glazing systems but BIPV/T systems in general. One challenge in determining the SHGC for STPV glazing include the electrical operating state of the STPV modules which would remove electrical energy and prevent that portion from converting into heat energy in the system, results in a lower effective SHGC when the STPV system is connected to a load and generating electricity. The correct determination of SHGC needs to account for this extraction of electrical energy depending on the operating state, such that two SHGC values, one for the open-circuit (OC) state and one for the maximum power point tracking (MPP) state are determined. The other is the inhomogeneity of optical properties of STPV systems, where parts of a STPV glazing pane have low solar transmittance (such as the PV cells) and parts of the pane are clear and have high solar transmittance, such that the determination of SHGC requires the measurement of optically representative areas or methods for area-weighted averaging of properties in dissimilar areas (Martín-Chivelet et al., 2022). Chapter 6.1 details a workflow proposed by IEA PVPS Task 15 to address these two challenges and theoretically determine the SHGC of STPV systems. Chapter 6.2 details a preliminary methodology for experimentally determining the SHGC through in-situ optical measurements, using a conventional insulated glazing unit (IGU) as an initial reference specimen for assessing the effectiveness of this experimental methodology.

6.1. Theoretical Determination of Effective SHGC & U-value for STPV

This theoretical determination method was used in Activity E1 as part of IEA PVPS Task 15 Phase 2 Subtask E – Pre-normative international research on Building Integrated Photovoltaic (BIPV) system characterization methods. The objective of Subtask E is to develop new and optimized characterization methods for BIPV systems. Activity E1 consists of developing a method to determine the Solar Heat Gain Coefficient (SHGC) of Semi-Transparent Photovoltaic (STPV) glazing while taking into account the generated and extracted electricity under the maximum power point tracking (MPP) electrical state.

To calculate the SHGC of glazing, building professionals may often use glazing simulation software such as WINDOW 7.7 in both early design and developed design workflows to perform calculations which satisfy the level of detail required by ISO 15099: Thermal Performance of

Windows, Doors and Shading Devices – Detailed calculations(Curcija et al., 2018; Rentfro and Gumpertz, 2020). However, these software programs currently cannot simulate STPV glazing components while taking into account the electricity generation's effect on the glazing properties. As such, the following method is developed to be compatible with existing software by only modifying the optical property inputs.

In general, for solar radiation on a semi-transparent surface, the following relation holds:

$$\rho(\lambda,\theta) + \tau(\lambda,\theta) + \alpha(\lambda,\theta) = 1 \qquad (6.1.1)$$

Where (λ,θ) indicates the property as being spectral and angular dependent, ρ is the solar reflectance, τ is the solar transmittance, α is the solar absorptance.

In the case of semi-transparent photovoltaic (STPV) glazing, the absorbed solar radiation includes electrical conversion:

$$\alpha(\lambda,\theta) = N_{out}\alpha(\lambda,\theta) + N_{in}\alpha(\lambda,\theta) + \eta_{el}(\lambda,\theta) \qquad (6.1.2)$$

Where N_{out} is the fraction of absorbed solar radiation is remitted by the glazing system towards the exterior by convection and long-wave radiation (outward flowing fraction), N_{in} is the fraction of absorbed solar radiation is remitted by the glazing system towards the interior by convection and long-wave radiation (inward flowing fraction), and η_{el} is the electrical conversion efficiency of the STPV glazing system (fraction of energy extracted from the system).

According to ASHRAE Handbook - Fundamentals(American Society of Heating, Refrigerating and Air-Conditioning Engineers, 2013), SHGC is defined by:

$$SHGC(\lambda,\theta) = \tau(\lambda,\theta) + N_{in}\alpha(\lambda,\theta) \qquad (6.1.3)$$

Where $SHGC(\lambda,\theta)$ is the spectral and angular dependent solar heat gain coefficient.

From Equations (6.1.1) to (6.1.3),

$$SHGC(\lambda,\theta) = 1 - \rho(\lambda,\theta) - \eta_{el}(\lambda,\theta) - \alpha(\lambda,\theta) + \eta_{el}(\lambda,\theta) + N_{in}(\alpha(\lambda,\theta) - \eta_{el}(\lambda,\theta) + \eta_{el}(\lambda,\theta) \qquad (6.1.4)$$

The main difference between modelling of conventional glazing and STPV is the need to account for the conversion of solar radiation to electricity which proportional to the electrical conversion efficiency η_{el}. Given that glazing simulation software such as WINDOW 7.7 is unable to account for η_{el} within SHGC calculations, modification to the solar optical properties input into the software is needed. The effective solar reflectance ρ_{eff} and absorptance α_{eff} are the modified inputs necessary for this approach with WINDOW 7.7. They are defined as:

$$\rho_{eff}(\lambda,\theta) = \rho(\lambda,\theta) + \eta_{el}(\lambda,\theta) \qquad (6.1.5)$$
$$\alpha_{eff}(\lambda,\theta) = \alpha(\lambda,\theta) - \eta_{el}(\lambda,\theta) \qquad (6.1.6)$$

Equation (6.1.4) then becomes:

$$SHGC(\lambda,\theta) = 1 - \rho_{eff}(\lambda,\theta) - \alpha_{eff}(\lambda,\theta) + N_{in}\alpha_{eff}(\lambda,\theta) + N_{in}\eta_{el}(\lambda,\theta) \qquad (6.1.7)$$
$$SHGC(\lambda,\theta) - N_{in}\eta_{el}(\lambda,\theta) = \tau(\lambda,\theta) + N_{in}\alpha_{eff}(\lambda,\theta) \qquad (6.1.8)$$

In this exercise, the value of ρ_{eff} is used in place of ρ as the input into the program, which means the SHGC calculated by the program would be modified to:

$$SHGC_{eff}(\lambda,\theta) = \tau(\lambda,\theta) + N_{in}\alpha_{eff}(\lambda,\theta) \quad (6.1.9)$$

Compared to the original value of SHGC (which does not account for η_{el}) the modified SHGC value will be smaller in magnitude (derived from Equations (6.1.8 and (6.1.9):

$$SHGC_{eff}(\lambda,\theta) = SHGC(\lambda,\theta) - N_{in}\eta_{el}(\lambda,\theta) \quad (6.1.10)$$

This suggests that if the inward flowing fraction of solar heat gain N_{in} can be determined (based on the indoor convective and long-wave radiative heat transfer), then the effective solar heat gain coefficient in the MPP state can be determined from the solar heat gain coefficient in OC state.

The WINDOW 7.7 simulation program can determine the overall (spectral average) Effective SHGC from the following equation(ISO, 2003; National Fenestration Rating Council, 2013):

$$SHGC_{eff} = \frac{q_{in} - q_{in(I_s=0)}}{I_s} \quad (6.1.11)$$

Where $q_{in} - q_{in(I_s=0)}$ is the difference between the heat flux flowing into the interior conditioned space with and without the presence of solar radiation, and I_s is the incident solar irradiance.

For this exercise, the overall value of $SHGC$ is first determined for the glazing configurations in open-circuit ($i.e.\eta_{el} = 0$). The value of $SHGC_{eff}$is then determined as a comparison for the same glazing configurations under maximum power point tracking ($i.e.\eta_{el} > 0$).

After examining three different approaches to account for electricity generation, a simplified approach using Equation (6.1.5) was considered appropriate. Details of this examination are shown in Appendix 9.12.

For Task 15 Activity E1, 96 total variations of STPV configuration, solar spectrum, incident irradiance, exterior and interior temperatures and convective coefficients were examined based on Approach 1.

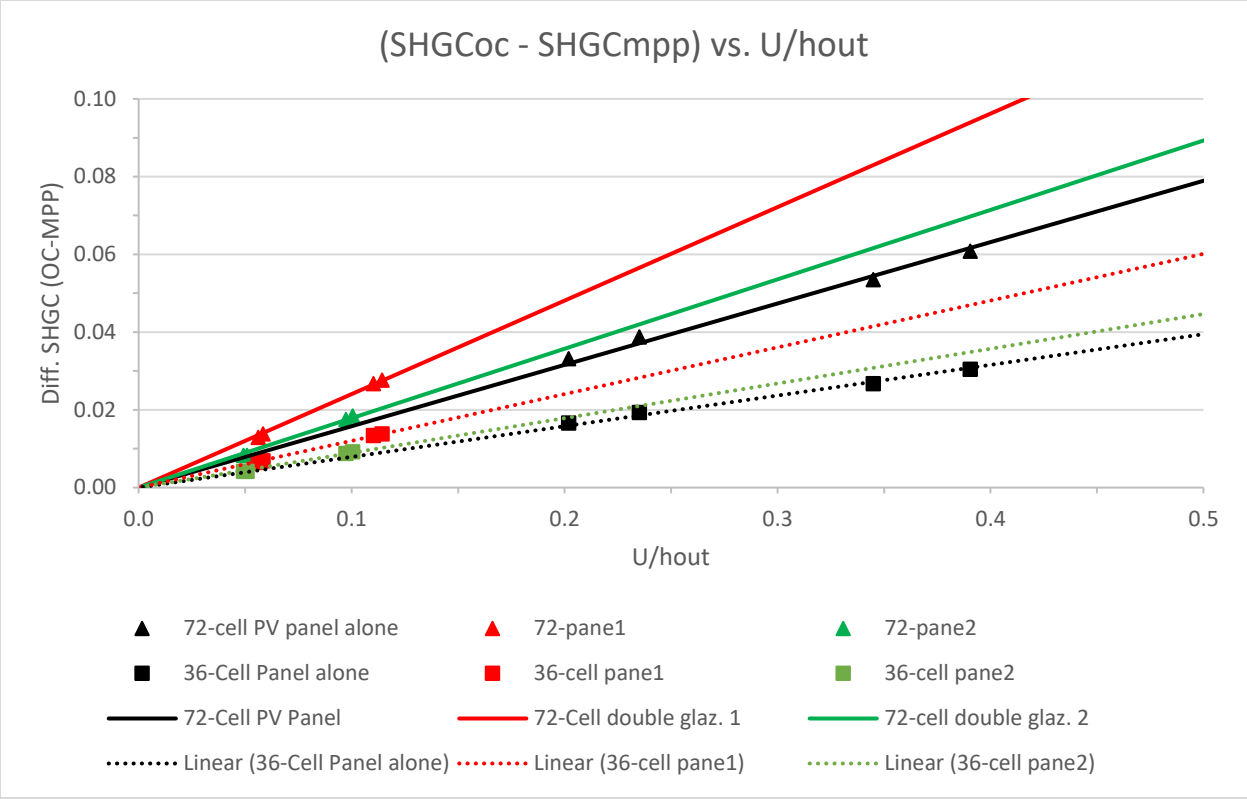

Figure 6.1.1: Comparison of change in SHGC value between OC and MPP states and $\frac{U}{h_{out}}$. The change in SHGC between states appears to be most sensitive to the ratio between the U-value (glazing system's overall heat transfer coefficient) and h_{out} (outdoor combined convective and radiative heat transfer coefficient). The relationship appears approximately linear. (72-cells have 92.2% coverage and 36-cells have 46.1% coverage.)

Examining the results of the SHGC calculations show that the difference between OC and MPP state SHGC values are directly proportional to the ratio of heat transfer coefficients $\frac{U}{h_{out}}$. This is consistent with one of the conventional approaches to estimate SHGC for engineering calculations(Bhandari and Bansal, 1994; Wright, 1996):

$$SHGC = \tau_{sol} + U\frac{\alpha}{h_{out}} \qquad (6.1.12)$$

This indicates that the difference between OC and MPP state SHGC values can be reduced when the STPV glazing configuration has better thermal performance (lower U-value) and changes seasonally (higher h_{out} resulting in less SHGC difference during windy winter conditions, lower h_{out} resulting in greater SHGC difference during less windy summer conditions).

In summary, the modified STPV calculation approach is as follows:

1. Determine spectral averages of solar optical properties of 0% cell coverage glazing configurations and 100% cell coverage glazing configurations respectively (NFRC 300)
2. Determine boundary conditions & heat transfer coefficients (ISO15099 Summer & Winter Conditions, NFRC 300 & custom inputs)
3. Solve energy balance equations (ISO 15099)

4. Compute centre of glass (CoG) U and $SHGC$ for open-circuit states of 0% and 100% cell coverage configurations respectively (ISO 15099)
5. Replace the $\rho(\lambda)$ input with $\rho_{eff}(\lambda)$ for the 100% cell coverage glazing configuration
6. Compute CoG U_{eff} and $SHGC_{eff}$ for MPP states of 0% and 100% cell coverage configurations respectively
7. Perform area-averaging of solar optical properties, *U*, and *SHGC* values for the actual % cell coverage (interpolate from 0% and 100% configuration results) for both open-circuit and MPP states

This is done using Optics 6 and WINDOW 7.7. An example of the area averaging procedure is described in Appendix 9.13. The results show that the $SHGC_{eff}$ calculated using this approach is in line with expected trends. Under the MPP electrical state, SHGC decreased by about 10% to 15% for a 92.2% cell coverage STPV system, and by about 1% to 5% for a 46.1% cell coverage system. The U-Value remains unaffected by electrical state (OC or MPP) and outdoor boundary conditions (h_{out}, h_{in}) do not affect solar optical properties $\tau, \rho_f, or\ \alpha$. Higher PV cell coverage results in greater decrease in SHGC under MPP state, with the decrease in SHGC due to MPP state being more significant in glazing configurations with higher U-value and the decreasing relationship being approximately linear in proportion to U/h_{out} as shown in Figure 6.1.1.

The limitations of this calculation approach is that only ρ_f in the STPV glazing layer (assumed to be outermost layer in this exercise) is increased (to in turn decrease α_f) while other properties (τ, ρ_b, α_b) remain the same under MPP electrical state. This method may not apply when the active STPV is not the outermost layer of the overall glazing configuration (e.g. bifacial PV).

The energy balance based on the radiosity method used for the calculation process in WINDOW 7.7 is available from the WINDOW Technical Documentation (Curcija et al., 2018).

6.2. Methodology for in-situ determination of dynamic SHGC

A preliminary experiment was performed to measure SHGC of an insulated glazing unit (IGU) as a proof-of-concept for a measurement methodology that does not require a guarded hot-box calorimeters discussed in Chapter 2.3, but instead incorporates direct measurements from pyranometers and a pyrgeometer. The intent is to develop a methodology that can measure the SHGC much more quickly than the guarded hot-box calorimeter method and can be applied to measuring the SHGC of STPV glazing under field conditions. Two methods, one using only thermocouple for indirectly measuring the long-wave radiation heat exchange, and one using a pyrgeometer to directly measure the long-wave radiation emitted by surfaces were used to measure the SHGC of the IGU in the month of June. The preliminary results show that there are significant discrepancies in the indoor long-wave radiation exchange component of this measurement methodology which produce inconclusive results. Conditions with high incident solar irradiance (about 600 W/m^2) appear to reduce the influence of the long-wave radiation issue. In general, more work is needed to improve the accuracy of results from this methodology.

Theoretical background

A method for determining the effective solar optical properties and solar heat gain coefficient (SHGC) of semi-transparent photovoltaic (STPV) glazing is being developed. The method is based on the idea that the main components of solar heat gain Q_{SHGC} can be measured directly by instruments sensitive to the corresponding wavelengths in the short-wave (solar) and long-wave (infrared) radiation spectra. The following energy balance equations consider the case of a clear double-pane insulated glazing unit (IGU) with an air-filled cavity. Representative area specific measurements may be necessary for determining the SHGC in the case where the exterior glazing pane is replaced by an optically inhomogeneous STPV glazing pane, however, the general principle remains the same.

$$Q_{SHGC}(\theta) = G_{trans}(\theta) + Q_{c,in} + Q_{r,in} \qquad (6.2.1)$$

Where $Q_{SHGC}(\theta)$ is the angular dependent solar heat gain from outdoors to indoors in W/m^2 .

$$G_{trans}(\theta) = G_{trans,direct}(\theta) + G_{trans,diffuse} \qquad (6.2.2)$$

Where $G_{trans}(\theta)$ is the angular dependent total transmitted solar radiation through the glazing system in W/m^2 , $G_{trans,direct}(\theta)$ is the angular dependent direct component of the transmitted solar radiation in W/m^2 based on the angle of incidence of the solar radiation on the glazing surface, and $G_{trans,diffuse}$ is the hemispherical component of the transmitted solar radiation in W/m^2 which does not depend on the angle of incidence.

The $G_{trans}(\theta)$ can be measured directly by placing a pyranometer that is sensitive to the range of wavelengths between 0.35μm to 2.5μm on the indoor side of a test cell as shown in Figure 6.2.1.

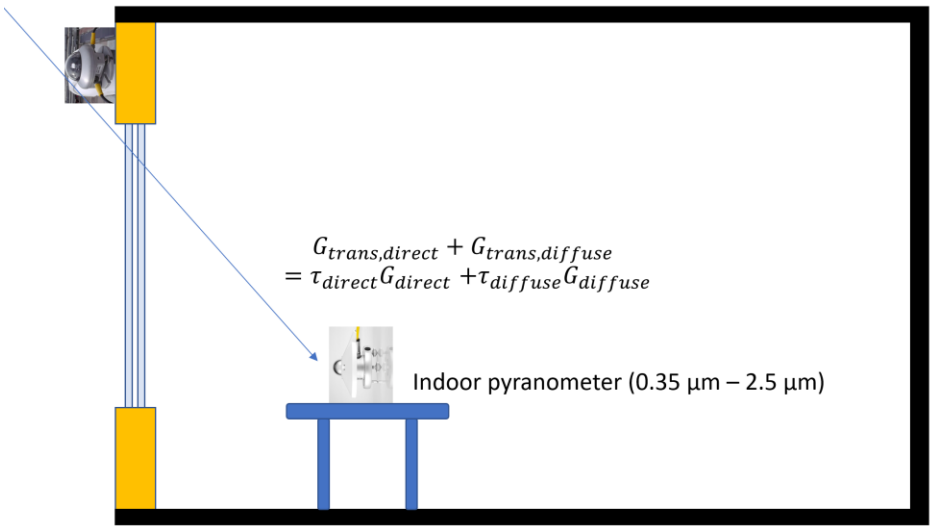

Figure 6.2.1: Schematic diagram of using an indoor pyranometer to directly measure the transmitted solar radiation.

The direct and diffuse components of the transmitted solar radiation depend on the angular dependent direct solar transmittance τ_{direct} and the hemispherical diffuse solar transmittance $\tau_{diffuse}$ of the glazing system. However, these two components are not separately considered for this initial experiment and only the combined $G_{trans}(\theta)$ is measured and analyzed.

The inward flowing heat gain due the solar radiation absorbed by the IGU is composed of two components: the convective heat transfer from natural convection $Q_{c,in}$ on the interior side of the IGU's surface #4, and the long-wave (infrared) radiation $Q_{r,in}$ exchanged between IGU's surface #4 and the interior surfaces of the test cell. The determination of these components can be more difficult.

For the indoor convective component:

$$Q_{c,in} = h_{c,in}(T_4 - T_{in}) \qquad (6.2.3)$$

Where $Q_{c,in}$ is the indoor convective heat transfer from natural convection in W/m^2, $h_{c,in}$ is the indoor convective heat transfer coefficient in W/m^2K, T_4 is the center of glass temperature in °C of surface #4 of the IGU and T_{in} is the air temperature of the Test Cell in °C.

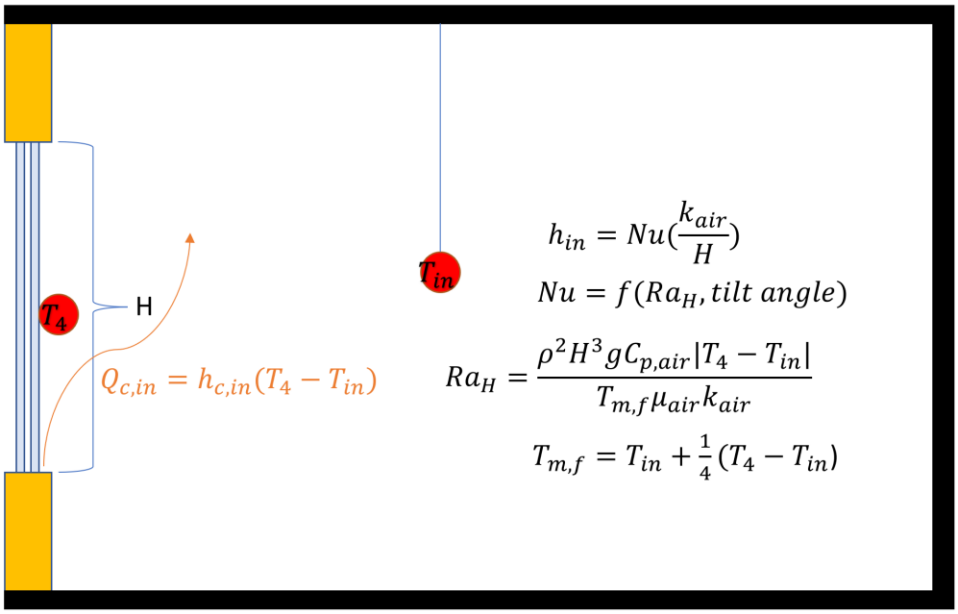

Figure 6.2.2: Schematic diagram of using two thermocouples T_4 and T_{in} to indirectly measure the indoor convective heat transfer through empirical correlations.

The interior convective heat transfer can be estimated using correlations based on the Nusselt number Nu, which is influenced by the airflow rate due to temperature differential and buoyancy at the glass-air interface. Measuring $Q_{c,in}$ is difficult in that the FBL test cell is not set up as a calorimeter which can more directly quantify the convective heat transfer. Instead, the difficulty is in choosing an empirical correlation for indoor natural convection's convective heat transfer coefficient, based on the Nusselt number or more simply the temperature differential between the glass surface temperature and the ambient indoor temperature. There are a number of correlations published in literature (Fohanno and Polidori, 2006; François et al., 2020; Garay-Martinez et al., 2023; Khalifa and Marshall, 1990; Michalak, 2021; Munaretto et al., 2018; Peeters et al., 2011; Rahimi et al., 2019), and it is unclear which is the most suitable for the FBL test cell conditions. In the end, the correlation used by WINDOW was chosen to attempt to have more consistency between the WINDOW calculation results and the experimental results.

The empirical correlations used by WINDOW 7.7(Curcija et al., 2018) are as follows:

$$T_{m,f} = T_{in} + \frac{1}{4}(T_4 - T_{in}) \qquad (6.2.4)$$

Where $T_{m,f}$ is the mean film temperature in °C between glass-air interface, which is the temperature that the various physical properties of air are to be evaluated at. For the purposes of this experiment, it is assumed that the changes in air properties are negligible when evaluated at an average indoor air temperature of T_{in}=21.0°C and a surface #4 center of glass (CoG) temperature of T_4=30.6°C. The air properties evaluated at these temperatures are the air density $\rho_{air} = 1.19\frac{kg}{m^3}$, specific heat capacity $C_{p,air} = 1006\frac{J}{kgK}$, dynamic viscosity $\mu_{air} = 1.83 \times 10^{-5}\frac{kg}{ms}$, and thermal conductivity $k_{air} = 0.02613\frac{W}{mK}$.

The dimensionless Rayleigh number Ra_H which is driven by the buoyancy of air is given by:

$$Ra_H = \frac{\rho_{air}^2 H^3 g C_{p,air} |T_4 - T_{in}|}{T_{m,f} \mu_{air} k_{air}} \quad (6.2.5)$$

Where H is the height of the glazing surface in m (H=1.92m for the IGU being tested), and the acceleration due to gravity of Earth is $g = 9.81 m/s^2$.

And the dimensionless critical Rayleigh number Ra_C is given by:

$$Ra_C = 2.5 \times 10^5 \left(\frac{e^{0.72\theta}}{\sin\theta} \right)^{\frac{1}{5}}, \qquad Ra_H < Ra_C \quad (6.2.6)$$

Where θ is the angle position in degrees of the glazing surface from the horizontal plane ($\theta = 90°$ for the tested IGU). This evaluates to $Ra_C = 1.06 \times 10^{11}$.

After confirming that $Ra_H < Ra_C$ for all the datapoints collected in this experiment, the dimensionless Nusselt number Nu can be determined by the correlation:

$$Nu = 0.56(Ra_H \sin\theta)^{\frac{1}{4}} \quad (6.2.7)$$

And the indoor convective heat transfer coefficient can be found by:

$$h_{c,in} = Nu \left(\frac{k_{air}}{H} \right) \quad (6.2.8)$$

As shown by Equations (6.2.4) to (6.2.8), $h_{c,in}$ is influenced by the temperature values at the CoG of the IGU's surface #4 (T_4) and the indoor air temperature T_{in}.

For the indoor long-wave radiation component:

The infrared heat exchange is composed of the inward directed infrared radiation from IGU's surface #4, and the outward directed infrared radiation from the interior surfaces of the test cell. These can be measured using a pyrgeometer, estimated based on temperatures, or estimated from data extracted from thermal imaging using an infrared camera. The three different methods are described below.

Method A:

This method uses thermocouples at CoG and at interior room air near wall surface to measure the CoG temperature and room air temperature respectively, then estimating long-wave radiation exchange based on the Stefan-Boltzmann law.

$$Q_{r,in} = E_{4,in} - E_{rm,out} \quad (6.2.9)$$
$$E_{4,in} = \varepsilon_4 \sigma T_4^4 + (1 - \varepsilon_4) \varepsilon_{rm} \sigma T_{rm}^4 \quad (6.2.10)$$
$$E_{rm,out} = \varepsilon_{rm} \sigma T_{rm}^4 \quad (6.2.11)$$

Where the $Q_{r,in}$ is the total long-wave radiative heat gain of the indoor environment in W/m^2, $E_{4,in}$ is the long-wave radiation emitted by interior surface of the IGU (surface #4) in W/m^2, $E_{rm,out}$ is the long-wave long-wave radiation emitted by indoor surface of the Test Cell room in W/m^2, $\varepsilon_4 = 0.84$ is the emissivity of the IGU surface #4 (based on data from the International

Glazing Database (IGDB) of both glazing panes in the IGU and calculation of the combined effective emissivity from WINDOW), T_4 is the surface temperature of IGU surface #4 in K, ε_{rm} is the emissivity of the Test Cell room surface (assumed ε_{rm}=0.9), T_{rm} is the surface temperature of the Test Cell room surface in K, and $\sigma = 5.67 \times 10^{-8}\ W/m^2K^4$ is the Stefan-Boltzmann constant.

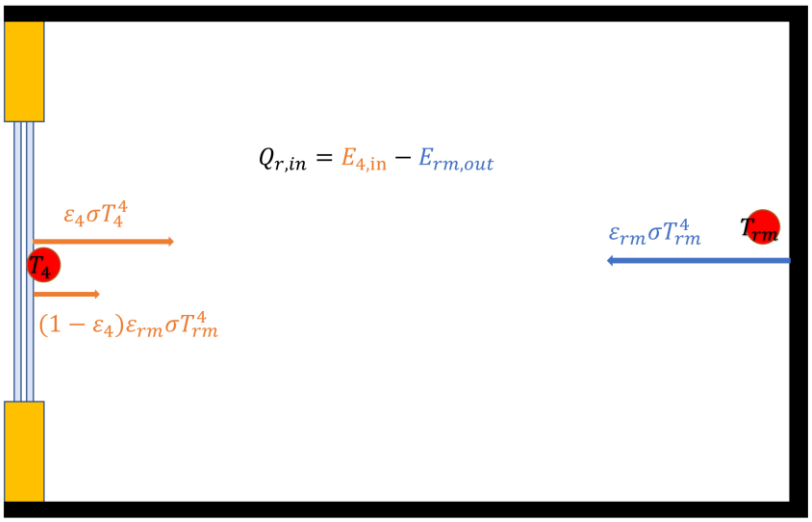

Figure 6.2.3: Schematic diagram of Method A, using two thermocouples T_4 and T_{rm} to indirectly measure the long-wave radiative heat transfer (estimated based on Stefan-Boltzmann law).

With the measured surface temperatures, the simplified radiative heat transfer coefficient can be estimated by:

$$h_{r,in_{simple}} = 4\sigma\varepsilon_4\left(\frac{(T_{rm}+T_4)}{2}\right)^3 \qquad (6.2.12)$$

Where the $h_{r,in_{simple}}$ is the radiative heat transfer coefficient in W/m^2K, and both T_{rm} and T_4 are in K. Determining the radiative heat transfer coefficient can be used for linearizing radiative heat transfer energy balance to estimate the combined indoor convective and radiative heat transfer coefficient h_{in} in W/m^2K.

Method B:

This method uses a pyrgeometer sensitive to the wavelengths in the range of 8 to 15 μm in the interior of the test cell, facing the IGU's CoG, to measure the inward directed long-wave radiation, and uses a Type-T thermocouple at the interior room air near wall surface to estimate the outward directed long-wave radiation.

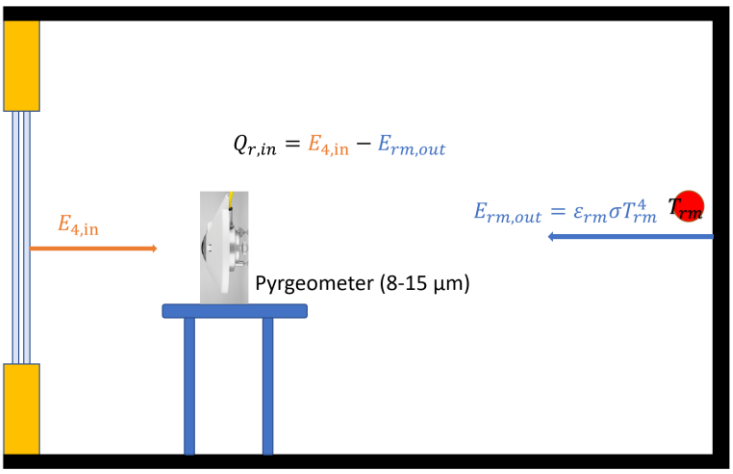

Figure 6.2.4: Schematic diagram of Method B, using a pyrgeometer to directly measure the long-wave radiation gain from the glazing to the indoor environment and using thermocouple T_{rm} to indirectly measure the long-wave radiation lost from the indoor surface to the exterior (estimated based on Stefan-Boltzmann law).

The total long-wave radiative heat gain $Q_{r,in}$ and outward directed long-wave radiation emitted by the indoor surface $E_{rm,out}$ is determined using Equations (6.2.9) and (6.2.11) respectively.

If the temperature of the IGU surface #4 is also measured by a thermocouple (as shown in Figure 6.2.3), the radiative heat transfer coefficient can be determined by:

$$h_{r,in} = \frac{\left(E_{4,in} - E_{rm,out}\right)}{T_4 - T_{rm}} \qquad (6.2.13)$$

Where $h_{r,in}$ is the radiative heat transfer coefficient in W/m^2K, $E_{4,in}$ is the inward directed long-wave radiation in W/m^2 measured by the pyrgeometer, and $E_{rm,out}$ is the long-wave long-wave radiation emitted by indoor surface of the Test Cell room in W/m^2 determined from Equation (6.2.11.

Method C:

This method uses infrared thermography with a camera sensitive to the wavelengths in the range of 8 to 15 μm to measure IGU temperature, and using a thermocouple to measure the indoor room air temperature, then estimating long-wave radiation exchange based on the Stefan-Boltzmann law.

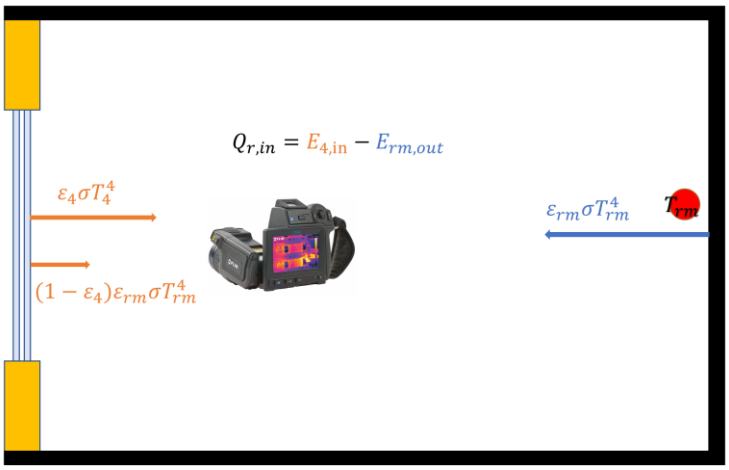

Figure 6.2.5: Schematic diagram of Method B, using an infrared camera to measure the glazing surface temperature T_4 to estimate long-wave radiation gain from the glazing to the indoor environment and using thermocouple T_{rm} to indirectly measure the long-wave radiation lost from the indoor surface to the exterior (estimated based on Stefan-Boltzmann law).

Equations (6.2.9) to (6.2.11) from Method A are used for this method as well. The advantage of this method is that the camera can measure the temperature distribution of the entire glazing surface simultaneously. This can be difficult to achieve using thermocouples, which can significantly reduce the transmittance of the glazing when too many thermocouples are installed onto the glazing surface, and the temperature measurements of these thermocouples can be affected by exposure to solar radiation (as discussed in Chapter 6.3).

To determine the SHGC using monitoring data, the ratio between the solar energy entering into the Test Cell and the solar energy incident from the exterior of the IGU is calculated. Considering all three modes of heat transfer described above, the transmitted solar radiation in both direct and diffuse forms, the natural convective heat transfer moving the some absorbed solar energy, which was absorbed by the IGU and converted into heat, into the test cell interior, and the long-wave thermal radiation exchange between the IGU indoor surface heated by solar radiation and the interior air-conditioned test cell wall surfaces, the SHGC can be determined by:

$$SHGC(\theta) = \frac{Q_{SHGC}(\theta)}{G_{out}(\theta)} \qquad (6.2.14)$$

$$SHGC(\theta) = \frac{G_{trans}(\theta) + Q_{c,in} + Q_{r,in}}{G_{out}(\theta)} \qquad (6.2.15)$$

Where $SHGC(\theta)$ is the dimensionless angular dependent solar heat gain coefficient, $G_{out}(\theta)$ is the angular dependent solar radiation incident on the IGU from the exterior in W/m^2as measured by a pyranometer as shown in Figure 6.2.1, $G_{trans}(\theta)$ is the total solar radiation transmitted through the IGU to the indoor environment in W/m^2, $Q_{c,in}$ is the indoor convective heat transfer from natural convection in W/m^2 as determined by temperature measurements and Equations (6.2.3) to (6.2.8), and $Q_{r,in}$ is the total long-wave radiative heat gain of the indoor environment in W/m^2 as determined using Method A, B or C described above.

Instrumentation

Test Cell 5 at the FBL was used to perform the initial experimental implementation of the in-situ SHGC measurement method.

Two SMP22 Pyranometers and one SGR4 Pyrgeometer were used in the experimental setup.

The exterior SMP22 is used to measure the direct and diffuse incident solar irradiance at the exterior, while the interior SMP22 is used to measure the transmitted solar irradiance. The spectrum measured by the SMP22 sensors corresponds to the wavelengths between 210 to 3600nm.

The SGR4 is used to measure the infrared radiation re-emitted by the insulated glazing unit (IGU). The spectrum measured by the SGR4 sensor corresponds to the wavelengths between 4400 to 50000nm.

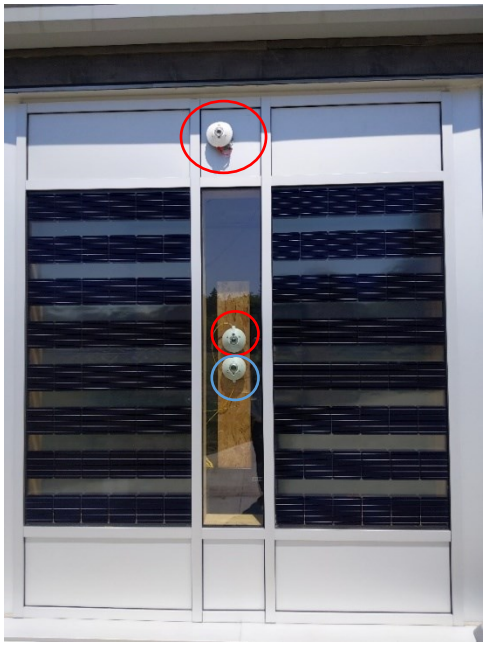

Figure 6.2.6: SMP22 Pyranometers (in red), one on the exterior, one interior, and SGR4 Pyrgeometer (in blue).

Figure 6.2.7: Indoor SMP22 Pyranometer (in red) and SGR4 Pyrgeometer (in blue) mounted on a wooden stand.

The IGU at the centre of the Test Cell 5's façade have known properties given by the manufacturer in the International Glazing Database (IGDB). The exterior glazing pane is a 5.639mm thick Comfort E^2 from AGC Glass Co. N.A. (IGDB ID#910) with the low-E coating located on surface

#2. The interior glazing pane is a 5.664mm thick Optifloat Clear from Pilkington North America (IGDB ID#9804). The IGU cavity is filled with 12mm of air.

Type-T thermocouples with $\pm 0.5°C$ error were used to measure the temperature of the indoor air and various surfaces. When directly exposed to solar radiation, as in the case of measuring the CoG temperature, the thermocouple measurements needed to be corrected. Details are discussed in Appendix 9.14.

The instruments used to determine the variables used in Equations (6.2.1) to (6.2.15) are summarized below:

G_{trans}: SMP22 Pyranometer on the interior of the test cell, facing centre of glass (CoG)

G_{out}: SMP22 Pyranometer on the exterior of the test cell

$Q_{c,in}$: Type-T Thermocouple measuring temperature at CoG, then estimating natural convection heat transfer based on temperature differential (Equations (6.2.3) to (6.2.8)).

Figure 6.2.8: Type-T thermocouple covered in reflective tape positioned at center of glass (CoG) on surface #4

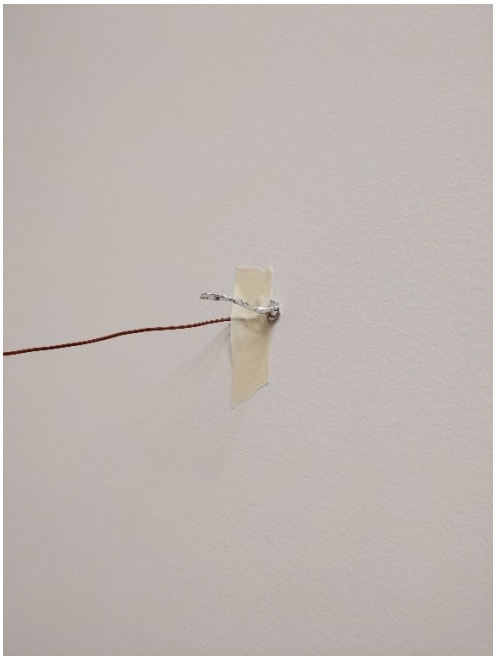

Figure 6.2.9: Type-T thermocouple positioned near a wall on the interior surface of the Test Cell

$Q_{r,in}$: Using Method A, B, or C depending on the experimental setup

Method A:

Type-T thermocouple at CoG and at interior room air near wall surface, to measure the CoG temperature and room air temperature respectively, then estimating long-wave radiation exchange based on the Stefan-Boltzmann law (Equations (6.2.9) to (6.2.11)).

Method B:

SGR4 Pyrgeometer on the interior of the test cell, facing CoG, to measure the inward directed long-wave radiation, and Type-T thermocouple at the interior room air near wall surface to estimate the outward directed long-wave radiation (Figure 6.2.8 and Figure 6.2.9).

Method B2, a variation of Method B, where the pyrgeometer is set up to face the indoor surface is shown in Figure 6.2.10. This was done for the June 14 to June 20 monitoring period to confirm that the pyrgeometer measurement of the long-wave radiation emitted from the indoor surface is in line with the estimates calculated from Equation (6.2.11).

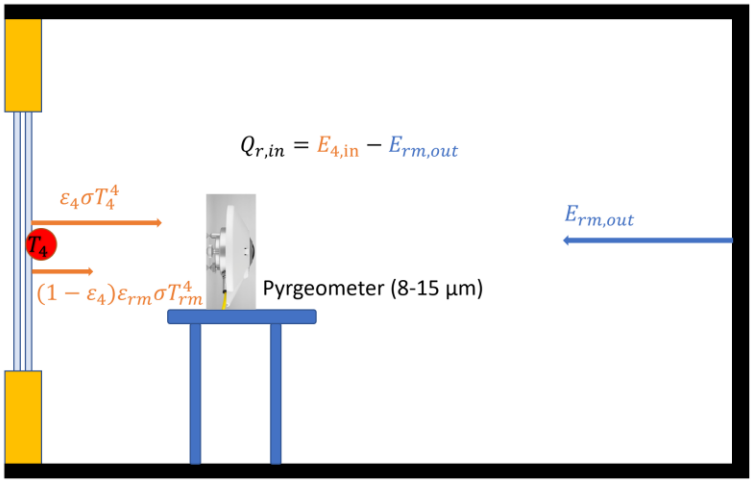

Figure 6.2.10: Schematic diagram of Method B2, using a pyrgeometer to directly measure the long-wave radiation lost from the indoor surface to the exterior and using thermocouple T_4 to indirectly measure the long-wave radiation gain from the glazing to the indoor environment (estimated based on Stefan-Boltzmann law).

Method C:

FLIR T540-42 infrared camera to measure IGU temperature T_4, then estimating long-wave radiation exchange based on the Stefan-Boltzmann law (Equations (6.2.9) to (6.2.11)).

SHGC Measurement Procedure

1. To eliminate the effects of solar radiation absorption and transmission from the STPV glazing units on the sides of the test cell, cover them with a reflective insulation (reflective insulation is used because it's opaque (blocks short wave radiation) and low emissivity (reflects infrared radiation)). The insulating surface is sealed with sheathing tape.

Figure 6.2.11: Reflective insulation applied to the exterior of glazing units not being tested.

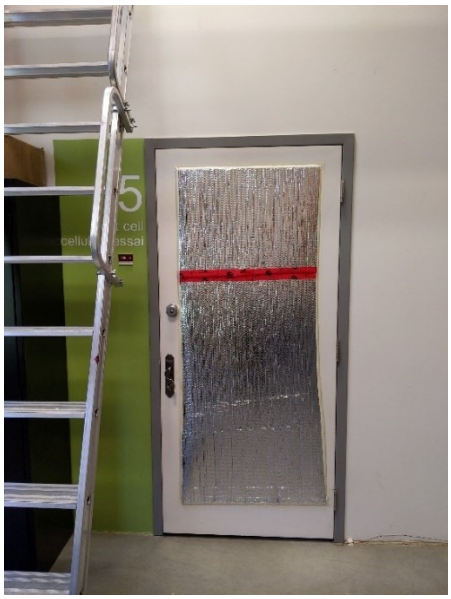

Figure 6.2.12: Reflective insulation applied to the interior test cell door

2. To eliminate other sources of radiation coming from the interior test cell door, the glass on the test cell door is also covered with reflective insulation and sheathing tape
3. To eliminate reflection of long-wave radiation on the interior surfaces, the potential reflective surfaces (interior sides of the STPV glazing units and the test cell door glazing) were covered with black Bristol board paper and sealed using masking tape.
4. To reduce the effects of direct solar radiation on measured values, cover the thermocouples with reflective foil tape from the thermocouple tip to the about the first 35°Cm length of the thermocouple wire.
5. Place the thermocouples in the following monitoring locations
    a. Centre of glass of the IGU
    b. Near edge of glass (about 25°Cm from the bottom edge of glass)
    c. Edge of glass (as close as possible to the edge without touching the rubber gasket or wood frame)
    d. On the wall near the test cell door, setting the thermocouple to protrude from the wall to measure air temperature
    e. Centre of the test cell door
6. Mount one SMP22 sensor on the exterior façade, drilling 3 holes through the spandrel panel to accommodate the bolts and the data cable then sealing them with caulking and sheathing tape.
7. Mount the other SMP22 sensor on a vertical wooden stand along with the SGR4 sensor, to allow the two sensors to take measurements at the centre of glass when facing the IGU

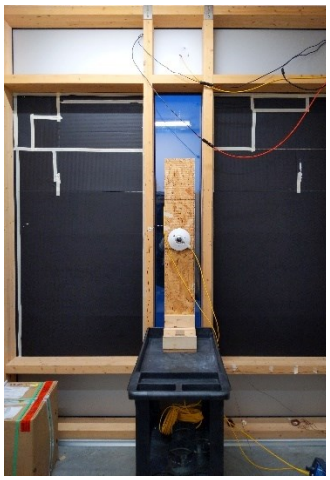

Figure 6.2.13: Black Bristol board applied to the interior of glazing units not being tested.

Figure 6.2.14: Black Bristol board insulation applied to the interior test cell door. Type-T thermocouples positioned on the door surface and near the wall.

Figure 6.2.15: SGR4 pyrgeometer facing indoor surface for Method B2

8. Power exterior SMP22, interior SMP22 and interior SGR4 sensors with a 12V power source through a mini voltage converter connected to the test cell's AC power outlet, making sure the ground wire in each of the three cables is also connected to the ground on the mini voltage converter
9. Connect the data output wires of the exterior SMP22, interior SMP22, and interior SGR4 sensors and the thermocouples to the DAQ970A data acquisition system
10. Set the DAQ970A to collect monitoring data at 1 min intervals and save the data to a USB drive.
11. Leave the test cell to prevent the long-wave radiation from any occupants from affecting the measurements.

SHGC was also measured at differing heights of the IGU to observe the effect of self-shading and incident angle on uniformity. In addition to the steps above, the following steps were taken to collect the data at different heights (the results are shown in Appendix 9.18):

12. Raise or lower the SMP22 and SGR4 wooden stand onto stacked rigid objects to match the sensors to be level at about 50°Cm from the top or bottom edge of glass to take measurements for the Top SHGC and Bottom SHGC respectively.
13. Set the DAQ970A to collect monitoring data at 10s intervals and save the data to a USB drive.
14. Leave the test cell for about 2 minutes.
15. Use the FLIR T540-42 to take infrared images of the IGU from 2m away, and take images at close up locations near the thermocouples.

The SHGC can be calculated through Equations (6.2.1) to (6.2.15) based on the collected data and compared to the theoretical SHGC value calculated for the IGU from WINDOW.

6.3. Experimental results of initial implementation of in-situ methodology

Angle of Incidence

As the earth rotates, the solar altitude and azimuth changes throughout the day. This constantly changes the angle of incidence on the surface exposed to the sun. In this experiment, the entire south façade of the FBL and the IGU being studied is positioned facing true south ($\psi = 0$), and the IGU is a vertical surface ($\beta = 90°$). For this experiment, which is located in Montreal, the latitude is 45.5. Given this information, the angle of incidence on the IGU can be determined theoretically using a simple sun position model for any given day at any given time.

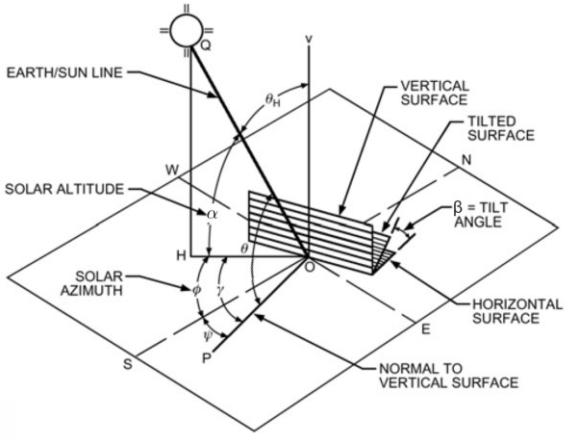

Figure 6.3.1: Schematic diagram visualizing the definition of various angular components related to sun position and angle of incidence (American Society of Heating, Refrigerating and Air-Conditioning Engineers, 2013)

For the following single day experiment, the angle of incidence is calculated for every hour throughout the day. An angle of incidence $\theta = 0°$ indicates a direct normal angle of incidence (the angle at which SHGC is determined for standard indoor testing), and an angle of incidence $\theta \geq 90°$ or $\theta < 0°$ indicates that the sun is positioned outside the line of sight (behind the glazing or below the horizon) of the IGU, and no direct solar radiation would be incident on the IGU.

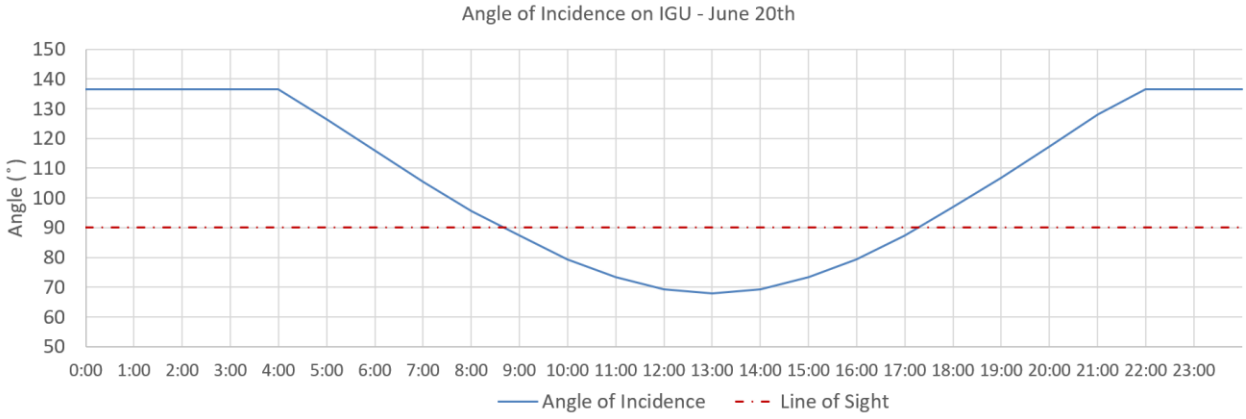

Figure 6.3.2: Angle of Incidence on June 20/ June 21

The IGU is exposed to direct solar radiation from about 8:30 to 17:30 when the angle of incidence is below 90°. Around solar noon (12:00 to 14:00), the angle of incidence is about 68° to 69°. Between June 20 and June 21, the sun path and angle of incidence profile changes insignificantly (within $\pm 0.04°$), therefore the graph above is also representative of the conditions during the experiment on June 21.

June 20th to June 21st monitoring day

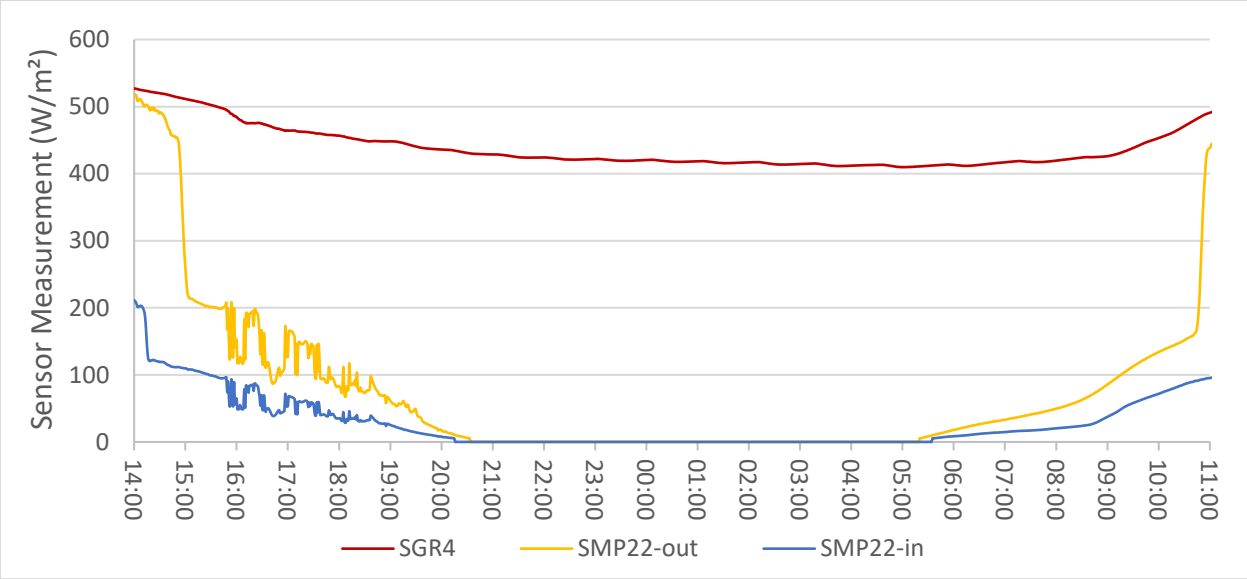

Figure 6.3.3: Measurements of G_{out} from the exterior SMP22 G_{trans} from the interior SMP22 and $E_{4,in}$ from the interior SGR4 sensors throughout June 20 14:00 to June 21 11:00, 2023.

The incident solar irradiance from June 20 to June 21 appear to be a mix of sunny and cloudy conditions. The sky appears to be mostly from June 20 14:00 until 15:00, followed by cloudy ($< 200\ W/m^2$ incident solar irradiance as measured by the exterior SMP22 sensor) conditions until nighttime. The morning of June 21st was also cloudy until around 10:00 in the morning.

The measurement of G_{trans} and G_{out} are straight forward, but when comparing the transmittance value (G_{trans}/G_{out}) between the experimental measurement using the SMP-22 pyranometers and the theoretical values calculated by WINDOW 7.7, it appears to be significantly lower, and the time period at which the transmittance becomes undefined due to the lack of solar radiation appears to not match up between the two. One potential source of this issue could be reflection from the nearby HU building during sunset discussed in Appendix 9.4.

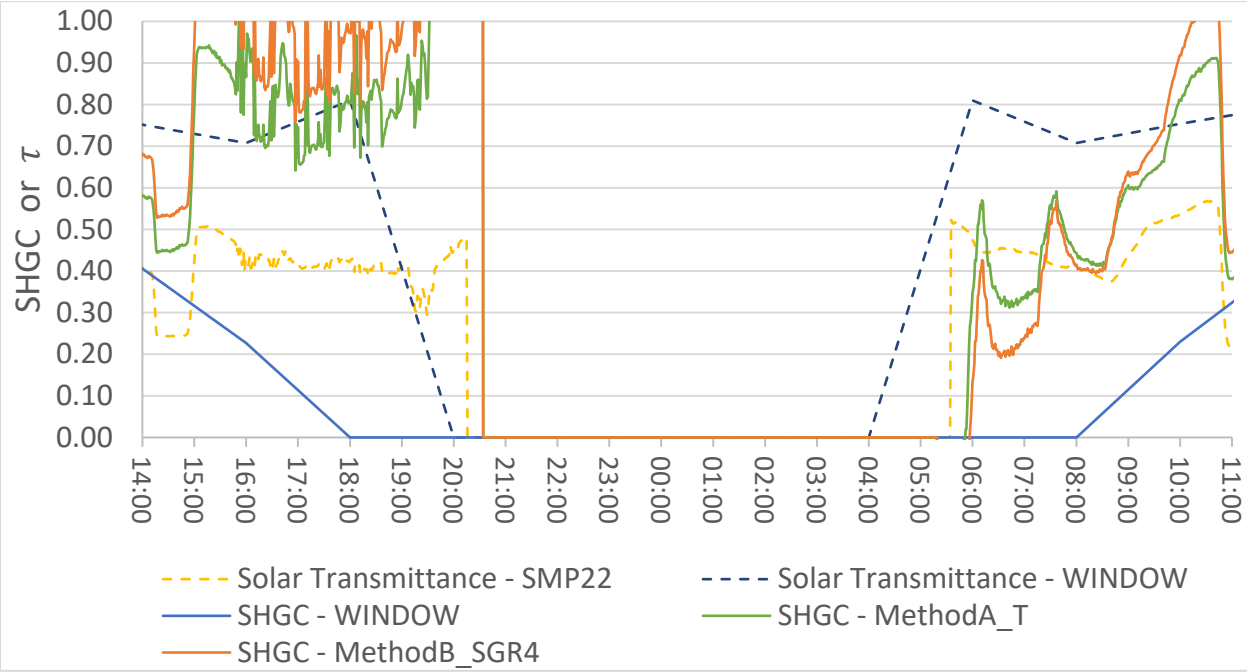

Figure 6.3.4: Comparison of solar transmittance τ , SHGC calculated from WINDOW and Methods A and B

In terms of theoretical determination of SHGC, WINDOW 7.7 was used by taking the manufacturer glazing properties in the International Glazing Database (IGDB) as the input. At normal solar angle of incidence, the SHGC at center-of-glass (CoG) is 0.627. For the dynamic angular dependent SHGC, there are discrepancies between the values determined using WINDOW 7.7 with the procedure described in Appendix 9.15. The solar transmittance outputs from the W6MatrixReader are 0.3 to 0.8 higher than the angular dependent SHGC values calculated from the workflow. Given that the SHGC values expected to be greater than solar transmittance values, these results suggest that this workflow using WINDOW 7.7 for angular dependent SHGC is significantly flawed. Possible reasons for this are discussed at the end of Appendix 9.15. More work is needed to develop a workflow that provide accurate results of the SHGC at angles of incidence that differ from normal incidence.

In terms of SHGC determined from measured data, the average SHGC determined by Method A and Method B in the afternoon of June 20th are about 0.80 and 0.90 respectively. These results appear too high, especially those determined by Method B (using SGR4's measurements of the IGU long-wave radiation), since the SHGC determined exceeds 1.00 at certain periods. The trend of SHGC determined from the experiment on June 20th also does not follow the same trend as those determined by WINDOW, the SHGC is not decreasing as expected as the incident angle increases farther away from normal incidence. However, this trend is followed by the SHGC values determined in the morning of June 21st. The SHGC determined from the experiment appears to average at about 0.40 and 0.45 for Method A and Method B respectively. It may be important to consider that the period shown only had sunny conditions between June 20th 14:00 to 15:00 and June 21st 10:00 to 11:30 while the rest was cloudy. This may have influenced the determined SHGC substantially. There are discrepancies between the expected long-wave radiation values

calculated from temperature measurements and those measured directly by the pyrgeometer. More details of the discrepancies shown in Appendix 9.16. In general, these values suggest that both the theoretical workflow using WINDOW 7.7 and experimental measurement methods produce inconclusive SHGC results and need significant improvement.

June 14th to June 20th monitoring period

The SGR4 pyrgeometer turned around and facing the indoor surface for the measurements taken between June 14 16:00 to June 20 11:00, 2013. This was done to examine the discrepancies in indoor long-wave radiation measurements while also still being able to collect enough data to determine SHGC using Method B2. Details of the long-wave radiation measurements are discussed in Appendix 9.17.

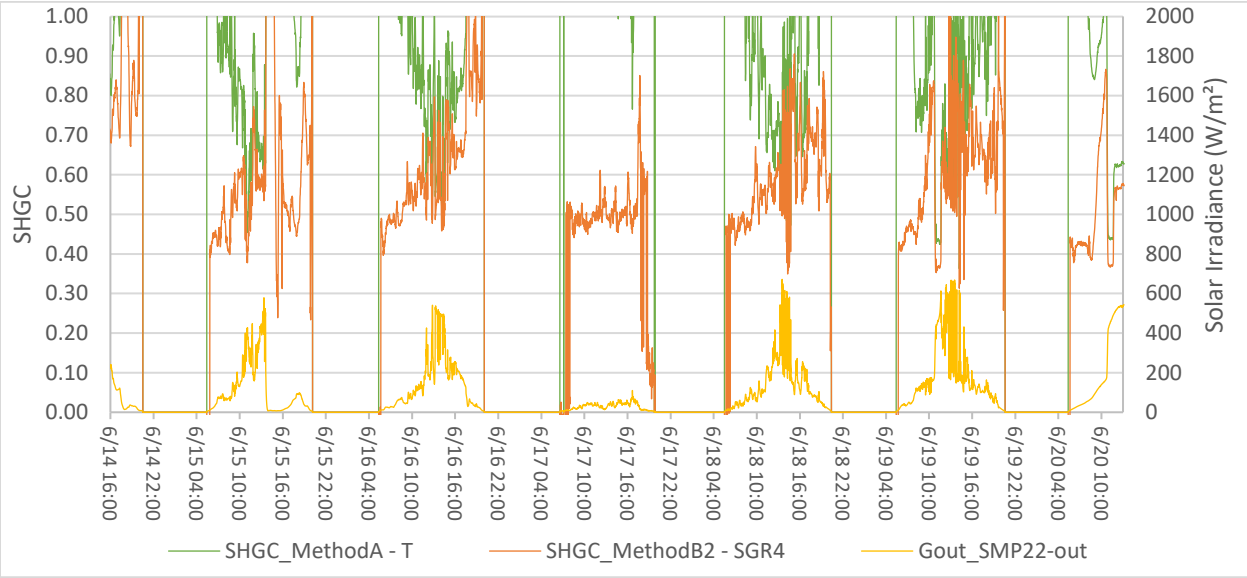

Figure 6.3.5: Comparison of SHGC calculated from Method A and Method B2, with incident solar irradiance on the right axis for visual reference, from June 14 to June 20, 2023

In this case, the SHGC determined using Method B2 uses the Type-T thermocouple at the IGU CoG, and the measured $Q_{r,rm_{out}}$ from the SGR4. The main difference between SHGC determined from Method A and Method B2 is the inward heat flux $Q_{r,rm_{out}}$ which is less than 47 W/m^2 (40.5 W/m^2 on average) throughout the monitoring period, but it appears to have made a significant difference in daily SHGC trends. The difference between the SHGC determined from the two methods become much smaller at higher solar irradiance. This suggests that the SHGC values determined using this methodology is highly sensitive to incident solar irradiance and may be much more unreliable in cloudy conditions when solar irradiance is low.

In general, these initial in-situ SHGC tests show that the results can influenced significantly by the long-wave radiation heat transfer which has significant discrepancies between the temperature based values calculated from Equations (6.2.9) to (6.2.11) in Method A or partially measured by

the SGR4 pyrgeometer in Method B. The resulting SHGC values sometimes present reasonable values such as SHGC=0.500 as shown in Figure 6.3.5, while in other cases appear too high (SHGC=0.700 to SHGC>1.000) Figure 6.3.4. There is a significant difference between the SHGC determined from WINDOW (SHGC=0.400 around noon on June 20) and the SHGC derived from measured data (SHGC=0.500 to >1.000 around noon on June 20 and SHGC=0.400 to >1.000 around noon on June 21). The discrepancy can be attributed to WINDOW not being able to represent changing angles of incidence correctly using the workflow described in Appendix 9.15 (discrepancy between solar transmittance $\tau = 0.700$ to 0.800 while SHGC=0.400), the use of empircal correlations to estimate indoor convective heat transfer, and higher-than-expected measured values from using a pyrgeometer indoors. The SHGC values determined from Methods A and B from the in-situ measurement methodology also appears to increase dramatically when the incident solar irradiance decreases, due to the indoor convective and radiative heat transfer components of solar heat gain reducing less significantly than the proportion of both the incident solar irradiance and transmitted solar radiation which experience steep reductions in the afternoons as shown in Figure 9.17.7. The lack of steady-state conditions during the monitoring period may be a factor in the high influence $Q_{c,in}$ and $Q_{r,in}$ have on the final SHGC results.

In addition to the lack of steady-state conditions, the limitations of this experimental method include the large reliance on thermocouple temperature measurements and the correlations which use these temperature values to obtain the convective and radiative heat gain of the indoor environment. The calculated long-wave radiation emitted by surfaces depends on the measured temperature and the assumed emissivity of the surfaces. The emissivity of the surfaces may be measured experimentally using an emissometer. The Emissometer can be used to measure the emissivity of the IGU and test cell room's interior surfaces to get better estimates of the infrared radiation exchange. Due to time constraints, this was not done for the experiment. The emissivities of the surfaces are assumed from values typically given for each material, and in the case of the glazing unit its emissivity value is determined from the values of the manufacturer's data from the IGDB. The uncertainty from the emissivity values is potential source of error.

7. Summary and Conclusions

7.1. Thesis summary

This thesis presented the performance measurement of BIPV building envelope and integration. Studies were done to examine four topics: BIPV/T curtain wall thermal performance, HRV performance enhancement due to BIPV/T integration, hygrothermal modelling of BIPV cladding wood-frame construction, and glazing solar heat gain coefficient. The main findings in each of the four studies are summarized below.

BIPV/T thermal performance was monitored and modeled for the 2m tall curtain wall section at Test Cell 2 of the Future Buildings Laboratory (FBL)at Concordia University. Analysis of the BIPV/T system was focused on the time periods with high solar irradiance, which are the hours around noon from 10:00 to 14:00. Comparisons were also made between the measured data and those predicted by a simple finite different steady state thermal network model. For a typical sunny day in April, the temperature rise from the bottom to the top of the BIPV/T air cavity is about 9.6°C. The model overestimates the BIPV/T temperature rise by 0.9°C. The convective heat transfer coefficient within the air cavity around noon time was determined as 14.3 W/m^2K on average from the monitoring data, which is in line with expected value of 13 W/m^2K from the model and correlations developed from previous studies. Thermal performance based on monitoring data shows thermal efficiency of 42.4% in the hours around noon time. The model slightly overestimates the thermal efficiency by 5.7% on average, up to a maximum of 9.8%. The heat energy captured from 10:00 to 14:00 is about 0.44kWh per hour on average. The Model overestimates the thermal energy captured by 13% on average, up to a maximum of 19.1%

HRV performance improvement was quantified for the same Test Cell 2 BIPV/T system at the FBL. A prototype manifold was developed through equal friction method sizing calculations and assembled using 3D printed parts. The manifold was installed for BIPV/T+HRV integration in a field monitoring experiment in January-February. The manifold inlet showed acceptable airflow temperature uniformity with the maximum hourly average difference between any single inlet temperature and the average of the three temperatures being $\pm$ 1.2 °C. From the monitoring data, empirical correlations for the temperature increase at the BIPV/T manifold, the heat gain from losses from the room air to the duct from the BIPV/T manifold to the inlet air of the HRV were developed using outdoor temperature and the incident solar irradiance. The performance improvement through BIPV/T integration was quantified by the increase in the HRV supply air outlet temperature $\Delta T_{SA,HRV}$, which was shown to be dependent on incident solar irradiance. A BIPV/T integration improvement factor $F_{BIPV/T}$ for $\Delta T_{SA,HRV}$ was calculated based on the sensible recovery efficiency (SRE) and constants in outdoor ambient air to manifold (k_1) and manifold to inlet air (k_3) correlations. The results showed that the HRV SRE remained effectively constant at 83.8 to 83.9% in both HRV-only and BIPV/T integrated scenarios. The BIPV/T integration factor $F_{BIPV/T}$ was determined to be about 0.0046°C/(W/m²). The corresponding $\Delta T_{SA,HRV}$ for this HRV+BIPV/T integration is determined to be about 1°C to 5°C throughout the January/February monitoring period when the incident solar irradiance of ranges from 200 to 1070 W/m^2.

Hygrothermal performance of BIPV and BIPV/T exterior wall in low-rise residential wood frame construction was modeled using WUFI Pro. Various air cavity ventilation rates behind the BIPV cladding were simulated to examine their effect on the moisture content and relative humidity in the oriented strand board (OSB) layer over time. The simulations over multiple years show that, compared to a wall of the same construction with conventional fiber cement cladding, the fiber cement wall have lower moisture content and relative humidity, and lower mould index at low air cavity ventilation rates. However, the cavity ventilation rate is increased to 20ACH and above, the BIPV and BIPV/T walls can have better hygrothermal performance, with the highest moisture content being 11% and relative humidity of 75% in the OSB layer, and a mould growth index below 1. As such, a minimum air cavity ventilation rate of 20ACH is recommended for BIPV facades. For the typical operation of BIPV/T systems of at least 0.5m/s of cavity air velocity, the cavity ventilation rate already exceeds 600ACH, which suggests that moisture issues are not a concern.

The methods for theoretically and experimentally determining the SHGC of STPV were examined. As part of the IEA Task 15 exercise, the SHGC were determined using Optics6 and WINDOW 7.7. To account for the electrical operating state of the STPV, spectral averaging of electrical efficiency was examined, and an adjustment to the solar reflectance of the front surface based on the electrical conversion efficiency was introduced. To account for the inhomogeneity of the PV cells and clear glass areas in STPV glazing, an area-weighted averaging method based on first determining the properties 0% cell area coverage and 100% cell area coverage was applied. The resulting theoretical SHGC values from the various boundary conditions and glazing configurations confirm that the SHGC can decrease significantly when going from OC to MPP state. This difference in SHGC is higher when the overall thermal performance (U-Value) of the STPV is higher and when outdoor heat transfer coefficient h_{out} is lower. A methodology for in-situ measurement of SHGC is explored as a potential method to determine the actual SHGC of STPV glazing in field conditions. A conventional double pane insulated glazing unit (IGU) was used as a test specimen as proof of concept. The method mainly uses the optical measurements of pyranometers and a pyrgeometer, as well as supplemental temperature measurements of thermocouples and an infrared camera to evaluate the SHGC. The initial SHGC field measurement experiments show inconclusive results with widely varying SHGC values which may be significantly influenced by errors in long-wave radiation measurements. The effect of long-wave radiation errors is reduced for conditions with high incident solar irradiance.

7.2. Contributions

The work done in this dissertation examined the performance of integrated BIPV systems from different perspectives of thermal energy performance, systems integration, hygrothermal performance and solar optical performance through a combination of modeling and field monitoring. The following contributions were made:

- Monitored and documented field performance data of a short 2m tall BIPV/T curtain wall façade system integrated with an HRV
- Calibrated and compared a simplified thermal network finite difference BIPV/T model in Python with the field monitoring data to evaluate its accuracy in modelling
    - Air cavity convective heat transfer coefficient
    - BIPV/T air cavity temperature
    - Heat energy captured
    - Thermal efficiency
- Designed a prototype three-inlet BIPV/T manifold which enable the integration of a BIPV/T curtain wall with an HRV
- Evaluated HRV performance improvement due to BIPV/T integration in terms of
    - HRV inlet air temperature increase
    - HRV supply air outlet temperature increase
    - Sensible recovery efficiency
- Defined a BIPV/T integration improvement factor $F_{BIPV/T}$ to determine the solar irradiance dependent HRV supply air outlet increase $\Delta T_{SA,HRV}$
- Modeled hygrothermal performance of BIPV and BIPV/T wood framed wall assemblies in WUFI Pro
- Recommended maintaining cavity airflow rate above 20 ACH to reduce risk of moisture damage
- Described workflow to determine theoretical SHGC of STPV glazing systems using WINDOW
- Described preliminary methodology for in-situ measurement of angular dependent SHGC of glazing systems using pyranometers and pyrgeometer
- Performed proof-of-concept experiment using the described in-situ measurement methodology showing much more improvements are needed

These studies are a starting point to future research to be done in these different aspects of BIPV/T performance characterization. The demonstration of successful coupling of the HRV with the BIPV/T system with and the simple methodology to quantify the integration benefits under field conditions in this thesis can be useful for future studies of this type of BIPV integration. The measurement of the real field performance of a BIPV/T system with short air cavity length, while not a demonstration of optimal BIPV/T design, can still be a useful point of reference for future designs considering BIPV in low-rise residential construction. The hygrothermal performance simulation study using WUFI suggests that typical applications of BIPV cladding in wood frame construction should be safe from moisture accumulation issues. The challenges with characterizing solar heat gain coefficient of STPV under field conditions still have not been overcome, and the study done in this thesis shows that the methodologies would still require significant improvement for conclusive results.

7.3. Future Work

Overall, there is much work to be done in the evaluation of BIPV as active building envelope systems. These initial studies serve as a foundation for upcoming research into various aspects of BIPV, BIPV/T and STPV performance characterization. Future work stemming from these studies may include:

- Further developing the in-situ dynamic SHGC measurement methodology for rapid determination of SHGC for STPV specimen
    - Minimizing measurement errors due to incorrect determination of indoor long-wave radiation (pyrgeometer) and convective heat transfer (empirical correlations)
    - Modeling dynamic angular dependent SHGC of STPV glazing for comparison with measurement methodology
    - Developing a calibrated energy model to estimate SHGC
- Developing in-situ methodology for measuring the U-value of BIPV wall assemblies under field conditions
- Testing of energy recovery ventilator performance and defrost operation improvement from BIPV/T integration
- Performing field monitoring of a BIPV-clad wood-framed wall assembly
- Developing a work-flow using industry standard software to perform whole building energy simulation with BIPV/T active building envelope systems
- Examining the effect of thermal bridging on the heat energy captured by BIPV/T
- Further refining the simplified thermal network BIPV/T model to perform thermal energy modeling of the BIPV/T cavity temperature with higher accuracy
- Examining the effect of high PV surface temperature on condensation resistance of STPV IGUs
- Testing of air & water tightness of BIPV wall assemblies
- Optimizing the BIPV/T manifold to minimize size while maintaining airflow uniformity

8. References

Abdel-Ghany, A.M., Ishigami, Y., Goto, E., Kozai, T., 2006. A Method for measuring Greenhouse Cover Temperature using a Thermocouple. Biosystems Engineering 95, 99–109. https://doi.org/10.1016/j.biosystemseng.2006.05.014

Agathokleous, R.A., Kalogirou, S.A., 2020. Status, barriers and perspectives of building integrated photovoltaic systems. Energy 191, 116471. https://doi.org/10.1016/j.energy.2019.116471

American Society of Heating, Refrigerating and Air-Conditioning Engineers, 2013. 2013 ASHRAE Handbook - Fundamentals. American Society of Heating, Refrigerating and Air-Conditioning Engineers, Inc., Atlanta,GA.

ASTM International, 1996. ASTM E903-96 standard test method for solar absorptance, reflectance, and transmittance of materials using integrating spheres. ASTM Internacional, West Conshohocken.

Bhandari, M.S., Bansal, N.K., 1994. Solar heat gain factors and heat loss coefficients for passive heating concepts. Solar Energy 53, 199–208. https://doi.org/10.1016/0038-092X(94)90482-0

Bloem, J.J., Lodi, C., Cipriano, J., Chemisana, D., 2012. An outdoor Test Reference Environment for double skin applications of Building Integrated PhotoVoltaic Systems. Energy and Buildings 50, 63–73. https://doi.org/10.1016/j.enbuild.2012.03.023

Bonomo, P., Eder, G., Martin Chivelet, N., Eisenlohr, J., Frontini, F., Kapsis, C., Scognamiglio, A., Wilson, H.R., Yang, R., 2021. Categorization of BIPV Applications. IEA- PVPS T15-12:2021.

Brozovsky, J., Nocente, A., Rüther, P., 2023. Modelling and validation of hygrothermal conditions in the air gap behind wood cladding and BIPV in the building envelope. Building and Environment 228, 109917. https://doi.org/10.1016/j.buildenv.2022.109917

Canadian Standards Association., 1993. Energy performance evaluation of windows and sliding glass doors ; User guide to CSA standard A440.2-93, Energy performance evaluation of windows and sliding glass doors, CSA special publication, 0317-5669 ; A440.3-93. Canadian Standards Association, Rexdale, Ont.

Canadian Wood Council, 2000. Moisture and Wood-Frame Buildings.

Candanedo, L.M., Athienitis, A., Park, K.-W., 2011. Convective Heat Transfer Coefficients in a Building-Integrated Photovoltaic/Thermal System. Journal of Solar Energy Engineering 133, 021002. https://doi.org/10.1115/1.4003145

Candanedo, L.M., Athienitis, A.K., Candanedo, J.A., O'Brien, W., Chen, Y., 2010. Transient and Steady State Models for Open-Loop Air-Based BIPV/T Systems 116, 14.

Charron, R., Athienitis, A.K., 2006. Optimization of the performance of double-façades with integrated photovoltaic panels and motorized blinds. Solar Energy 80, 482–491. https://doi.org/10.1016/j.solener.2005.05.004

Chen, F., Wittkopf, S.K., Khai Ng, P., Du, H., 2012. Solar heat gain coefficient measurement of semi-transparent photovoltaic modules with indoor calorimetric hot box and solar simulator. Energy and Buildings 53, 74–84. https://doi.org/10.1016/j.enbuild.2012.06.005

Chen, Y., Athienitis, A., Fazio, P., Concordia University (Montréal, Q., 2012. Design and Evaluation of Façade-Integrated Solar Technologies Suitable for High-Latitude Applications. Concordia University, Montréal.

Chen, Y., Athienitis, A.K., Galal, K., 2010. Modeling, design and thermal performance of a BIPV/T system thermally coupled with a ventilated concrete slab in a low energy solar house: Part 1, BIPV/T system and house energy concept. Solar Energy 84, 1892–1907. https://doi.org/10.1016/j.solener.2010.06.013

Cornaro, C., Bucci, F., Pierro, M., Bonadonna, M.E., Siniscalco, G., 2015. A new method for the thermal characterization of transparent and semi-transparent materials using outdoor measurements and dynamic simulation. Energy and Buildings 104, 57–64. https://doi.org/10.1016/j.enbuild.2015.06.081

Cornaro, C., Renzi, L., Pierro, M., Di Carlo, A., Guglielmotti, A., 2018. Thermal and Electrical Characterization of a Semi-Transparent Dye-Sensitized Photovoltaic Module under Real Operating Conditions. Energies 11, 155. https://doi.org/10.3390/en11010155

Curcija, C., Vidanovic, S., Hart, R., Jonsson, J., Mitchell, R., 2018. WINDOW Technical Documentation.

Falk, J., Sandin, K., 2013. Ventilated rainscreen cladding: Measurements of cavity air velocities, estimation of air change rates and evaluation of driving forces. Building and Environment 59, 164–176. https://doi.org/10.1016/j.buildenv.2012.08.017

Fohanno, S., Polidori, G., 2006. Modelling of natural convective heat transfer at an internal surface. Energy and Buildings 38, 548–553. https://doi.org/10.1016/j.enbuild.2005.09.003

François, A., Ibos, L., Feuillet, V., Meulemans, J., 2020. Novel in situ measurement methods of the total heat transfer coefficient on building walls. Energy and Buildings 219, 110004. https://doi.org/10.1016/j.enbuild.2020.110004

Garay-Martinez, R., Arregi, B., Lumbreras, M., 2023. Surface heat transfer coefficients in building envelopes: Uncertainty levels in experimental methods. Journal of Building Physics 47, 62–91. https://doi.org/10.1177/17442591221150250

Hahne, E., Pfluger, R., 1996. Improvements on PASSYS test cells. Solar Energy, Selected Proceedings of the ISES 1995: Solar World Congress. Part II 58, 239–246. https://doi.org/10.1016/S0038-092X(96)00080-1

HARRISON, S.J., 1992. Uncertainties in the Evaluation of Window SHGC and U-Values Measured Using an Indoor Solar Simulator Facility. ASHRAE Transaction.

Harrison, S.J., Collins, M.R., 1999. Queen's university solar calorimeter–design, calibration, and operating procedure, in: Solar Energy Society of Canada Conference, Edmonton, AB.

HARRISON, S.J., VAN WONDEREN, S.J., 1994. Determining window solar heat gain coefficient. ASHRAE j 36, 26–32.

Hottel, H.C., 1976. A simple model for estimating the transmittance of direct solar radiation through clear atmospheres. Solar Energy 18, 129–134. https://doi.org/10.1016/0038-092X(76)90045-1

Howell, R.H., Coad, W.J., Sauer, H.J., 2013. Principles of heating ventilating and air conditioning: a textbook with design data based on the 2013 ASHRAE handbook fundamentals, 7th edition. ed. ASHRAE, Atlanta, GA.

Hukka, A., Viitanen, H.A., 1999. A mathematical model of mould growth on wooden material. Wood Science and Technology 33, 475–485. https://doi.org/10.1007/s002260050131

Huwald, H., Higgins, C.W., Boldi, M.-O., Bou-Zeid, E., Lehning, M., Parlange, M.B., 2009. Albedo effect on radiative errors in air temperature measurements. Water Resources Research 45.

Idel′chik, I.E., Ginevskiĭ, A.S., 2007. Handbook of hydraulic resistance, 4th ed. rev. and augmented. ed. Begell House, Redding, CT.

ISO, I., 2003. 15099: 2003 Thermal performance of windows, doors and shading devices-Detailed calculations. International Organization for Standardization, Geneva, Switzerland.

Jakica, N., Kragh, M., Yang, R., W.M., P., Wijeratne, U., Too, E., Wakefiled, R., Eisenlohr, J., Boddaert, S., Bonomo, P., Saretta, E., Frontini, F., Zanelli, A., Freitas, S., Alamy, P., Leloux, J., 2019. BIPV Design and Performance Modelling : Tools and Methods. Report IEA-PVPS T15-09:2019.

Kapsis, K., Athienitis, A., Harrison, S., 2017. Determination of Solar Heat Gain Coefficients for Semitransparent Photovoltaic Windows: An Experimental Study. ASHRAE Transactions 123.

Khalifa, A.J.N., Marshall, R.H., 1990. Validation of heat transfer coefficients on interior building surfaces using a real-sized indoor test cell. International Journal of Heat and Mass Transfer 33, 2219–2236. https://doi.org/10.1016/0017-9310(90)90122-B

Klems, J.H., 2000. Solar Heat Gain Through Fenestration Systems Containing Shading: Procedures for Estimating Performance from Minimal Data (No. LBNL--46682, 834476). https://doi.org/10.2172/834476

Kuhn, T.E., 2014. Calorimetric determination of the solar heat gain coefficient g with steady-state laboratory measurements. Energy and Buildings 84, 388–402. https://doi.org/10.1016/j.enbuild.2014.08.021

Kuhn, T.E., Erban, C., Heinrich, M., Eisenlohr, J., Ensslen, F., Neuhaus, D.H., 2021. Review of technological design options for building integrated photovoltaics (BIPV). Energy and Buildings 231, 110381. https://doi.org/10.1016/j.enbuild.2020.110381

Kumar, N., Ukey, P.D., Francis, V., Singh, R.P., Sahu, S., 2022. Chapter 16 - Plastic pellets, in: Izdebska-Podsiadły, J. (Ed.), Polymers for 3D Printing. William Andrew Publishing, pp. 307–323. https://doi.org/10.1016/B978-0-12-818311-3.00019-7

Liu, Y., Harris, D.J., 2007. Full-scale measurements of convective coefficient on external surface of a low-rise building in sheltered conditions. Building and Environment 42, 2718–2736. https://doi.org/10.1016/j.buildenv.2006.07.013

Lstiburek, J., Ueno, K., Musunuru, S., Corporation, B.S., 2016. Strategy Guideline: Modeling Enclosure Design in Above-Grade Walls 37.

Lundström, H., Mattsson, M., 2021. Modified Thermocouple Sensor and External Reference Junction Enhance Accuracy in Indoor Air Temperature Measurements. Sensors 21, 6577. https://doi.org/10.3390/s21196577

Ma, L., Ge, H., Wang, Lin, Wang, Liangzhu, 2021. Optimization of passive solar design and integration of building integrated photovoltaic/thermal (BIPV/T) system in northern housing. Build. Simul. 14, 1467–1486. https://doi.org/10.1007/s12273-021-0763-1

Mahmoodzadeh, M., Gretka, V., Hay, K., Steele, C., Mukhopadhyaya, P., 2021. Determining overall heat transfer coefficient (U-Value) of wood-framed wall assemblies in Canada using external infrared thermography. Building and Environment 199, 107897. https://doi.org/10.1016/j.buildenv.2021.107897

Maref, W., Manning, M., Lacasse, M.A., Kumaran, M.K., Cornick, S.M., Swinton, M.C., 2007. Laboratory Demonstration of Solar Driven Inward Vapour Diffusion in A Wall Assembly 13.

Martín-Chivelet, N., Kapsis, K., Wilson, H.R., Delisle, V., Yang, R., Olivieri, L., Polo, J., Eisenlohr, J., Roy, B., Maturi, L., Otnes, G., Dallapiccola, M., Upalakshi Wijeratne, W.M.P., 2022. Building-Integrated Photovoltaic (BIPV) products and systems: A review of energy-related behavior. Energy and Buildings 262, 111998. https://doi.org/10.1016/j.enbuild.2022.111998

McIntyre, D.A., 1985. In situ measurement of U-values. Building Services Engineering Research and Technology 6, 1–6. https://doi.org/10.1177/014362448500600101

Michalak, P., 2021. Experimental and Theoretical Study on the Internal Convective and Radiative Heat Transfer Coefficients for a Vertical Wall in a Residential Building. Energies 14, 5953. https://doi.org/10.3390/en14185953

Munaretto, F., Recht, T., Schalbart, P., Peuportier, B., 2018. Empirical validation of different internal superficial heat transfer models on a full-scale passive house. Journal of Building Performance Simulation 11, 261–282. https://doi.org/10.1080/19401493.2017.1331376

National Fenestration Rating Council, 2013. NFRC 201-2020 [E0A0] Procedure for Interim Standard Test Method for Measuring the Solar Heat Gain Coefficient of Fenestration Systems Using Calorimetry Hot Box Methods.

Olivieri, L., Frontini, F., Polo-López, C., Pahud, D., Caamaño-Martín, E., 2015. G-value indoor characterization of semi-transparent photovoltaic elements for building integration: New equipment and methodology. Energy and Buildings 101, 84–94. https://doi.org/10.1016/j.enbuild.2015.04.056

Peeters, L., Beausoleil-Morrison, I., Novoselac, A., 2011. Internal convective heat transfer modeling: Critical review and discussion of experimentally derived correlations. Energy and Buildings 43, 2227–2239. https://doi.org/10.1016/j.enbuild.2011.05.002

Pillai, D.S., Shabunko, V., Krishna, A., 2022. A comprehensive review on building integrated photovoltaic systems: Emphasis to technological advancements, outdoor testing, and predictive maintenance. Renewable and Sustainable Energy Reviews 156, 111946. https://doi.org/10.1016/j.rser.2021.111946

Rahimi, A., Dehghan Saee, A., Kasaeipoor, A., Hasani Malekshah, E., 2019. A comprehensive review on natural convection flow and heat transfer: The most practical geometries for engineering applications. HFF 29, 834–877. https://doi.org/10.1108/HFF-06-2018-0272

Rentfro, S., Gumpertz, S., 2020. CALCULATING FENESTRATION SYSTEM U-FACTOR, SHGC, AND VT USING PARTIALLY AUTOMATED WORKFLOWS.

Rounis, E., Ioannidis, Z., Sigounis, A.-M., Athienitis, A., Stathopoulos, T., 2022. "A novel approach for the modelling of convective phenomena for building integrated photovoltaic thermal (BIPV/T) systems." Solar Energy 232, 328–343. https://doi.org/10.1016/j.solener.2021.12.058

Rounis, E.D., Athienitis, A., Stathopoulos, T., 2021. Review of air-based PV/T and BIPV/T systems - Performance and modelling. Renewable Energy 163, 1729–1753. https://doi.org/10.1016/j.renene.2020.10.085

Sigounis, A.-M., 2022. Control-oriented modelling and Model Predictive Control for air-based Building-Integrated Photovoltaic/Thermal systems. Concordia University.

Somboonwit, N., Boontore, A., Rugwongwan, Y., 2017. Obstacles to the Automation of Building Performance Simulation: Adaptive Building Integrated Photovoltaic (BIPV) design. E-BPJ 2, 343. https://doi.org/10.21834/e-bpj.v2i5.619

Toffanin, R., Ge, H., Athienitis, A., 2019. Integration of Building Integrated Photovoltaic/Thermal (BIPV/T) System with Heat Recovery Ventilators for Improved Performance Under Extreme Cold Climates, in: Johansson, D., Bagge, H., Wahlström, Å. (Eds.), Cold Climate HVAC 2018, Springer Proceedings in Energy. Springer International Publishing, Cham, pp. 97–110. https://doi.org/10.1007/978-3-030-00662-4_9

Trombe, A., Moreau, J.A., 1995. Surface temperature measurement of semi-transparent material by thermocouple in real site experimental approach and simulation. International Journal of Heat and Mass Transfer 38, 2797–2807. https://doi.org/10.1016/0017-9310(95)00027-7

Wright, J.L., 1996. Summary and comparison of methods to calculate solar heat gain. ASHRAE Transactions 37, 37.

Yang, R.J., 2015. Overcoming technical barriers and risks in the application of building integrated photovoltaics (BIPV): hardware and software strategies. Automation in Construction 51, 92–102. https://doi.org/10.1016/j.autcon.2014.12.005

Yang, T., Athienitis, A.K., 2016. A review of research and developments of building-integrated photovoltaic/thermal (BIPV/T) systems. Renewable and Sustainable Energy Reviews 66, 886–912. https://doi.org/10.1016/j.rser.2016.07.011

Yang, T., Athienitis, A.K., 2015. Experimental investigation of a two-inlet air-based building integrated photovoltaic/thermal (BIPV/T) system. Applied Energy 159, 70–79. https://doi.org/10.1016/j.apenergy.2015.08.048

Yu, G., Yang, H., Yan, Z., Kyeredey Ansah, M., 2021. A review of designs and performance of façade-based building integrated photovoltaic-thermal (BIPVT) systems. Applied Thermal Engineering 182, 116081. https://doi.org/10.1016/j.applthermaleng.2020.116081

9. Appendix

9.1. BIPV/T Curtain Wall: Air cavity bottom inlet temperature

For the simplified BIPV/T model, the temperature gradient from the bottom to top of the air cavity is given by the following exponential relationship (Charron and Athienitis, 2006):

$$T_{cav\,i} = \frac{T_{pv,avg} + T_{b,avg}}{2} + \left(T_{out} - \frac{T_{pv,avg} + T_{b,avg}}{2}\right) e^{-\frac{2X_i}{a}} \qquad (9.1.1)$$

At T_{cav1}, the distance from the bottom inlet X_1=0, the equation then simplifies to $T_1 = T_{out}$. The monitoring data shows that this result is often incorrect.

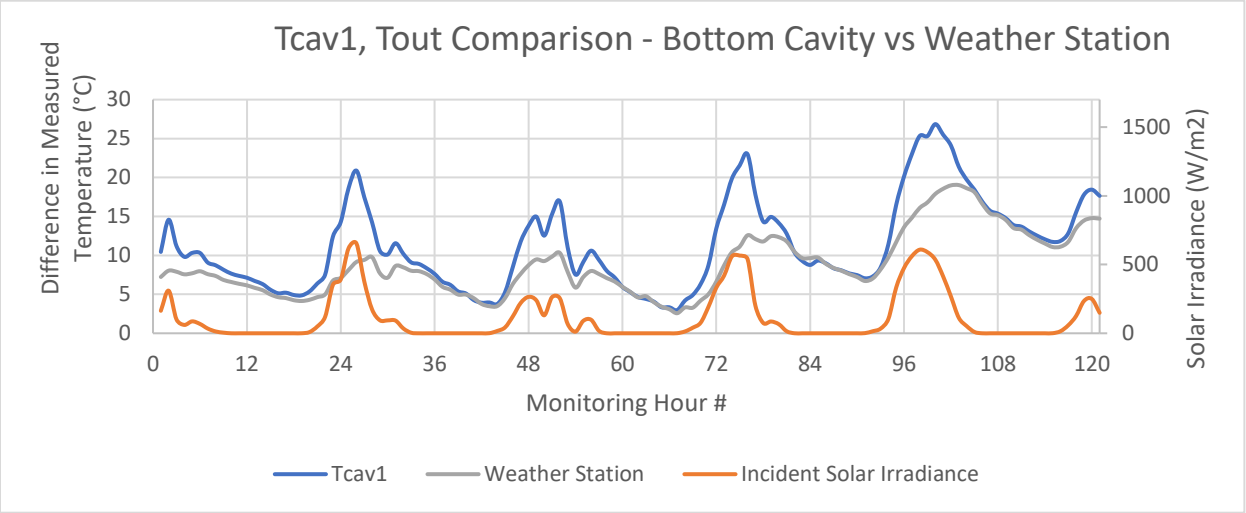

Figure 9.1.1: Comparison of T_{cav1}, T_{out} (measured by weather station) and their trends with incident solar irradiance.

The bottom inlet cavity temperature T_{cav1} is significantly different from T_{out} (temperature measured by the weather station). T_{cav1} tends to always be higher in temperature, and the largest difference in temperature can be over 15°C. The large differences between T_{cav1} measured from the bottom inlet and T_{out} measured from the weather station always coincide with the presence of incident solar irradiance.

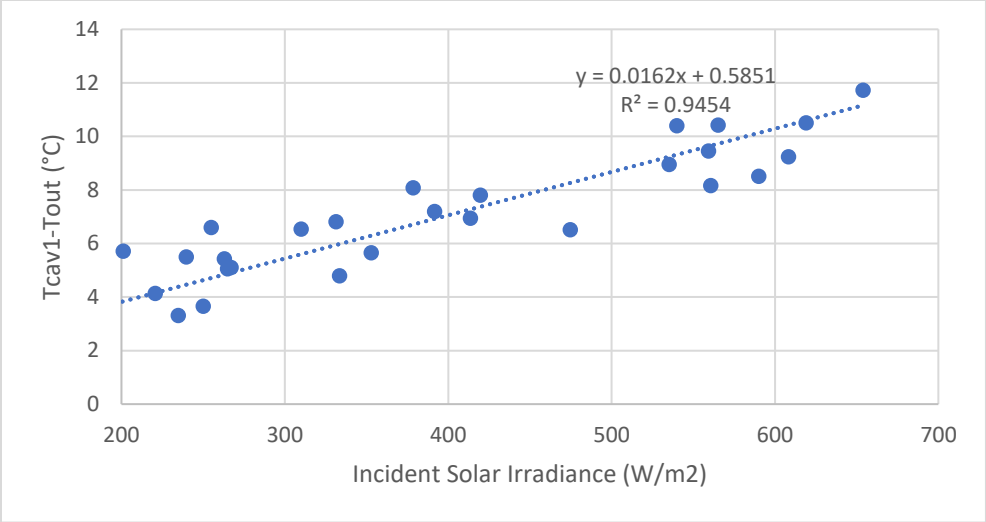

Figure 9.1.2: Temperature difference between T_{cav1} and T_{out} due to incident solar irradiance

For the purposes of this model, T_{cav1} is used in place of T_{out} in the cavity temperature gradient equation to better match the monitored conditions. The good linear correlation with $R^2 = 0.9454$ suggests that, if T_{cav1} data is unavailable but the T_{out} data from a weather station is, it may be appropriate to infer the value of T_{cav1} using the equation:

$$T_{cav1} = T_{out} + 0.0162I_s + 0.5851 \quad (9.1.2)$$

9.2. BIPV/T Curtain Wall: Exterior wind effects

The weather station is aligned at 360 degrees for true north, and the south façade with the BIPV/T is facing directly at true south, so recorded wind direction angles from 90 – 270 degrees are considered the windward direction, while 0 – 90 degrees and 270 – 360 degrees are the leeward direction.

For windward direction:

$$h_c = 2.08V_{wind,roof} + 2.97 \quad (9.2.1)$$

For leeward direction:

$$h_c = 1.57V_{wind,roof} + 2.64 \quad (9.2.2)$$

Where h_c is the exterior convective heat transfer coefficient in $\frac{W}{m^2K}$ and $V_{wind,roof}$ is the wind speed measured by the rooftop weather station in m/s.

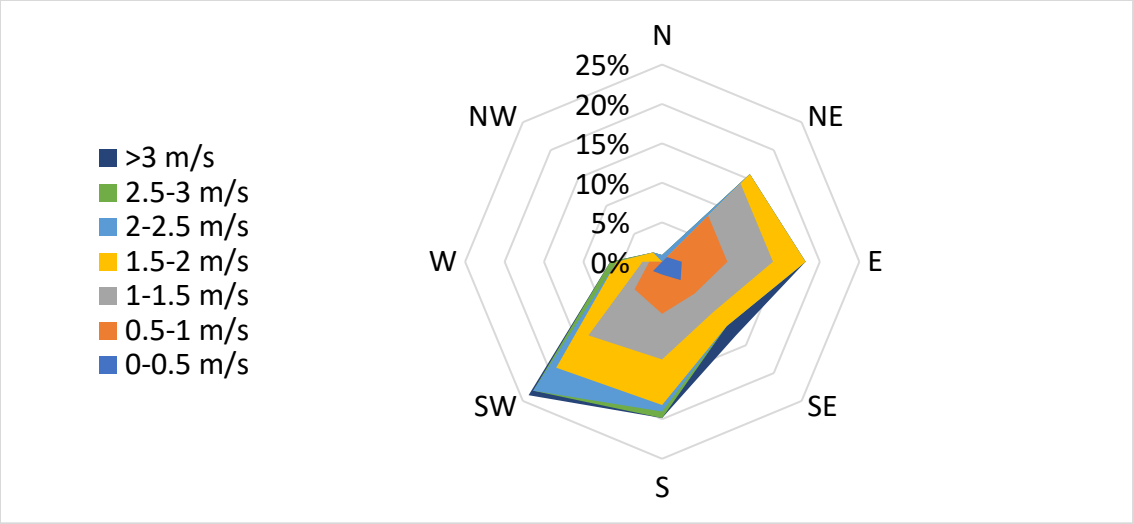

Figure 9.2.1: Frequency (% of total) of wind speed at each wind direction throughout the 2023 April 24-29 monitoring period

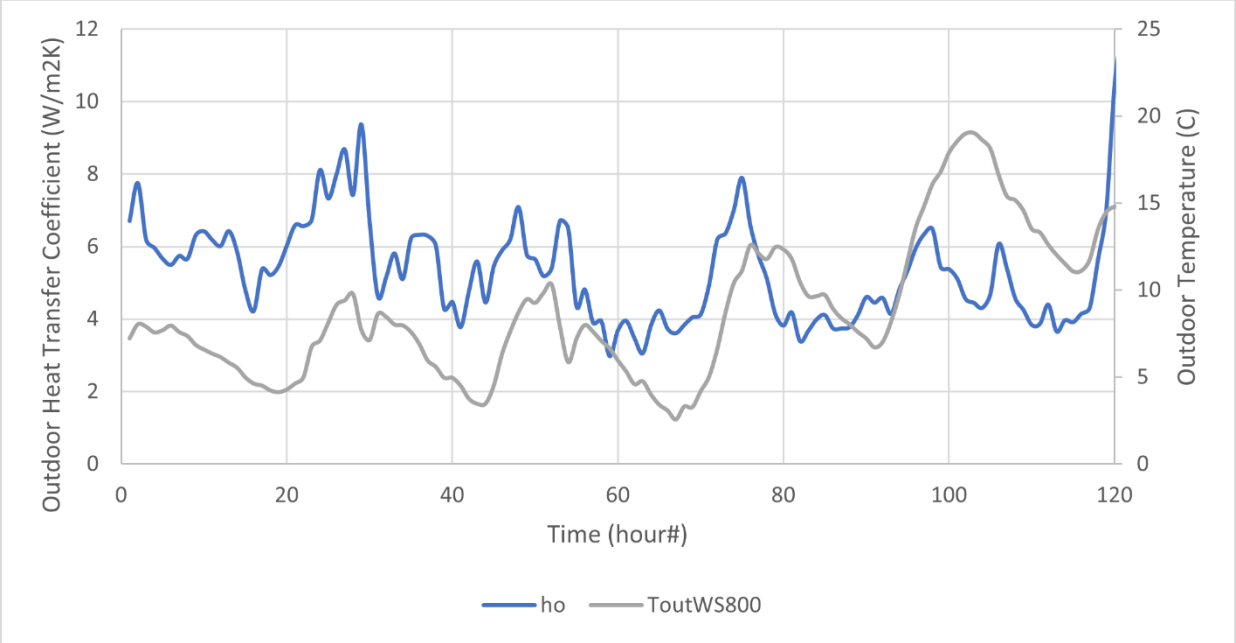

Figure 9.2.2: Calculated outdoor heat transfer coefficient and measured outdoor temperature throughout the 2023 April 24-29 monitoring period.

The outdoor heat transfer coefficient varied between 3 to 12 W/m^2K, with an average value of 5.3 W/m^2K during the monitoring period. Including the varying heat transfer coefficient slightly reduced the discrepancies between the modeled and measured cavity temperature profile.

9.3. BIPV/T Curtain Wall: Nusselt and Reynold's correlations

$$Nu = \frac{h_{PVT} D_h}{k_{air}} \tag{9.3.1}$$

Where h_{PVT} is the convective heat transfer coefficient within the BIPV/T air cavity as calculated from Equation (3.2.8), D_h is the hydraulic diameter of the BIPV/T air cavity in m, and k_{air} is the conductivity of air.

By plotting the Nu vs. Re graph, the exponential curve takes the form:

$$Nu = xRe^{y} \tag{9.3.2}$$

$$x = cPr^{0.43} \tag{9.3.3}$$

The Prandtl number Pr =0.7 for typical BIPV/T operating conditions, so assuming this factor remains constant, the coefficients c and y for Nu can be found:

$$Nu = cPr^{0.43} Re^{y} \tag{9.3.4}$$

Unfortunately, due to having a constant flowrate setting on the HRV during the monitoring period, the recorded range of Re was very narrow. The resulting plot is inconclusive about the Nu correlation, while the regression curve suggests that $cPr^{0.43} = 10^{11}$ and $y = -2.542$, the fit is poor at $R^2 = 0.009$.

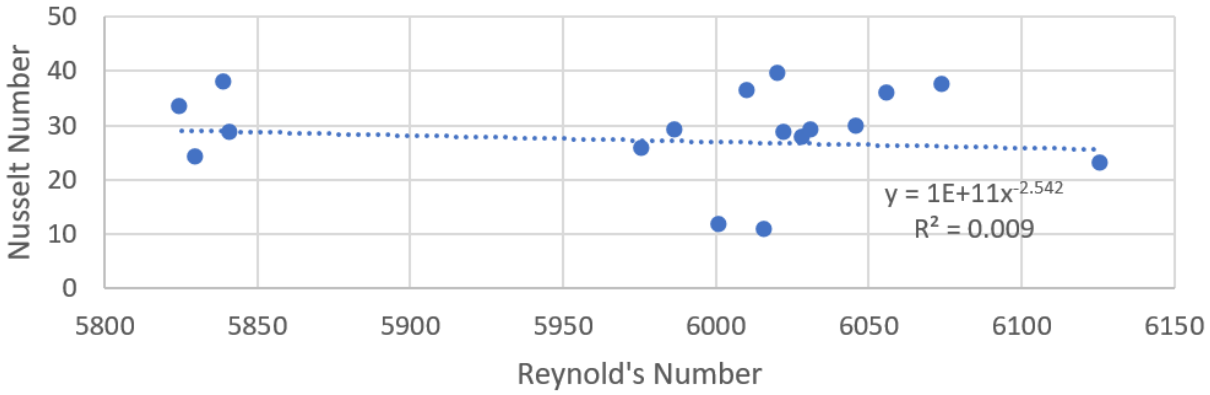

Figure 9.3.1: Nu vs. Re plot as determined from the monitored data from April 24 to April 29.

9.4. BIPV/T Curtain Wall: Sky clearness index

To examine the monitoring data and modeled results in more detail, clear days with high solar radiation were prioritized. The average clearness index K_T can be determined by:

$$K_T = \frac{I}{I_{ho}} \qquad (9.4.1)$$

The total horizontal extraterrestrial solar radiation I_{ho} was calculated by Hottel's clear sky model (Hottel, 1976). The total horizontal solar radiation I was measured by the WS800 weather station.

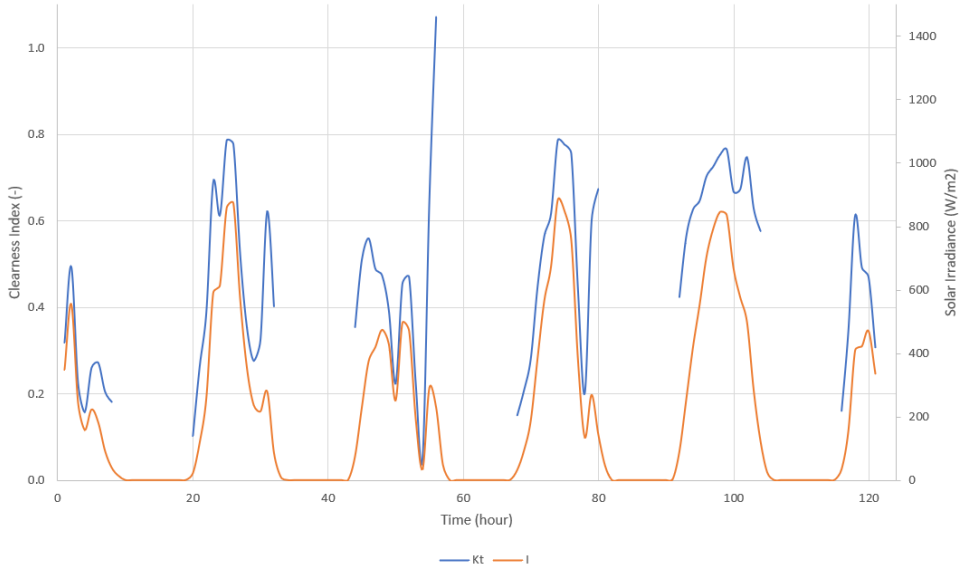

Figure 9.4.1: Clearness index K_t and total horizontal solar radiation I measured by the WS800 weather station during the 2023 April 24 to April 29 monitoring period.

The clearness index K_t values calculated are often undefined at sunset (6pm- 8pm) when weather station measured value $I < \frac{50W}{m^2}$ while the extraterrestrial horizontal solar radiation $I_{ho} = 0$. The clearness index and solar radiation also appear to increase significantly shortly before sunset on most days. In a single instance on April 26 at 6pm, an unreasonable value of K_T =1.07 is attained. A possible source of this issue could be that the weather station was measuring additional horizontal solar radiation values due to the reflection from the surroundings. In particular, the HU building (Figure 9.4.2) situated slightly south-east from the FBL has a highly reflective glazed façade. During sunset, the solar radiation at low solar altitude incident from the west can be reflected from the HU building to the weather station.

Figure 9.4.2: Reflective facade of the HU Building at Concordia University Loyola Campus which has direct line of sight from the WS800 weather station (circled in red).

For sunny days (peak $I > 800\ W/m^2$), the average K_T is approximately 0.54 throughout the day and 0.72 around noon (11:00-13:00). For cloudy days (peak $I < 600\ W/m^2$), the average K_T is approximately 0.39 throughout the day and 0.34 around noon. For this reason, the days with the long durations of $K_t > 0.7$ and peak $I > 800\ W/m^2$, April 27th and April 28th, 2023, were chosen for analysis in more detail.

9.5. BIPV/T Curtain Wall: Air cavity temperature gradient

As shown in Figure 3.2.3 and Figure 3.2.4, the air cavity temperature at different heights of the cavity were measured with thermocouples recorded to channels 211 to 215 on the DAQ. The temperature gradient over time throughout the monitoring period can then be examined by comparing between the measured and modeled values.

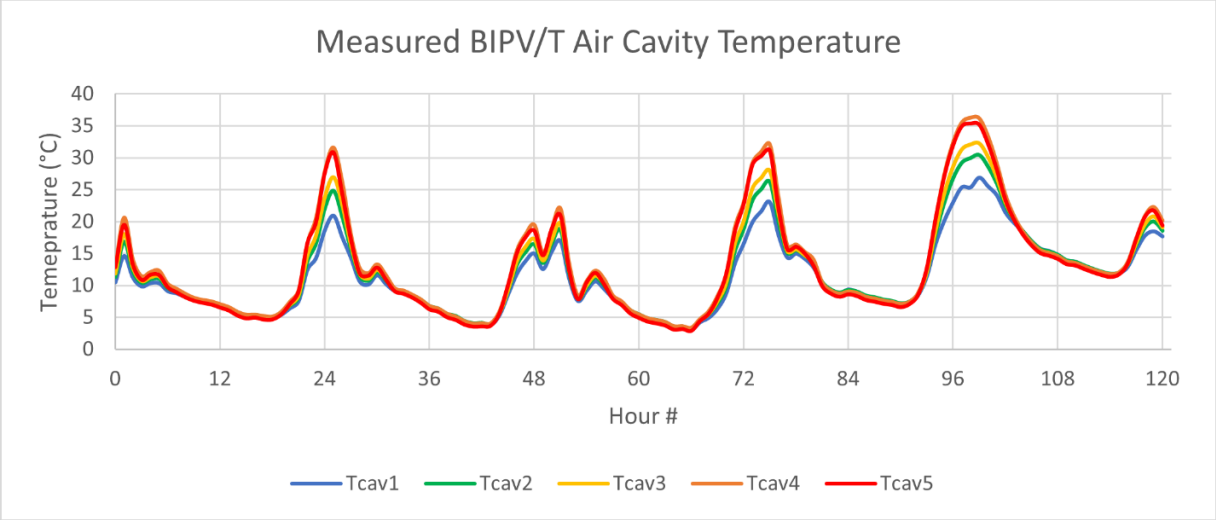

Figure 9.5.1: Measured BIPV/T cavity temperature gradient for the monitoring period between April 24 to April 29

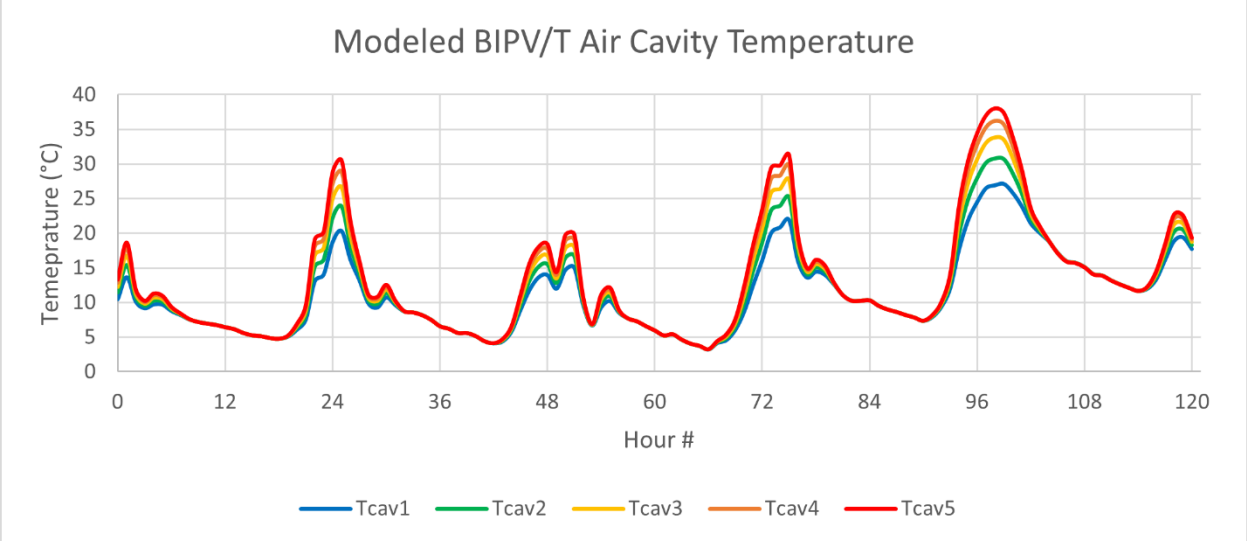

Figure 9.5.2: Modeled BIPV/T cavity temperature gradient for the monitoring period between April 24 to April 29

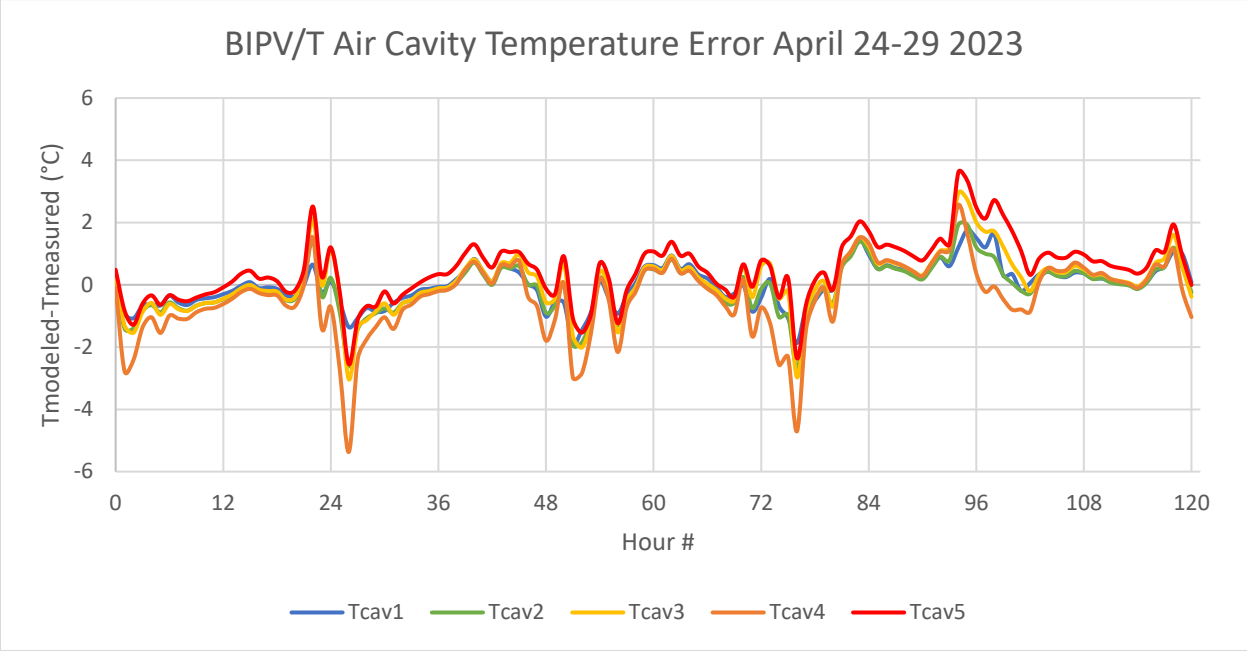

Figure 9.5.3: Error of the temperature profile predicted by the model (modeled temperature – measured temperature) over the 2023 April 24 to April 29 monitoring period.

Figure 9.5.3 shows that, over the 5-day monitoring period, the model deviates from the measured values from -5.37°C to +3.61°C at the extremes but stays between -0.39°C to +0.47°C on average. Table 9.5.1 shows the maximum and minimum deviations from the measured temperature values, the average error over the monitoring period, and the root mean square error (RMSE) at each different air cavity height temperature monitoring positions.

Table 9.5.1: Max, min, average and RMSE for modeled temperature errors at each monitoring position from 2023 April 24 to April 29

Error	T_{cav1}	T_{cav2}	T_{cav3}	T_{cav4}	T_{cav5}
Max (°C)	1.76	1.93	2.95	2.57	3.61
Min (°C)	-1.88	-2.71	-3.03	-5.37	-2.55
Average (°C)	0.00	-0.09	0.09	-0.39	0.47
RMSE (°C)	0.67	0.78	0.93	1.25	1.09

It can be seen from Figure 9.5.1 that T_{cav5}, the temperature measurement at the top of the BIPV/T air cavity, from the monitored data is often slightly lower than the temperature at the monitoring position below it T_{cav4}. This is different from Figure 9.5.2 where the model predicts that T_{cav5} always has the highest temperature within the air cavity. This suggests that the presence of the BIPV/T manifold and turbulent airflow around it can influence the temperature measurement at the top of the BIPV/T cavity.

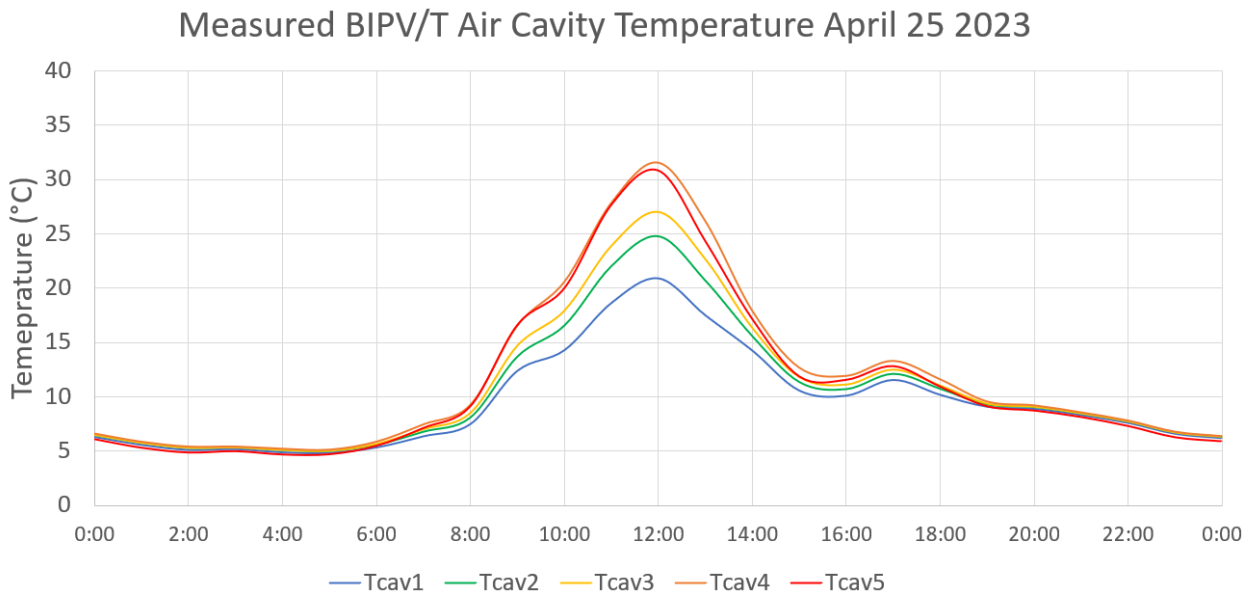

Figure 9.5.4: Measured BIPV/T air cavity temperature gradient for April 25

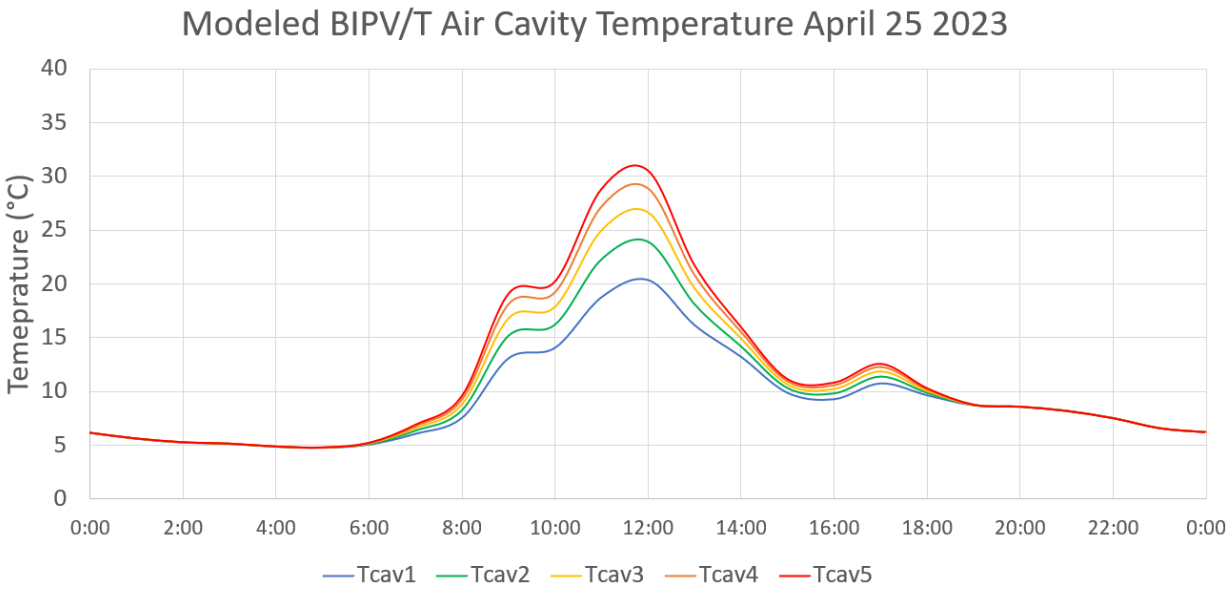

Figure 9.5.5: Modeled BIPV/T air cavity temperature gradient for April 25

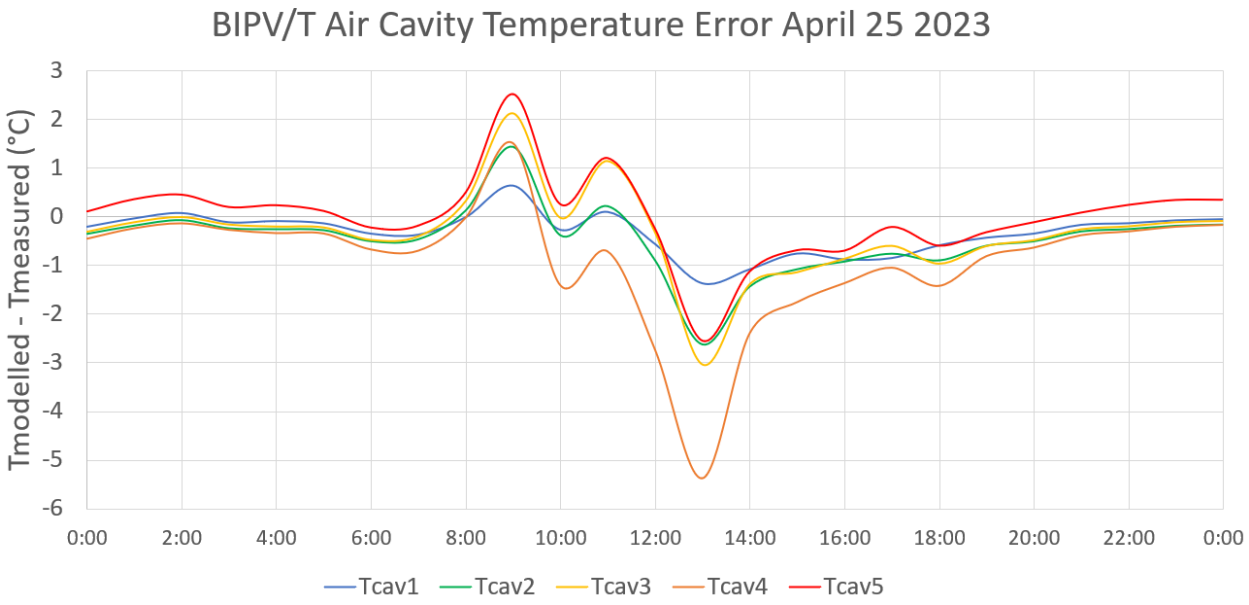

Figure 9.5.6: Error of the temperature profile predicted by the model (modeled temperature – measured temperature) for 2023 April 25.

Table 9.5.2: Max, min, average and RMSE for modeled temperature errors at each monitoring position on 2023 April 25

Error	T_{cav1}	T_{cav2}	T_{cav3}	T_{cav4}	T_{cav5}
Max (°C)	0.65	1.44	2.13	1.51	2.52
Min (°C)	-1.36	-2.62	-3.03	-5.37	-2.55
Average (°C)	-0.31	-0.46	-0.33	-0.89	0.00
RMSE (°C)	0.52	0.82	0.93	1.52	0.85

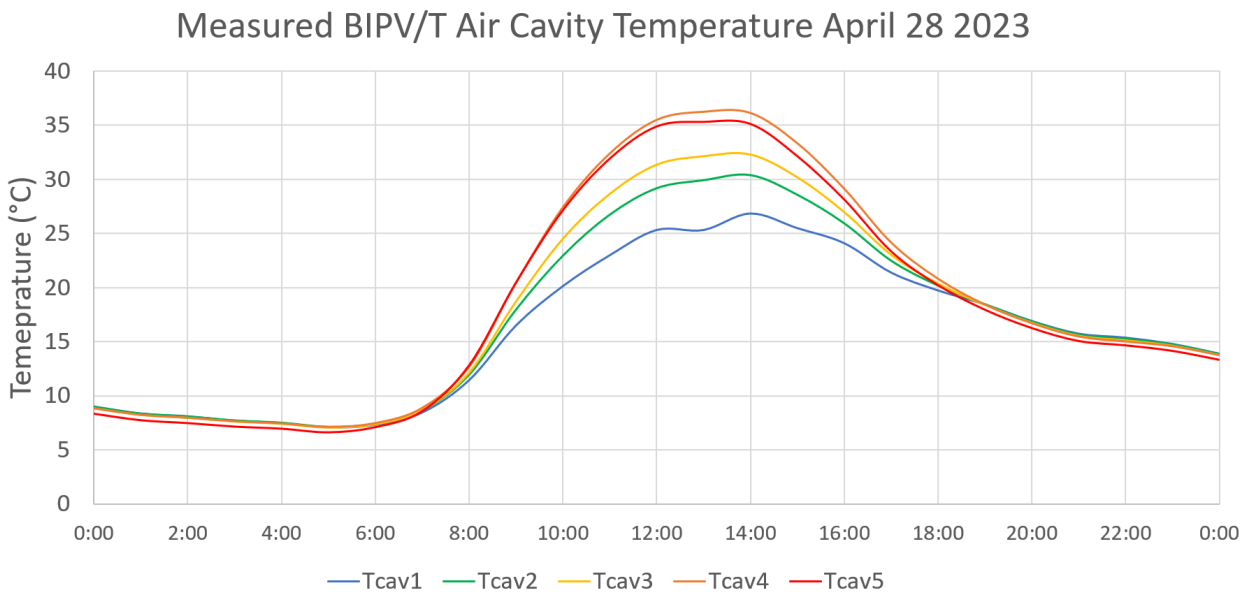

Figure 9.5.7: Measured BIPV/T air cavity temperature gradient for April 28

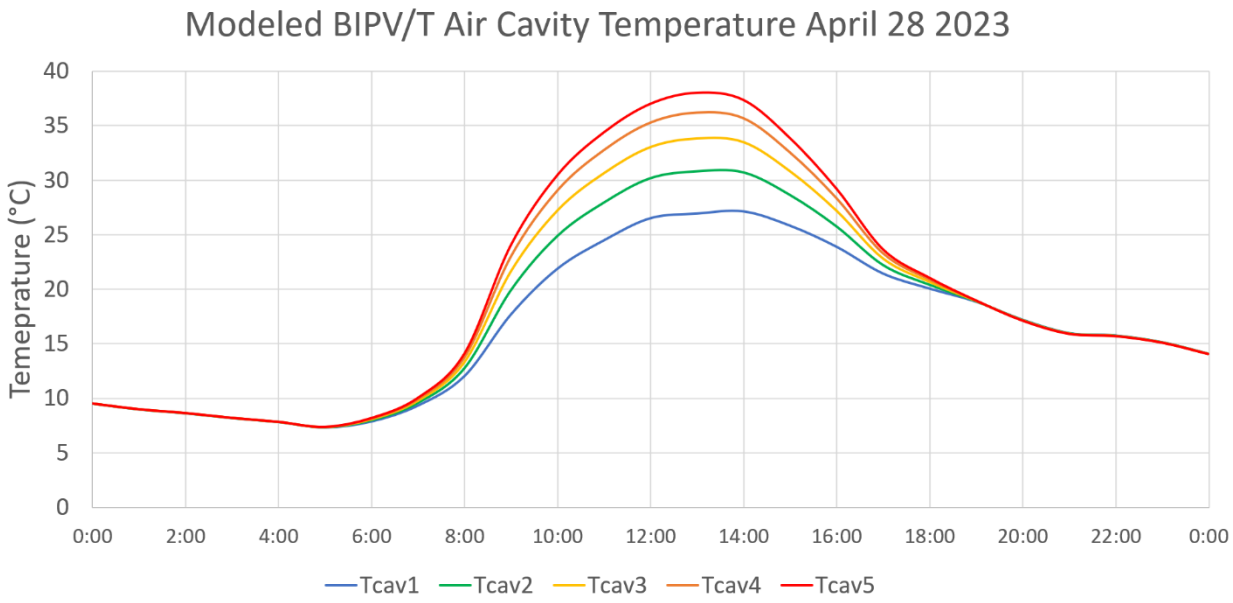

Figure 9.5.8: Modeled BIPV/T air cavity temperature gradient for April 28

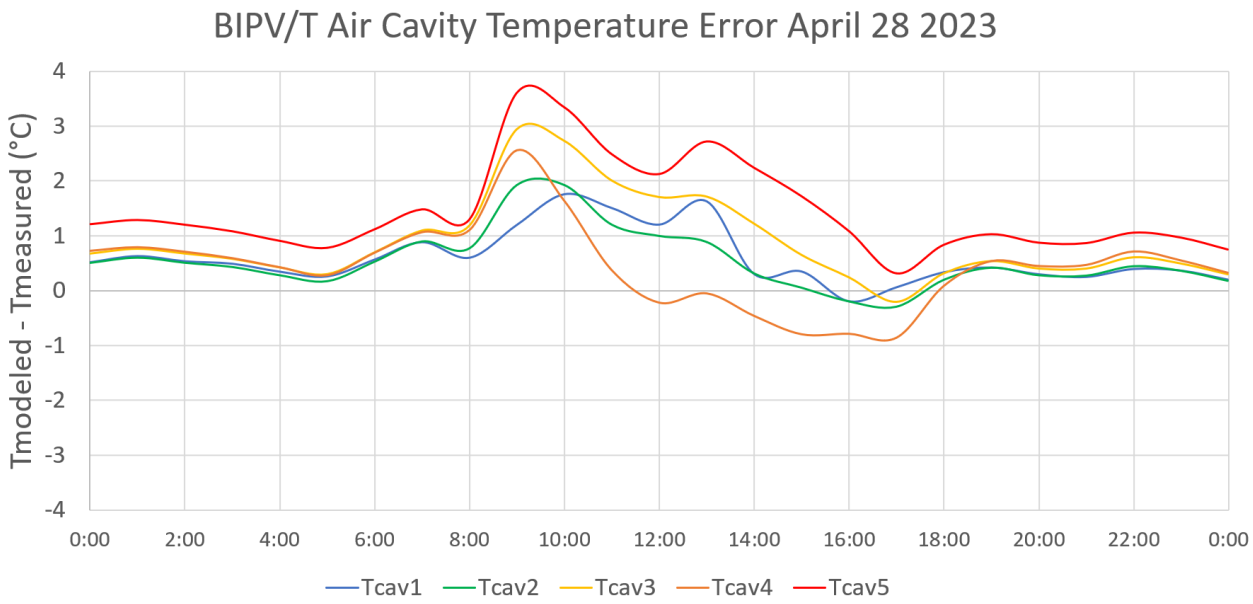

Figure 9.5.9: Error of the temperature profile predicted by the model (modeled temperature – measured temperature) for 2023 April 28.

Table 9.5.3: Max, min, average and RMSE for modeled temperature errors at each monitoring position on 2023 April 28

Error	T_{cav1}	T_{cav2}	T_{cav3}	T_{cav4}	T_{cav5}
Max (°C)	1.76	1.93	2.95	2.57	3.61
Min (°C)	-0.20	-0.29	-0.20	-0.86	0.32
Average (°C)	0.59	0.55	0.90	0.44	1.46
RMSE (°C)	0.77	0.76	1.18	0.86	1.67

Closer inspection on these individual days shows that the error in modeled temperature is highest when the BIPV/T curtain wall is heating up and cooling down, while the error for the peak temperature around noon and the lowest temperature in the evening are closer to 0. Comparing Table 9.5.2 and Table 9.5.3 shows that depending on the day, the model may tend to overestimate (April 28) more than underestimate (April 25) on average. While both days have total horizontal radiation $> 800W/m^2$ and incident solar irradiance on the façade that's $> 600W/m^2$, the clear sky conditions of $K_t > 0.7$ was consistently present around noon for longer during April 28 than for April 25, which may have allowed the BIPV/T system to operate in conditions that were closer to steady state than the dynamic conditions caused by rapid changes in solar irradiance. This suggests that there is some thermal capacitance in the BIPV/T curtain wall which may need to be included in the model to improve the model accuracy.

9.6. BIPV/T Curtain Wall: Limitations and sources of error

The model energy balance errors can be examined by comparing the thermal energy captured Qu determined from Equation (3.2.9 by using an alternate method:

$$Qu_2 = U_a(T_{pv} - T_{ma}) + U_b(T_b - T_{ma}) \quad (9.6.1)$$

$$U_a = h_{PVT}A_{PVT} \quad (9.6.2)$$

Where Qu_2 (denoted with subscript "2" to distinguish the calculation method) is the heat energy captured in Wh, U_a and is the overall heat transfer coefficient at the back surface of the PV module (facing the air cavity) in W/K and U_b (assumed to be equal to U_a) is overall heat transfer coefficient at the surface of the back pan (black aluminum exterior to the XPS) in W/K, T_{pv} is the surface temperature in $°C$ of the PV module (estimated by averaging the measurement of thermocouples T201 to T205 for measured calculations), T_{ma} is the mean air temperature of the cavity in $°C$ (estimated by averaging the measurement of thermocouples T211 to T215 for measured calculations), and T_b is the back pan surface temperature in $°C$ (estimated by averaging the measurement of thermocouples T301 to T305).

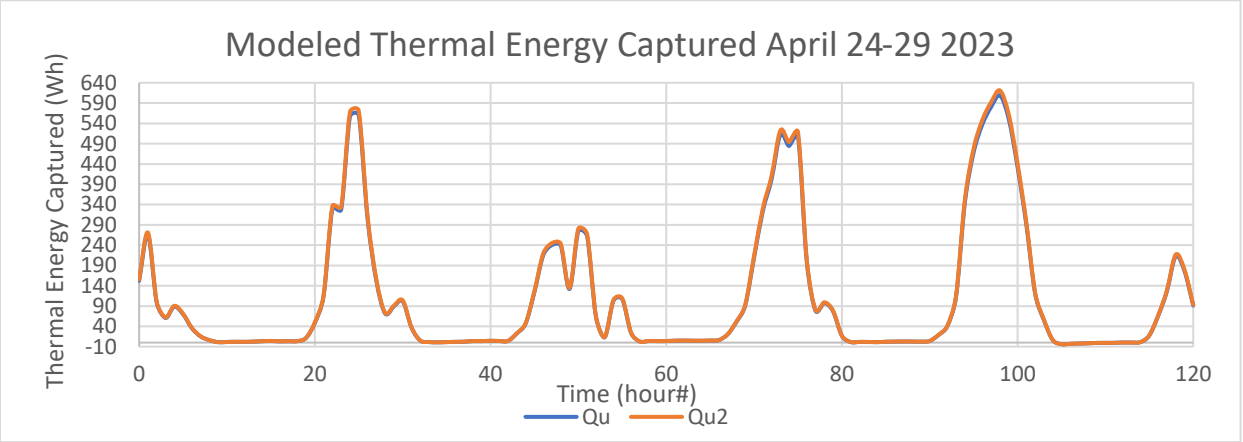

Figure 9.6.1: Comparison of modeled thermal energy captured determined through both Equations (3.2.9 and (9.6.1 for the monitoring period between 2023 April 24 to April 29.

Theoretically, both Qu and Qu_2 should be equal. From the model's outputs, the thermal energy captured Qu and Qu_2 show good agreement. The difference between the two calculation methods is about 1.5% on average. This indicates that the energy balance within the model is consistent, and the convergence of iterative solutions based on the tolerance setting of <0.001$°C$ relative difference for T_b, T_R and T_{pv} is acceptable.

The thermal energy lost to outdoors Q_{out} can be compared between the modeled and measured results to examine if issues related to outdoor boundary conditions and heat transfer coefficients within the model are significant contributors to the error. This can be determined by using the outdoor heat transfer coefficient estimated from wind speed, wind direction and outdoor temperature:

$$Q_{out} = U_{out}(T_{pv} - T_{out}) \quad (9.6.3)$$

$$U_{out} = h_{out} A_{PVT} \quad (9.6.4)$$

$$h_{out} = h_c + h_r \quad (9.6.5)$$

$$h_r = 4\sigma \left(\frac{T_{pv} + T_{out}}{2} + 273.15 \right)^3 \quad (9.6.6)$$

Where Q_{out} is the thermal energy lost to outdoors in Wh, U_{out} is the overall outdoor heat transfer coefficient in W/K, h_c is outdoor convective heat transfer coefficient determined from Equations (9.2.1 and (9.2.2 in W/m^2K, h_r is the outdoor radiative heat transfer coefficient in W/m^2K, A_{PVT} is the area of the PV module (=$2m^2$ in this experiment), the combined outdoor heat transfer coefficient h_{out} in W/m^2K is the same between the modeled and measured calculations (as their convective and radiation heat transfer coefficient components are determined using the same equations), T_{pv} is the surface temperature in $°C$ of the PV module (estimated by averaging the measurement of thermocouples T201 to T205 for measured calculations), and T_{out} is the outdoor air temperature in $°C$ measured by the weather station.

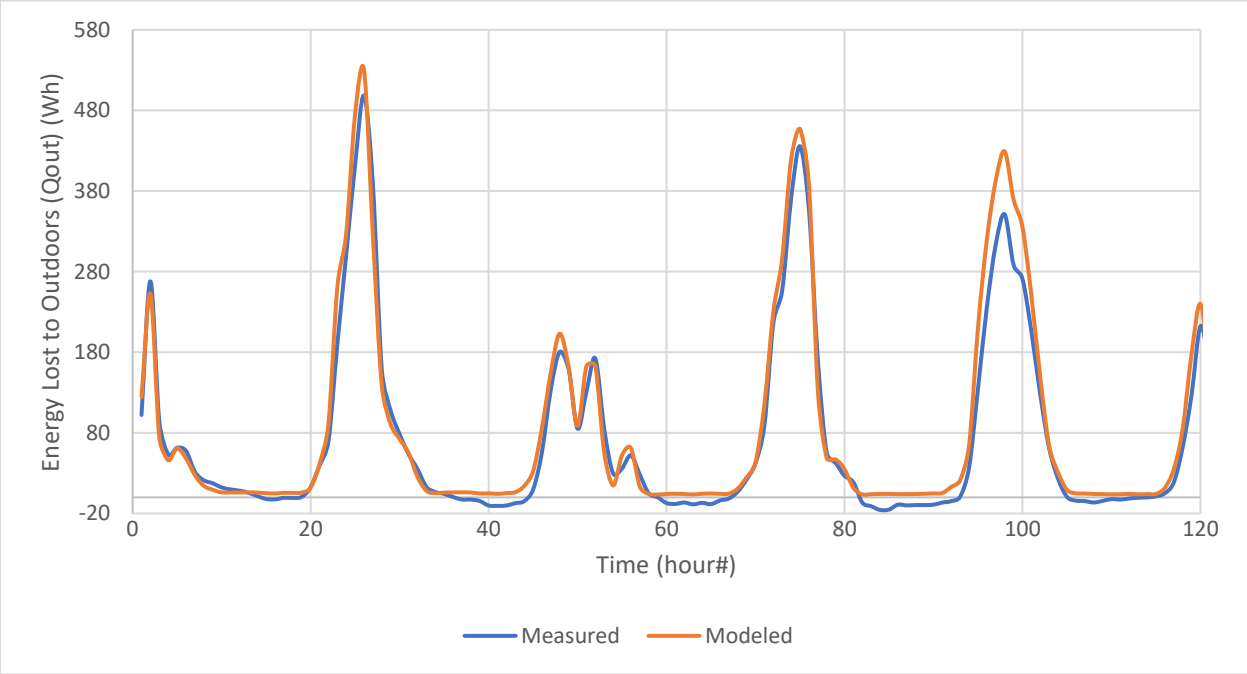

Figure 9.6.2: Comparison of modeled and measured thermal energy lost from BIPV/T air cavity to the outdoors Q_{out} for the monitoring period from 2023 April 24 to April 29.

Throughout the modeled period between April 24 to April 29, the difference the model's calculated Q_{out} and the field measurements is about 17% in terms of the sum total energy. The instantaneous % error ranges between -20% to +30% during day time. The RMSE between the modeled and measured Q_{out} over the period is 25.7 Wh. The model slightly overestimates the heat loss to the exterior during daytime and neglects the heat loss during night time.

Thermal energy can also be lost or gained from the air cavity to the indoors. The loss of pre-heated cavity air thermal energy towards the interior occurs during the day when the air cavity is at a higher temperature. This can be compared between the modeled and measured results to examine

if issues related to indoor boundary conditions and heat transfer coefficients within the model are significant contributors to the error. This can be determined by:

$$Q_{in} = U_{in}(T_b - T_R) \qquad (9.6.7)$$

Where Q_{in} is the thermal energy lost from the BIPV/T air cavity to the indoors in Wh, U_{in} is the overall heat transfer coefficient in W/K between the backpan surface and the indoor room air, based on the insulation level of the XPS layer (for this experiment it is $65mm$ thick, $RSI = 1.6\frac{m^2}{W}$) and an indoor heat transfer coefficient of 8 W/m^2K, T_b is the back pan surface temperature in $°C$ (estimated by averaging the measurement of thermocouples T301 to T305 for determining measured Q_{in}, or determined based on thermal network for determining modeled Q_{in}), and T_R is the indoor room air temperature in $°C$ (identical between measured and modeled).

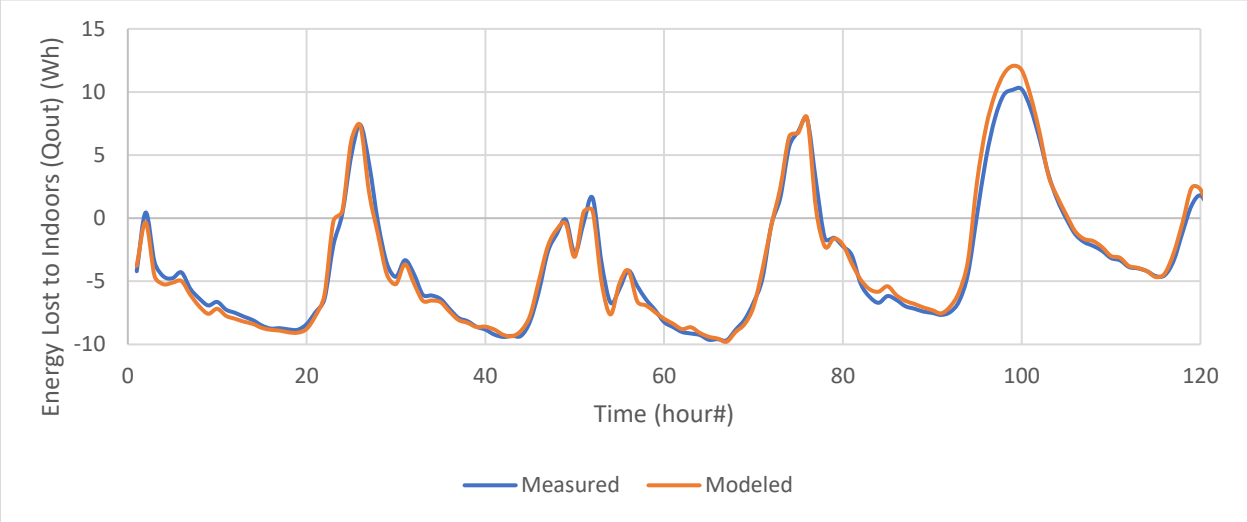

Figure 9.6.3: Comparison of modeled and measured thermal energy lost from BIPV/T air cavity to the indoors Q_{in} for the monitoring period from 2023 April 24 to April 29.

Throughout the modeled period between April 24 to April 29, the difference the model's calculated Q_{in} and the Q_{in} determined from field measurements is about -2.5% in total. The RMSE during this period is 0.76 Wh. The model slightly over- or underestimates the heat loss to the interior during the day, with the greatest differences occurring during sunrise and sunset. Unlike the heat loss to outdoors, there does not appear to be any significant difference for the nighttime heat loss towards the interior. Overall, the magnitude of these losses is very small, and the overall difference over the period is $< 3\%$. This indicates that the calibration for the model's interior (room side) heat transfer coefficient would only make a very small difference in the overall model outputs and can be modeled conventional assumptions.

Energy balance between the solar energy received and the energy captured/lost can also be compared to examine that the energy balance errors within the model are within an acceptable range. Theoretically, the thermal energy gained from solar radiation S_{pv} in Wh should be equal to the sum of air cavity heat energy captured and energy lost to the outdoors and indoors:

$$S_{pv} = Qu + Q_{out} + Q_{in} \qquad (9.6.8)$$

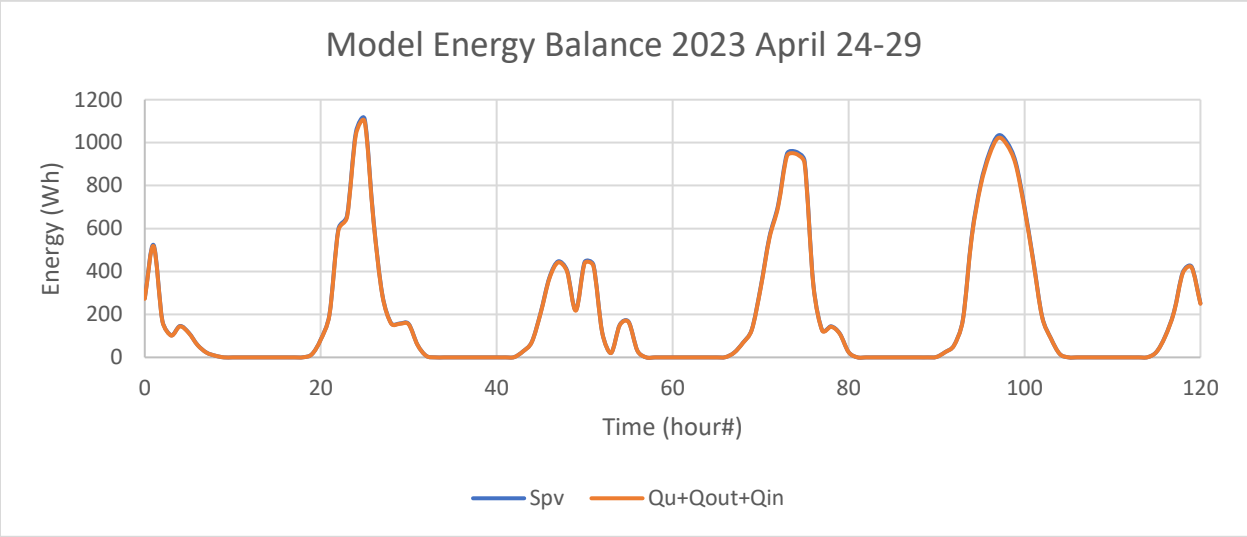

Figure 9.6.4: Comparison of energy balance between S_{pv} and $Qu + Q_{out} + Q_{in}$ from the model outputs for the monitoring period from 2023 April 24 to April 29.

The difference between S_{pv} and the sum of Qu, Q_{out}, Q_{in} is about 4.8% on average throughout the modeled period. This average is skewed by periods with small energy values ($S_{pv} = 0.19Wh, Qu + Q_{out} + Q_{in} = 0.17Wh$) when there is nearly no solar irradiance. Excluding these periods, the average difference is about 1.2%. This indicates that the energy balance within the model is consistent and acceptable.

Shading of the LI-COR LI-200 pyranometer from the roof overhang of the FBL appears to be an issue during periods of monitoring close to the summer months. Noticeable shading on the LI-200 pyranometer can be seen in the Appendix during the month of June. It is unclear if the shading issue has been affecting the measurements to the same degree during April 24 to April 29. Compared to the LI-200, the SMP22 pyranometer installed at the south façade of Test Cell 5 of the FBL experiences less shading due to its mounting position being extended farther outwards from the façade. Comparing the measured values between the two pyranometer shows that the LI-200 may measure up to 17% lower than the SMP22 during noon time. This suggests that the measured incident solar irradiance values in this experiment may have been lower than actual values. However, given that the current model is already over-estimating the heat energy captured, correcting the incident solar irradiance measurement to higher values may result in even larger over-estimations.

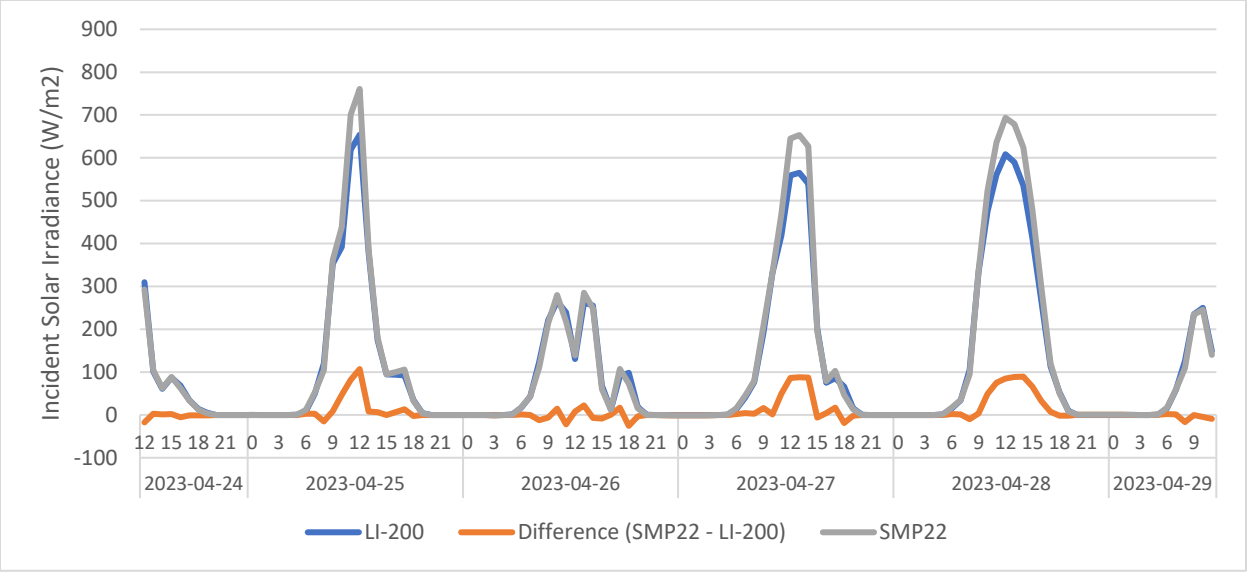

Figure 9.6.5: Comparison of incident solar irradiance measurements from the LI-200 (potentially more shaded) pyranometer and the SMP22 (potentially less shaded) pyranometer

Another potential source of error is that the zeroing of the flowmeter in the ductwork at the HRV inlet has the potential to drift over time. The integrity of the zero has not been verified since February 2023. This may have caused the HRV inlet flowrate, and consequently the BIPV/T air cavity flowrate, to be measured higher or lower than the actual value. However, the measured flowrate value is within expected range and consistent with the manufacturer's design flowrates of 35 to 89 L/s supply airflow depending on the external static pressure.

On April 18, the thermocouples within the BIPV/T curtain wall cavity were inspected. As shown in the Appendix, many thermocouples are not positioned correctly on the surfaces they were supposed to measure or have drifted from the center depth of the air cavity where they were positioned to measure the cavity air temperature. The positioning of these thermocouples was corrected, and additional sheathing tape and reflective foil tape have been used to fix the thermocouples in place, however, the adhesives on the tape loosening over time and causing the thermocouples within the air cavity moving out of alignment is a possibility due to the air cavity being exposed to large variations in outdoor temperature, humidity and wind conditions. The high temperature of the BIPV cladding during periods of high solar irradiance may also contribute to this issue.

Errors in propagation of uncertainty in measured temperature, wind speed and direction, solar irradiance, and air flowrates from the instruments may also contribute to the model errors. The uncertainty analysis for this field monitoring experiment will be examined in the future.

9.7. HRV Integration: Equal friction method for sizing manifold

Equal friction method as applied to the manifold design:

Continuity:

$$V = \frac{Q}{A} \tag{9.7.1}$$

Where V is the air velocity in m/s, A is cross-sectional area of the air flow section in m², and Q is the volumetric flowrate of the air flow in m^3/s.

Rectangular to Circular Equivalent duct diameter:

$$D_e = \frac{1.3(HW)^{0.625}}{(H+W)^{0.25}} \tag{9.7.2}$$

Where D_e is the equivalent duct diameter in m, H is the designed height of the duct section in m, W is the designed width of the duct section in m.

Total pressure loss:

$$p_t = p_s + p_v \tag{9.7.3}$$

Where p_t is the total pressure loss through the airflow path in Pa, p_s is the total static pressure loss through the airflow path in Pa, p_v is the total dynamic pressure loss through the airflow path in Pa.

Darcy equation:

$$\Delta p_f = \frac{(1000fL)}{D_h} \times \frac{(\rho V)^2}{2} \tag{9.7.4}$$

Where Δp_f is the friction pressure loss in Pa, f is the friction factor from Equation (9.7.5), L is length of the duct section, D_h is the hydraulic diameter of the duct section from Equation (9.7.7) in m, ρ is the density of the air at $1.244\frac{kg}{m^3}$, and V is the velocity of the airflow in m/s.

Colebrook Equation:

$$\frac{1}{\sqrt{f}} = -2\,log\left(\frac{\varepsilon}{3.7D_h} + \frac{2.51}{Re\sqrt{f}}\right) \quad (9.7.5)$$

Where ε is the duct roughness surface coefficient (assume=0.046 for plastic (3D printed ABS)), and Re is the Reynold's number from Equation (9.7.6). The Colebrook and Darcy equations are solved iteratively until the solutions converge.

$$Re = \frac{D_h V}{1000\nu} \quad (9.7.6)$$

Where Re is the Reynold's number and ν is the kinematic viscosity of air.

$$D_h = \frac{4A}{P} \quad (9.7.7)$$

Where A is the rectangular cross-sectional area of the duct in m² and P is the perimeter of the duct in m.

Loss coefficients:

$$\Delta p_t = C_o p_{v,o} \quad (9.7.8)$$

Where Δp_t is the increase in total pressure loss due to a duct transition (bends, diverging or converging flows) in Pa. C_o is the duct transition's loss coefficient from various reference tables based on empirical correlations, and $p_{v,o}$ is the dynamic pressure loss in Pa of the airflow at the duct transition.

9.8. HRV Integration: Limitations of experimental setup

Thermal Transmission Losses

The monitored data may be sensitive to thermal transmission losses from the room air to the duct section between the BIPV/T manifold and the outside air inlet port of the HRV. As shown by Figure 4.1.3 and the energy balance in the Appendix, the expected changes in $T_{OA,HRV}$ and SRE are only true if $\dot{m}, c_p, T_{room}$ are constant and the average BIPV/T manifold inlet temperature $T_{manifold}$ (without the BIPV cladding) is some linear function of $T_{outdoor}$. The monitoring data has shown small fluctuations in the $\dot{m}$, T_{room} variables, and although $T_{manifold} = f(T_{outdoor})$ is shown to be mostly linear the correlation is not exact (discussed in Figure 4.3.2, Chapter 4.3). To minimize the uncertainty of the results in the ongoing monitoring experiment, multiple layers of additional insulation were installed on the manifold and duct section. There is also some air exfiltration from the indoor to the outdoor noted during the experiment, which can lead to the manifold inlet temperature $T_{manifold}$ to be higher than the outdoor ambient temperature even at night. The air exfiltration effect has not been quantified separately from the correlations shown in Chapter 4.3, but should be examined in future work.

Outdoor Temperature Measurement

The outdoor temperature during this HRV performance monitoring experience from January 26 to February 8 was measured using an improvised outdoor thermocouple mounted a wooden stick (shown Figure 3.1.9).

From the monitoring data after the WS800 weather station was installed, it can be seen that the outdoor temperature measurements taken from the thermocouple mounted on a wooden stick can be significantly higher than the outdoor temperature measurements from the rooftop weather station. At higher solar irradiance, the difference between the stick and weather station measurements become more pronounced.

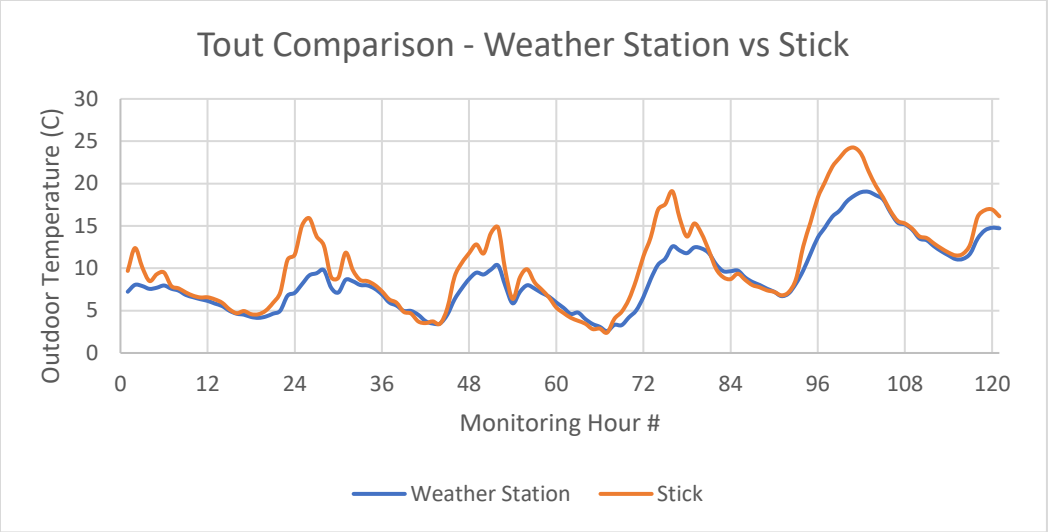

Figure 9.8.1: Comparison of outdoor temperature measured by the WS800 weather station and the improvised thermocouple on a wooden stick from April 24 11:00 to April 29 11:00, 2023.

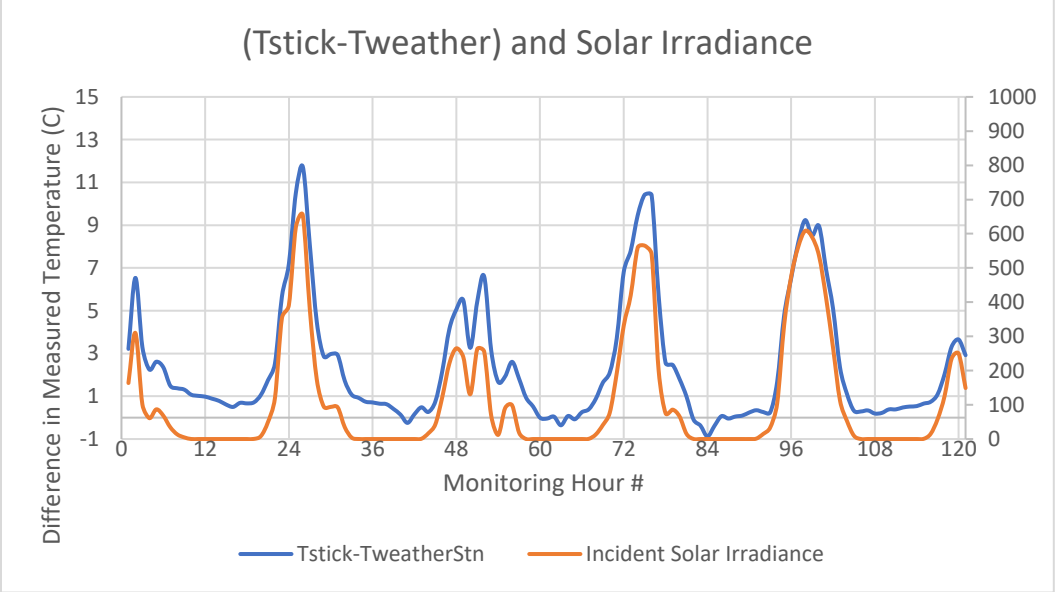

Figure 9.8.2: Comparison of the extra temperature difference measured by the stick thermocouple with the incident solar irradiance throughout April 24 to April 29, 2023.

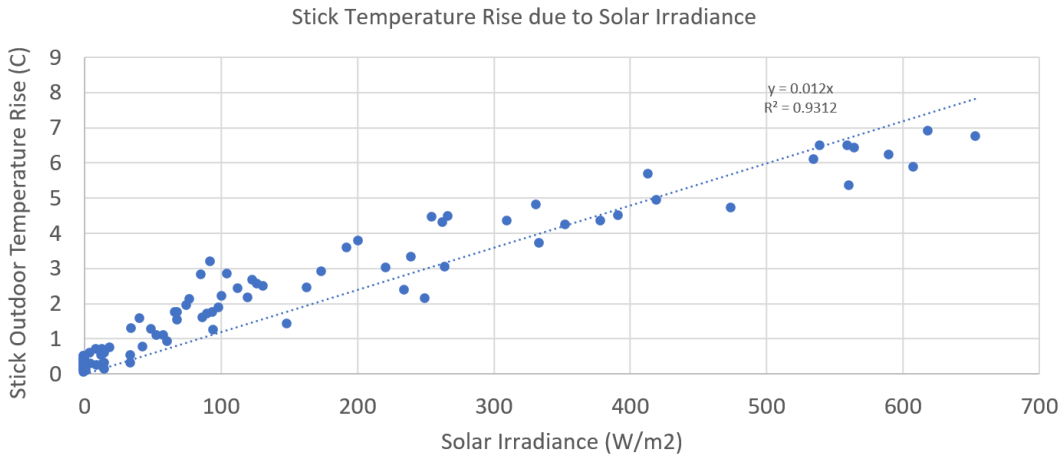

Figure 9.8.3: Correlation for extra stick outdoor thermocouple temperature when exposed to solar irradiance measured by the LI-200 pyranometer based on data from April 24 to April 29, 2023.

The increased temperature readings on the outdoor stick thermocouple can then be corrected using the equation:

$$T_{out*} = T_{stick} - 0.012 I_s \qquad (9.8.1)$$

Where T_{out*} is the estimated actual outdoor air temperature based on the correlation in °C, T_{stick} is the outdoor air temperature measured by the improvised stick thermocouple in °C, and I_s is the incident solar irradiance measured by the LI-200 pyranometer.

Knowing the temperature and the energy balance in Figure 4.1.3 can then allow the HRV outdoor air inlet temperature in the HRV-only scenario to be estimated from monitoring data of the BIPV/T+HRV scenario. Details are shown in the Appendix.

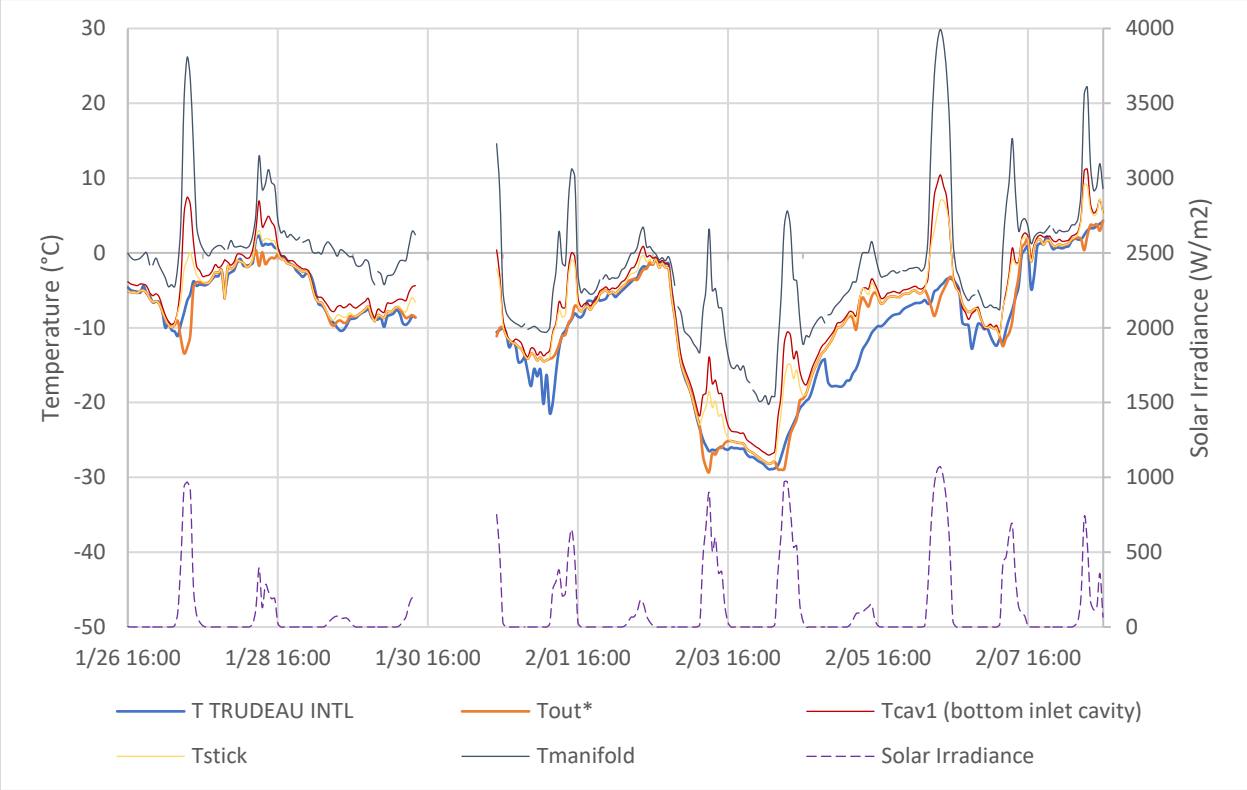

Figure 9.8.4: Comparison of estimated outdoor temperature and other measured temperature profiles over the HRV performance monitoring period from January 26 to February 8, 2023. Incident solar irradiance on the BIPV/T façade is included on the right axis for reference.

The T_{out*} has been determined based on the measured T_{stick} data using Equation (9.8.1) for the HRV performance monitoring period from January 26 to February 8, 2023. The hourly historical weather data collected from the Pierre Elliot Trudeau International Airport $T_{Trudeau\ INTL}$(Climate ID 702S006) published by the Government of Canada is used as a reference for comparison with the estimated outdoor temperature. Assuming that the local outdoor air temperature should not be significantly lower than the airport temperature, Figure 9.8.4 shows that the T_{out*} tends to overcompensate for the temperature increase due to solar irradiance in the presence of high incident solar irradiance (>600 W/m^2). The T_{out*} value can be up to 8.6°C lower than $T_{Trudeau\ INTL}$ when incident solar irradiance approaches 1000 W/m^2 (as seen on January 27, and to a lesser degree on February 3, February 4 and February 6). This is likely due to the error produced by extrapolating the Equation (9.8.1) correlation beyond its measured solar irradiance range where data only up to 660 W/m^2 have been recorded. It should be possible to improve this T_{out*} correlation by collecting more monitoring data and correcting the Equation (9.8.1) correlation for the data within this monitoring period in the future. Aside from the overcompensation during these high solar irradiance periods, the value of T_{out*} appear to be reasonably close to $T_{Trudeau\ INTL}$ (within about 0.7°C difference on average), which suggests that Equation (9.8.1) can reasonably estimate the outdoor temperature from T_{stick} during the rest of the January 26 to February 8 monitoring period.

Figure 9.8.4 also shows that the average manifold inlet temperature (average of T309, T310 and T311 from Figure 3.2.4) $T_{manifold}$ and bottom cavity inlet temperature T_{cav1} are both consistently higher than T_{stick}, T_{out*} and $T_{Trudeau\ INTL}$ even in the absence of solar irradiance. $T_{manifold}$ is about 5.3°C higher while T_{cav1} is about 1.7 °C higher than $T_{Trudeau\ INTL}$ on average. Since the air cavity temperature is expected to be lower than the ambient outdoor air temperature at night due to radiative losses to the sky, the data suggests that there is significant heat gain from sources not considered in ideal models, such as heat loss from the interior side of the curtain wall (average $T_{room} = 21°C$) into the air cavity from thermal bridging effects and air exfiltration, which is being captured and recovered by the BIPV/T cavity airflow.

Method for Comparison of BIPV/T+HRV vs. HRV-only

Three different methods for the field performance comparison were considered for this experiment. Their benefits and drawbacks are summarized below.

Method 1:

A detailed side-by-side comparison of these two cases, which would require simultaneous monitoring of two identical HRV experimental setups with one curtain wall section integrated with BIPV/T while the other curtain wall section is installed without a PV cladding and is designed to let an HRV to intake outdoor air directly from an opening at the same height as the BIPV/T manifold. This method requires the most resources and experimental setup time.

Method 2:

A before-and-after comparison using only one BIPV/T+HRV integrated experimental setup, which would require monitoring of the experimental setup with the PV cladding removed for the HRV-only case at a range of outdoor boundary conditions and subsequently monitoring the same experimental setup with the PV cladding installed at the same range of outdoor boundary conditions. This method requires less resources and experimental setup time than Method 1 but is at risk of not being able to attain the same outdoor boundary conditions throughout the separate monitoring periods for each of the two cases.

Method 3:

A simplified comparison using only one BIPV/T+HRV integrated experimental setup but analyzing the monitoring data from daytime and nighttime separately. This method assumes that the main difference between a test case of a BIPV/T curtain wall integrated with an HRV and an HRV-only reference condition of where an HRV operates without a BIPV/T system is that there would be no effect from the presence of a PV cladding. In general, the two cases (BIPV/T+HRV vs. HRV-only) should be approximately equal in the absence of solar irradiance (no absorption of solar energy and conversion into heat by the PV cladding) with the exception of some amount of radiative heat loss to the sky at night resulting in the BIPV/T case performing slightly worse than HRV-only at night (due to the PV cladding and air cavity being slightly colder than ambient outdoor temperature). However, the nighttime radiative loss is not a significant concern for this

analysis due to expectation that a practical design of a BIPV/T system when constructed will include dampers which can switch the HRV from intaking outdoor air from the BIPV/T air cavity to directly intaking outdoor air from the ambient outdoor air instead. The effect the nighttime radiative loss may have on the system may only make the analyzed improvement due to BIPV/T integration slightly underestimated (more conservative). This method is considered to require less experimental setup time than Method 2 and was chosen as the method of comparison for this analysis.

9.9. HRV Integration: Additional correlations examined

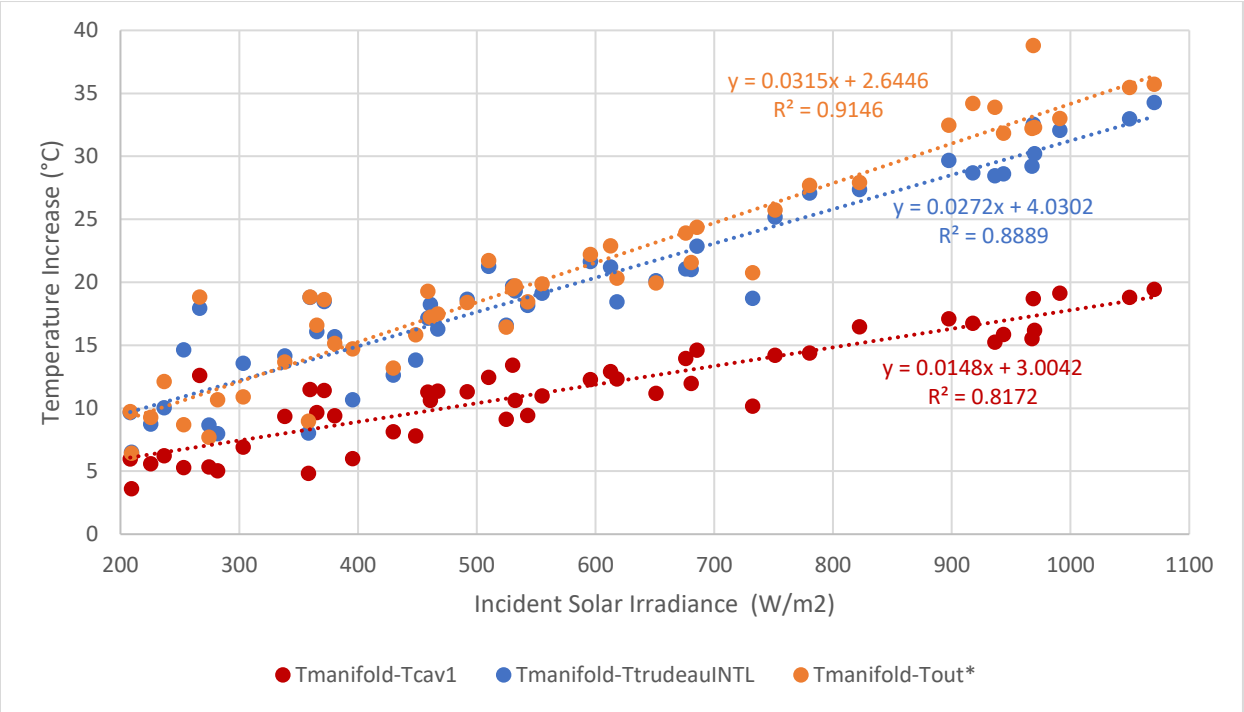

Figure 9.9.1: Comparison of linear regression correlations for manifold inlet $T_{manifold}$ temperature increase based on different points of reference, for ($T_{manifold} - T_{Trudeau\ INTL}$), ($T_{manifold} - T_{out*}$), and ($T_{manifold} - T_{cav1}$) respectively for the monitoring period from January 26 to February 8, 2023.

Due to the overcompensation issue noted in Appendix 9.7, using T_{out*} to determine the temperature increase from BIPV/T integration can lead to overestimation of the temperature increase. Conversely, using the bottom cavity inlet temperature T_{cav1} (T211 from Figure 3.2.4), where the thermocouple is affected by the heat absorption of solar irradiance from the PV module and forced convection within the air cavity, can measure temperature values even higher than those of T_{stick}. Therefore, the most conservative estimate of temperature increase due to BIPV/T integration is between the value of those determined from the difference between the average manifold inlet temperature (average of T309, T310 and T311 from Figure 3.2.4) $T_{manifold}$ and bottom cavity inlet temperature T_{cav1}, and the least conservative estimate of the temperature increase are those determined from the difference between $T_{manifold}$ and T_{out*}. The true value is expected to fall somewhere between these two estimates. The estimate of temperature increase assuming that the local outdoor temperature at the FBL is equal to $T_{Trudeau\ INTL}$ has also been included in Figure 4.3.2Figure 9.9.1 reference.

These linear regression correlations follow the form:

$$T_{manifold} = k_1 I_s + k_2 + T_{out,ref} \qquad (9.9.1)$$

Where $T_{out,ref}$ is the reference outdoor temperature in °C such as $T_{Trudeau\ INTL}$, $T_{out,estimated}$ or T_{cav1} , I_s is the incident solar irradiance in W/m^2, and k_1 and k_2 are constants obtained from the linear regression using the measured field monitoring data.

There is an offset (y-intercept) 2.6°C to 4.0°C temperature increase for the correlations in Figure 9.9.1 at incident solar irradiance = $0W/m^2$ which may be due to the non-ideal thermal losses from the interior of Test Cell 2 to the air cavity through conduction and air leakage.

The average solar irradiance during the hours around noon (10:00 to 14:00) throughout the same period is 430 W/m^2, which corresponds to an average of temperature increase of 9.4°C, 16.2°C, and 15.7°C using the T_{cav1} , T_{out*}, and $T_{Trudeau\ INTL}$ correlations respectively.

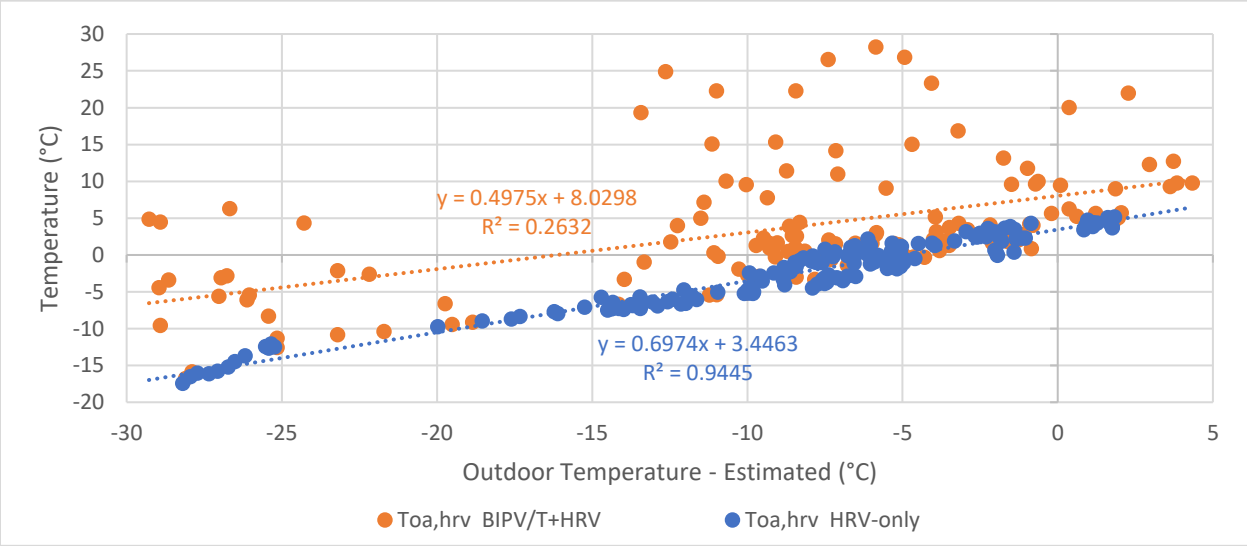

Figure 9.9.2: Comparison of HRV Outdoor Air inlet temperature $T_{OA,HRV}$ between the integrated BIPV/T+HRV and HRV-only test cases during the monitoring period from January 26 to February 8, 2023

As discussed in Chapter 4.3, the performance of the HRV in terms of sensible recovery efficiency (SRE) and defrost time depend significantly on the temperature of the airflow entering the HRV's inlet air ($T_{IA,HRV}$). The data recorded for the experimental setup during daytime (when incident solar irradiance >0 W/m^2, from 6:00 to 18:00) was separated from the data recorded during nighttime. The daytime data are considered to reflect the operating conditions of the integrated BIPV/T+HRV case, while the nighttime data are considered to reflect the HRV-only case. The data were recorded at 1-minute intervals and averaged on an hourly basis for this analysis.

Figure 9.9.2 shows the measured $T_{IA,HRV}$ for each case. The linear regression shows that $T_{IA,HRV}$ can be greater in the integrated BIPV/T+HRV case by about 3.6°C to 10.5°C compared to the HRV-only case. However, while there is a good linear correlation for the HRV-only case ($R^2 = 0.9445$), the coefficient of determination for the BIPV/T+HRV case is poor ($R^2 = 0.2632$). This is because the outdoor ambient temperature did not correlate well with the incident solar irradiance during the monitoring period from January 26 to February 8, 2023. Figure 9.8.4 shows that there

can be days where the outdoor temperature is as low as -25°C while the peak incident solar irradiance is at around 1000 W/m^2, while on warmer days of -5°C the peak incident irradiance is below 200 W/m^2. The value of $T_{OA,HRV}$ has a strong correlation with the incident solar irradiance because it depends mostly on the average BIPV/T manifold inlet temperature $T_{manifold}$, and as shown below, $T_{manifold}$ in the BIPV/T+HRV case increases depending on the incident solar irradiance on the PV cladding.

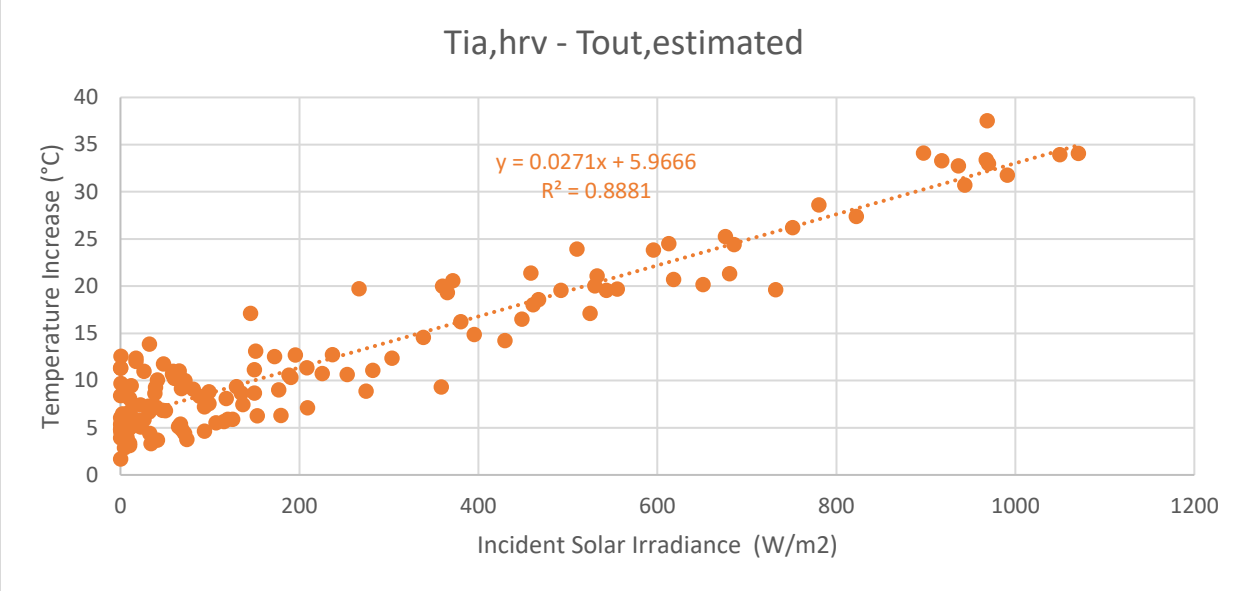

Figure 9.9.3: Correlation of temperature increase from T_{out*} to $T_{IA,HRV}$ depending on incident solar irradiance during the monitoring period from January 26 to February 8, 2023.

However, to minimize the propagation of errors from combining multiple regression correlations, linear regression can be performed directly between the $T_{IA,HRV}$ and the outdoor reference temperature such as T_{out*} as shown in the Figure 9.9.3.

The results based on the three different outdoor reference temperatures are summarized in Table 9.9.1.

Table 9.9.1: Summary of BIPV/T+HRV regression correlations and $F_{BIPV/T}$

$T_{out,ref}$ correlation	**k_1**	**k_2**	**R^2** Equation (9.9.1	**k_3**	**k_4**	**R^2** Equation (4.3.2	**SRE** (%)	**$F_{BIPV/T}$** ($°C/\frac{W}{m^2}$)
$T_{Trudeau\ INTL}$	0.0272	4.0302	0.8239	0.9058	1.4901	0.9986	83.91	0.003964
$T_{out,*}$	0.0315	2.6446	0.8975	0.9058	1.4901	0.9986	83.91	0.004591
T_{cav1}	0.0148	3.0042	0.7329	0.9058	1.4901	0.9986	83.91	0.002157

9.10. HRV Integration: Derivation of $F_{BIPV/T}$

From the sensible recovery efficiency equation:

$$SRE = \frac{T_{SA,HRV} - T_{IA,HRV}}{T_{room,HRV} - T_{IA,HRV}} \quad (4.3.3)$$

$$T_{SA,HRV} = (1 - SRE)T_{IA,HRV} + SRE(T_{room}) \quad (9.10.1)$$

$$T_{IA,HRV} = k_3 T_{manifold} + k_4 \quad (9.10.2)$$

$$T_{manifold} = k_1 I_s + k_2 + T_{out} \quad (9.10.3)$$

The temperature increase from BIPV/T integration is the difference between the $T_{SA,HRV}$ for the HRV+BIPV/T case ($T_{SA,HRV}$ affected by incident solar irradiance) and the HRV-only case ($T_{SA,HRV}$ without effect from solar irradiance).

$$\Delta T_{SA,HRV} = T_{SA,HRV_{(\mathbf{HRV+BIPV/T}\ I_s>0)}} - T_{SA,HRV_{(\mathbf{HRV}\ I_s=0)}} \quad (9.10.4)$$

Substitute the above equations and simplify:

$$\Delta T_{SA,HRV} = (1 - SRE)(T_{\mathbf{IA},HRV_{(\mathbf{HRV+BIPV/T}\ I_s>\mathbf{0})}} + SRE(T_{room}) - (1 - SRE)T_{\mathbf{IA},HRV_{(\mathbf{HRV}\ I_s=\mathbf{0})}} - SRE(T_{room}) \quad (9.10.5)$$

$$\Delta T_{SA,HRV} = (1 - SRE)(T_{\mathbf{IA},HRV_{(\mathbf{HRV+BIPV/T}\ I_s>\mathbf{0})}} - T_{\mathbf{IA},HRV_{(\mathbf{HRV}\ I_s=\mathbf{0})}}) \quad (9.10.6)$$

$$\Delta T_{SA,HRV} = (1 - SRE)(k_3 T_{manifold_{(\mathbf{HRV+BIPV/T}\ I_s>\mathbf{0})}} + k_4 - k_3 T_{manifold_{(\mathbf{HRV+BIPV/T}\ I_s>0)}} - k_4 \quad (9.10.7)$$

$$\Delta T_{SA,HRV} = (1 - SRE)(k_3 T_{manifold_{(\mathbf{HRV+BIPV/T}\ I_s>\mathbf{0})}} - k_3 T_{manifold_{(\mathbf{HRV+BIPV/T}\ I_s>0)}}) \quad (9.10.8)$$

$$\Delta T_{SA,HRV} = (1 - SRE)(k_3(k_1 I_s + k_2 + T_{out,ref}) - k_3(k_2 + T_{out,ref})) \quad (9.10.9)$$

$$\Delta T_{SA,HRV} = (1 - SRE)(k_3 k_1 I_s + k_3(k_2 + T_{out,ref}) - k_3(k_2 + T_{out,ref})) \quad (9.10.10)$$

$$\Delta T_{SA,HRV} = (1 - SRE)k_3 k_1 I_s \quad (9.10.11)$$

9.11. BIPV Hygrothermal Modeling: Effect of electrical operating state

Aside from wind-driven rain, moisture transfer occurs between layers of the wall assembly through vapour diffusion. Moisture in the form of water vapour would move from a layer at high vapour pressure to a layer at low vapour pressure. Figure 9.11.1 shows the difference in vapour pressure between the air cavity and the OSB layer throughout year 3 of the simulation without any cavity ventilation, with positive values indicating the driving pressure to transfer moisture towards the interior OSB layer while negative values indicating the direction towards the exterior. Without cavity ventilation, the moisture stored within the wall assembly (including rain deposit) in both BIPV options are strongly driven to migrate inwards and become trapped on the OSB layer rather than to dry towards the exterior. However, the MPP-state option consistently experiences slightly less pressure differential, with the most significant difference appearing in the winter months.

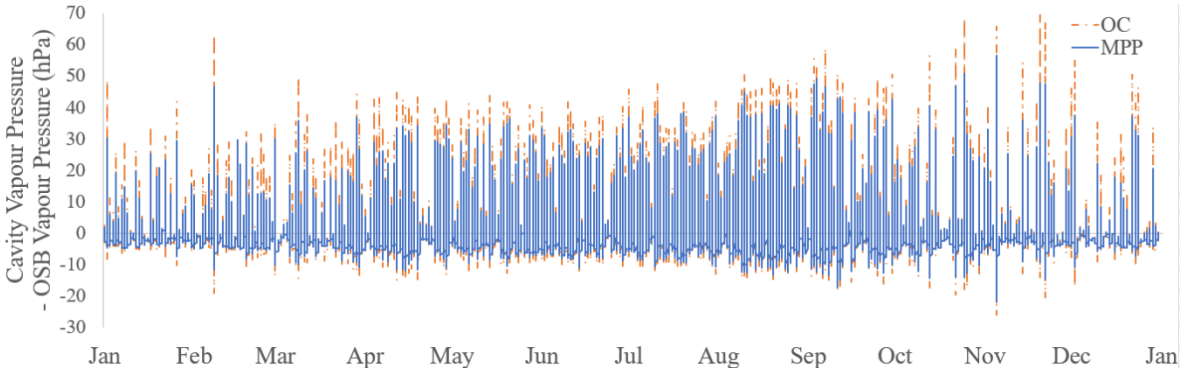

Figure 9.11.1. Comparison between OC and MPP states on the vapour pressure differential between the air cavity and the OSB layer with no cavity ventilation (0 ACH).

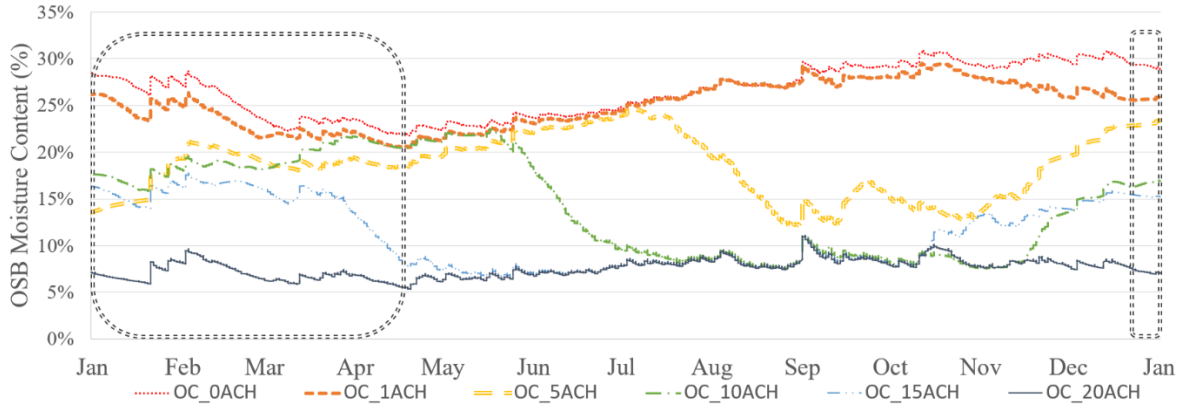

Figure 9.11.2. OSB moisture content profile in the BIPV-OC assembly at various cavity ventilation rates throughout year 3 of the hygrothermal simulation.

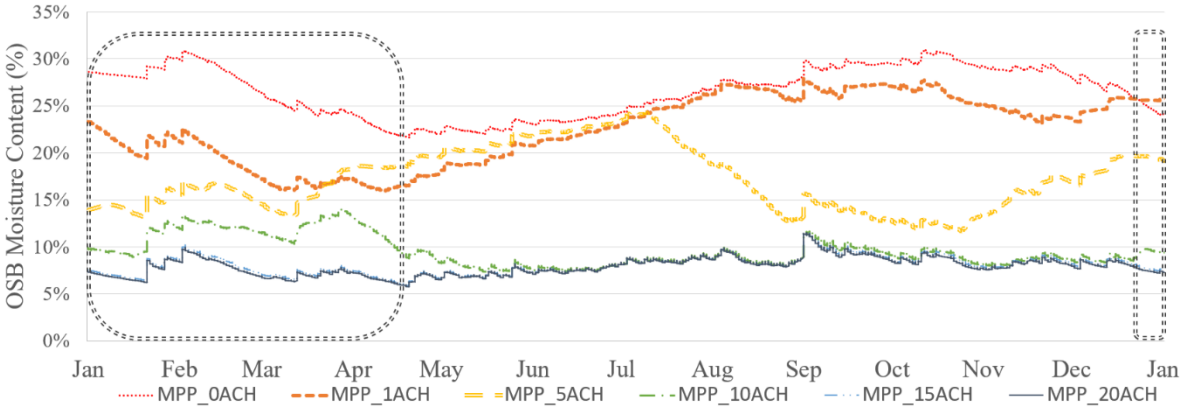

Figure 9.11.3. OSB moisture content profile in the BIPV-MPP assembly at various cavity ventilation rates throughout year 3 of the hygrothermal simulation.

Figure 9.11.2 and Figure 9.11.3 compare the annual MC profile at the OSB layer of each BIPV operating state at various cavity ventilation rates. As the ventilation increases, the MC during early fall and the summer begin to lower significantly. However, as noted by the grey windows, the moisture accumulation during months between January and April needed the highest cavity ventilation rate to be reduced to an acceptable level in both BIPV states. It appears that the MPP-state cases only need 15ACH of cavity ventilation to reduce OSB moisture content to below 10%, while the OC-state cases need 20ACH. The reason for this may be explained in terms of solar-driven moisture. The solar irradiance the wall assembly is exposed to is less intense and with shorter duration in the summer cooling season compared to the heating season. Solar-driven moisture accumulation occurs when the exterior layers of the wall assembly are heated to high temperatures by solar irradiation while the interior layers remain at a lower temperature. This directly affects the resultant vapour pressure differential, causing vapour diffusion in the direction from a layer with higher temperature to one with a lower temperature (Maref et al., 2007). Due to lower solar altitude, the solar-driven moisture effect can occur in winter for these vertical BIPV walls with high solar absorption.

As shown in Figure 9.11.4, the temperature difference between the exterior layer and the OSB layer can reach higher than 40°C. The lower cladding temperature during the solar exposure hours in the MPP state allows it to have less overall moisture accumulation in the OSB throughout the simulated years. Having less severe solar-driven moisture accumulation is likely what allows the wall assembly in its MPP-state to reduce its OSB moisture content to within the acceptable range with only 15 ACH of cavity ventilation as opposed to 20 ACH of cavity ventilation for the OC state.

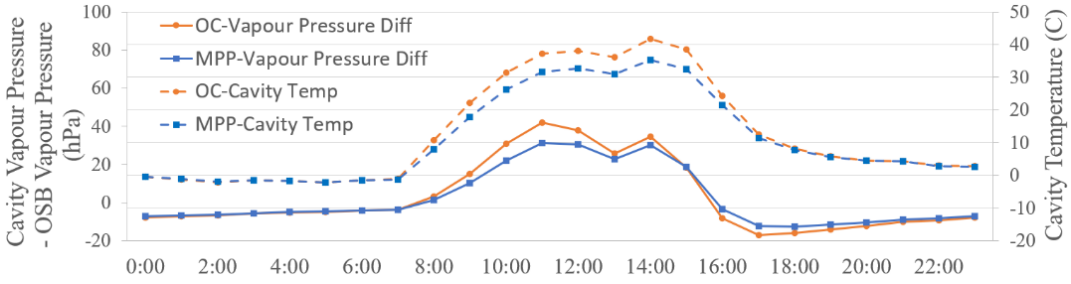

Figure 9.11.4. Comparison of vapour pressure differential and cavity temperature of BIPV states on October 26th.

The effect of solar-driven moisture accumulation is much more significant in the BIPV options than those seen in the fiber cement option because the fiber cement cladding layer has much higher vapour permeability compared to the BIPV cases. This helps moisture accumulated due to rain leakage dry toward the exterior in the fiber cement cases whereas in the BIPV cases the accumulated moisture remains trapped between the cladding and the interior layers. The higher vapour pressure differential due to solar irradiance then drives the trapped moisture inwards toward the OSB layer, leading to the initially worse hygrothermal performance of the BIPV cases compared to the fiber cement cases at low cavity ventilation rates.

9.12. SHGC Characterization: Spectral response and electrical conversion

The modification of $\rho(\lambda,\theta)$ to $\rho_{eff}(\lambda,\theta)$ in Equation (6.1.5) can be done with 3 different approaches:

Approach 1:

$$\rho_{eff}(\lambda,\theta) = \rho(\lambda,\theta) + C_1 \quad ,[300 \le \lambda \le 2500] \tag{9.12.1}$$

$$\frac{\int_{300}^{2500} C_1 E_s(\lambda) d\lambda}{\int_{300}^{2500} E_s(\lambda) d\lambda} = \eta_{el} \tag{9.12.2}$$

Approach 2:

$$\rho_{eff}(\lambda,\theta) = \rho(\lambda,\theta) + C_2 \quad ,[400 \le \lambda \le 1100] \tag{9.12.3}$$

$$\frac{\int_{400}^{1100} C_2 E_s(\lambda) d\lambda}{\int_{300}^{2500} E_s(\lambda) d\lambda} = \eta_{el} \tag{9.12.4}$$

Approach 3:

$$\rho_{eff}(\lambda,\theta) = \rho(\lambda,\theta) + C_3 \quad ,[300 \le \lambda \le 2500] \tag{9.12.5}$$

$$\frac{\int_{300}^{2500} C_3 r_s(\lambda) E_s(\lambda) d\lambda}{\int_{300}^{2500} E_s(\lambda) d\lambda} = \eta_{el} \tag{9.12.6}$$

Where C_1, C_2, C_3 are solved iteratively to satisfy the equations when the electrical conversion efficiency η_{el} and the spectral response r_s of the BIPV or STPV is known.

48 variations of STPV configurations were modeled using each of the approaches (using C_1, C_2 or C_3) to determine the SHGC in each case. The comparison of the results show that all three approaches shown are nearly identical in terms of SHGC, with negligible differences in solar spectrum optical properties, but more significant differences in visual spectrum optical properties.

Determining the solar optical properties and SHGC using the three approaches showed that the differences between these methods are negligible at best when only the solar optical and energy behavior of the glazing system are of interest. Out of the results calculated for the 48 variations of boundary conditions (ranging from $h_{out} = 12\ to\ 25\ W/m^2K$, $h_{in} = 6.6\ to\ 8.1\ W/m^2K$, and electrical state= OC or MPP) and for different STPV glazing configurations (ranging from PV cell area coverage = 46.1% to 92.2%, and configuration= STPV panel alone or STPV panel + 25.4 mm air + low-e pane 1 or STPV panel + 12 mm Argon + low-e pane 2), the results for SHGC, τ, ρ_{eff} and α were identical between Approach 3 and Approach 1. The difference between Approach 2 and Approach 1 is insignificant, with the SHGC being lesser in Approach 2 by 0.000461 to 0.000922 in 2 out of the 48 variations, ρ_{eff} being greater in Approach 2 by 0.000692 (0.19%) to 0.00138 (0.58%) and α being lesser in Approach 2 by 0.000645 (0.13%) to 0.001383 (0.20%). All of these differences between Approach 2 and Approach 1 only appear when calculating for the MPP state configurations.

Since Approach 1 (using C_1 from Equation (9.12.1) and (9.12.2) is the simplest to calculate since the equation effectively simplifies to Equation (6.1.5) and results in the same SHGC, this was the method adopted for further analysis to determine the theoretical SHGC of various STPV configurations.

9.13. SHGC Characterization: Area averaging

For STPV glazing studied in this exercise, the overall measured optical properties such as the spectrally dependent surface 1 front reflectance $\rho_{f,1}(\lambda_i)$ and surface 2 front reflectance $\rho_{f,2}(\lambda_i)$ are unknown, due to the alternating opaque PV sections and transparent glass sections being on the same pane. To determine the overall optical properties of the STPV, the optical properties of the opaque and transparent sections must be averaged using the following area weighted method:

$$Coverage = A_{cells}/A_{total} \quad (9.13.1)$$

For this exercise, two types of STPV were investigated – 72-cell panels and 36-cell panels.

Using Equation (9.13.1), $Coverage = 0.922$ for 72-cell panels and $Coverage = 0.461$ for 36-cell panels respectively.

The spectrally averaged optical properties should then be calculated from the process defined in this section for special cases of cell coverage – "all cell" where $Coverage = 1$ and "0 cell" where $Coverage = 0$. The spectrally averaged optical properties must be calculated from measured spectral data for these two special cases for the outer pane (pane 1) and measured spectral data of the inner pane (pane 2, clear glazing or low-e glazing for this exercise).

The area averaged optical properties of the STPV with the $coverage$ of interest can then be found using the following equations:

$$P_{avg,STPV} = coverage \times P_{avg,allcell} + (1 - coverage) \times P_{avg,0cell} \quad (9.13.2)$$

Where $P_{avg,STPV}$ is any spectrally averaged optical property as well as SHGC of the STPV coverage of interest. For example, to calculate the spectrally averaged transmittance and the SHGC of the 72-cell panel in this exercise:

$$\tau_{1,72cell} = 0.922 \times \tau_{1,allcell} + (1 - 0.922) \times \tau_{1,0cell} \quad (9.13.3)$$

$$SHGC_{72cell} = 0.922 \times SHGC_{allcell} + (1 - 0.922) \times SHGC_{0cell} \quad (9.13.4)$$

9.14. SHGC Characterization: Thermocouple correction for solar radiation

Although the thermocouples used for measurements in this experiment have been wrapped in reflective foil tape, there still appears to be a significant difference in temperature measurements when comparing the temperature readings of a sensor that's exposed to direct solar radiation to that of the same sensor when shaded.

A comparison of this was done using the thermocouple that was mounted on the wall near the test cell door. On June 21st at approximately 14:00, the thermocouple was moved from the wall to the centre of the room and positioned at a height close to the centre of glass height of the IGU. Temperature measurements by the thermocouple were recorded at 10s intervals for several minutes after the initial temperature measurement was stabilized. The room was left vacant during the measurement as well. After this measurement, the thermocouple was repositioned using masking tape onto the wooden stand where the SMP22 and SGR4 were mounted at the height near the centre of glass. This position exposes the thermocouple to the direct solar radiation that has been transmitted through the IGU. The 10s interval measurements were taken the same way as the previous measurement for several minutes. The measurements over the minutes are then averaged to get the comparison.

Table 9.14.1: Effect of solar radiation exposure on thermocouple measurement

Scenario	Solar radiation on thermocouple I_s (W/m^2)	Thermocouple measurement T (°C)
Thermocouple Shaded	0	19.7
Thermocouple Exposed	544	22.5

There is a temperature difference of about $2.7°C$. The increase in temperature due to solar radiation may follow a relationship similar to the concept of sol-air temperature.

(Trombe and Moreau, 1995) shows the difference between a type-K thermocouple's measured values and the real surface temperature values measured on an exterior semi-transparent material can differ by up to $0.6°C$ at exterior ambient temperatures around $10°C$, incident solar radiation of $770\frac{W}{m^2}$, and wind speed of $< 1.6m/s$. The derived correction equations in the study only apply to a type-K thermocouple on the exterior surface and a different energy balance including the infrared radiation exchange would be needed for correcting the measurements from an interior thermocouple. (Huwald et al., 2009) shows that the difference in measured temperature compared to the real temperature increases as incident solar radiation increases and wind speed decreases, and that even for the same instrument, the same correction factor cannot be applied for different locations unless ground reflectance is considered. (Abdel-Ghany et al., 2006) used type-T thermocouples to measure the surface temperature of a greenhouse cover. The correction factor was determined using regression from the data collected under different solar radiation conditions. The results showed that the relationship between the correction factor and solar radiation becomes more non-linear as solar radiation increases, and that the thermocouple also measures a lower value than the real surface temperature at nighttime due to radiative losses to the sky.

The current experiment is mainly concerned with the measurement of SHGC, which cannot be defined in nighttime conditions, so accounting for the radiative losses to the night sky would not

affect the final analysis of the presented results. From the literature review, the main factors relevant to the difference in measured vs. real surface temperature in this experiment are the absorption of solar radiation, the convective and radiative heat transfer between the thermocouple and the interior ambient air. Performing a detailed analysis of these factors and their influence on thermocouple measurement is outside the scope of this experiment, but a simplified assumption for now can be that the correction factor is some function of $\alpha, h_{c,in,T_{couple}}$ and $h_{r,in,T_{couple}}$, such that:

$$T_{(I_s>0)} - T_{(I_s=0)} = f\left(\alpha, h_{c,in,T_{couple}}, h_{r,in,T_{couple}}\right) I_s \quad (9.14.1)$$

$$T_{(I_s>0)} - T_{(I_s=0)} = c_s I_s \quad (9.14.2)$$

Where I_s is the incident shortwave solar radiation on the thermocouple, $T_{(I_s>0)}$ is the surface temperature measured by the thermocouple while exposed to solar radiation, $T_{(I_s=0)}$ is the real temperature of the surface being measured, and c_s is the thermocouple's correction factor based on solar radiation. Given long-term monitoring data with two thermocouples measuring $T_{(I_s>0)}$ and $T_{(I_s=0)}$, c_s can be determined through regression using the same method as (Abdel-Ghany et al., 2006).

For a quick estimate, the simple test performed on June 21st only measures a single condition within a short duration. Assuming the relationship is mostly linear for this condition, the temperature difference can be estimated by assuming c_s as a constant. Based on the measured values in Table 9.14.1, the $c_s = 0.01207$.

This is only a basic estimate of the correction factor, since both the convective and radiative heat transfer coefficients $h_{c,in,T_{couple}}$ and $h_{r,in,T_{couple}}$ are not constant and are dependent on the temperature difference between the thermocouple and the test cell room air. However, since the temperatures rise and fall on both the glass and the thermocouple mostly depending on the presence and absence of solar radiation at this time (lower wind speeds and outdoor ambient temperature close to test cell temperature $\approx 20°C$), the c_s value estimate may be slightly accounting for this temperature dependence.

However, this cannot be confirmed unless further long-term monitoring data of a scenario where a thermocouple exposed to solar irradiance (measuring $T_{(I_s>0)}$) and a thermocouple in close proximity but completely shaded (measuring $T_{(I_s=0)}$) are compared side-by-side. The c_s may then be obtained as an I_s dependent equation from regression and compared against a theoretical derived value from an energy balance similar to (Trombe and Moreau, 1995).

The "correct" temperature value that the thermocouple should be measuring without the influence of direct solar radiation can be estimated in reverse assuming $c_s = 0.01207$ for the thermocouples in Test Cell 5.

$$T_{(I_s>0)} - c_s I_s = T_{(I_s=0)} \quad (9.14.3)$$

To examine the potential impact of the correction in CoG temperature measurement, the following graphs show the comparison of results between corrected and uncorrected thermocouple temperatures.

Throughout 6 days from June 14th to June 20th, the difference between the corrected and uncorrected temperatures for the thermocouple at the centre of glass is 3.5℃ at maximum. In terms of infrared radiation gain from surface 4, the difference between the radiation values which were calculated based on the centre of glass temperature is $18W/m^2$ (4.73%) about at maximum. In terms of convective heat transfer, there is also a slight difference not only due to the lower centre of glass temperature value when corrected, but also due to $h_{c,in}$ being affected by the temperature difference as well. The maximum difference between corrected and uncorrected convective heat gains is $13.86W/m^2$ (Corrected $Q_{c,in} = 16.43W/m^2$, uncorrected $Q_{c,in} = 30.29W/m^2$, an 84% difference).

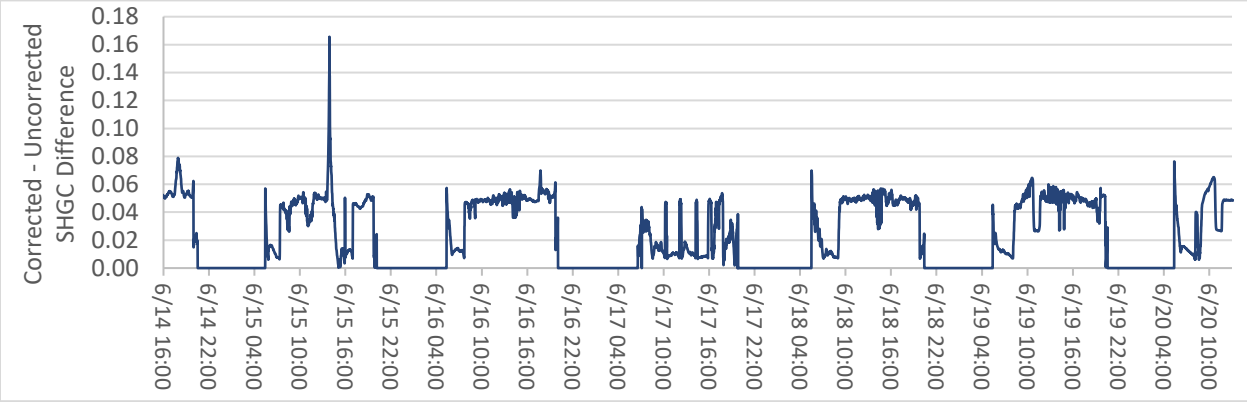

Figure 9.14.1: Comparison of corrected and uncorrected SHGC values over the monitoring period from June 14 16:00 to June 20 11:00, 2023

Figure 9.14.1 shows the final calculated SHGC values over the course of the monitored period. These differences result in a maximum difference in the final calculated SHGC of about 0.160 with a typical difference of 0.050 in sunny conditions. This is significant as it can lead to a consistent overestimate of 10% considering a typical SHGC of 0.500 in the hours around noon.

9.15. SHGC Characterization: Determining angular dependent SHGC in WINDOW

WINDOW 7.7 was used to determine the expected theoretical SHGC for the IGU tested in the experiment. While the outputs in the program are made with normal angle of incidence ($\theta = 0°$) as the default, using it to determine the SHGC at a different angle of incidence is not as straight forward. The only input which can directly influence the angle of incidence is the "Tilt" input.

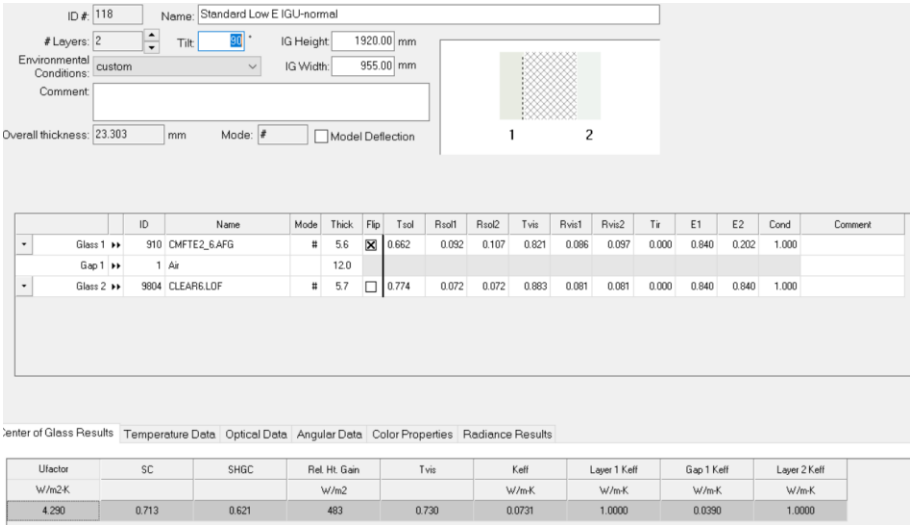

Figure 9.15.1: Tilt input adjustment in WINDOW 7.7 highlighted in blue

However, this only modifies the tilt angle β. In theory, by assuming all other parameters being equal (solar altitude $\alpha = 0$, solar azimuth $\phi = 0$, surface azimuth $\psi = 0$), one can determine a tilt angle β which would result in a desired equivalent incident angle θ by using the relationship:

$$cos\theta = cos\alpha \cdot cos|\phi - \psi| \cdot sin\beta + sin\alpha \cdot cos\beta \qquad (9.15.1)$$

By adjusting β between 90 to 180 degrees, the incident angle would be modified between 0 to 90 degrees as needed. However, the resulting SHGC values only decrease negligibly when altering β to achieve θ between 0 to 89 degrees, then increases much more significantly at $\theta = 90$ degrees. However, the U-value output is then reduced significantly, from 4.489 W/m^2K at $\theta = 89$ degrees to 3.607 W/m^2K at $\theta = 90$ degrees.

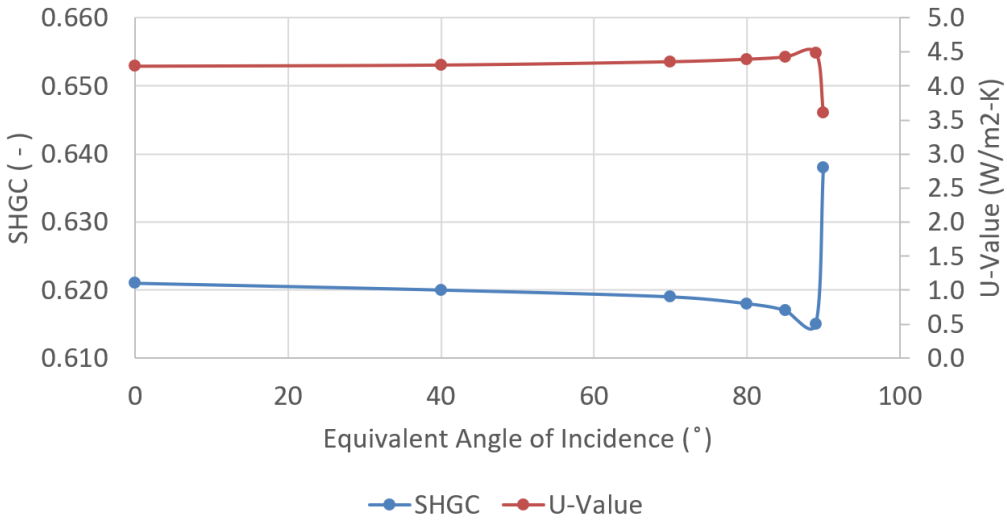

Figure 9.15.2: Calculation results from WINDOW 7.7 by varying tilt angle β to adjust θ

These outputs from WINDOW are likely from 2 main factors in the programming. First, there are different correlations used to calculate the heat transfer coefficients $h_{c,in}, h_{c,cav}, h_{c,out}$ depending on the tilt angle, and there is a significant difference in the correlation used between a slightly tilted surface compared to a fully horizontal surface ($\beta = 180°, \theta = 90°$). Second, simply adjusting the tilt angle does not modify any of the angular dependent solar optical properties, so the transmittance τ_s, reflectance ρ_s, and absorptance α_s all remain in their default values which were evaluated at $\theta = 0$.

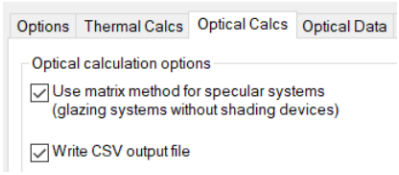

Figure 9.15.3: WINDOW 7.7 output preference

Enabling the matrix method and writing the CSV output file in the preferences allows some angular dependent solar optical properties to be viewed using the W6MatrixReader, but the angular dependent SHGC values are not shown as outputs there. However, it is possible to obtain the hourly outputs for the direct and diffuse solar radiation incident on the glazing, as well as the amount of transmitted solar radiation.

Table 9.15.1: Transmitted solar radiation from WINDOW

Transmitted Solar Radiation							**W/m2**
Hour	**DEC**	**JAN-NOV**	**FEB-OCT**	**MAR-SEP**	**APR-AUG**	**MAY-JUL**	**JUNE**
0	12	1	2	3	4	5	6
0	0	0	0	0	0	0	0
1	0	0	0	0	0	0	0
2	0	0	0	0	0	0	0
3	0	0	0	0	0	0	0
4	0	0	0	0	0	0	0
5	0	0	0	0	0	5.0	14.2
6	0	0	0	0	19.0	38.8	46.5
7	0	0	12.7	82.2	57.3	63.5	70.0
8	16.2	126.3	280.4	257.5	173.6	120.0	103.7
9	384.9	449.4	498.3	442.4	315.9	229.2	196.9
10	606.9	643.2	656.5	581.1	443.5	333.5	290.2
11	724.5	751.8	753.3	669.9	525.3	406.2	356.3
12	761.4	786.8	785.8	700.3	552.1	432.1	379.9
13	724.5	751.8	753.3	669.9	525.3	406.2	356.3
14	606.9	643.2	656.5	581.1	443.5	333.5	290.2
15	384.9	449.4	498.3	442.4	315.9	229.2	196.9
16	16.2	126.3	280.4	257.5	173.6	120.0	103.7
17	0	0	12.7	82.2	57.3	63.5	70.0
18	0	0	0	0	19.0	38.8	46.5
19	0	0	0	0	0	5.0	14.2
20	0	0	0	0	0	0	0
21	0	0	0	0	0	0	0
22	0	0	0	0	0	0	0
23	0	0	0	0	0	0	0
24	0	0	0	0	0	0	0

WINDOW determines that there is no direct solar radiation before 8:00 or after 17:00 in the month of June. However, diffuse solar radiation is accounted for starting at 5:00 and is still present until 20:00. This will be discussed further in the workaround methodology to determine angular SHGC.

Table 9.15.2: Direct Solar Radiation from WINDOW

Direct Solar Radiation							**W/m2**
Hour	**DEC**	**JAN-NOV**	**FEB-OCT**	**MAR-SEP**	**APR-AUG**	**MAY-JUL**	**JUNE**
0	12	1	2	3	4	5	6
0	0	0	0	0	0	0	0
1	0	0	0	0	0	0	0
2	0	0	0	0	0	0	0
3	0	0	0	0	0	0	0
4	0	0	0	0	0	0	0
5	0	0	0	0	0	0.0	0.0
6	0	0	0	0	0.0	0.0	0.0
7	0	0	15.0	92.5	25.8	0.0	0.0
8	17.2	133.8	294.8	270.6	163.3	74.7	37.4
9	397.8	462.2	505.6	436.0	300.8	195.9	151.3
10	619.1	652.2	655.7	565.8	412.4	295.3	245.0
11	736.4	758.8	747.4	648.1	484.4	359.7	306.0
12	774.1	793.8	778.3	676.2	509.2	382.0	327.0
13	736.4	758.8	747.4	648.1	484.4	359.7	306.0
14	619.1	652.2	655.7	565.8	412.4	295.3	245.0
15	397.8	462.2	505.6	436.0	300.8	195.9	151.3
16	17.2	133.8	294.8	270.6	163.3	74.7	37.4
17	0	0	15.0	92.5	25.8	0.0	0.0
18	0	0	0	0	0.0	0.0	0.0
19	0	0	0	0	0	0.0	0.0
20	0	0	0	0	0	0	0
21	0	0	0	0	0	0	0
22	0	0	0	0	0	0	0
23	0	0	0	0	0	0	0
24	0	0	0	0	0	0	0

Table 9.15.3: Diffuse Solar Radiation from WINDOW

Diffuse Solar Radiation							**W/m2**
Hour	**DEC**	**JAN-NOV**	**FEB-OCT**	**MAR-SEP**	**APR-AUG**	**MAY-JUL**	**JUNE**
0	12	1	2	3	4	5	6
0	0	0	0	0	0	0	0
1	0	0	0	0	0	0	0
2	0	0	0	0	0	0	0
3	0	0	0	0	0	0	0
4	0	0	0	0	0	0	0
5	0	0	0	0	0	6.1	17.5
6	0	0	0	0	23.4	47.9	57.4
7	0	0	1.9	30.4	58.5	78.3	86.5
8	1.1	10.1	34.9	58.9	83.7	101.8	109.2
9	27.5	36.9	57.5	79.7	103.1	120.1	127.0
10	45.0	53.6	73.1	94.6	117.3	133.5	140.1
11	54.9	63.3	82.4	103.8	126.0	141.7	148.1
12	58.2	66.5	85.6	106.8	128.9	144.5	150.8
13	54.9	63.3	82.4	103.8	126.0	141.7	148.1
14	45.0	53.6	73.1	94.6	117.3	133.5	140.1
15	27.5	36.9	57.5	79.7	103.1	120.1	127.0
16	1.1	10.1	34.9	58.9	83.7	101.8	109.2
17	0	0	1.9	30.4	58.5	78.3	86.5
18	0	0	0	0	23.4	47.9	57.4
19	0	0	0	0	0	6.1	17.5
20	0	0	0	0	0	0	0
21	0	0	0	0	0	0	0
22	0	0	0	0	0	0	0
23	0	0	0	0	0	0	0
24	0	0	0	0	0	0	0

These outputs allow for an estimate to be made for the angular dependent solar transmittance of the IGU in a typical day in June.

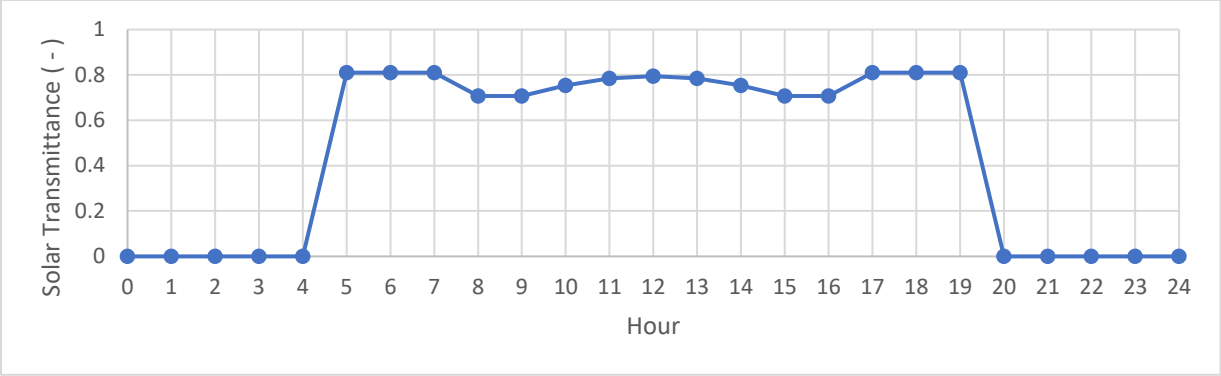

Figure 9.15.4: Solar Transmittance of IGU on a day in June estimated from WINDOW 7.7

The workaround methodology involves manually creating each pane with a specified set of solar optical properties based on its angular dependent properties.

	0	10	20	30	40	50	60	70	80	90	Hemis
Tsol	0.662	0.662	0.658	0.654	0.649	0.636	0.596	0.500	0.313	0.000	0.598
Abs1	0.246	0.247	0.250	0.251	0.250	0.247	0.242	0.224	0.161	0.000	0.237
Rfsol	0.092	0.091	0.092	0.095	0.101	0.117	0.162	0.276	0.526	1.000	0.154
Rbsol	0.107	0.106	0.108	0.110	0.116	0.132	0.176	0.288	0.534	1.000	0.169
Tvis	0.821	0.821	0.816	0.811	0.805	0.789	0.739	0.620	0.388	0.000	0.742
Rfvis	0.086	0.085	0.087	0.089	0.095	0.111	0.157	0.272	0.523	1.000	0.149
Rbvis	0.097	0.096	0.097	0.100	0.106	0.122	0.166	0.280	0.528	1.000	0.159

Figure 9.15.5: Angular properties of the outer pane (IGDB#910)

	0	10	20	30	40	50	60	70	80	90	Hemis
Tsol	0.774	0.774	0.771	0.765	0.754	0.732	0.685	0.579	0.349	0.000	0.693
Abs1	0.154	0.155	0.157	0.161	0.167	0.173	0.179	0.180	0.165	0.000	0.167
Rfsol	0.072	0.072	0.072	0.073	0.079	0.095	0.137	0.241	0.487	1.000	0.130
Rbsol	0.072	0.072	0.072	0.073	0.079	0.095	0.137	0.241	0.487	1.000	0.130
Tvis	0.883	0.882	0.881	0.878	0.871	0.851	0.803	0.687	0.427	0.000	0.804
Rfvis	0.081	0.081	0.082	0.083	0.090	0.107	0.153	0.268	0.528	1.000	0.145
Rbvis	0.081	0.081	0.082	0.083	0.090	0.107	0.153	0.268	0.528	1.000	0.145

Figure 9.15.6: Angular properties of the inner pane (IGDB#9804)

From these outputs, the properties for the specific angles of incidence, which will be used for comparison with the experimental measurements, are then found through linear interpolation.

Table 9.15.4: Angular properties of the outer pane (IGDB#910) from linear interpolation

Incident Angle	68	69	79
Tsol	0.519	0.510	0.332
Abs	0.228	0.226	0.167
Rfsol	0.253	0.265	0.501
Rbsol	0.266	0.277	0.509
Tvis	0.644	0.632	0.411
Rfvis	0.249	0.261	0.498
Rbvis	0.257	0.269	0.503

Table 9.15.5: Angular properties of the outer pane (IGDB#9804) from linear interpolation

Incident Angle	68	69	79
Tsol	0.600	0.590	0.372
Abs	0.180	0.180	0.167
Rfsol	0.220	0.231	0.462
Rbsol	0.220	0.231	0.462
Tvis	0.710	0.699	0.453
Rfvis	0.245	0.257	0.502
Rbvis	0.245	0.257	0.502

Figure 9.15.7:Manually creating new panes in the glass library for each specific angle of incidence.

For each angle of incidence to be investigated, new inner and outer glass panes are manually added to the Glass Library in WINDOW 7.7 by inputting the desired angular solar optical properties in placed of the “spectrally averaged” solar optical properties as shown in Figure 9.15.8.

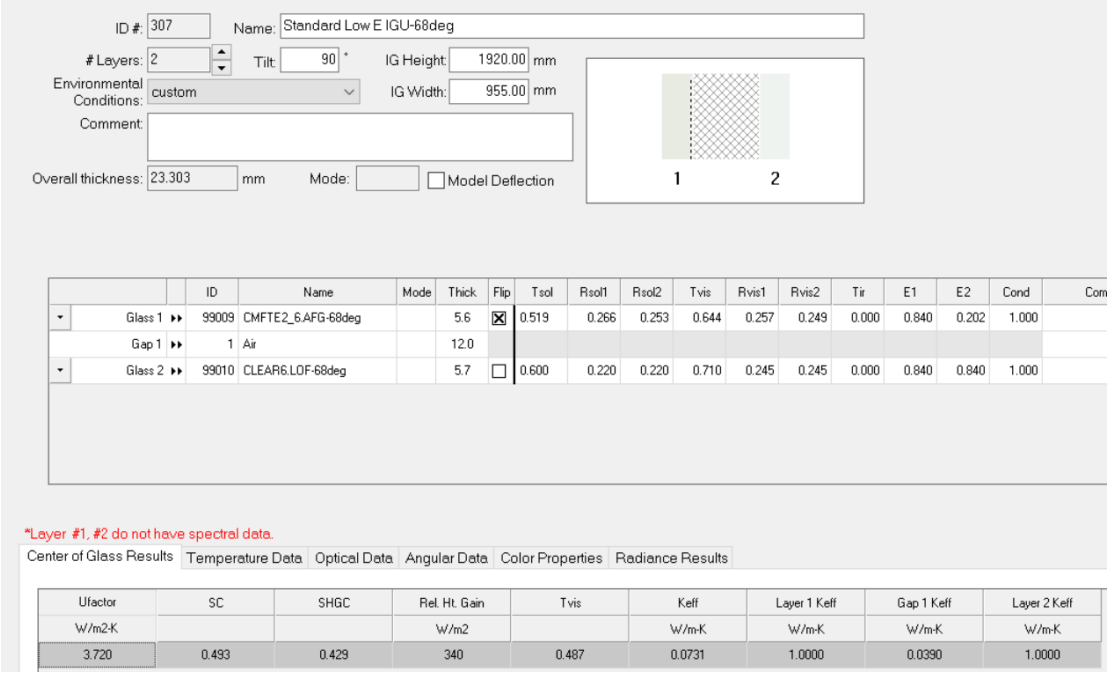

Figure 9.15.8: Creating an angle specific glazing system configuration for calculation

The manually created panes are then used for calculation as shown in Figure 9.15.9.

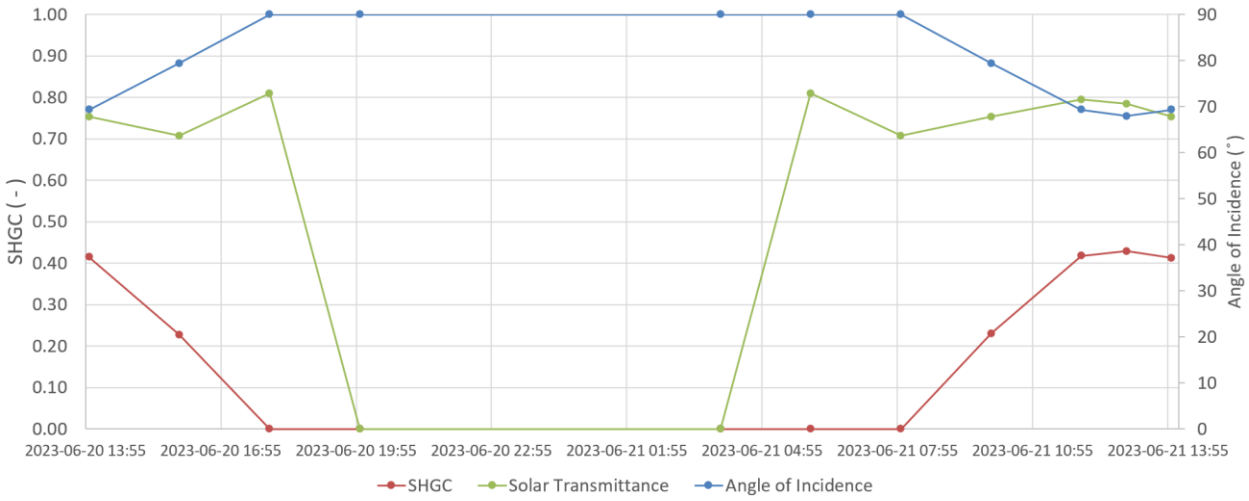

Figure 9.15.10: Calculated SHGC using experiment boundary conditions in WINDOW

Using this workaround method in WINDOW, the SHGC is calculated for different incident angles with boundary conditions matching those of the June 20th to June 21st experiment and summarized in Figure 9.15.10.The solar transmittance values are taken from Figure 9.15.11 for comparison. It

can be seen that the hours during sunrise and sunset, between 5:00 to 8:00 and 17:00 to 20:00, there is some transmitted solar radiation that has not been accounted for, hence the large discrepancy between the solar transmittance and the SHGC shown. In most cases, the SHGC should be greater than the solar transmittance. The missing SHGC values during periods of diffuse solar radiation indicates that the transmitted diffuse solar radiation may have been significantly underestimated throughout the entire day.

The limitations of this method are:

1. The spectral data of each IGU pane are lost when opting to manually overwrite the solar optical properties inputs.
2. WINDOW determines the angular dependent properties of coated glass based on regression equations; it is stated that these solutions are not exact and need improvement (Curcija et al., 2018). The low-e coating on IGU's surface 2 makes the calculation less accurate than an IGU with uncoated glass.
3. The hemispherical solar optical properties require the integration of the true solar optical properties at each angle of incidence. Since the true values of the $\theta = 0$ properties are manually replaced, the rest of the angular properties determined by WINDOW will be incorrect, and the hemispherical solar optical properties will also be affected. This results in an incorrect amount of transmitted and reflected diffuse solar radiation, which becomes more pronounced when attempting to calculate the SHGC for θ approaching 90°. Due to this, at $\theta = 90$, the hemispherical properties become $\tau_{sol} = 1$ and results in SHGC=0, and the diffuse solar radiation is entirely unaccounted for.

	0	10	20	30	40	50	60	70	80	90	Hemis
Tsol	0.331	0.331	0.326	0.320	0.313	0.299	0.269	0.206	0.101	0.000	0.280
Abs1	0.246	0.246	0.254	0.260	0.261	0.265	0.279	0.293	0.247	0.001	0.263
Abs2	0.100	0.100	0.099	0.099	0.098	0.096	0.090	0.075	0.050	0.000	0.090
Rfsol	0.323	0.323	0.320	0.321	0.328	0.340	0.362	0.426	0.602	0.999	0.357
Rbsol	0.314	0.314	0.313	0.313	0.317	0.326	0.349	0.415	0.585	1.000	0.346
Tvis	0.489	0.489	0.483	0.475	0.465	0.447	0.405	0.314	0.160	0.000	0.418
Rfvis	0.360	0.360	0.356	0.356	0.361	0.371	0.390	0.449	0.620	0.999	0.387
Rbvis	0.375	0.375	0.374	0.376	0.381	0.393	0.419	0.493	0.674	1.000	0.413

Figure 9.15.11: Incorrect hemispherical properties resulting from the workaround method

9.16. SHGC Characterization: June 20 to June 21, indoor convective and long-wave radiation components

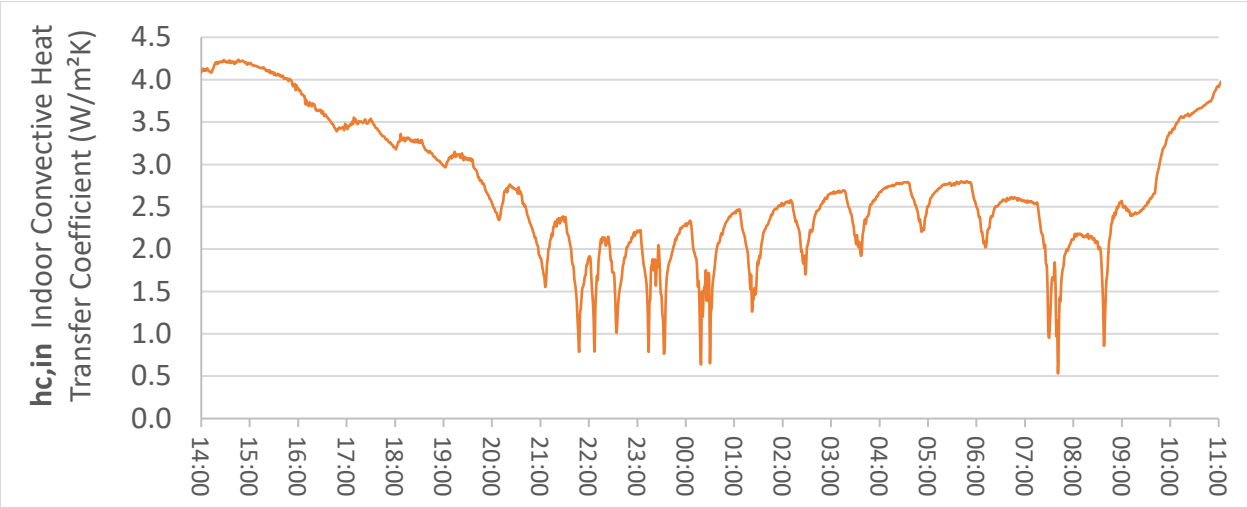

Figure 9.16.1: Calculated convective heat transfer coefficient over time determined from measured temperature from June 20 14:00 to June 21 11:00, 2023

The convective heat transfer coefficient was calculated based on Eq (6.2.4) to (6.2.8).

The $h_{c,in}$ ranges between 0.5 and 4.2 W/m^2K, it fluctuates largely depending on the temperature difference between the CoG and indoor air. As expected, it is higher during the daytime when the CoG is warmer, and much lower at night when the CoG is close to the indoor air temperature which fluctuates somewhat due to the air conditioning cycling on and off.

Even though there seem to be multiple ways to obtain the value for $Q_{r,in}$, the long-wave radiation heat transfer is difficult because the values obtained from Method A tend to be significantly lower than those from Method B. It is unclear which method presents the more representative values.

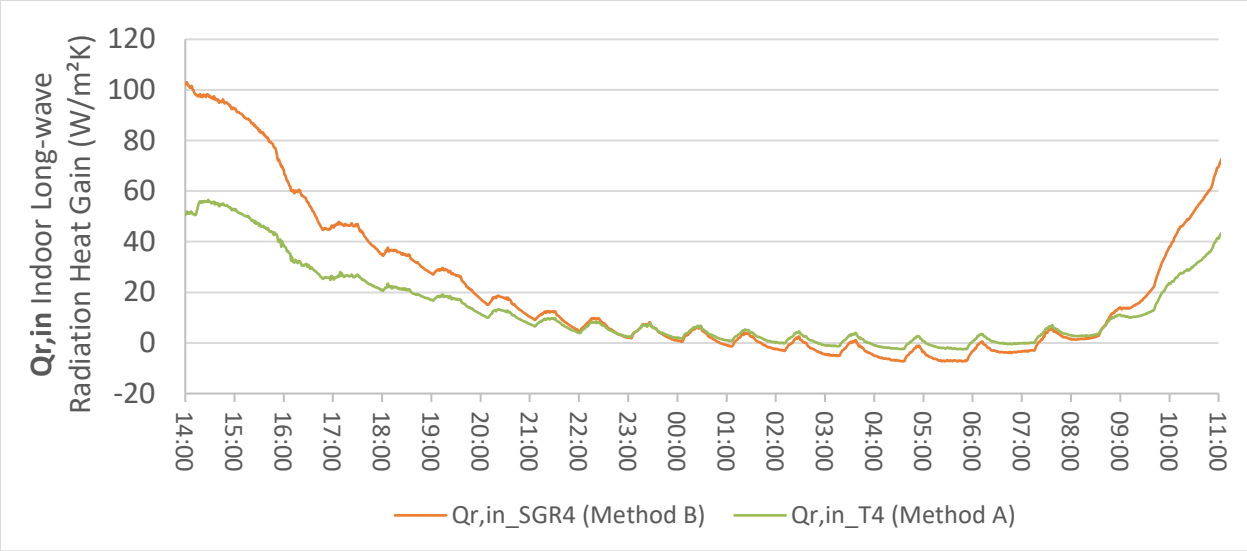

Figure 9.16.2: Comparison of measured and calculated long-wave radiation emitted by IGU surface #4 from June 20 14:00 to June 21 11:00, 2023

During the day, when solar radiation is present and the IGU is warmer, the values obtained from Method B (using SGR4 data) can be twice as high as those found from Method A (using temperature data only).

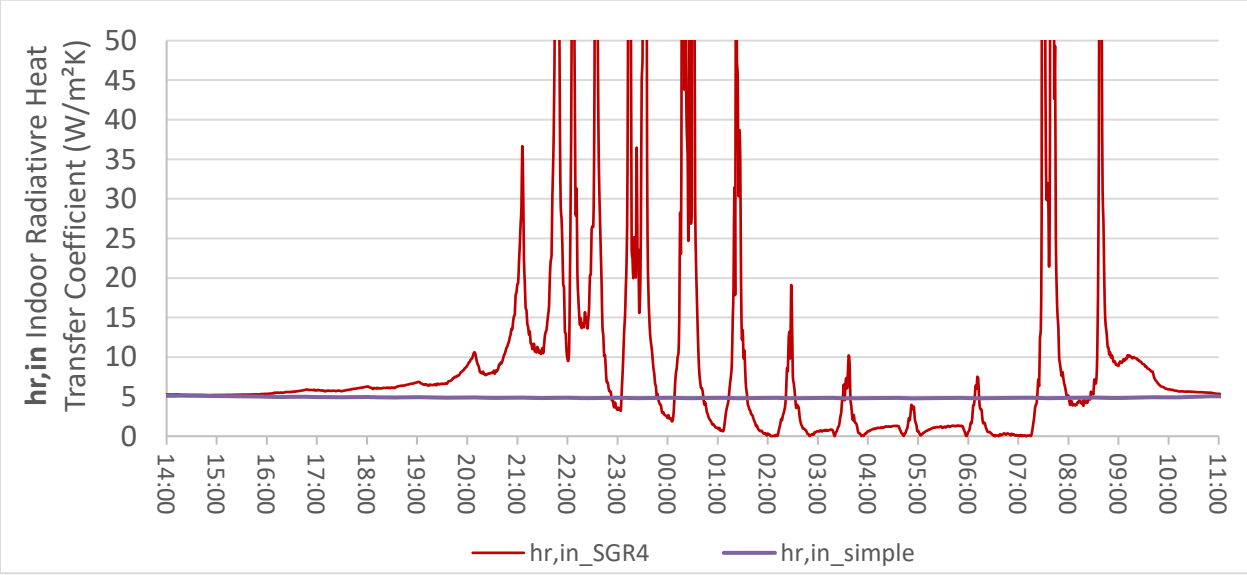

Figure 9.16.3: Comparison of indoor radiative heat transfer coefficient from Equations (6.2.12) and (6.2.13) from June 20 14:00 to June 21 11:00, 2023.

The interior radiative heat transfer coefficient were determined using Equations (6.2.12) and (6.2.13). The value determined by $h_{r,in_{simple}}$ is quite stable throughout the entire day at about 5

W/m^2K. The $h_{r,in}$ determined from Method B stays stable around noon time, but often spikes up to 1000 $\frac{W}{m^2K}$ at from late afternoon to mid morning, which may be due to the changing CoG temperature and indoor temperature spikes from the air conditioning.

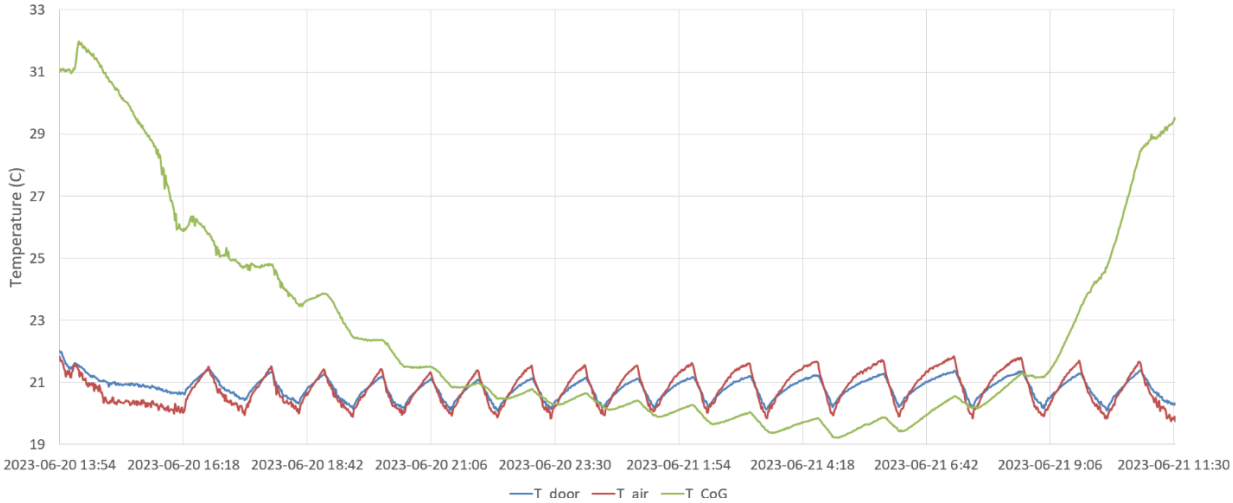

Figure 9.16.4: Comparison of temperature of Test Cell 5 room air, door surface, and IGU surface #4's CoG

The air temperature near the door and the temperature of the door surface (covered by black Bristol board) measured by the Type-T thermocouples are close, within less than $0.7°C$ difference between each other. The door surface has a slightly higher temperature during the afternoon, while the air temperature is slightly higher during the morning and night. The IGU's CoG temperature follows the same oscillating trend as the air and door temperatures in the evening, presumably due to the cycling of air conditioning with a $20°C$ thermostat setpoint and a $\pm 2°C$ deadband.

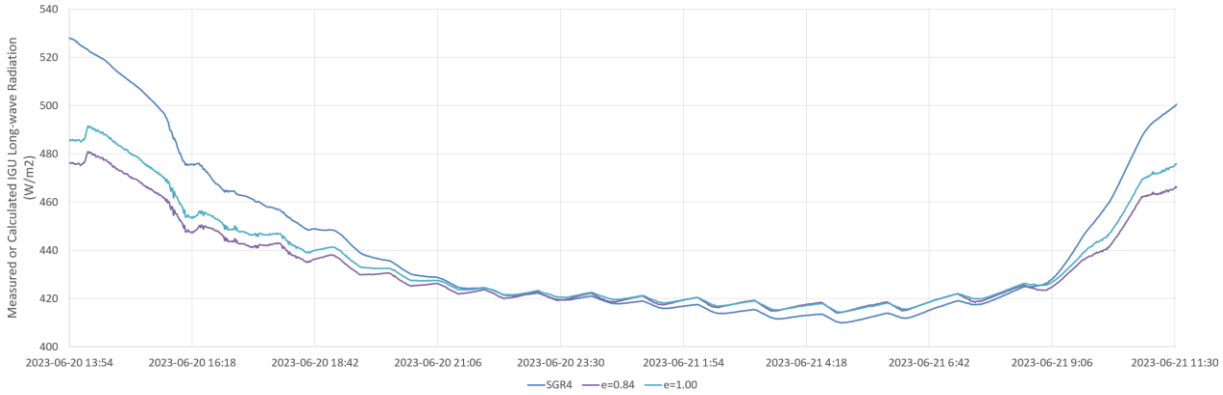

Figure 9.16.5: Comparison of measured (SGR4 data) and calculated (from T_4 data) long-wave radiation emitted by IGU surface #4

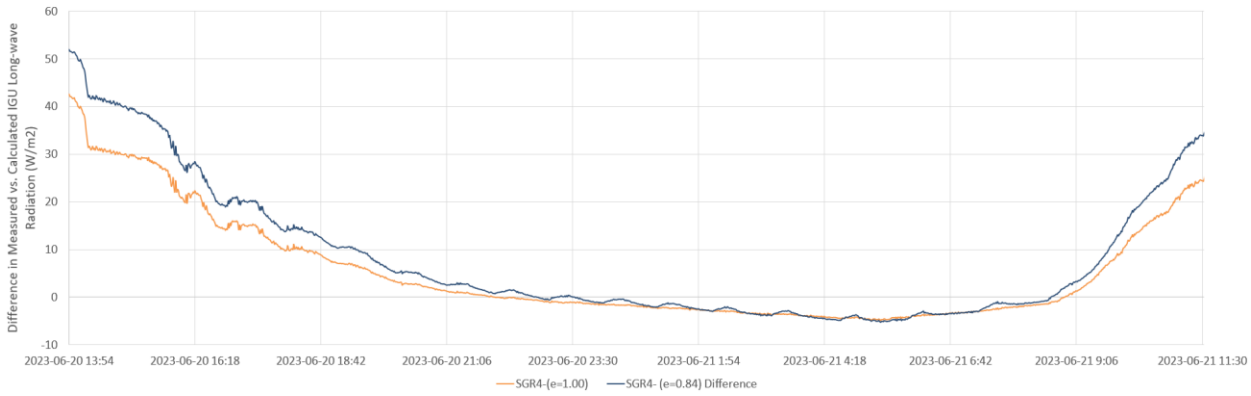

Figure 9.16.6: Comparison of difference of measured $E_{4,in}$ from the SGR4 pyrgeometer and the calculated $E_{4,in}$ between assumptions of $\varepsilon_4 = 0.84$ and $\varepsilon_4 = 1.00$

Assuming $\varepsilon_4 = 0.84$ (according to IGDB and WINDOW) and $\varepsilon_{rm} = 0.9\,0$, using Equation (6.2.10), $E_{4,in}$ is about 50 W/m^2 lower than the value measured by the SGR4 pyrgeometer (which is measuring $Q_{r,4}$ directly) at high solar irradiance, while it is about 10 W/m^2 higher than the SGR4 value past mid-night until early morning, perhaps due to night time radiative losses to the sky from the IGU. SGR4's measured values are still higher than the maximum possible assumption of $\varepsilon_4 = 1$ by 40 W/m^2. The reason for the higher values from the SGR4 sensor is unclear. A "black box test" was performed to examine this issue.

9.17. SHGC Characterization: June 14 to June 20 Long-wave radiation measurement discrepancies

Black box test to examine pyrgeometer response

To investigate the behaviour of the SGR4 sensor, the sensor setup was encased in a box made of black tri-fold display board. The box was expected to act as a cavity absorber with thermal radiation absorbed with $\varepsilon \approx 1$. The box is placed close to the IGU, allowing solar radiation to heat up the box from the outside during the day. Images of the experimental setup and graphs of the results are shown in Figures Figure 9.17.1 to Figure 9.17.3.

The box can be considered a sealed cavity with black inner surfaces. As expected, the tri-fold black box was heated up by the solar heat gains through the IGU and emitted higher infrared radiation during the day. The SGR4 sensor responded to these changes at the same time as the temperature of the box changed. The expected emissivity is between $0.95\ to\ 1$. However, the SGR4 sensor still recorded values about 65 W/m^2 higher at noon than the calculated infrared radiation when assuming $\varepsilon = 1$ (about 14% difference above expected value).

Figure 9.17.1: SGR4 test setup inside the black Tri-Fold cardboard box enclosure

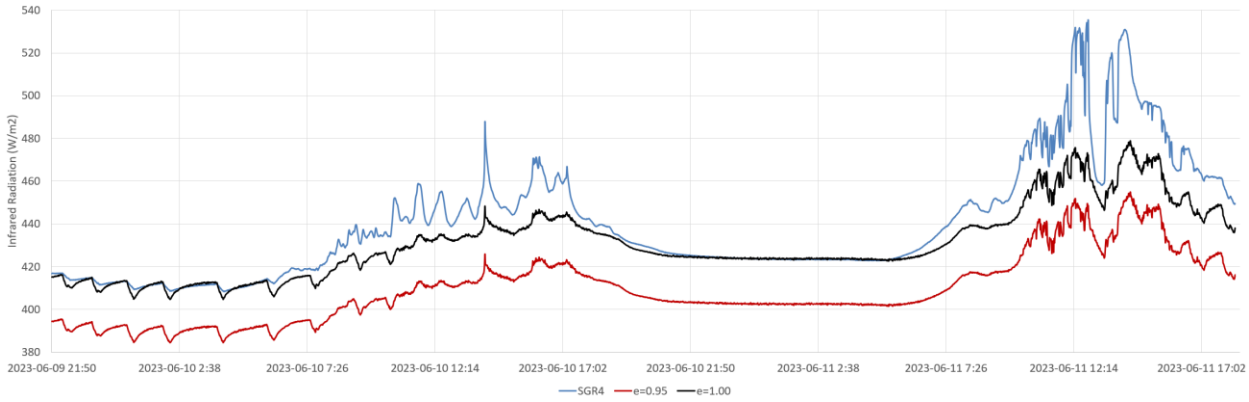

Figure 9.17.2: Comparison of calculated and measured long-wave radiation emitted by the black cardboard box surface

The $\varepsilon \approx 0.95$ and $\varepsilon \approx 1$ infrared radiation values were calculated from the thermocouple box temperature readings based on the Stefan-Boltzmann law.

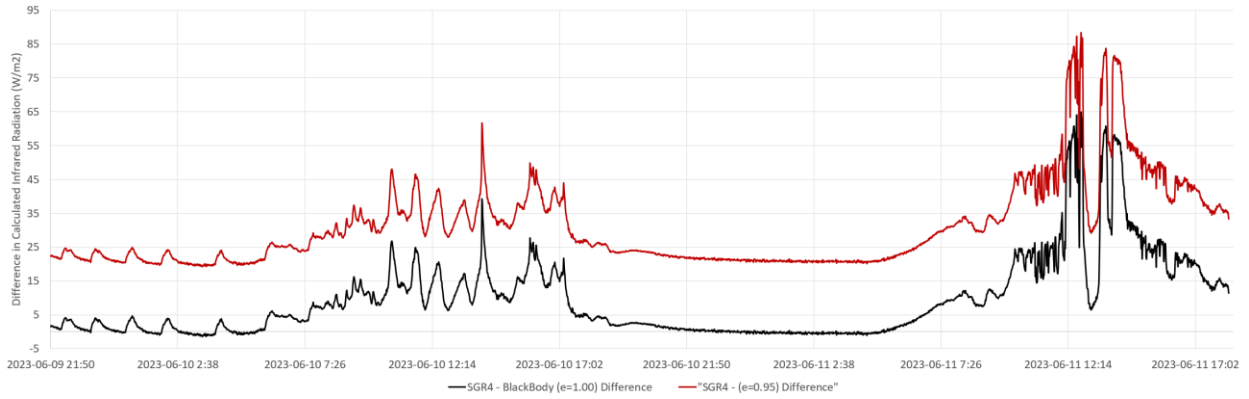

Figure 9.17.3: Comparison of differences in calculated and measured long-wave radiation emitted by the black cardboard box surface

Pyrgeometer facing indoor surfaces

A longer monitoring period was also setup with the SGR4 sensor facing the indoor surfaces to measure $E_{rm,out}$ directly. Since only one SGR4 sensor was available, the infrared radiation from the IGU could not be measured directly and were determined from the CoG thermocouple temperature readings instead.

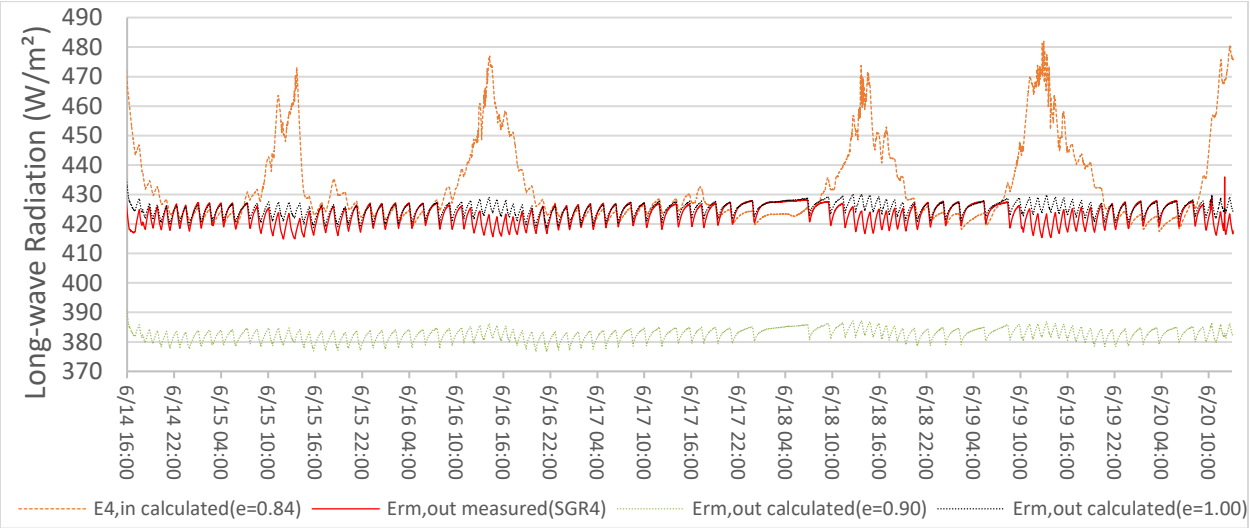

Figure 9.17.4: Comparison of measured and calculated long-wave radiation from June 14 16:00 to June 20 11:00, 2023.

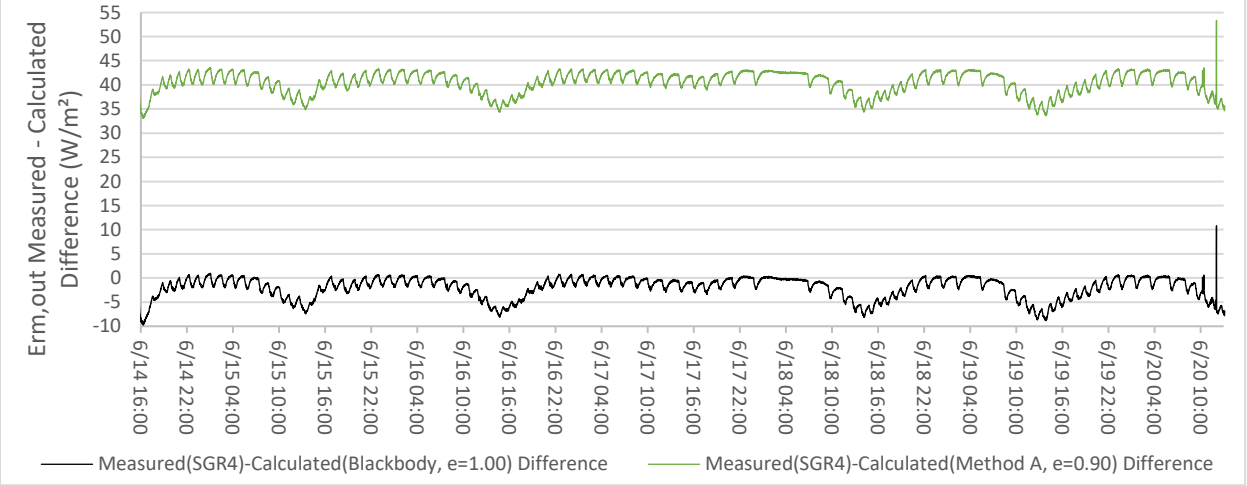

Figure 9.17.5: Comparison of difference of measured long-wave radiation reemitted by the room surface $E_{rm,out}$ from the SGR4 pyrgeometer and the calculated $E_{rm,out}$ between assumptions of $\varepsilon_4 = 0.90$ and $\varepsilon_4 = 1.00$

Between June 14th to June 20th, the measured outgoing infrared radiation from the room is has about 9.6% (or 40.5 W/m²) difference on average from the calculated infrared radiation estimated from assuming the room's effective emissivity as $\varepsilon = 0.90$, or about 0.5% (or 2.0 W/m²) difference on average assuming the room behaves as a blackbody ($\varepsilon = 1.00$). In this case, the value measured from SGR4 is somewhere between the two, as opposed to being higher than the value estimated from the Stefan-Boltzmann law with $\varepsilon = 1.00$ as seen in other cases. This suggests that the method of estimating the outgoing infrared radiation from the room (for use in the Method A and Method B calculations for $E_{rm,out}$) used in analyzing experimental data from

other monitoring periods can be made consistent with the value measured by the SGR4 instrument if the room emissivity is assumed to be close to $\varepsilon = 1.00$, while the assumption of $\varepsilon = 0.90$ based on the room's white painted walls can produce larger long-wave radiation discrepancies with the SGR4 measured values. More investigation is needed to determine why the SGR4 measures infrared radiation higher than those expected from black body ($\varepsilon = 1.00$) surfaces, as important conditions of the experimental setup have been overlooked.

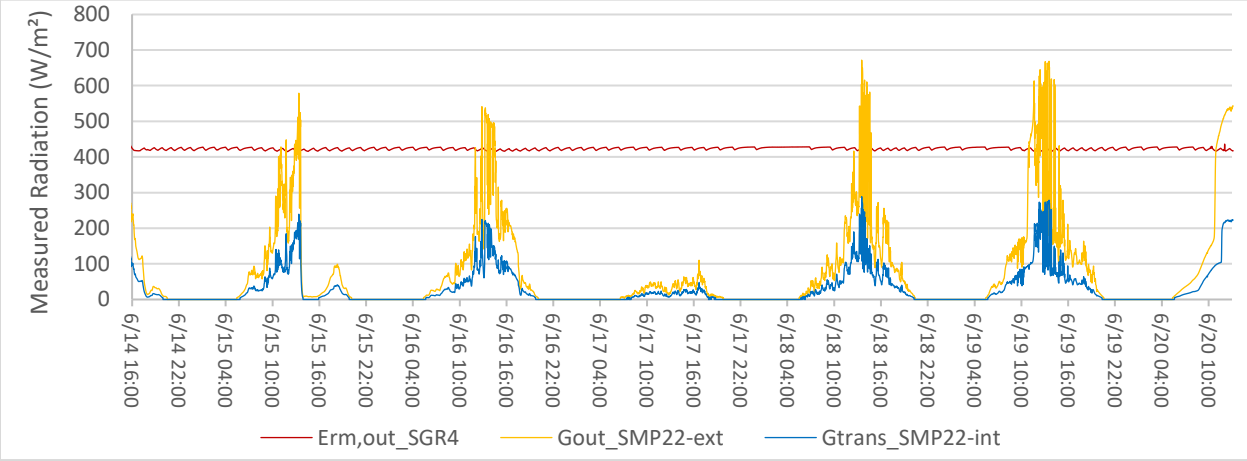

Figure 9.17.6: Measurements of incident solar irradiance G_{out} from the exterior SMP22, transmitted solar radiation G_{trans} from the interior SMP22 and long-wave radiation remitted by the room surface $E_{rm,out}$ from the interior SGR4 sensors throughout June 14 16:00 to June 20 11:00, 2023.

As expected, the measured outgoing infrared radiation from the test cell room is relatively constant throughout the monitored days since the room temperature is maintained by the air conditioning to be at about $20°C$.

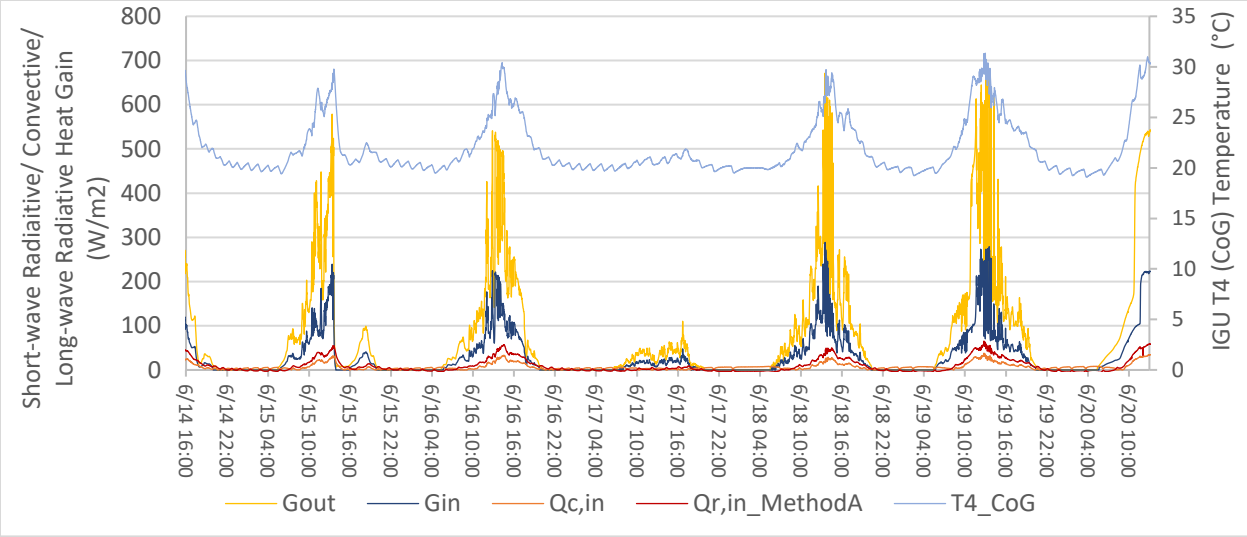

Figure 9.17.7: IGU temperature, Inward flowing convective and long-wave radiative heat gain, incident solar radiation and transmitted solar radiation from June 14 16:00 to June 20 11:00, 2023

The component values which were used to determine SHGC are shown in Figure 9.17.7. As expected, the heat gain from convective and infrared radiation are comparable in magnitude, while the largest component of SHGC is coming from the transmitted solar radiation.

9.18. SHGC Characterization: Measurement at different heights

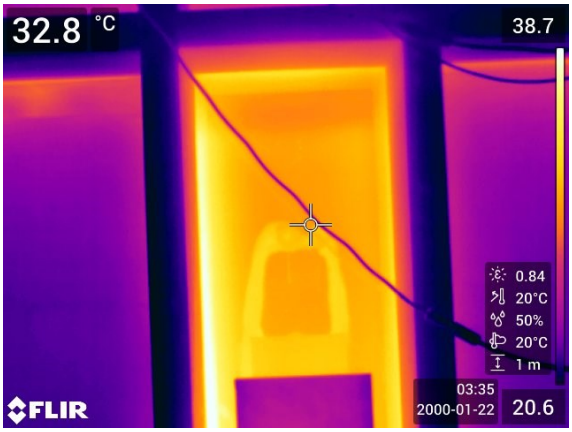

Figure 9.18.1: Infrared camera measurement of the glass temperature near the top portion of the IGU

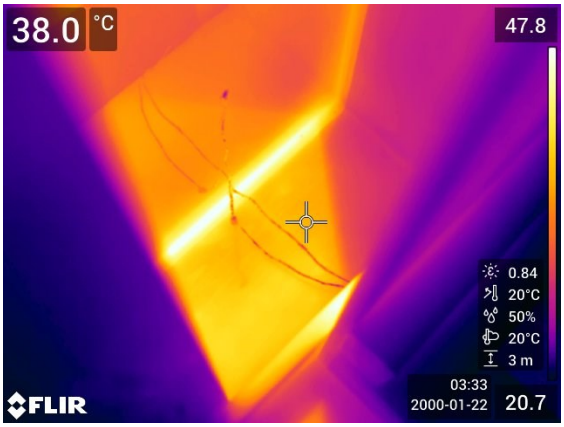

Figure 9.18.2: Infrared camera measurement of the wood frame temperature at the bottom of the IGU

Short duration measurements were made to determine SHGC at different heights on June 21st between 12:30 to 14:30. For the top portion of the IGU, the SHGC was determined using Method C (using the FLIR T540-42 to measure the temperature of the top portion of the glazing) due to having direct normal line of sight (the wooden stand for the SMP22 and SGR4 does not cover up the top portion of the IGU), while for the bottom portion of the IGU, Method B was used (a Type-T thermocouple has been positioned there). The SMP22 and SGR4 sensor stand were adjusted to match these heights. The results are shown in Figure 9.18.3. Although the values appear to fall between the solar transmittance and SHGC values determined from WINDOW 7.7, due to reasons discussed in Appendix 9.15 and Chapter 6.3, these results are inconclusive and further improvements to the methodologies are required.

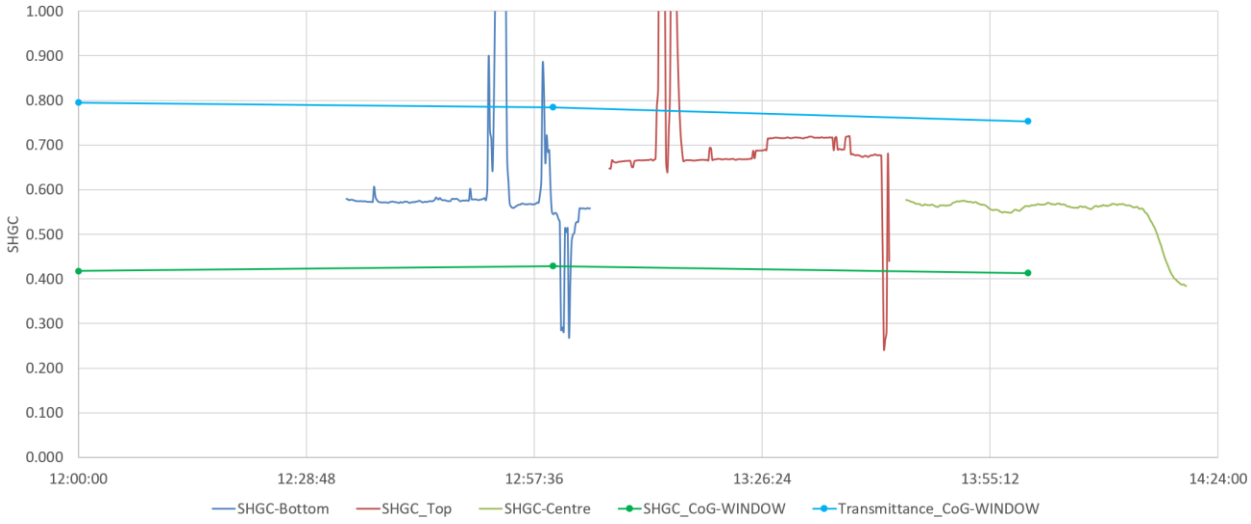

Figure 9.18.3: SHGC at different heights using in-situ methodology compared to WINDOW calculations